

CFD ANALYSIS OF SOLID-LIQUID-GAS INTERACTIONS IN FLOTATION VESSELS

by

Mohsen Karimi

Dissertation presented for the Degree

of

DOCTOR OF PHILOSOPHY
(Extractive Metallurgical Engineering)



in the Faculty of Engineering
at Stellenbosch University

Supervisor

Prof. G. Akdogan

Co-Supervisor

Prof. S.M. Bradshaw

April 2014

DECLARATION

By submitting this dissertation electronically, I declare that the entirety of the work contained therein is my own, original work, that I am the sole author thereof (save to the extent explicitly otherwise stated), that reproduction and publication thereof by Stellenbosch University will not infringe any third party rights and that I have not previously in its entirety or in part submitted it for obtaining any qualification.

...Mohsen Karimi...

Signature

.....14 February 2014....

Date

ABSTRACT

A Computational Fluid Dynamics (CFD) model was developed for the prediction of flotation rate constants in a stirred flotation tank and validated against experimental data. The model incorporated local, time-varying values of the turbulent flow field into an existing kinetic flotation model based on the Generalised Sutherland Equation to predict the overall flotation rate constant. Simulations were performed for the flotation of various minerals at different operational conditions and the predictions were compared with experimental data. It was found that the CFD-based model yielded improvements in the prediction of flotation rate constant for a range of hydrophobicities, agitation speeds and gas flow rates compared with existing methodologies, which use volume-averaged empirical expressions for flow variables. Moreover, comparing to the available CFD alternatives for the flotation modelling this approach eliminates the need for solving an extra partial differential equation resulting in a more computationally economic model.

The model was developed in three stages. In the first, a single-phase model was used to establish the requirements for successful modelling of the velocity components and turbulent properties of water inside flotation tanks. Also, a novel use of the Grid Convergence Index for this application was carried out, which allowed determination of the maximum achievable reduction in numerical uncertainties through systematic grid refinement and adaptation. All subsequent simulations were performed at the optimal discretization level determined in this manner. It was found that the Moving Reference Frames (MRF) method was adequate for representation of the impeller movement when the rotational zone was located close to the impeller, using a time step advance of between 10° and 15° of impeller rotation. Comparison of the different turbulence models for the single-phase modelling revealed that the standard k- ϵ and Large Eddy Simulation turbulence models both performed equally well and that the computational requirement was lower for the standard k- ϵ model, making it the method of choice. Validation of the methodology was done by comparison with experimental data for two different stirred tanks including an unbaffled mixer and a fully baffled standard Rushton turbine tank. The validation against experimental data showed that the model was capable of predicting the flow pattern, turbulent properties and the generation of trailing vortices.

The second stage of modelling used an Eulerian-Eulerian formulation for gas-liquid modelling of gas-sparged fully baffled vessels (2.25 l, 10 l and 50 l) using a Rushton turbine. It was determined that the minimum model uncertainty resulting from simulation of the sparger was achieved using a disk sparger with a diameter equal to 40% of the impeller diameter. The only significant interfacial force was found to be the drag force, and this was included in the multiphase methodology. A parametric study on the available formulations for the drag coefficient was performed which showed that the effect of turbulence on the air bubbles can accurately be represented using the proposed model of Lane (Lane, 2006). Validation of the methodology was conducted by comparison of the available experimental gas holdup measurements with the numerical predictions for three different scales of Rushton turbine tanks. The results verified that the application of the designed sparger in conjunction with Lane drag coefficient can yield accurate predictions of the gas-liquid flow inside the flotation tank with the error percentage less than 6%, 13%, and 23% for laboratory, pilot and industrial scale Rushton turbine tanks, respectively.

The last stage of this study broadened the Eulerian-Eulerian framework to predict the flotation rate constant. The spatially and temporally varying flow variables were incorporated into an established fundamental flotation model due to Pyke (Pyke, 2004) based on the Generalized Sutherland equation for the flotation rate constant. The computation of the efficiency of the flotation sub-processes also incorporated the turbulent fluctuating flow characteristics. Values of the flotation rate constants were computed and volume-weight averaged for validation against available experimental data. The numerical predictions of the flotation rate constants for quartz particles for a range of particle diameters showed improvements in the predictions when compared with values determined from existing methodologies which use spatially uniform values for the important hydrodynamic variables as obtained from empirical correlations. Further validations of the developed CFD-kinetic model were carried out for the prediction of the flotation rate constants of quartz and galena floating under different hydrophobicities, agitation speeds and gas flow rates. The good agreement between the numerical predictions and experimental data (less than 12% error) confirmed that the new model can be used for the flotation modelling, design and optimization. Considering the limited number of CFD studies for flotation modelling, the main contribution of this work is that it provides a validated and optimised

numerical methodology that predicts the flotation macro response (i.e., flotation rate constant) by integrating the significance of the hydrodynamic flow features into the flotation micro-processes. This approach also provides a more economical model when it is compared to the available CFD models for the flotation process. Such an approach opens the possibility of extracting maximum advantage from the computed parameters of the flow field in developing more effective flotation devices.

OPSOMMING

'n Wye verskeidenheid van industriële toepassings gebruik meganiese geroerde tenks vir doeleindes soos die meng van verskillende vloeistowwe, verspreiding van 'n afsonderlike fase in 'n deurlopende vloeistoffase en die skeiding van verskillende komponente in 'n tenk. Die hoofdoel van die tesis is om 'n numeriese model te ontwikkel vir 'n flotteringsstank. Die kompleksiteit van die vloeï (drie-dimensioneel, veelvuldige fases en volledig turbulent) maak die voorspelling van die werksverrigting van die flottasieproses moeilik. Konvensioneel word empiriese korrelasies gebruik vir modellering, ontwerp en die optimalisering van die flotteringsstanks. In die huidige studie word 'Computational Fluid Dynamics' (CFD) egter gebruik vir die modelleringsdoel, aangesien dit 'n alternatief bied vir empiriese vergelykings deurdat dit volledig inligting verskaf aangaande die gedrag van vloeï in die tenk. Die model is ontwikkel in drie agtereenvolgende stadiums. Dit begin met 'n strategie vir enkelfase modellering in die tenk, vorder dan na 'n gas-vloeïstof CFD model en brei dan die tweede stap uit om 'n CFD model te skep vir die skeidingsproses deur flottering.

'n Enkelfase model, gebaseer op die kontinuïteits- en momentumvergelykings, dien as basis vir die flottasie model. Die 'Multiple Reference Frames' (MRF) metode word gebruik om die rotasie van die stuurer na te boots, terwyl die dimensies van die rotasie-sone gekies is om die gepaardgaande onsekerhede, insluitend die model- en numeriese foute veroorsaak deur die dimensies van die roterende sones, te verminder. Die turbulensie model studie het getoon dat die standaard $k-\epsilon$ turbulensie model redelike akkuraatheid kon lewer in die numeriese voorspellings en die resultate verskil in gemiddeld net minder as 15% van die eksperimentele lesings, terwyl die rekenaartyd min genoeg was om die simulاسies op 'n persoonlike rekenaar uit te voer. Verder het die 'Grid Convergence Index' (GCI) metode die inherente onsekerhede in die numeriese voorspellings gerapporteer en gewys dat die onderskatting van die turbulensie wat algemeen plaasvind reggestel kan word deur van 'Large Eddy' (LES) of 'Direct Numerical Simulations' (DNS) gebruik te maak. Die metode wat ontwikkel is, is op twee tipes geroerde tenks getoets, naamlik 'n onafgeskorte menger en 'n standaard Rushton turbine tenk. Die numeriese resultate is teen eksperimentele data gevalideer en het gewys dat die model in staat is om die vloeïpatrone, turbulensie einskappe en die vorming van agterblywende

vortekse te voorspel. Die CFD resultate het getoon dat die vloeipatroon twee simmetriese rotasies siklusse bo en onder die roterende sone vorm, terwyl die vlak van die ooreenkoms tussen die numeriese voorspellings van die turbulente eienskappe en die eksperimentele lesings met minder as 25% verskil.

As die tweede stap van hierdie navorsing is 'n Eulerian-Eulerian struktuur ontwikkel vir die gas-vloeistof modellering binne 'n standaard Rushton turbine flotteringstenk. Soos vir die enkelfase modellering is die Reynolds spanningstensor opgelos deur die standaard k- ϵ turbulensie model, terwyl die lugborrels ingevoer/versamel is in/van die tenk deurmiddel van bron/sink terme. Verskeie 'sparger' rangskikkings is in die tenk geïmplementeer om die onsekerheid in die model weens die metode van luginspuiting te verminder. Verder is verskillende korrelasies vir die sleursyfer vergelyk vir laminêre en turbulente vloei in die tenk. Daar is gevind dat die skyf 'sparger', met 'n deursnee gelykstaande aan 40% van die stuur deursnee, in samewerking met die voorgestelde model van Lane (Lane, 2006) vir die bepaalde sleursyfer die naaste ooreenkoms met die eksperimentele metings lewer (met 'n gemiddelde verskil van minder as 25%). 'n Vergelykende studie is ook uitgevoer om die gevolge van die gas vloeitempo en roerspoed vir drie verskillende geroerde tenks met volumes van 2.5 l, 10 l en 50 l te ondersoek. Die resultate van hierdie afdeling bevestig dat die CFD metode in staat was om die gas-vloeistof vloei in die flotteringstenk korrek te voorspel.

Die veelvuldigefase model wat ontwikkel is, is uitgebrei vir flottasie modellering. Dit behels die integrasie van die CFD resultate met die fundamentele flottasie model van Pyke (Pyke, 2004) vir die flotteringstempo konstant. Die CFD model is toegerus met Pyke se model deur aanvullende gebruiker gedefinieerde funksies. Die CFD-kinetiese model is geëvalueer vir die flottering van kwartsdeeltjies en die resultate het die geloofwaardigheid van die model bevestig, aangesien die gemiddelde verskil tussen die numeriese voorspellings vir die flotteringstempo konstante en die eksperimentele data minder as 5% was. Die resultate is ook vergelyk met die analitiese berekeninge van Newell en daar is bevind dat die model vergelykbare voorspellings van die flotteringstempo konstantes lewer, met die 'root mean square deviations' (RMSD) gelyk of minder as die RMSD waardes vir die analitiese berekeninge. Verdere ondersoeke van die CFD-kinetiese model bestaan uit 'n parametriese studie wat die gevolge van die roertempo, gas vloeitempo en die

oppervlak hidrofobisiteit op die flottering van kwarts- en galenietdeeltjies bestudeer. Die aanvaarbare ooreenkoms tussen die numeriese voorspellings en eksperimentele data (oor die algemeen minder as 12% fout) bewys dat die nuwe model gebruik kan word vir flotterings modellering en optimalisering.

ACKNOWLEDGEMENTS

First and foremost I sincerely thank my supervisor, Professor Guven Akdogan, for his endless supports, and invaluable discussions. Thanks also go to my co-supervisor, Professor Steven M. Bradshaw, for his supervision, assistance and encouragement throughout my PhD study.

I would also like to thank the OSP funding and the South African Minerals to Metals Research Institute (SAMMRI) for the financial supports.

Many thanks to Dr. Kiran H. Dellimore for helping me in coding and bringing the GCI method from aerospace to mineral processing. Appreciation is also expressed to QFINSOFT Co. staff, specifically Dr. Danie de Kock and Stephan Schmitt, for their consultants.

To my colleagues and friends, Deside, Henri, Takura, Iku, Bawemi, KJ, Amir, and Hamed, thank you for your advice and friendships that made this research enjoyable.

Never enough thanks to my mom, dad, sister and brother who cared enough about me to ask how it was all going and for their never-ending good wishes and encouragements from afar.

TABLE OF CONTENTS

Chapter 1 Introduction	1
1.1. General background.....	1
1.2. Objectives	6
1.3. Limitations.....	8
1.4. Contributions and Novelty	9
1.5. Organization of this thesis	11
Chapter 2 Literature review	13
2.1. Introduction	13
2.2. Single-phase simulations of stirred tanks	15
2.3. Summary of single-phase simulations of stirred tanks	32
2.4. Gas-liquid simulations of stirred tanks	38
2.5. Summary of gas-liquid simulations of stirred tanks	51
2.6. Flotation.....	54
2.6.1. Kinetic-based models for the flotation separation.....	55
2.6.2. CFD-based models for the flotation separation.....	62
2.7. Conclusion.....	71
Chapter 3 Development of a CFD methodology for single-phase flow in stirred tanks	74
3.1. Introduction	74
3.2. Governing equations.....	75
3.3. Results and discussion	80
3.3.1. Simulations of single-phase flow inside an unbaffled mixer	80
3.3.2. Simulations of single-phase flow inside a standard Rushton turbine.....	101
3.4. Conclusion.....	129
Chapter 4 Development of a CFD methodology for gas-liquid flow in stirred tanks	132

4.1. Introduction	132
4.2. Governing equations.....	136
4.3. Results and discussion.....	141
4.3.1. Sparger design	142
4.3.2. Comparison of different drag coefficient correlations	148
4.3.3. Simulations of the gas-liquid flow for different operational and geometrical conditions	157
4.4. Conclusion.....	167
Chapter 5 CFD modelling of the flotation sub-processes.....	170
5.1. Introduction	170
5.2. Fundamental flotation model due to Pyke.....	173
5.2.1. Limitations and simplifying assumptions in the fundamental flotation model due to Pyke.....	178
5.3. Results and discussion.....	190
5.3.1. Numerical approach.....	191
5.3.2. Limitations of the numerical approach.....	196
5.3.3. Validation of the model for quartz flotation rate constants	207
5.3.4. Validation of the model for galena flotation rate constants	219
5.3.5. Comparison of the developed CFD methodology with the available alternatives	224
5.4. Conclusion.....	225
Chapter 6 Conclusions and Recommendations.....	229
6.1. Research summary.....	229
6.2. Summary of the fundamental findings	231
6.3. Recommendations	234
Bibliography	238

Appendix A: CFD results of the tangential velocity predicted by different turbulent models	250
Appendix B: Results of the gas-liquid simulations for different operational and geometrical conditions	263
Appendix C: An user defined function example for the flotation sub-processes modelling	264
Appendix D: Summary of the operational conditions for the flotation simulations.	267

LIST OF FIGURES

Figure 1-1 Schematic illustration of a flotation vessel	2
Figure 3-1 Schematic of the entire unbaffled mixer tank.	81
Figure 3-2 Two examples of the rotational zone dimensions for the unbaffled mixer	82
Figure 3-3 Numerical predictions of the dimensionless velocity components as a function of non-dimensional distance from the shaft on plane 71: (a) axial velocity, (b) tangential velocity	84
Figure 3-4 The impeller positions at time step=0 and time step=1	85
Figure 3-5 Numerical predictions of non-dimensional tangential velocity (a) and turbulent kinetic energy (b) as a function of non-dimensional distance from the shaft	86
Figure 3-6 Schematic illustration of the boundary conditions for the slice modelling	88
Figure 3-7 Values of y^+ for seven different mesh schemes on the centre line of the blade.....	90
Figure 3-8 Values of y^+ for seven different mesh schemes on the centre line of the blade after mesh refinement.....	91
Figure 3-9 Maximum value of y^+ as a function of number of cells and CPU time for seven cases tested for slice modelling	92
Figure 3-10 Contour plots of the y^+ value for the case with 704, 818 cells.....	92
Figure 3-11 Locations of the selected points for the grid sensitivity test in the slice modelling	93
Figure 3-12 Tangential velocity as a function of cell number for the depicted points on Figure 3-11.....	94
Figure 3-13 Turbulent kinetic energy as a function of cell number for the depicted points on Figure 3-11	95
Figure 3-14 Numerical predictions of the tangential velocity with the RANS-based turbulence models for plane 233 mm from the bottom of the unbaffled mixer.....	97
Figure 3-15 LES predictions of the tangential velocity for plane 233 mm from the bottom of the unbaffled mixer	98

Figure 3-16 Numerical predictions of the tangential velocity on plane 233 mm from the bottom of the unbaffled mixer with k- ϵ standard and LES-kinetic energy..... 100

Figure 3-17 The schematic illustration of the Rushton turbine tank used for the water modelling 102

Figure 3-18 Measurement locations of Newell for the standard Rushton turbine tank 103

Figure 3-19 Numerical predictions of the tangential velocity as a function of vertical position for four different rotational zone dimensions in the standard Rushton turbine tank..... 104

Figure 3-20 Numerical predictions of velocity components as a function of non-dimensional distance from top of the tank in the high-turbulent region: (a) axial, (b) tangential, (c) radial 110

Figure 3-21 Numerical predictions of velocity components as a function of non-dimensional distance from top of the tank in the medium-turbulent region (d) axial, (e) tangential, (f) radial 111

Figure 3-22 Numerical predictions of turbulent kinetic energy (k) and turbulent dissipation rate (ϵ) as a function of non-dimensional distance from top of the tank (a and b) high turbulent region, (c and d) medium turbulent region..... 113

Figure 3-23 Locations of the examining points for the grid independence study in the standard Rushton turbine tank 114

Figure 3-24 Numerical variations of the axial velocity (a-c) and the turbulent kinetic energy (d-f) as a function of cell numbers for the standard Rushton turbine tank 115

Figure 3-25 Numerical predictions of resultant velocity as a function of non-dimensional distance from the top of the tank with different RANS-based turbulence model for standard Rushton turbine tank..... 117

Figure 3-26 LES predictions of resultant velocity as a function of non-dimensional distance from the top of the tank with sub-grid scale models for standard Rushton turbine tank 118

Figure 3-27 Numerical predictions of the resultant velocity; comparison of the k- ϵ standard turbulence model and LES with kinetic-energy subgrid scale model for the standard Rushton turbine tank	120
Figure 3-28 The predicted flow pattern for three different angular velocities of the Rushton turbine tank.....	121
Figure 3-29 The predicted contour plots of the turbulent kinetic energy for three different angular velocities of Rushton turbine tank.....	123
Figure 3-30 Numerical predictions of maximum turbulent kinetic energy as a function of angular velocity for the standard Rushton turbine tank.....	124
Figure 3-31 Predicted contour plots of the turbulent energy dissipation rate for three different angular velocities of Rushton turbine	124
Figure 3-32 Numerical predictions of maximum turbulent energy dissipation rate as a function of angular velocity for the standard Rushton turbine tank	125
Figure 3-33 Contour plots of velocity distribution and iso-surfaces of vorticity around the blades at three different impeller speeds for the standard Rushton turbine tank .	127
Figure 4-1 Schematic diagram of the ring and disk spargers.....	143
Figure 4-2 Schematic illustration of the laboratory-scale Rushton-turbine flotation tank showing the boundary conditions used in all simulations.....	145
Figure 4-3 Numerical predictions of the gas holdup for different sparger designs (a) ring sparger, (b) disk sparger, under laminar and turbulent flow	146
Figure 4-4 Numerical predictions of gas holdup with four different drag coefficient correlations for laminar flow regime inside the standard Rushton turbine tank.....	149
Figure 4-5 Numerical predictions of gas holdup with five different drag coefficient correlations for turbulent flow regime inside the standard Rushton turbine tank.....	151
Figure 4-6 Comparison of the air velocity vectors for the drag coefficient correlations at 350 rpm (a) Schiller-Naumann, (b) Bakker, and (c) Lane.....	152
Figure 4-7 Comparison of the air cavity locations for the different drag coefficients at 350 rpm (a) Schiller-Naumann, (b) Bakker, and (c) Lane.....	155

Figure 4-8 Comparison of the vorticity contours for the drag coefficient correlations at 350 rpm (a) Schiller-Naumann, (b) Bakker, and (c) Lane. 157

Figure 4-9 Numerical predictions of the gas holdup for the 2.5 l tank at four different impeller speeds (a) 350 rpm (b) 450 rpm (c) 550 rpm (d) 800 rpm as a function of superficial gas velocity 162

Figure 4-10 Numerical predictions of the gas holdup for the 10 l tank at three different impeller speeds (a) 300 rpm (b) 380 rpm (c) 470 rpm as a function of superficial gas velocity..... 164

Figure 4-11 Numerical predictions of the gas holdup for the 50 l tank at two different impeller speeds (a) 225 rpm (b) 330 rpm as a function of superficial gas velocity... 166

Figure 5-1 Schematic representation of the flotation sub-processes 171

Figure 5-2 Bond number as a function of particle size for different impeller speed. 185

Figure 5-3 Different slices inside the domain for the local investigation of the Bond number. 186

Figure 5-4 Stability probability as a function of particle size for four different impeller speeds..... 187

Figure 5-5 Rheometer measurements of relative viscosity as a function of angular velocity for different weight solid percentages of pulp 192

Figure 5-6 Elghobashi guideline for coupling between phases in multiphase flows (Elghobashi, 1991)..... 198

Figure 5-7 Particulate loading factor as a function of volume fraction for quartz and galena 205

Figure 5-8 Stokes number as a function of angular velocity of impeller for quartz and galena 206

Figure 5-9 (a) flotation rate constant as a function of particle size (b) comparison of the CFD and Newell computation errors for the prediction of the flotation rate constant [Operational conditions: $J_g = 0.35$ cm/s and impeller speed = 350 rpm].... 209

Figure 5-10 (a) flotation rate constant as a function of particle size (b) comparison of the CFD and Newell computation errors for the prediction of the flotation rate constant [Operational conditions: $J_g = 0.35$ cm/s and impeller speed = 450 rpm].... 210

Figure 5-11 (a) flotation rate constant as a function of particle size (b) comparison of the CFD and Newell computation errors for the prediction of the flotation rate constant [Operational conditions: $J_g = 0.35$ cm/s and impeller speed = 550 rpm]...212

Figure 5-12 (a) flotation rate constant as a function of particle size (b) comparison of the CFD and Newell computation errors for the prediction of the flotation rate constant [Operational conditions: $J_g = 0.35$ cm/s and impeller speed = 800 rpm]...214

Figure 5-13 Flotation rate constant of quartz as a function of particle size for two contact angles, $\theta_a = 73^\circ$ and $\theta_a = 80^\circ$ [Operational conditions: $J_g = 0.45$ cm/s and impeller speed = 470 rpm]216

Figure 5-14 Flotation rate constant of quartz as a function of particle size for two impeller rotational speeds, 470 rpm and 650 rpm [Operational conditions: $J_g = 0.35$ cm/s and $\theta_a = 73^\circ$]217

Figure 5-15 Flotation rate constant of quartz as a function of particle size for two gas flow rates, 3.5 l/min and 4.5 l/min [Operational conditions: impeller speed = 470 rpm cm/s and $\theta_a = 73^\circ$]219

Figure 5-16 Summary of the CFD simulations for the investigation of the effect of hydrophobicity and agitation speed on the flotation rate constant of galena.....220

Figure 5-17 Flotation rate constant of galena as a function of particle size for two contact angles, $\theta_a = 72^\circ$ and $\theta_a = 79^\circ$ [Operational conditions: $J_g = 0.55$ cm/s and impeller speed = 650 rpm]221

Figure 5-18 Flotation rate constant of galena as a function of particle size at different agitation speeds of impeller (a) for $\theta_a = 72^\circ$ and (b) for $\theta_a = 79^\circ$ [Operational conditions: $J_g = 0.55$ cm/s]223

LIST OF TABLES

Table 2-1 The CFD solvers and their capabilities (Schwarz, 1991).....	14
Table 2-2 Different cases studied by Brucato (Brucato et al., 1998a).....	20
Table 2-3 Summary of LES simulations by Bakker (Bakker and Oshinowo, 2004)...	24
Table 2-4 Classification of the previous literature on single-phase modelling of stirred tanks regarding to input, model and numerical uncertainties	34
Table 2-5 Summary of reviewed literature on gas-liquid simulations of stirred tanks	52
Table 2-6 Summary of reviewed literature on the CFD modelling of flotation separation process	69
Table 3-1 Model constants for Eq. 3.7 and Eq. 3.8	77
Table 3-2 Geometrical details of the unbaffled mixer	80
Table 3-3 Recommended skewness scale to evaluate the mesh quality	87
Table 3-4 Mesh details for the slice modelling.....	89
Table 3-5 Geometrical details of the standard Rushton turbine tank.....	102
Table 3-6 Mesh details used for the GCI test on the standard Rushton turbine tank	108
Table 3-7 Mesh details for the grid independence study of the standard Rushton turbine tank	114
Table 4-1 Different sparger designs tested in this study.....	144
Table 4-2 Numerical predictions of the gas holdup for two sparger configurations at three different positions	147
Table 4-3 Geometrical details of the three different Rushton turbine tanks.....	158
Table 4-4 Description of the different operational and geometrical conditions tested for the gas-liquid modelling.....	159
Table 5-1 Summary of forces exerted on a solid particle.	184
Table 5-2 Different methods of coupling between the dispersed phase and the continuous phase and ANSYS Fluent implementation.....	197

NOMENCLATURE

A	Induction time constant
Bo	Bond number
C^*	Fixed value for Bakker drag coefficient model
$C_{1\varepsilon}$	Model constant
$C_{2\varepsilon}$	Model constant
$C_{3\varepsilon}$	Model constant
C_A	Added mass coefficient
C_μ	Model constant
C_D	Drag Coefficient
$C_{D,0}$	Drag coefficient for stagnant liquid
d_b	Bubble diameter
d_p	Particle diameter
E	Constant
E_1^{fine}	Error in the solution for the fine mesh
E_2^{coarse}	Error in the solution for the coarse mesh
E_a	Bubble-particle attachment probability
E_c	Bubble-particle collision probability
E_{coll}	Bubble-particle collection efficiency
E_{c-GSE}	Generalized Sutherland Equation for bubble-particle collision performance
E_s	Bubble-particle stability probability
f	Drag function
\vec{F}	External body force
f_i	Flow solution for i^{th} grid spacing
\vec{F}_{lift}	Lift force
\vec{F}_{vm}	Virtual mass force
F_s	Safety factor
\vec{g}	Gravitational acceleration
G_b	Generation of turbulent kinetic energy due to buoyancy
GCI_1^{fine}	GCI value for fine mesh
GCI_1^{coarse}	GCI value for coarse mesh
G_{fr}	Gas flow rate
G_k	Generation of turbulent kinetic energy due to mean velocity gradient
h_i	Grid spacing
I	Unit tensor
k	Turbulent kinetic energy
k	Flotation rate constant
K	Correlation constant for Brucato model
K_{pq}	Interphase momentum exchange coefficient
k_{lq}	Covariance of the velocities for the water phase
\dot{m}_{pq}	Mass transfer from the p^{th} phase to the q^{th} phase
\dot{m}_{qp}	Mass transfer rate from q^{th} phase to the p^{th} phase
n	Coordinate normal to the wall
N_b	Bubble number concentration
N_p	Particle number concentration
p	Pressure
r	Grid refinement ratio
R_c	Capturing radius
Re	Reynolds number
Re_p	Particle Reynolds number
\vec{R}_{pq}	Interfacial force

S_m	Source term
S_k	Source term of turbulent kinetic energy
S_ε	Source term of turbulent dissipation rate
Stk	Stokes number
t	Time
t_{ind}	Induction time
T_L	Integral time scale
t_r	Residence time
\bar{U}^2	Mean squared velocity deviation of the fluid
U^*	Dimensionless velocity
u^*	Friction velocity
u_a	Axial velocity
\bar{U}_b^2	Average velocity of bubble relative to the liquid phase
\bar{u}_i	Mean velocity
u'_i	Instantaneous velocity
\bar{U}_p^2	Average velocity of particle relative to the liquid phase
U_S	Slip velocity
U_T	Terminal velocity
u_t	Tangential velocity
\vec{v}	Velocity vector
v_b	Bubble velocity
\vec{v}_{dr}	Drift velocity
\vec{v}_{pq}	Relative velocity between phase p and q
V_q	Volume of phase q
V_r	Reference volume
y^*	Dimensionless distance from the wall
y_P	Distance from point P to the wall
z	Bubble-particle collision kernel
Z_{pb}	Bubble-particle collision rate
Greek symbols	
α_q	Volume fraction of q^{th} phase
β	Attachment efficiency constant
ε	Energy dissipation rate
τ_i	Bubble/particle relaxation time
θ_a	Collision angle
θ_{max}	Largest angle in control volume
θ_{min}	Smallest angle in control volume
θ_r	Contact angle of the solid particle to the air bubble
θ_t	Maximum collision angle
κ	von Karman constant
λ	Kolmogorov turbulent scale
μ	Fluid viscosity
ν	Kinematic viscosity
ξ	Vorticity
ρ_b	Bubble density
ρ_f	Fluid density
ρ_p	Particle density
σ	Surface tension
σ_ε	Model constant
σ_k	Model constant
τ_w	Wall shear stress
$\vec{\omega}$	Angular velocity

Acronyms

<i>ASM</i>	Algebraic Stress Model
<i>CARPT</i>	Computer-Automated Radioactive Particle Tracking
<i>CFD</i>	Computational Fluid Dynamics
<i>CPU</i>	Central Processing Unit
<i>CT</i>	Computed Tomography
<i>DNS</i>	Direct Numerical Simulation
<i>EASM</i>	Explicit Algebraic Stress Model
<i>EFD</i>	Experimental Fluid Dynamics
<i>GCI</i>	Grid Convergence Index
<i>GHz</i>	Gigahertz
<i>GSE</i>	Generalized Sutherland Equation
<i>HPC</i>	High Performance Computer
<i>IBC</i>	Impeller-Boundary Condition
<i>IO</i>	Inner-Outer Method
<i>LDA</i>	Laser Doppler Anemometer
<i>LDV</i>	Laser Doppler Velocimetry
<i>LES</i>	Large Eddy Simulation
<i>LIF</i>	Laser Induced Fluorescence
<i>MRF</i>	Multiple Reference Frames
<i>MUSIG</i>	Multi-Size-Group
<i>PBT</i>	Pitched Blade Turbine
<i>PBE</i>	Population Balance Equation
<i>PDE</i>	Partial Differential Equation
<i>PIV</i>	Particle Image Velocimetry
<i>PLIF</i>	Planar Laser Induced Fluorescence
<i>RAM</i>	Random Access Memory
<i>RANS</i>	Reynolds Averaged Navier-Stokes
<i>RMS</i>	Root Mean Squared
<i>RNG</i>	ReNormalization Group
<i>RSM</i>	Reynolds Stress Model
<i>SIMPLE</i>	Semi-Implicit Method for the Pressure-Linked Equation
<i>QUICK</i>	Quadratic Upstream Interpolation for Convective Kinematics
<i>SM</i>	Sliding Mesh
<i>SST</i>	Shear Stress Transport
<i>UDF</i>	User Defined Function
<i>UDS</i>	User Defined Scalar
<i>VOF</i>	Volume Of Fluid

Chapter 1 Introduction

1.1. General background

Mechanically agitated vessels are used in a range of industrial applications such as minerals separation, chemicals production, papers recycling and the associated industries where the mixing is of vital importance. The mixing tank, with the help of an agitation system, provides the appropriate environment for the desired process to occur. For instance, the contacting of the liquid phase with the dispersed gas phase in the different types of converters or the solid suspension for the flotation separation process can be achieved using stirred tanks. There are two types of mixing patterns generated by impellers: axial-flow and radial-flow (Oldshue, 1983). The radial-flow stirring mechanism ejects the fluid toward the periphery of the vessel creating two upward and downward streams which is favourable for the gas-liquid, liquid-liquid and other multiphase dispersion applications. On the other hand, the axial-flow impeller forms vertical currents along with the impeller shaft. This type of mixing pattern is, however, more suitable for blending and heat transfer (Joshi et al., 2011b).

In this research radial-flow impellers are used to study the single-phase, multiphase and the flotation sub-processes in the mechanically stirred tanks. The major aim of this investigation is to develop a methodology for the flotation modelling based on the hydrodynamic aspects of the process. The single-phase and the gas-liquid modelling parts are, therefore, prerequisite steps for the flotation modelling. The findings of these two stages will be transferred for the flotation sub-processes modelling.

Flotation is a three-phase separation process where the valuable minerals are preferentially transferred to the froth phase by the aid of air bubbles. The process initiates when the air bubbles and solid particles collide; the hydrophobic surface of the valuable minerals helps the particles to attach to the air bubbles and form bubble-particle aggregates. The stable bubble-particle aggregates then rise up to the surface of the vessel where they can be successfully recovered. Figure 1-1 shows the flotation separation process. In this figure the froth zone is illustrated at the top of the vessel

where the hydrophobic (or valuable) minerals are removed. The pulp phase, where the flotation sub-processes take place, is also demonstrated. As seen from the zoomed image of one air bubble, the solid particles from the pulp phase collide with the air bubbles and particles with hydrophobic surfaces will attach to the air bubbles. Figure 1-1 shows the importance of the mixing phenomenon inside a mechanically agitated flotation tank, since it provides gas dispersion and solid suspension, which in turn establish a suitable environment for the flotation process to occur.

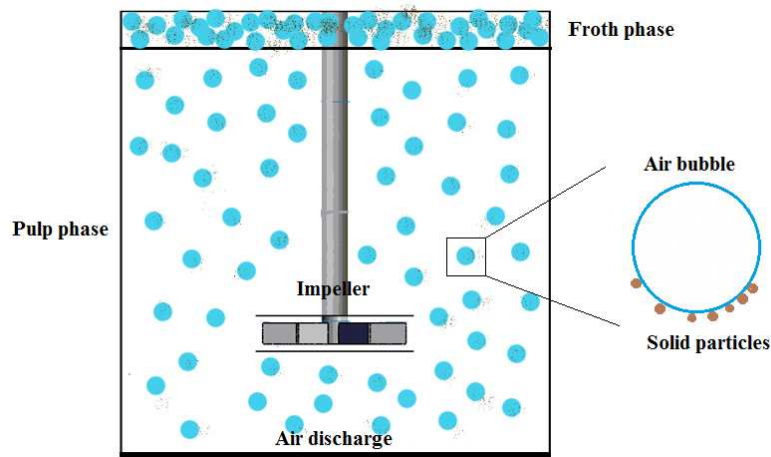


Figure 1-1 Schematic illustration of a flotation vessel

The procedure of design and optimization of the stirred tanks (especially flotation tanks) is a challenging task. Firstly, it is subjected to a particular operation and according to that the process design engineer should adjust two different categories of parameters, operational and geometrical, in order to achieve the required performance. Of the various apparatus factors, the impeller geometry, the impeller position, and degree of baffling are decisive, while one can change the fluid flow regime (i.e., laminar or turbulent) by aligning the impeller speed, or modify the secondary phase purging rate based on the operation's purposes.

As seen the presence of numerous factors for the stirred tank complicates the modelling and the design procedure of the process. Besides, from the hydrodynamics point of view the three dimensional turbulent flow within the vessel encounters a lot of complexities (e.g. the existence of vortices) that elaborates the modelling job. Hence, a realistic modelling scheme should embody as much possible as of the stated factors to accurately explain the stirred tank's effectiveness.

Over the years experimental attempts have been tried to correlate the vessel responses to the hardware and operational factors. These studies have resulted in empirical and semi-empirical expressions dealing with the global variables such as mixing time, power draw, flotation rate constant, mass transfer rate and etc. As a case in point, Schubert and Bischofberger (Schubert and Bischofberger, 1978) emphasized the role of turbulence on the flotation process and drew expressions for the power intensity based on the air rate and the impeller speed. More studies with the similar nature can also be found elsewhere (Abrahamson, 1975, Kresta and Wood, 1991, Lu et al., 1997, Gezork et al., 2001, Kumaresan et al., 2005). Consequently, design, modelling and optimization of agitated tanks have been dealt with by the combination of empirical/semi-empirical models and the practical experience (Lane, 2006). The common practice of either design a new vessel or modelling a working tank starts with a set of laboratory scale experiments leading to a calibrated (or new) empirical model(s) for the global variables. The scale-up criteria are then utilized to transfer the laboratory scale findings to the plant scale implementation steps. The precision of such an approach strongly relies on the range of experimental conditions in which the model is developed as well as the practical experience of the engineer. Furthermore, the global parameters do not evaluate the underlying hydrodynamics of the turbulent flow within the tank and the scale-up factors approximately transfer the small scale data into the large scale stage of the design or modelling (Bartels et al., 2002). Thus, the application of empirical/experimental methods to study the mechanically agitated tank involves inherent uncertainties caused by the correlations, narrow range of experimental conditions, and the scale-up parameters. Therefore, it is important to alter the current modelling approach toward studying the physics of the fluid flow to gain more information for the design and optimization of the actual process conditions.

There are two methods for studying the detailed physics of the fluid flow including Experimental Fluid Dynamics (EFD), and Computational Fluid Dynamics (CFD). The experimental fluid dynamics approach has enabled researcher to visualize and measure the internal structure of the flow in a laboratory scale. Armenante et al. in 1997, for example, measured the velocity profiles and illustrated the velocity distribution in a stirred tank using laser Doppler velocimeter (Armenante et al., 1997). Other experimental methods such as Particle Image Velocimetry (PIV) have been also

used to study the fluid flow inside the agitated vessels (Yoon et al., 2001b). The EFD method is limited to the small scale studies and for the industrial scale tanks its applicability is restricted. Another drawback of EFD is that for the high temperature or high pressure processes the experimenter should trust on the water or air models and as a result the experimental data will not be an accurate representative of the actual process.

The second method of studying the fluid flow is the Computational Fluid Dynamics (CFD). CFD, through a numerical process, solves the governing equations of the fluid flow and the associated phenomenon (e.g., turbulence) inside the stirred tank. The CFD results can be utilized for:

- Parametric study of a new design (e.g., a novel design for the tank, impeller or shaft).
- Model and optimize an actively running vessel.
- Troubleshooting.
- Model an industrial scale tank.
- Extract detailed data where the EFD is unable.
- Obtain reliable data in an economical fashion.

A typical CFD analysis of a stirred tank begins with the mathematical formulation of the physical flow inside the tank. The region of interest or the computational domain is then discretized into small control volumes called mesh. The fluid properties inside each control volumes are defined. With an appropriate initial values and boundary conditions for the problem, solving the governing equations can commence. During the process of computation, CFD employs certain numerical methods (i.e., discretization schemes) to convert the partial differential equations into the algebraic forms. The simultaneous solution of the system of equations delivers the flow variables in each cell. Further details of the governing equations and the solution methods are discussed in Chapters 3 and 4.

According to Daskopoulos and Harris (Daskopoulos and Harris, 1996) the first CFD studies for the stirred tank started in 1970s when the models were simplified for a 2D and laminar flow field. Also, most of the CFD works were conducted for modelling of water inside the tank. One of the other challenges for the stirred tank modelling, that had been the subject of many researches, was the impeller modelling.

Historically, experimental velocity profiles were prescribed at the impeller boundary conditions to simulate the rotational behaviour of the blades. This approach strongly depended on the accuracy of the measurements and accordingly less precise data equalled to an unreliable CFD model. The other major problem that a CFD engineer should cope with was the presence of a secondary dispersed phase (i.e., air bubbles). The hurdles for the multiphase modelling were mainly related to how the air bubbles interact with the continuous phase and the other air bubbles. Although these difficulties have hampered the CFD modelling of stirred tanks, the advances in computational resources has benefited the CFD simulations in a progressing manner. In other words, higher computational power leads to inclusion of more fundamental fluid flow details such as turbulent, coalescence and break-up of the air bubbles, which yields a more trustworthy CFD model. Therefore, the current CFD modelling methods should undergo a constant development in order to improve the reliability of the model.

Moreover, the application of CFD for the flotation modelling has been limited to only the works of Koh and Schwarz (Koh and Schwarz, 2003b, Koh and Schwarz, 2006b). In their studies, they have incorporated the first order kinetic model with the flotation sub-processes via CFD. However, there have been many non-CFD research studies of the principles of the flotation separation in order to develop novel expressions for the flotation sub-processes (Bloom and Heindel, 1999, Dai et al., 1999, Nguyen, 2003b, King, 2001, Derjaguin and Dukhin, 1993, Dukhin et al., 1995, Sutherland, 1948, Schubert and Bischofberger, 1978, Schulze, 1977, Dobby and Finch, 1987, Arbiter and Harris, 1969). The developed models are either analytical, based on idealised assumptions, or based on the experimental data. They treat the hydrodynamic properties of the fluid flow as having constant values, uniformly distributed throughout the entire tank. Henceforth, these models are potential candidates to compare with the CFD results to investigate their probable improvements. Application of CFD allows one to determine locally the hydrodynamically important characteristics of the flow inside the vessel and therefore address a significant weakness in current flotation modelling methodologies. Considering the fact that there exist limited number of studies for the CFD modelling of flotation separation and only certain models for the sub-processes have been tested, further development of a CFD model for the flotation process should involve a

combination of CFD data and other sub-process models. Based on the above discussion, a number of key challenges will be investigated in this dissertation:

- The local values of hydrodynamic properties in flotation tanks should be accurately captured using a CFD methodology. These include the flow pattern, the velocity components as well as the turbulence characteristics of the flow inside the tank.
- The dispersed phase behaviour (i.e., air bubbles) should be simulated with a predictive CFD approach. This method should be able to predict the overall gas holdup and elucidate the influential interphase forces on the air bubbles.
- The methodology should implement local and fluctuating values of the flow variables into the available flotation sub-processes expressions. This will provide an answer to the question of whether the application of the local values enhances the capability of the commonly used models for the flotation micro-phenomena.

The flotation rate constant, as a macro response of the flotation process, will be simulated by incorporating the flow field parameters from the CFD simulation into a kinetic flotation model.

1.2. Objectives

The main objective of this study is to utilize Computational Fluid Dynamics (CFD) for flotation modelling. The results of the numerical analysis are intended to improve the current state of flotation modelling, since they provide fundamental information about the physics governing the behaviour of the flow. In order to achieve this goal, this research is divided into three consecutive steps.

Firstly, it is aimed to develop a methodology for single phase modelling of water within a stirred tank. The established method should be as general and comprehensive as possible so that one can apply the same approach for the single-phase modelling of other type of stirred tanks. Thus, in the first stage the concepts that shall be dealt with for the single phase modelling are as follows:

- Degree of discretization
- Turbulence modelling

- Impeller modelling

Secondly, in order to establish strategies and techniques to simulate the gas-liquid flow inside the stirred tank with a computationally inexpensive CFD methodology, the developed CFD model should be able to handle the following features of the air-water system within a mechanically agitated tank:

- Application of different air purging systems (i.e., sparger designs).
- Encompassing the proper formulation of the significant interphase force(s) between the continuous and the dispersed phases.
- Determination of the influential factors on the gas holdup inside the tank.

The final step of this research is to expand the developed CFD model for the flotation separation process. The methodology should take advantage of the CFD derived data, specifically the turbulence characteristics and the velocity components of the flow, to precisely model the sub-processes of the flotation. It is the aim of the final stage that the commonly used approach for dealing with the flow variables, as spatially uniform, constant values, will be modified. The implementation of local and fluctuating values of the flow field enhances the commonly used modelling strategies for flotation. The typical approaches for flotation modelling (specifically sub-processes modelling) utilize spatially uniform values of the significant flow variables obtained from correlations. The use of hydrodynamic values generated by CFD allows more realistic simulation of the separation process inside a flotation tank.

The constructed model will then be used to investigate and improve the understanding of the flotation performance by studying the impact of the following factors on the flotation rate constant:

- Particle size
- Contact angle
- Gas flow rate
- Rotational speed
- Different minerals

In order to validate the developed methodology from each stage, comparison with the available published experimental data will ensure the accuracy and

trustworthiness of the CFD models. The single phase results, including velocity components and turbulent properties, will be validated for two different geometries (i.e., an unbaffled mixer and a standard Rushton turbine tank). The gas holdup predictions from the gas-liquid modelling in the second step of this study will be compared with the experimental data under different operating conditions. Finally, the flotation rate constants obtained by incorporation of the CFD data will be evaluated with experimental measurements for quartz and galena.

1.3. Limitations

In order to achieve the defined objectives for this research, the following limitations were also specified:

- It is beyond of the scope of this work to derive new formulations for the flotation sub-processes. Instead the objective was to use available and commonly-accepted expressions and improve their predictive abilities by implementation of spatially and temporally varying flow variables into the relevant analytical formulations. However, weaknesses in the assumptions underlying these existing formulations are noted in this thesis.
- Due to the current limitations on computational resources, the solid particles in this study were included into the CFD framework as the pulp phase. The alternative is to include different phases corresponding to the different particle sizes. This demands an additional set of continuity and momentum equations for each phase. Further, the slip velocity and the phase interactions (between all available phases within the computational domain) should be modelled. This would require computational resources rendering such a strategy currently impractical.
- This work is limited to the application of ANSYS Fluent CFD solver. The methodologies developed throughout this dissertation have treated the various phases as interpenetrating continua. Clearly modelling the phase interactions in a real flotation vessel should ideally be done through high order coupling between the discrete phases and the continuous phase. However, this demands the use of the Discrete

Element Method to solve the equation of motion for the particles along with an algorithm to integrate the CFD and DEM data to account for the interphase interactions. The requirements of this strategy would increase the computational time significantly compared to treating various phases as continua. Nevertheless, fundamental studies can be conducted in order to address the significant aspects of the high order coupling and the results can be incorporated with the practical modelling strategy, developed in this work, to enhance the credibility of the flotation modelling methods.

- The bubble sizes in this study were assumed to be constant on a per-simulation basis. Even though the bubble size was assumed to be constant for each simulation, it was changed for different simulations with regard to the reported experimental data by Newell (Newell, 2006) and Pyke (Pyke, 2004). In that, the corresponding bubble size for different operational conditions (i.e., different angular velocities of the impeller and superficial gas velocities) was taken from the experiments and prescribed for each simulation.

1.4. Contributions and Novelty

Considering the fact that the number of CFD studies concentrating on the flotation process is limited, the major contribution of this study is that it offers a CFD-kinetic based flotation model, validated against experimental data, in which the flotation rate constant is predicted by incorporating the turbulent fluctuating flow variables into the micro processes of the flotation. This study is the first to apply such methodology in a clear, original and systematic way. Throughout this dissertation many numerical challenges have been dealt with, resulting in the following CFD methodologies and guidelines for future studies in the field of flotation modelling:

- A single-phase modelling approach has been developed capable of predicting the flow features of water inside stirred tanks.
- For the single-phase modelling, the GCI test was applied to minimize the level of numerical uncertainties of the CFD predictions. Previous literature on CFD modelling of stirred tanks has not reported the

application of this diagnostic test and they only assess this type of uncertainty by the typical grid independence study.

- A gas-liquid modelling methodology has been formulated for the prediction of gas holdup and the behaviour of air bubbles within the flotation tank.
- For gas-liquid modelling, detailed information was provided on the issue of sparger simulation, which is not well-reported elsewhere.
- In order to embody the effects of turbulent eddies on the air bubbles inside the stirred tank, all the available equations for the drag coefficient correlations were compared for two different flow regimes. This study then suggested that the proposed drag formulation of Lane (Lane, 2006) can be applied for the future simulations. In this way, the one-way coupling method between the continuous and dispersed phase was applied for the gas-liquid modelling with focus on the influence of turbulence level on the air bubbles.
- A CFD-kinetic model, founded on the micro and macro scale phenomena inside the flotation tank, has been established for the prediction of flotation rate constant.
- The weakness (i.e., the application of invariant flow parameters) of property based models for the flotation process has been assessed and improved by implementing the locally determined flow variables into the available flotation models.
- The validations against published experimental data for two minerals under different operational conditions confirmed the predictive capability of the new methodology to be applied for future flotation modelling.
- The review of existing methodologies applied in the Generalized Sutherland Equation for the fundamental property-based formulation for the flotation rate constant highlights the weaknesses in the derivations and simplifying assumptions implicit in those models. Thus, it provides an indication of where improvements could be made in future work.

1.5. Organization of this thesis

This chapter has introduced the modelling concepts of the mechanically agitated flotation tank. The difficulties encountered with the empirical and experimental approaches were outlined and then, the computerized modelling was proposed as the alternative that can simulate the flow inside the stirred tank through the numerical solution of the equations governing the flow hydrodynamics. The objectives of this study have also been presented.

Chapter 2 comprehensively reviews the previous published literature from four perspectives. Studies where the single-phase modelling of stirred tanks were the focal points are explored to investigate the effects of the input, model and the numerical uncertainties. Multiphase modelling efforts are also articulated in terms of different multiphase modelling approaches, gas injection methods, turbulence models, and interphase forces. In addition, literature on flotation modelling is grouped into the models for the flotation sub-processes and the use of CFD for the flotation modelling.

Chapter 3 starts with deriving the governing equations for modelling of water inside a stirred tank. Different modelling methods of turbulence and impeller are compared with the experimental data. The grid independence study and the Grid Convergence Index (GCI) guarantee the adequate level of discretization for the computational domain. The generality of the single-phase methodology is also tested by applying the method on another type of stirred tank (i.e., Rushton turbine). The capability of the model is demonstrated by its ability to predict the velocities, turbulence parameters, pressure profile and the flow pattern.

Chapter 4 describes how a computational model for the gas-liquid modelling of the stirred tank is established. The governing equations are explained and the different drag coefficient correlations are compared for the CFD model. It also introduces the concept of coupling between the different phases and explains how this study applies the one-way coupling for the gas-liquid modelling inside the stirred tank. In order to predict the overall gas holdup inside the tank different sparger designs are also explored. Finally, the optimized drag coefficient model is tested under different operational conditions for three different stirred tanks. The numerical predictions of the gas holdup values validated against the experimental measurements.

Chapter 5 begins with explaining the fundamental equation for the flotation rate constant as used by Pyke (Pyke, 2004), followed by the formulations of the flotation sub-processes models applied in this research. It also describes the limitations and simplifying assumptions in derivation of this model. CFD simulations are then conducted to evaluate the effect of the influential parameters on the flotation performance. Numerical predictions of the flotation rate constants for a range of particle size at different gas flow rates, angular velocities of the impeller, and ore types are compared to experimentally measured data.

Chapter 6 is the conclusion of the thesis. It summarizes the major contributions achieved at each stage (i.e., single-phase, multiphase and flotation sub-processes modelling). It also recommends the potential aspects of the flotation separation process modelling that can be promoted by further studies.

Chapter 2 Literature review

2.1. Introduction

Having discussed the main objectives of this study toward developing a CFD-based model for the flotation process, it is now useful to start surveying previous research on the CFD modelling of stirred tanks and flotation cells. This review is intended to recognize what is already well established in the CFD modelling of stirred tanks. For example, almost all the previous studies emphasized the computationally economical method of Multiple Reference Frames (MRF) for the impeller modelling. Moreover, the debatable issues affecting the single-phase, gas-liquid and flotation sub-processes modelling of the stirred tank are addressed. For instance, what level of mesh refinement around the blades is enough to capture all the details of the flow behaviour?

Historically, the analytical solution of the fluid mechanics equations allowed researchers to study a limited number of flows. Of course, the analytical solutions could not be used for modelling of such a complex flow inside the stirred tank. The availability of high computational power and storage resources has, however, altered the researcher approach in the direction of using numerical techniques. With the aid of computational means the partial differential equations of the flow such as continuity and momentum balance equations can be transformed to the algebraic formats. Additionally, the numerical methods, such as CFD, function with a few simplifying assumptions for the flow modelling, while they are able to offer a complete solution for all of the fluid variables. This advancement has accelerated the application of CFD for the industrial fluid flow simulations.

Schwarz (Schwarz, 1991) outlined the application of CFD for the minerals industries. He suggested that for a typical mineral processing operation the flow modelling procedure should begin by formulating the governing equations, determining the calibration factors, solving the equations and eventually it ends with validating the results against the experimental measurements. Although the procedure to simulate a mineral processing unit seems fairly straightforward, two major challenges, turbulence and multiphase effects were pointed out. The author also

summarized the capabilities of the available solvers in terms of their solution methods and their ability to deal with the multiphase flow (at that time) (Table 2-1).

Table 2-1 The CFD solvers and their capabilities (Schwarz, 1991)

	PHOENICS	FLUENT	FIDAP
Method	Finite volume	Finite volume	Finite element
Two phase (two fluid)	yes	no	no
Two phase (Lagrangian)	yes	yes	no
Free surface	yes	no	yes
Compressible flow	yes	yes	no

As identified by Schwarz (1991), the multiphase modelling of the mineral processing fluid flows is generally thought to be a complicated task. The slurry in a flotation tank, in particular, is a three dimensional and fully turbulent field in which the continuous liquid phase interacts with the air bubbles and the solid particles. Thus, one must tackle this problem in a step-wise manner starting with the modelling of the turbulent water flow within the tank. The results of this stage will assist in the understanding of the flow pattern, velocity distribution and pressure profiles inside the tank. This information, then, leads to knowledge of the regions where the mixing is severe or the chances of collision between solid particles and air bubbles are higher. In other words, classifying the high turbulence regions within the flotation tank highlights the zones with high probabilities of collision and attachment. Likewise, modelling of the air bubbles within the tank helps the CFD engineer to determine the overall volume fraction of gas phase and the air bubble velocities at different parts of the tank without interfering with the flow (i.e., without the probes used in experimental methods that disturb the flow). Therefore, the prerequisite water and air-water modelling of the mechanically agitated tank serves as a bridge between the single-phase/multiphase information and the flotation sub-processes modelling. Accordingly, this literature review is structured to categorize three types of research in the field of CFD modelling of stirred tanks. The first sub-section focuses on the studies dealt with the modelling of water inside stirred tanks. The second sub-section summarizes the features of the gas-liquid dispersion modelling in stirred tanks. The published works that have been centred on the flotation sub-processes models and the application of CFD for the flotation separation are articulated at the third sub-section. This chapter is finally finished with a conclusion that shows the current state of the modelling for the single-phase and multiphase methods continued by specifying the

potential features of the flotation sub-processes modelling that can be incorporated within the CFD framework.

2.2. Single-phase simulations of stirred tanks

Since the turbulent flow of water inside the agitated tank is affected by many factors, over the years, many researchers have applied the CFD technique to investigate the significant parameters on the flow pattern. These studies have tried to come up with an accurate, yet computationally cost-effective way to simulate the flow of water inside the tank. The most important parameters that have been investigated are impeller modelling method, turbulence models, and the required number of control volumes for the tank.

In the previous studies, the level of accuracy of the numerical predictions was solely examined by comparison with the experimental measurements. However, this approach did not account for the uncertainties inherent in the numerical predictions. This section, contrary to common surveying of literature for the single phase modelling of the stirred tank e.g. (Joshi et al., 2011b), critically reviews the previous efforts and highlights the inherent uncertainties in the CFD results. The importance of different types of uncertainties and how they affect the numerical predictions are addressed.

Three different types of uncertainties are identified by Freitas (Freitas, 2002) including (a) input uncertainty, (b) model uncertainty, and (c) numerical uncertainty. The input uncertainties arise from the definition of the material properties. For instance, an incorrect value for the viscosity of water can change the flow from Newtonian to non-Newtonian regime. This type of uncertainty can be excluded by using more accurate values. The model uncertainties are caused by different formulations, structures and implementations (Freitas, 2002). For the case of stirred tank, the impeller modelling, different turbulence models, or different discretization schemes can trigger the model uncertainty. The last type of uncertainty, the numerical uncertainty, occurs due to the discretization and iterative errors. Of the various types of uncertainties, the latter mode cannot be removed completely, although the first two have the possibilities to be eliminated. It is therefore crucial to investigate the origins of uncertainties in the previous works in order to minimize or remove them for a new CFD methodology.

One of the earliest works in 1990s was the work of Takeda (Takeda et al., 1993) who used a multi-block meshing method, implemented in an in-house code “RFLOW”, to model the mixing flows in agitated vessels with impellers and baffles. Three different cases were tested in this study. The first geometry was a typical agitated tank with four paddle impellers and four equally spaced baffles. The predicted velocity vectors showed that the mixing phenomena in horizontal and vertical directions were well-presented. They also showed the presence of vortices behind the baffles. The second 2D example was a tank equipped with four impellers rotating in a cylinder. In order to model this case the computational domain was divided into 5 blocks; 4 zones for the rotating impellers and 1 for the rest of the cylinder. The results of this case signified that the mixing behaviour can be numerically shown using this approach. The last case tested was a complex two-step impeller with an inlet and outlet. The domain was grouped into five blocks, two blocks representing the impellers, two blocks corresponds to the inlet and outlet pipes and the other block for the fixed section of the tank. Testing three different cases by the multi-block meshing method and “RFLOW” solver showed that they were successful to minimize the model uncertainty caused by the formulation. However, the numerical uncertainties and degree of mesh refinement were not mentioned in this study.

Dong and his colleagues (Dong et al., 1994a, Dong et al., 1994b) one year later experimentally and numerically studied an unbaffled stirred tank with a flat-paddle-eight-bladed impeller. In their first article, the experimental work, the mean and fluctuating components of velocity were measured (via Laser Doppler anemometer: LDA) for three different cases differentiated by impeller clearance and rotational speed of impeller. The mean flow results showed that the tangential components of velocity are identical at different locations except near the impeller tip. The mean radial velocity profiles showed that the fluid moves away from the impeller blades and the profile of mean axial velocity illustrated how the circulation loops at the bottom and top part of the tank was formed by two upward and downward flow motions close to the wall and the shaft, respectively. The Root Mean Squared (RMS) tangential and radial velocity components were analogous with the mean velocities. However, the RMS axial velocity exhibited a maximum close to the impeller tip which gradually reduced toward the side walls. The calculated turbulent kinetic

energy, k , demonstrated that the turbulence was anisotropic and dominant in the radial direction. However, the value of k for the bulk region of the tank was reasonably constant and small. The same 3D geometry was also numerically modelled using Fluent version 2.97. The Reynolds averaged continuity and momentum equations in conjunction with the k - ϵ turbulence model in the cylindrical polar coordinate system were solved for a steady-state fully turbulent flow. In order to reduce the influence of iterative uncertainties the solution was assumed to be converged when the normalized residuals were below 1.0×10^{-3} and the 4 digits of the predicted velocities did not vary for the last 50 iterations. Further, the numerical uncertainties produced by discretization were tested through using three different grids with $39 \times 23 \times 11$, $30 \times 15 \times 7$, and $39 \times 23 \times 11$ number of nodes in the axial, radial and tangential directions, respectively. Interestingly, they reported no significant variations in the solutions by using these different grid resolutions. The predictions of all velocity components showed that the applied method could reasonably predict the velocities at the upper part of the tank, while near the rotational zone the velocity predictions suffered from an unsatisfactory agreement with the measurements. Similar findings were also stated for the turbulent kinetic energy and turbulent dissipation rate. The discrepancies between the numerical predictions and experimental measurements were attributed to the model uncertainties caused by the k - ϵ turbulence model.

Two types of uncertainties, model and numerical uncertainties, for the single phase flow of three stirred tanks (disc-turbine, an A315 hydrofoil impeller, and a pitch blade turbine) were investigated by Bakker and van den Akker (Bakker and Van den Akker, 1994). The Laser Doppler Velocimetry (LDV) data were used to validate the predicted flow field. Two causes of model uncertainty, the impeller modelling method and the turbulence models were tested in this study. The experimental measurements of tangential and axial velocity components were applied to define the impeller boundary conditions. Also, the standard k - ϵ turbulence model and Algebraic Stress Model (ASM) were compared to account for the turbulence effects and it was shown that due to the anisotropic nature of the turbulence ASM predicted the flow better than the standard k - ϵ . The numerical uncertainties were accounted for by three grid sizes, $50 \times 25 \times 20$, $40 \times 25 \times 25$, and $52 \times 27 \times 17$ grid nodes in (z, r, ϕ) , for a 90° slice of the vessel. For the disc-turbine agitating system, two main circulation loops were visualized through the velocity vectors. It should be noted here that for the first time

they found that the centre of the loops differed for the various planes in the tank. For the axial flow impeller the flow pattern contained a large loop and a small recirculation loop below the impeller. Similar to the works of Dong (Dong et al., 1994a) the measurements revealed the anisotropic nature of the turbulence. The authors suggested that the single-phase flow pattern was able to explain the mixing processes, should a 3D grid with an anisotropic turbulence model used.

Since the anisotropic characteristics of the turbulence was confirmed, Eggels (Eggels, 1996) applied direct and large eddy simulation for modelling of a standard 6-bladed disc turbine vessel with 4 baffles. The lattice-Boltzmann scheme for the discretization of momentum balance equations was used. The numerical uncertainty of the solution was checked by two adequately refined mesh schemes with 1.73×10^6 and 13.8×10^6 grid points. The computational expense for one impeller rotation was one hour on 8 nodes for the first case and 8.8 hours on 16 nodes for the second mesh resolution. Apart from the high computational demand of this methodology, the authors claimed that it could reduce the numerical uncertainties for investigation of different impeller and tank configurations.

Similar to the experimental and numerical work of Dong (Dong et al., 1994a), Armenante et al., (Armenante et al., 1997) also measured and predicted the flow of water inside a stirred tank. Two turbulence models, k- ϵ and ASM, were compared to match the LDV measurements of velocities and turbulence properties. The no-slip boundary conditions were implemented for all the walls including the cylindrical walls, bottom, top, and the shaft, while the velocities and turbulent kinetic energy measurements were imposed at the bottom and top surfaces of the impeller region acting as its boundary conditions. A 60° slice of the entire tank was meshed into $30 \times 40 \times 17$ (r - Z - θ) nodes with finer grid resolution around the impeller. The lower level of model uncertainties resulting from use of the ASM turbulence model, improved the agreement between numerical predictions and the LDV data and this observation was attributed to the anisotropic nature of this turbulence model.

As seen in the works of Dong (Dong et al., 1994a) and Armenante (Armenante et al., 1997), using experimental measurements for the impeller modelling can increase the model uncertainties. Moreover, the availability of the experimental velocity measurements around the impeller is limited to only a few geometries. For these reasons, Ranade (Ranade, 1997) proposed the “snapshot” approach for impeller

modelling. In Ranade's method, appropriate source and sink terms at the back and front sides of the blades were applied to mimic the suction and ejection of the flow from the blades. He utilized the new method to model half of a standard Rushton turbine tank with 2 baffles and 3 blades. The Fluent 4.3.1 code was equipped with subroutines to define the source and sink terms for the impeller blades modelling and a range of angular velocities corresponding to laminar and turbulent regimes were tested. The numerical predictions of velocity components showed satisfactory agreement with the experimental data. However, the turbulent kinetic energy was overpredicted. The case of Ranade's study is a clear example that demonstrates the role of model uncertainty. Using a new approach for impeller modelling not only reduces the possibility of input uncertainty but also shows how controlling the model uncertainty can enhance the accuracy of the numerical predictions. Lane (Lane and Koh, 1997) also showed the influence of model uncertainty for the CFD simulation of a Rushton turbine tank. They applied the sliding mesh facility of the CFX code to model the impeller. The computational domain was divided into the rotating inner zone and the stationary block whereas refined mesh was used for the inner block. Three profiles of the velocity (radial, axial, and tangential) at 4 heights were time-averaged over 24 positions of the impeller with respect to the baffles. The results showed reasonably good agreement for all the velocity predictions. The global parameters of the tank, power number and flow number, were also computed and showed a good comparability with the literature data. The authors recommended that applying a finer grid and accounting for the anisotropic characteristics of the turbulence, corresponding to the numerical and model uncertainties respectively, can improve the predictions.

Brucato (Brucato et al., 1998a) performed a thorough investigation on the different sources of uncertainties in the single-phase modelling of stirred tanks. He categorized three procedures of the impeller modelling including impeller boundary condition (IBC), inner-outer method (IO), and sliding-grid method (SG). The impeller boundary condition method (IBC) was a steady-state approach in which the measured values of velocities and turbulence quantities were imposed on either horizontal or vertical planes swept by the impeller movement. The IO steady procedure divided the tank into two zones, the inner including the blades, and the outer containing the baffles. In the inner region the equations were solved in a rotating reference frame,

but a stationary reference frame was used to solve the equations of the outer zone. In contrast to the first two methods, SG was a transient approach with division of the computational domain to inner and outer zones without overlapping domains. In addition to the impeller modelling approaches, other features of the numerical methodology for stirred tanks such as different shapes of impeller, grid resolution, turbulence model and discretization schemes were also explored using CFDS-FLOW3D package. A summary of various cases tested in this study are shown in Table 2-2 representing the impeller modelling methods tested, the grid resolutions and the overall CPU times.

Table 2-2 Different cases studied by Brucato (Brucato et al., 1998a)

Geometry	Impeller modelling approach	Grid resolution			CPU time (h)
		r	θ	z	
A: Rushton-turbine (clearance = 1/3)	IBC	28	24	40	12
		14	9	21	
B: Rushton-turbine (clearance = 1/2)	IBC	22	12	35	~12
		33	18	49	
		58	24	70	
		IO	58	24	
	SG	28	48	40	~80
C: Dual Rushton impeller	IO	43	18	86	--
D: Axial impeller	IO	58	24	70	--

Using the experimental data for the IBC method, the general flow pattern including two recirculation loops for geometries A and B were achieved. The grid convergence study for the geometry B showed that, except for the very coarse mesh, the other grid schemes produced relatively similar results (i.e., the velocity components and the power number). They also checked the modelling uncertainties generated by the various coefficients for the k- ϵ standard turbulence model in geometry B and concluded that the modified coefficients did not provide particular improvement in the numerical predictions.

The IO scheme was investigated for three different geometries using a fine grid. For geometry B an acceptable agreement with the experimental mean velocity and turbulence field was observed. For the dual Rushton impeller, different locations (three different configurations) varied the predicted flow pattern with a remarkable agreement with experiments. Finally, the simulation of the axial impeller resulted in the mean flow pattern inside the tank but due to the lack of experimental data, a comparison was not made. The sliding-grid method was also applied for the geometry

B and the results were averaged. The contour plots of the turbulence energy showed that this quantity was significantly underpredicted. However, the mean flow field and the power number were closer in agreement with the measurements comparing to the same condition with IO approach. The overall results of this investigation on different origins of uncertainties showed that of the three modelling methods the SG was the most accurate one, though it demanded higher computational resources than the other two methods.

Similar to Lane, Ng et al., (Ng et al., 1998) assessed the capability of the sliding mesh method by comparing the numerical predictions for a Rushton turbine tank with LDA measurements. 3D simulations were performed for a standard Rushton turbine tank with 100 mm diameter with four grid resolutions ranging from 46,000 to 240,000 cells using STAR-CD code. Vector and contour plots of the numerical predictions and the LDA measurements were compared in order to evaluate the accuracy of the predictions. These comparisons showed that the mean velocity profiles agreed quantitatively, while only qualitative agreement was observed for the predicted profiles of the turbulent kinetic energy. The authors pointed out that the grid size, time step size, wall functions and turbulence model could be the reasons for the numerical uncertainties as well as the experimental uncertainties raised from the number of data samples. They consequently suggested that a grid size with more than 1 million cells and a turbulence model without isotropic assumption would reduce the numerical errors.

The model uncertainties associated with a combination of Large Eddy Simulation (LES) and sliding mesh method for the simulation of the mixing pattern for two types of stirred tanks (i.e., pitched blade axial turbine (PBT) and a radial Rushton turbine) was shown by Bakker et al. (Bakker et al., 2000). Fluent version 5 was used to solve the filtered Navier-Stokes equations in 527,000 unstructured hexagonal elements and 763,000 hexagonal elements of the two tanks. The instantaneous vector plots, predicted for the PBT, showed the transient and asymmetric characteristics of the flow field and compared well with the literature PIV data. The author claimed that LES and SM combination was able to capture the formation of trailing vortices and the recirculating loops and it showed that the mixing did not have a symmetrical pattern.

Oshinowo et al., (Oshinowo et al., 2000) intended to find the regions inside the stirred tank where a negative tangential velocity (reverse swirl) exists using the Multiple Reference Frames (MRF) method. The uncertainties resulting from the turbulence model and the grid resolution were examined. Three different turbulence models, standard k - ϵ , RNG k - ϵ and RSM, for five grid densities, 68,000, 197,000, 255,000, 350,000, and 450,000, were investigated. The investigation of different turbulence models revealed that the k - ϵ models had a similar reverse swirl distribution, while RSM eliminated this behaviour around the shaft. They suggested that the appearance of the reverse swirl can be excluded by a refined grid around the impeller at the discharge stream and an adequate definition of MRF interface zone.

Since the influence of the impeller on the mixing pattern within stirred tanks was clarified through experimental works e.g., (Wu et al., 2001), several researcher tried to implement an accurate numerical approach to simulate the rotational behaviour of the blades inside the tank. As discussed, Brucato (Brucato et al., 1998a) has a significant contribution when he compared the IBC approach (imposing experimental data around the impeller) with the numerical methods. Another considerable research on the comparison of the impeller modelling formulations was carried out by Lane (Lane et al., 2000a). He tried to compare MRF and SM in terms of their accuracy and the computational demands. These two types of formulations can significantly cause model uncertainties for the solution. The standard k - ϵ turbulence model computed the turbulent eddy viscosity for one half of the tank. The results of this study showed that the MRF method was more economical than the SM method with a factor of one tenth. Moreover, the MRF method predicted the mean velocity components with the same level of accuracy as the SM approach. Both methods, however, underpredicted the turbulent properties, significantly. Nonetheless, in the bulk region of the tank both methods predicted similar values. The authors also recommended that for the gas-liquid modelling where the rate of bubble break-up and coalescence are dependent upon the k and ϵ care should be taken.

Even though the numerical formulations for the impeller modelling showed promising results, the experimental works were advanced in parallel toward gaining more insights about the details of the flow. Due to this reason, Mavros (Mavros, 2001) reviewed all the available experimental techniques including: single points measuring, Pitot tubes, hot-wire anemometry, laser-Doppler Velocimetry and

ultrasound Doppler Velocimetry, and ensemble measuring, imaging, flow-followers, colour change, thermography, particle image Velocimetry, laser-induced fluorescence, tomography, for the stirred vessels. He indicated that the usage of LDV and PIV were more common due to their simple operations and three-dimensional information. Two examples, where the PIV measurements were utilized to study the details of the fluid flow inside stirred tanks are the works of Yoon et al., (Yoon et al., 2001b) and Ranade et al. (Ranade et al., 2001). Yoon evaluated the three-component flow field around the impeller using 2D and 3D PIV data. The measurements were obtained to be imposed for the impeller boundary condition and validate the CFD results. The experimental measurements showed that the flow around the impeller comprised three components: a dominant circumferential flow, a tangential jet and pairs of tip vortices. Analytical expressions were also derived to explain the impeller-induced flow. They also tended to be used for the generalization and scaling of the stirred tanks in a narrow range of impeller Reynolds numbers. Although the 3D CFD results qualitatively agreed with the measurements, the authors suggested that the numerical uncertainties could be reduced using transient RANS, direct or large eddy simulations. The second example is the study of Ranade (Ranade et al., 2001) on the trailing vortices behind the impeller blades of a Rushton turbine using both PIV and CFD. He applied his proposed formulation for the impeller modelling (i.e., snapshot approach introduced at (Ranade, 1997)). Two aspects of model uncertainty, standard and RNG $k-\epsilon$ turbulence models along with QUICK discretization scheme, were investigated. The predicted iso-surface of high vorticity regions identified the presence of trailing vortices behind the blades. The PIV data also located the locus of the trailing vortices. For the observed underprediction of the turbulent kinetic energy they recommended reducing the numerical uncertainty by performing a mesh refinement around the impeller. In order to investigate the credibility of the “snapshot” approach Ranade presented a further study (Ranade et al., 2002). In this study he attempted to capture the flow features around the rotational system by “snapshot” method. Two stirrers including a six-bladed Rushton turbine and a 45° pitched blades turbine were modelled in Fluent 4.5.2. Using fine mesh resolutions, 630,800 cells for the Rushton-turbine (80×83×95 in $r-\theta-z$ directions) and 269,667 cells for pitched-blade (57×57×83 in $r-\theta-z$ directions), the authors claimed that the number and quality of the grid were more influential than an isotropic turbulence

model such as the standard k- ϵ model. In that, they emphasized that the numerical uncertainty in the CFD modelling of the stirred tank was more important than the model uncertainty. The predicted flow patterns for both tanks agreed well with the expectations, meaning two circulation loops for the Rushton-turbine and one downward vortex for the pitched-blade. Similar to his previous work, contours of the turbulent kinetic energy and the iso-surface of vorticity around the impellers assured the existence of vortices. The vortices generally moved towards the tank wall and their predicted strengths were lower than the measurements. The numerical predictions of mean velocities showed acceptable agreement, however the CFD data for the turbulent kinetic energy only captured the experimental trend and the values were higher than the measurements. Although the overall performance of the “snapshot” approach was acceptable, the authors highlighted that future works should explore other turbulence models with finer grid around the impeller to reduce both model and numerical uncertainties.

Bakker in 2000 briefly investigated the potential of LES simulation for the stirred tank modelling. In 2004, Bakker (Bakker and Oshinowo, 2004) expanded his previous work and applied LES methodology to compare the produced level of turbulence for 5 different impeller shapes (summarized in Table 2-3). The iterative uncertainties were minimized by small time step size and using a developed RANS flow field to initialize the LES solutions.

Table 2-3 Summary of LES simulations by Bakker (Bakker and Oshinowo, 2004)

Impeller type	Angular velocity (rpm)	Reynolds Number	Grid type	No. Cells	Simulated flow time (s)	Initialization	Time-step (s)
45° pitched-blade	60	1.0×10^4	Non-uniform, Hexahedral	527,000	178	Zero-velocity field	0.01
Rushton-turbine	290	2.2×10^4	Non-uniform, Hexahedral	763,000	4.6	Developed steady-state RANS field	0.00345
High-efficiency (HE-3)	60	1.3×10^4	Hexahedral	500,000	46	Developed steady-state RANS field	0.00923
4 × A310	300	4.7×10^4	Hexahedral	500,000	23.6	Developed steady-state RANS field	0.005
Glass-lined retreat curve impeller (RCI)	180	3.0×10^6	Hybrid, tetrahedral-hexahedral	630,000	10	Developed steady-state RANS field	0.00556

All the LES simulations were conducted on Fluent with the RNG subgrid scale model and the sliding mesh method for the impeller movement. The vector plots and the time series of axial velocity for the PBT system showed the transient flow pattern coincided with the literature experimental data. All the other flow patterns predicted for HE-3, A310 and RCI demonstrated similar unsteady and fully turbulent structures in the swirling flow fields. The authors claimed that using large eddy simulation, one can reduce the level of model uncertainty and explain the previously complicated hydrodynamic phenomena inside the stirred tanks, although the required computational times were 1 or 2 order of magnitudes higher than RANS modelling.

After Bakker showed that the LES simulations were capable of simulating water inside the stirred tanks, Hartmann et al., (Hartmann et al., 2004) compared LES with the RANS simulations and determined which method yielded lower model uncertainty. In this work, the simulated flow with LES and RANS for a Rushton turbine tank was compared with LDA measurements. For the RANS simulations CFX 5.5.1 code with Shear Stress Transport (SST) turbulence model solved the equations over 228,096 cells. The impeller was modelled using the sliding mesh technique. The Large Eddy Simulations were, however, carried out in the lattice-Boltzmann solver over a 240^3 lattice cells. The LES results captured all the turbulent scales in the bulk flow, while in the impeller region a need for a refined mesh was shown. The averaged flow field and the formation of trailing vortices were successfully predicted with both RANS and LES simulations. Though, the RANS predictions of the turbulent kinetic energy around the impeller discharge flow were lower than experiments, whereas the LES predicted this quantity closer to the LDA data. The authors concluded that, except the turbulent kinetic energy, RANS models were able to predict the flow field around the impeller. LES, on the other hand, not only predicted the overall flow pattern but also accurate turbulent kinetic energy predictions were obtained.

The effect of model and numerical uncertainties on the mean velocity components, the turbulent quantities, and the global parameters of a down/up pumping pitched-blade stirred tank were investigated by Aubin et al. (Aubin et al., 2004). The impeller modelling strategies involved the MRF frozen-rotor method (MRF-FR), MRF with circumferential averaging (MRF-CA), and the sliding mesh (SM). Three methods accounted for the discretization of equations: upwind differencing (UW), high order upwind differencing (HUW), and QUCIK's

discretization schemes. It was found that the choice of impeller modelling methods did not affect the radial and axial flow patterns and a good agreement was observed. However, the mean tangential velocity profile and the turbulent kinetic energy were underpredicted. The second order and QUICK discretization schemes showed better agreement with the literature data. The authors, thus, suggested that for the multiphase modelling the influence of discretization schemes should be considered.

One of the applications of mixer tanks is in the pharmaceutical industries where the adequate mixing is of importance. For instance Akiti (Akiti et al., 2005) investigated whether there existed a correlation between the independent mixing variables such as angular velocity, impeller type, number of baffles, feed location, and liquid level with the yield, X_S . In their work they used a fractional factorial design to investigate the effects of different types of impeller systems: four-bladed 45° pitched blade, four-bladed 30° pitched blade, and an anchor. The numerical uncertainties inherent to this work might have risen from the mesh element type, as they discretized the applied geometries with tetrahedral shape cells (123,699 cells for 45° PBT, 127,270 cells for the anchor impeller, 284,879 and 277,248 for the baffled tanks). They reported an average value of 0.4-0.5 for the skewness which ensured the good quality mesh. Gambit was used to mesh the computational domain and the equations were solved using Fluent 6.1.22. The velocity distribution obtained by CFD confirmed the observed main effects and two-way interaction effects between the mixing variables and the system response (X_S). Furthermore, correlations between the local values of the energy dissipation rate and the yield were proposed for two types of impellers. The authors suggested that the errors relating to the scale-up process can be decreased using a combination of the design of experiments and CFD.

Another mixing time study was performed by Javed (Javed et al., 2006) who solved the species transport equations to numerically determine the mixing time in the turbulent flow of a Rushton turbine tank. They measured the concentration of an inert tracer with a laser induced fluorescence (LIF) technique and validated the numerical predictions of mixing times against the LIF data. The flow of water inside the tank was modelled by the standard k- ϵ turbulence model in conjunction with the sliding mesh method for the impeller rotation. The general mixing pattern was achieved by a time series of tracer concentration contour plots, which illustrated the importance of convective tracer transport rather than molecular diffusion. The concentration-time

plots for the tracer at different measurement points showed fluctuations at the first two seconds, but after almost 2 seconds flat lines were reported. They also identified discrepancies between the measured tracer concentrations and the predicted values. It was attributed to the fact that the tangential velocity component was high at the liquid surface leading to a faster mixing in the tangential direction at the top of the tank. The author suggested that the experimental measurements of the velocity components at the liquid surface are required in the future mixing study, since the common point of tracer injection is at the top of the tank.

In 2006, Deglon (Deglon and Meyer, 2006) reviewed the single-phase modelling uncertainties for the stirred tanks originating from the grid resolution, discretization scheme, impeller modelling and the choice of turbulence model. They highlighted that using standard k - ϵ turbulence model with the MRF for the impeller modelling resulted in poor predictions of the turbulent properties, whereas the same combination was able to reasonably predict the velocity components. The numerical uncertainties were accounted for by four different mesh resolutions ranging from 33,000 to 1,900,000 number of hexahedral control volumes. The influence of discretization schemes were also explored by applying QUICK, upwind and central schemes. They suggested that even though with a coarse mesh, one can obtain the general flow pattern inside the tank, high-order discretization schemes with adequately fine mesh are required to achieve challenging phenomena inside the tank such as the existence of vortices and accurate prediction of turbulent characteristics.

Fan (Fan et al., 2007) only investigated the model uncertainties caused by turbulence models. They compared LES with the standard k - ϵ turbulence model to display the flow instabilities made by a Rushton turbine. The PIV measurements of the instantaneous flow pattern and the fluctuation of velocity were used to validate the numerical predictions. Unstructured and non-uniform elements were used to mesh the 360° of the tank with local refinement around the impeller. The impeller rotation was modelled using the sliding mesh technique. The spatial discretization of momentum equation was achieved by the central differencing scheme, while a second-order implicit scheme was used for the time advancement. The axial and radial profiles of the velocity predicted by standard k - ϵ showed a steady state in the bulk region. The LES predictions, on the contrary, demonstrated a stochastic and complex flow with high and low fluctuations. In addition, the standard k - ϵ predicted circulation pattern

was similar to commonly seen flow pattern in stirred tanks (i.e., two symmetrical circulation loops above and below the impeller). LES simulation, however, revealed an asymmetric circulation pattern within the tank where the vortices were moving along the vertical axis. The model uncertainties induced by two different formulations for the turbulence significantly altered the numerical predictions of the flow pattern. The standard k - ϵ produced a symmetrical flow pattern and the LES led to an asymmetric prediction of the circulation pattern. Since they used a supercomputer with 128 dual processors the higher computational demand of LES was not a hindrance.

The influence of input uncertainties, made by the distance between the impeller and the tank bottom (i.e., clearance), on flow hydrodynamics and the mixing time was investigated by Ochieng (Ochieng et al., 2008). Three configurations including (a) the standard clearance = $0.33 \times$ tank diameter, (b) the low clearance = $0.15 \times$ tank diameter without a draft tube and (c) the low clearance = $0.15 \times$ tank diameter with a draft tube were simulated using CFX 4.4. Three grid resolutions, 216,000, 436,000, and 700,000, were used. The MRF method initialized the computational domain for the final simulations with the SM impeller modelling method. In order to obtain the mixing time a tracer was injected below the impeller and its concentration was monitored at five different locations inside the tank. The standard clearance showed a typical flow pattern including two circulation loops. Locating the impeller closer to the tank's base, however, eliminated the bottom loop and increased the axial velocity. It was also found that the draft tube increased the axial component of velocity significantly. The simultaneous usage of the low clearance and the draft tube reduced the mixing time up to 50%.

Vakili (Vakili and Esfahany, 2009) compartmentalized a baffled stirred tank according to either the turbulent kinetic energy dissipation gradient or the cumulative energy dissipation rate into three regions: impeller zone with high energy dissipation rate, a baffle zone with relatively high energy dissipation rate, and a circulation zone including rest of the tank with low energy dissipation rate. They investigated the impacts of input uncertainties comprising impeller speed, impeller diameter, impeller clearance and baffle width on the turbulent quantities. A 16 cm diameter tank was discretized into $31 \times 144 \times 100$ tetrahedral elements in r - z - θ directions. The combination of MRF and standard k - ϵ turbulence model was implemented into Fluent 6.0.12. The

CFD results showed that the agitation caused an increase in k and ε in all three compartments, while the effects of impeller clearance were insignificant (contrary to work of Ochieng et al.). An increase in the impeller diameter only led to a positive ε change for the impeller zone, yet no appreciable changes were observed for the other zones. Overall, this study showed that the compartmentalization of the stirred tank would help the CFD engineer to specifically focus on the flow behaviours in certain zones of interest.

Another study in 2009 was performed by Xia et al., (Xia et al., 2009) who investigated the effects of model uncertainties on the water simulation of an industrial scale Outotec flotation cell. Three different turbulence models namely, realizable k- ε , standard k- ε , and RSM were tested and the results were summarized into 5 properties of the fluid flow including flow pattern, velocity profiles, pressure coefficient, power draw and power number. The predicted flow pattern showed two different recirculation zones below and above the rotor, independent of the turbulence model applied. However, the local flow characteristics showed differences. For example, the predicted power draw by RSM turbulence model was higher than other turbulence models predictions and it was also closer the experimental data. The comparison of axial and radial velocities revealed that the numerical predictions of RSM differed from the k- ε models, but without comparison with experimental measurements one could not clarify the optimized model for velocity predictions. The authors suggested that the RSM is an adequate option for the accurate predictions, whereas the k- ε families are for the engineering purposes.

Amongst the various CFD investigations on the influence of several numerical approaches for the single-phase modelling of the stirred tanks, the published paper of Coroneo et al., (Coroneo et al., 2011) is one of the in-depth studies for the model and numerical uncertainties effects on the CFD predictions. They used the standard k- ε turbulence model with MRF to highlight the effects of grid size and discretization scheme on the global parameters, mean velocity, turbulent dissipation rate and homogenization. Four different grid resolutions, 2.7×10^5 , 1.9×10^6 , 3.6×10^6 , and 6.6×10^6 were used for the spatial discretization of the computational domain. The applied convergence criterion in this study was the strictest criterion compared to the previous works (i.e., the continuity residuals $< 10^{-3}$). They assumed that the solution was converged when the residuals for most of the variables dropped below 10^{-7} . In

order to study the homogenization, a scalar equation for the tracer concentration was also solved with the second order discretization scheme. The CFD predictions of power number revealed a strong dependency on the measurement methods and the grid resolution. However, with the fine mesh the observed discrepancy reduced to only 7% stressing the role of numerical uncertainties on the predictions of global parameters. Also, the fine grid showed better comparison with the dynamic measurements of the tracer concentrations determined by the planar laser induced fluorescence (PLIF). The author stated that the observed numerical issues in their study would be more prominent when multiphase modelling in stirred tanks is performed. This is because of the fact that the relevant phenomenon in the multiphase systems such as the bubble coalescence and the break-up rely on the accurate predictions of the turbulence quantities.

Joshi et al., (Joshi et al., 2011b, Joshi et al., 2011a) in two comprehensive review papers summarized the CFD research conducted on the radial and axial flow impellers. For the radial flow impellers different sources of input, model and numerical uncertainties were discussed. They pointed out that the impeller modelling, turbulence model, discretization scheme, and grid resolution were the subjects of all the CFD studies for the single-phase modelling of stirred tanks. By a quantitative comparison with experimental data (LDA or PIV) they showed the advantages and disadvantages of each modelling approaches. The two main methods for the impeller modelling, steady and unsteady techniques were evaluated. The steady methods included the black box or the impeller boundary condition where the experimental data around the impeller was required. Another member of this group was the source-sink method whereas the impeller was replaced by the source of momentum and the baffles were modelled as the sink term. Further, the inner-outer (IO) method divided the tank into the rotating inner side whilst the rest of the vessel was stationary. The improved version of IO method was the multiple reference frames (MRF) in which the governing equations for the inner rotating region were solved in a rotating reference frame. The final steady method was the snapshot approach where the ejection and suction of the fluid from the blades were modelled as source and sink terms. The unsteady group had three members including sliding mesh, moving deforming grid and the lattice-Boltzmann LES framework. They also performed different simulations to investigate the predictive capabilities of different impeller-

baffle interaction models and various turbulence models. The detailed comparisons were provided, though the general conclusion showed that the IBC was capable of predicting the axial and radial velocities in the bulk region while other approaches did not show promising results. The comparison of different turbulence models including standard k- ϵ , RNG k- ϵ and RSM with IBC, MRF, and SM was also performed. However, no general combination of a turbulence model with an impeller modelling method was recommended to be superior in the prediction of the flow behaviour. They also conducted LES simulations for 5 impeller configurations to predict mean velocity components as well as the turbulent quantities. In comparison with the RANS predictions the LES predictions of velocity components showed better agreement with the LDA data. The authors suggested that the level of agreement achieved by LES can explain the higher computational expenses of this model. The paper was finished by 25 conclusions and suggestions for the future research in this field. For instance, CFD studies should be performed on different types of impellers and since there is no attempt on the single-phase modelling of the industrial scale stirred tank, the authors highlighted this necessity. They also advised on defining a uniformly accepted criterion for the mixing-time study in the stirred tanks.

However, the CFD modelling of the single-phase inside the stirred tank is not yet exhausted and is an on-going progress. Feng et al., (Feng et al., 2012) introduced a new turbulence model, explicit algebraic stress model (EASM), for the water modelling inside the tank. The model is intended to resolve the anisotropic nature of the turbulence inside the tank. They evaluated the new formulation through comparison of the numerical predictions of the velocity components, turbulent kinetic energy, Reynolds stresses and turbulence energy dissipation with experimental data and other CFD methodology (e.g., k- ϵ and LES). The proposed 3D EASM was compiled in an in-house code and ran on a PC computer with 2.8 GHz CPU speed. Due to the convergence problem the simulations started with the standard k- ϵ turbulence model and the final converged solution with EASM was achieved when the relative residuals were below 2×10^{-4} . The velocity predictions of EASM were as good as LES predictions with the lower computational costs. In addition, similar to the RANS family of turbulence models the values of the turbulent kinetic energy were underpredicted. The authors finally claimed that the new turbulence model was able to predict the anisotropic flow characteristics close to the RSM with less required

computational resources. This work was another example highlighting the effect of model uncertainty. It showed that the development in the CFD methodology could be successful if it is in line with the reduction of the related uncertainties.

2.3. Summary of single-phase simulations of stirred tanks

The review of literature on the single-phase simulations of stirred tanks reveals several major points regarding to the input, model and numerical uncertainties. All of the previous studies reviewed in section 2.2 have been conducted for water modelling inside the tank. The input values of water such as its density and viscosity for the room temperature have been studied systematically and well established (Keslin, 1978, Martin and MacCutcheon, 1999). Therefore, the remaining source of input uncertainty raised in the previous works is the different rotational systems (i.e., various impeller shapes). This factor can also affect the quality of the generated mesh, leading to higher level of numerical uncertainties. For instance, achieving structured hexahedron elements for an upward or downward pitch-blade turbine has been shown to be difficult and for this case tetrahedron elements are more accessible. However, this type of control volume around the blades is not fully capable of rendering all the flow details (e.g., vortices). Thus, the numerical predictions of the flow produced by tetrahedron elements may be less accurate compared to the hexahedron elements.

Regarding to the model uncertainties, surveying the previous literature has indicated four different sources of the model uncertainty involving different:

- Solvers
- Turbulence models
- Impeller modelling techniques
- Spatial or temporal discretization of the equations

Different versions of Fluent or CFX have been dominant codes for solving the equations, although the in-house codes or other commercially available CFD codes have also been utilized. In most of the previous papers a few turbulence models have been investigated. Some of literature compared the isotropic turbulence models such as various versions of k- ϵ model, while others tried to compare the isotropic and anisotropic turbulence models such as LES with the standard k- ϵ . There is a

consensus in previous studies that LES modelling leads to higher accuracy of predictions with higher computational demands, whereas for the same case the standard k- ϵ turbulence model resulted in reasonable predictions with computationally less expensive method. In other words, for the design purposes, where precision is crucial, LES should be applied and when the time and computational resources are limited the standard k- ϵ turbulence model is the practical alternative.

The numerical uncertainties have been mostly produced by the various degrees of mesh resolutions and different methods of discretization schemes. However, the published numbers of papers on the influence of grid size have been more than those dealing with the discretization schemes. As a general guideline, it has been advised that a relatively coarse mesh (cell numbers between 50,000 to 150,000) is able to predict the velocity components and the global parameters with an acceptable degree of accuracy. However, the predictions of the flow around the impeller and the turbulent quantities (turbulent kinetic energy and turbulent dissipation rate) requires higher grid resolutions. An overall summary of the reviewed literature with respect to the different origins of uncertainties is provided in Table 2-4. The table also shows that the single-phase methodology developed in the current study is formulated based on a comprehensive comparison of the different modelling strategies for water modelling inside stirred tanks. Therefore, the uncertainties on the numerical predictions are minimized in an economical CFD framework.

Table 2-4 Classification of the previous literature on single-phase modelling of stirred tanks regarding to input, model and numerical uncertainties

Reference	Input uncertainty		Model uncertainty			Numerical uncertainty	
	Impeller type	Code	Impeller modelling	Turbulence modelling	Discretization (spatial/temporal)	Grid size	Convergence criteria
(Takeda et al., 1993)	Four paddle impeller Four horizontally distributed impeller Two-step impeller	In-home code "RFLOW"	Multi-block meshing with IO	Standard k-ε			
(Dong et al., 1994a, Dong et al., 1994b)	Flat-paddle-eight-bladed impeller	Fluent 2.97	Black-box	Standard k-ε	Power law	39×23×11 30×15×7 39×23×11 (z,r,φ)	Normalized residuals < 1.0×10 ⁻³ & negligible variation in the 4 digits of the velocities
(Bakker and Van den Akker, 1994)	Disc-turbine A315 hydrofoil impeller Pitch blade turbine (PBT)	Fluent 2.99	Black-box	Standard k-ε ASM	Power law	50×25×20 40×25×25 52×27×17 (z,r,φ)	
(Eggels, 1996)	Standard 6-bladed disc turbine	In-home lattice-Boltzmann solver	Varying force fields	DNS LES (Smagorinsky sub-grid)	lattice-Boltzmann scheme	1.73×10 ⁶ 13.8×10 ⁶	
(Armenante et al., 1997)	45° pitched-blade	Fluent 3.03	Black-box	Standard k-ε ASM		30×40×17 (r,z,θ)	
(Ranade, 1997)	Rushton-turbine	Fluent 4.3.1	Snapshot	Standard k-ε		28×28×78 (r,z,θ)	
(Lane and Koh, 1997)	Standard Rushton turbine	CFX 4	SM	Standard k-ε		48×38×60 (z,r,φ)	Until reaching periodically repeatable flow pattern
(Brucato et al., 1998a)	Rushton-turbine Dual Rushton impeller Axial impeller	CFDS-FLOW3D	IBC IO SG	Standard k-ε	Hybrid-upwind QUICK	28×24×40 14×9×21 22×12×35 33×18×49	

(Ng et al., 1998)	Standard Rushton turbine	STAR-CD	SM	Standard k-ε	Self-filtered central differencing scheme	58×24×70 42×18×86 46,000 to 240,000	
(Bakker et al., 2000)	PBT Rushton turbine	Fluent 5	SM	LES	Second-order/central differencing	527,000 763,000 68,000	
(Oshinowo et al., 2000)	PBT Rushton turbine	Fluent 4.5.2	MRF	Standard k-ε RNG k-ε RSM		197,000 255,000 350,000 450,000	Sum of residuals <5×10 ⁻⁵ for k-ε <2×10 ⁻⁴ for RSM
(Lane et al., 2000a)	Standard Rushton-turbine	CFX 4.2	MRF SM	Standard k-ε		112,000	Continuity residuals<1×10 ⁻³
(Yoon et al., 2001a)	Standard Rushton-turbine	Fluent	Black-box MRF			40×80×16 (r, θ, z)	
(Ranade et al., 2001)	Rushton-turbine	Fluent	Snapshot	Standard k-ε RNG k-ε	QUICK	80×83×95 (r, θ, z)	
(Ranade et al., 2002)	Rushton-turbine PBT	Fluent 4.5.2	Snapshot	Standard k-ε	QUICK	80×83×95 57×57×83 (r, θ, z)	Normalized continuity residuals<1×10 ⁻³
(ZHOU et al., 2003)	Rushton-turbine	CFX 4.3	SM	Standard k-ε RNG k-ε		39×36×60 (r, θ, z)	
(Bakker and Oshinowo, 2004)	45° pitched-blade Rushton-turbine High-efficiency (HE-3) 4 × A310 Glass-lined retreat curve impeller (RCI)	Fluent	SM	LES (RNG sub-grid)	Second-order/central differencing	527,000 763,000 500,000 500,000 630,000	
(Hartmann et al., 2004)	Rushton turbine	lattice-Boltzmann solver CFX 5.5.1	SM	LES (two sub-grids Smagorinsky and modified Smagorinsky) SST	A combination of first and second order discretization	240 ³ 228,096	RMS residuals<1×10 ⁻³
(Aubin et al., 2004)	Down/up pumping pitched-blade	CFX 4.4	MRF	Standard k-ε	Upwind	76,000	Normalized

			SM	RNG k-ε	High order upwind QUICK	155,000 350,000	residuals < 3×10^{-4}
(Akiti et al., 2005)	Four-bladed 45° pitched blade Four-bladed 30° pitched blade An anchor	Fluent 6.1.22	MRF	Standard k-ε		123,699 284,879 127,270	
(Javed et al., 2006)	Standard Rushton-turbine	Fluent 4.4	SM	Standard k-ε	Power law	74×38×40 (z, r, θ)	
(Deglon and Meyer, 2006)	Standard Rushton-turbine	Fluent 6.1	MRF	Standard k-ε	QUICK Upwind Central	33,000 230,000 800,000 1,900,000	Normalized continuity residuals < 1×10^{-4}
(Fan et al., 2007)	Rushton-turbine	CFX 5	SM	Standard k-ε LES	Central differencing/second-order		
(Ochieng et al., 2008)	Rushton turbine (3 clearances)	CFX 4.4	SM (with MRF for initialization)	Standard k-ε	Hybrid	216,000 436,000 700,000	
(Vakili and Esfahany, 2009)	Two-bladed	Fluent 6.0.12	MRF	Standard k-ε	First-order	31×144×100 (r, z, θ)	Residuals of continuity and turbulent equations < 1×10^{-5}
(Xia et al., 2009)	Outotec tank	Fluent	MRF	Realizable k-ε Standard k-ε RSM	Second-order	395,000 705,100	Scaled residuals < 10^{-3}
(Coroneo et al., 2011)	Rushton turbine	Fluent 6.3		Standard k-ε	First-order upwind Second-order upwind QUICK	2.7×10^5 1.9×10^6 3.6×10^6 6.6×10^6	Most of variables residuals < 1×10^{-7}
(Joshi et al., 2011b)	Disc-turbine	Fluent	IO IBC SM MRF	Standard k-ε RNG k-ε RSM LES		85,000	
(Feng et al., 2012)	Rushton-turbine	In-house code	IO	EASM Standard k-ε		93,312 194,400	Relative residuals < 1×10^{-4}

Current study	Unbaffled mixer Standard Rushton turbine	Fluent	MRF	LES	Second-order	432,00	Normalized continuity residuals $< 1 \times 10^{-3}$
				RANS based (standard k-e, RNG k-e, realizable k-e, transition SST, k- κ - omega, Spalart- Allmaras) LES (WALE, Smagorinsky- Lilly, kinetic- energy)		810,000 1,360,800	
						40,300 to 1,024,317 71,040 to 1,256,640 Application of GCI	

2.4. Gas-liquid simulations of stirred tanks

A large number of flows encountered in mineral processing and chemical industries are usually a mixture of two or three different phases. In chemical industries contacting liquids with gas bubbles defines the interfacial area and the mass transfer coefficient which in turn determine the total process efficiency. The flotation process, from the mineral processing view, is a three-phase separation procedure in which a continuous phase (i.e., water) interacts with two different dispersed phases (i.e., air bubbles and solid particles). These types of multiphase flows are categorized as “bubbly flows” where the discrete phase(s) streams in a continuous fluid and the volume fraction of the dispersed phase is lower than the primary phase.

The modelling methods of multiphase flow compared to the single-phase regimes reveal a high level of complexities. Napier-Munn and Lynch (Napier-Munn and Lynch, 1992) identified two approaches for categorizing the modelling methods for the mineral processing flow fields. The first method focuses on the process fundamentals and accordingly they pointed out three modelling approaches:

- Models based on the scientific principles of the process
- Phenomenological models
- Empirical models

The second system takes into consideration the time dependency of the process under investigation and two models being steady-state and dynamic models were introduced. Based on the classification, CFD models fall into the dynamic model’s group establishing on the underlying principles of the flow.

The complications for CFD simulations of the multiphase systems, especially for the gas-liquid modelling in stirred tanks, originate from the additional number of equations. The first extra set of equation is the conservation equations (mass and momentum) for the gas phase. The second difficulty, compared to the water modelling, is that an expression is required for the volume fraction of each presented phase in the domain. This quantity varies spatially and temporally and the sum of the volume fractions equals unity for each cell. Moreover, the accumulation of the secondary phase around the rotational system forms air ventilated cavities causing additional numerical challenges for the CFD modelling of gas-liquid inside stirred tanks (Rigby et al., 1997, Rigby et al., 2000).

Since there are two different phases in the vessel the interfacial forces are introduced for the momentum equations to couple between the phases. It is also important to assess the degree of interphase coupling between the different phases. In other words, one should decide on how the continuous liquid phase exchanges momentum with the secondary dispersed phase, which can be defined through the momentum exchange term in the momentum balance equation. Furthermore, the fluid flow inside the stirred tank is fully turbulent and the modelling issues arise for the turbulent effects on both continuous and dispersed phase increases the computational efforts.

The additional difficulties for the gas-liquid modelling of stirred tanks have challenged researchers for modelling of such a complex flow. However, the advancement in the CFD methods and the presence of high computational power has helped them to tackle this problem and mitigate the computational demands. Several aspects of the gas-liquid modelling have been reported in literature. Reviewing of the previous studies shows the gradual improvement of the modelling approach and reveals how the gas-liquid modelling has provided further physical insights into details of the gas-liquid flow. This sub-section, thus, articulates the previous published articles from 1990 until 2012 on the gas-liquid modelling of stirred tanks to investigate the followings:

- Geometry and impeller type
- Multiphase modelling approach
- Gas injection methods
- Turbulence model
- Impeller modelling
- Grid resolution
- Discretization scheme
- Interphase forces
- Bubble size modelling
- Validation

As one of the early studies, in 1992 Gosman et al., (Gosman et al., 1992) simulated the gas-liquid flow in a Rushton turbine tank. They used a very coarse mesh with 8,100 numbers of cells which can be justified by the limited computational

power. The black-box approach was used for the impeller modelling while a modified k - ϵ turbulence model was considered. In this work the bubble size was assumed to be constant and the additional mass and drag forces were also included. The numerical predictions of the gas holdup showed a general underprediction for the different points inside the tank. Another important study in the same year on the gas-liquid flow within the stirred tank was performed experimentally by Barigou (Barigou and Greaves, 1992). They provided comprehensive measurements of the bubble size distributions in different locations of a 1 m diameter agitated tank. Since the bubble size measurements of this study have been used to validate the predictions of bubble diameters in many CFD studies, it has been mentioned here.

Bakker and van den Akker (Bakker and Akker, 1994) expanded their single phase modelling of stirred tank (Bakker and Van den Akker, 1994) into a gas-liquid modelling, incorporated in an in-house code named GHOST! (Gas Holdup Simulation Tool). In this two-step modelling approach, Fluent solved the mass and momentum conservation equations with the algebraic stress model. The solution was then imported to the in-house code to compute a bubble number density equation. The bubble number density equation involved the rates of bubble break-up and coalescence. The effect of turbulent eddies on the air bubble movements were accounted for by the bubble Reynolds number modification. Knowing the gas holdup and bubble size, the authors incorporated another equation to calculate the mass transfer coefficient. The proposed methodology was applied for three different impeller systems: PBT, disc turbine, and Lightnin A315. Negligible changes in the bubble size, gas holdup and mass transfer coefficient were the criteria to stop the computations. The local gas holdup predictions showed good agreement with the experiments and the maximum gas holdup occurred close to the sparger at the lower circulation loop. Further, the local bubble sizes showed non-homogeneous gas dispersion with the maximum bubble diameter at the impeller discharge stream which demonstrated the dominant influence of the coalescence toward the walls. The authors suggested that their proposed model can work in the low gas flow rates and for research purposes. However, for the high gas flow rates in stirred tanks the model needs more attention on the local properties of the gas-liquid.

Morud and Hjertager (Morud and Hjertager, 1996) experimentally measured the mean and RMS gas velocity components in a 15 l stirred tank. The experimental

data were used for validation of a two-dimensional two-fluid CFD simulation of the gas flow pattern and its velocity. In order to perform the numerical simulations, an additional height was considered to define the degassing boundary condition at the top of the tank. The grid resolution comprised 47×24 elements in the axial and radial directions, respectively. The source and sink terms were applied to represent the impeller blades and baffles. The predicted gas flow pattern showed two recirculation loops close to the impeller and at the top of the vessel. Further, the high gas volume fractions were detected at the recirculation loops. The numerical predictions of the velocity components showed qualitative agreements, however the 3D effects were not considered. It was found, both experimentally and numerically, that the gas accelerated at the impeller tip due to the high turbulence kinetic energy in this zone. The author recommended that the methodology should be improved by taking into account the effects of 3D geometry and a better grid resolution at the high gradient regions of the tank.

Two experimental studies were performed in 1996 and 1998 and due to their significant contributions on the addressing of hydrodynamically important factors of the stirred tank they must be mentioned in this review. In the first one, Barigou and Greaves expanded their previous study (Barigou and Greaves, 1992) and measured the local gas holdups and the interfacial area distributions in a 1 m diameter Rushton turbine tank. The local gas holdup data showed that at the impeller zone the gas holdup decreased toward the wall. However, at the bulk region the complete gas dispersion was achieved with a maximum close to the centre. Further, computation of the interfacial area distributions revealed a high value around the agitation system and the authors proposed correlations for the interfacial area predictions. The latter case, the study of Brucato et al., (Brucato et al., 1998b) led to a new correlation for the drag coefficient for the turbulent flow of the liquid and gas. The experimental measurements of the particle settling velocities, obtained by a Couttee-type stirred vessel, were correlated by the other available empirical equations. The observed discrepancies with the previous empirical expressions directed them to include the particle size and Kolmogorov turbulent length scale¹ into the new correlation as follows:

¹ Kolmogorov theory defines the smallest turbulence scale at which the kinetic energy dissipates into heat.

$$\frac{\overline{c_D}}{c_{D,0}} = 1 - 8.76 \times 10^{-4} \left(\frac{d}{\lambda}\right)^3 \quad \text{Eq. 2.1}$$

where; $c_{D,0}$ is the drag coefficient in the stagnant liquid and λ is the Kolmogorov length scale and d is the particle diameter.

The authors stated that the constant in the equation might vary depending on the particle size. They also pointed out that the simplicity of the new equation might help studying the drag force decrease due to the turbulence situation. This drag coefficient correlation has been applied and compared with other available correlations in this study. The details are presented in Chapter 4.

Ranade et al., (Ranade and Deshpande, 1999) also followed up their single-phase study toward understanding the interactions of the trailing vortices and the gas bubbles in the gas-liquid flow of a Rushton turbine stirred tank. They first modelled only one blade of the impeller to investigate the effect of trailing vortices. This simplified geometry was also used to study the gas accumulation behind the blade. The single blade was modelled inside a sufficiently large computational domain with inlet and outlet boundary conditions representing entering and exiting of fluids. The flow over the blade showed trailing vortices similar to the rotating turbine and the gas phase were found to be trapped behind the blade. However, the volume fraction of the air phase did not reach to unity as expected for the gas cavity. In the second step the gas-liquid flow was modelled for half of a 0.3 m diameter stirred tank with two different grid resolutions, $r \times \theta \times z$: $17 \times 32 \times 32$ and $35 \times 63 \times 80$. They utilized the snapshot approach for the impeller modelling and the standard k- ϵ modelled the turbulence effects. The results showed the accumulation of the gas behind the blade coincided with the trailing vortices and this appearance reduced the turbulence intensity. They also showed that the impeller rotation forced the air bubbles to scatter radially at first and then they travelled to the top section of the tank. The authors concluded that for the underprediction of the gas holdup in the tank one should be able to capture the trailing vortices behind the blade, as they were the main factor for the gas cavity to occur.

Brucato's experimental study demonstrated the importance of the drag force on the gas-liquid flow inside the stirred tank. Lane et al., (Lane et al., 2000b) compared four different drag coefficient equations, Ishii-Zuber, Brucato, Bakker, and a modified version of Brucato's model, to examine the increasing influence of the

turbulence on the bubble drag coefficient. The steady-state Eulerian-Eulerian simulations of a 1 m diameter Rushton-turbine tank were performed at 180 rpm with a constant gas flow rate. The converged solution was obtained when an adequate reduction in the continuity residuals, a balance between the amounts of gas entering and exiting the tank, and a constant gas holdup were attained. The Ishii-Zuber results predicted the gas holdup values lower than the experimental data, although the gas distribution displayed a similar pattern to the experiments. The Brucato and Bakker models failed to predict both the gas holdup value and the gas pattern. However, the modified version of the Brucato's model with a lower constant (by two orders of magnitude) showed promising agreement both for the value of gas holdup and the air bubbles distribution within the tank. The authors expressed their doubts on the generality of the modified correlation and recommended further investigations for introducing a novel and general drag coefficient correlation.

Venneker et al., (Venneker et al., 2002) integrated a population balance equation (PBE) into an in-house (DAWN) code to predict the bubble size distribution inside an aerated agitated tank. The code was initialized with a developed single-phase 3D flow field to compute the PBE for a 2 dimensional domain. The authors named this method as 1.5-way coupling and specified that it was limited for the low gas holdup systems. The predicted contour plots of the gas distribution showed a good agreement with the measurements. In addition, the results predicted the main properties of a gas-liquid flow in a stirred tank comprising a region with high gas volume fraction around the impeller and close to the sparger and the presence of gas accumulation around the blade. The PBE solution revealed that the smaller bubble size existed around the impeller while the coalescence was dominant in the bulk region. The authors claimed that comparing to the Eulerian-Eulerian method their PBE methodology had a main advantage, since it was able to predict the bubble size distribution. However, the necessity to include the 3D effects on the bubble size distribution prediction was emphasized.

Lane et al., (Lane et al., 2002, Lane et al., 2003) continued their research on the CFD modelling of the gas-liquid flow inside the stirred tank and they reported their findings in 2002 and 2003. In the former study, they implemented an extra transport equation into CFX 4.2 to predict the bubble size distribution. In the equation the influence of bubble's break-up and coalescence were accounted for via source and

sink terms. The simulations were performed on a 60° slice of a Rushton turbine tank discretized into 43,920 cells. They also compared three different expressions for the drag coefficient including: Ishii-Zuber, Bakker and Brucato. Similar results to their previous study on the comparison of the drag coefficient correlations were reported. The predicted bubble size distribution revealed that high turbulence regions around the rotational zone increased the break-up rate, whereas the larger size bubbles above and below the impeller showed the dominant effects of bubbles' coalescence. Having compared the available drag coefficient equations they finally embodied the effects of turbulent eddies on the air bubbles movements into a new drag coefficient correlation. The new equation was established based on the ratio of the stagnant to the turbulent terminal velocity. The effects of gas cavity, the zones with high volume fraction of gas, were also comprised into this modelling approach. In order to examine the predictive capability of the new correlation, CFD simulations of a Rushton turbine (at two different operational conditions) and a Lightnin A315 impeller (at one operational condition) were performed using CFX4.4. MRF and SM simulated the rotation of the Rushton turbine and Lightnin A315 impellers, respectively. The comparison of the gas holdup predictions with the standard drag coefficient showed the advantage of the new approach. Also, the predicted gas flow pattern resembled the experimentally observed air bubbles distribution. In Chapter 4 the details of Lane's drag coefficient correlation and its predictive capability have been addressed.

In the study of Khopkar et al., (Khopkar et al., 2005) they applied computer-automated radioactive particle tracking (CARPT) and computed tomography (CT) methods to measure velocity components, gas distribution, and the local gas holdup values at two different flow regimes within a Rushton turbine tank. A two-fluid CFD model (i.e., Eulerian-Eulerian) with the standard $k-\epsilon$ turbulence model for the equations' closure was also used to predict the measured quantities. The authors highlighted the importance of the drag force among other interfacial forces and they applied a modified version of Brucato model with a lower constant to account for the drag force. The snapshot model was implemented for impeller rotation and the sparger was modelled as a solid wall with proper mass source term. The tank surface was defined as the velocity inlet boundary condition with a negative axial velocity equal to the terminal velocity of the bubbles. The observed upward motion of the flow field was attributed to the rising gas velocity and an increase in gas velocity increased the

upward disposition of the liquid velocity field. The discrepancy between the predicted tangential velocity and the measurements was assigned mostly to the inaccurate description of the drag force. The gas holdup predictions were compared to the CT results and an acceptable level of conformity was detected. In addition, the investigation of the flow around the impeller showed the gas accumulation due to the low pressure regions and the presence of trailing vortices. The authors claimed that the presented CFD model can be used for the industrial scale stirred tanks as well.

Laakkonen et al., (Laakkonen et al., 2005) reported the PIV measurements of the bubble size distribution, interfacial area between two different phases, gas holdups and the flow velocities in a stirred tank. The main aim of this study was to provide experimental data for the validation purposes. For the air-water system bubble size distribution showed a bimodal behaviour and it increased linearly with the angular velocity of the impeller. The variation of the gas holdup and interfacial were similar to each other which revealed the interconnection of these two hydrodynamic parameters inside the stirred tank. The presented results in this study showed a significant inhomogeneity of the flow field within the stirred tank.

Another contribution of Lane for the gas-liquid modelling of the stirred tanks was published in 2005 (Lane et al., 2005). They intended to improve the default approach for the two-phase modelling of the stirred tanks and as results four different improvements in the methodology enhanced the predictive capability of the multiphase approach. First, they included a turbulent dispersion term for the interfacial forces between the air and water. The new drag coefficient from their previous work was also added into the CFD framework. The third expansion was solving a bubble number density equation for the bubble size prediction which took into account the influence of the bubble break-up and coalescence. And finally the formation of the gas cavity was modelled by modifying the drag coefficient in high-air-contained zones (> 0.3). In order to model the gas cavity, an empirical correlation was used for the zones with high air content, which led to a progressive reduction in the drag force as the gas volume fraction increases. In addition, the gas phase was assumed to be turbulent and therefore the equations for the turbulent kinetic energy and dissipation rate were also included in this CFD framework. The methodology was tested on two types of impellers including Rushton turbine and Lightnin A315. The predicted gas volume fraction, bubble size, and power draw were compared with the

experimental data for different operational conditions. The default CFD model underpredicted the gas holdup, where the modified approach produced a reasonable agreement. The bubble size predictions obtained by the revised model also showed a good fit with experimental measurements. The authors, however, suggested that the generality of the model would be improved by exploring different liquids and adjust the breakup and coalescence rates. They also suggested that further improvements in gas cavity modelling can be achieved by integrating a surface tension force, and a surface sharpening algorithm in the homogeneous Eulerian model of Rigsby and Evans (Rigsby and Evans, 1998). These algorithms can be implemented into an Eulerian-Eulerian multiphase model to comprise the influence of gas cavity for the gas-liquid modelling of stirred tanks.

Khopkar (Khopkar et al., 2006) investigated the impact of hardware and operational conditions on the mixing patterns of a tall gas-liquid stirred vessel. The tank was equipped with three down-flow pitched blade impellers equally mounted in a concentric shaft. The applied CFD methodology was similar to their previous work in 2005 (Khopkar et al., 2005), except the drag coefficient correlation, where in this study the default drag coefficient was modified for the effect of turbulence. The Eulerian solution was applied as the initial solution for the Lagrangian computations of the circulation times. Half of the tank was discretized into $47 \times 94 \times 136$ elements in $r \times \theta \times z$ directions. The gas (with constant bubble size) was sparged using a source term at the ring sparger and collected at the top of the tank by a negative velocity inlet. The convergence in the solution was judged via adequate reduction in the residuals, a balanced gas flow rate in different levels of the tank, and negligible variations of the gas holdup and energy dissipation rates. Two distinct flow patterns were observed including a two-structured loop and a three-structured loop for the different velocities of the impeller. Qualitative comparison of the gas volume fraction contour plots with the experimental images of the gas distributions showed a reasonable agreement for the different flow regimes. Moreover, the Lagrangian calculations linked the observed local flow pattern with the overall mixing process. The average circulation time compared well with the experimental data from literature. Similar to their previous work, the authors stated the potential of their approach for industrial scale gas-liquid stirred vessels. They also followed up their work to simulate VC, S33, and L33 flow regimes (i.e., VC: vortex clinging, S33: small cavities, and L33: large cavities) for

gas-liquid reactors (Khopkar and Ranade, 2006). Contrary to their previous study, they compared the drag coefficient of Bakker and Brucato (with a modified constant) in this study and found that both of them were able to include the effect of turbulence on the air bubbles. The effect of including virtual mass as one of the interphase forces was evaluated but the results showed insignificant differences. The overpredictions of the gas holdups were observed for different flow regimes, yet the local gas holdup results matched the experiments reasonably good. Further, the predicted gas flow pattern around the impeller showed that the air bubbles accumulated around the blades, where the low-pressure regions existed. Although some discrepancies were found in their CFD models, the authors believed that their methodology is able to predict the gas holdup and the gas accumulation inside the Rushton turbine tank for three different flow regimes including VC, S33, and L33. Nonetheless, they recommended further investigations for the gas cavity modelling using a combination of VOF and Eulerian multiphase models.

The gas flow pattern, gas holdup and the bubble size distribution in a doubled Rushton turbine tank were numerically simulated by Kerdouss et al. (Kerdouss et al., 2006). An Eulerian-Eulerian multiphase method with the dispersed k- ϵ turbulence model was applied for half of the tank discretized into 280,000 tetrahedral elements. The gas phase was introduced into the computational domain using a velocity inlet boundary condition and the degassing boundary condition collected the air bubbles at the top surface. The proposed model of Bakker for drag coefficient was used with a modified constant to fit the experimental measurements of Alves et al. (Alves et al., 2002). Moreover, the bubble number density equation was added into the solver (Fluent 6.1) with two sources considering the bubble breakup and coalescence rates. The predicted flow patterns depicted two symmetrical vortices below and above the impeller which were close to the experimental observations. The flow pattern also showed the gas accumulation at two regions first at the low pressure zone around the impeller and second where circulation loops were located. Similar findings to the previous studies for the bubble sizes were reported. In other words, at the impeller discharge region the bubbles break-ups were prevailing, while above and below the impeller the coalescence effects were more pronounced.

Torre et al., (Torré et al., 2007) started the gas-liquid modelling of a partially baffled tank with the single phase solution. The results from the single-phase

modelling were compared to inhomogeneous multiphase flow model. They also predicted the free surface shape of the liquid during the agitation. An Eulerian-Eulerian method with the sliding mesh approach for the impeller rotation modelled the flow field. The stirred vessel was meshed using unstructured grid of 958,000 and 832,000 number of elements. They suggested that at least five numbers of rotations were required to break down the initial flow pattern. The free surface was predicted to be quasi-steady at 100 rpm. The authors, also, demonstrated the ability of RANS turbulence model (specifically k- ϵ turbulence model).

In the modelling work of Murthy et al., (Murthy et al., 2007) a CFD model was offered capable of predicting the gas-liquid, solid-liquid and gas-liquid-solid flow field in different types of stirred tanks. Different agitation systems, Rushton-turbine, downward and upward pitched blade impellers were compared for predicting the critical impeller speed for the solid suspension. In addition, the effects of geometrical and operational factors including impeller location, impeller speed, particle size, solid percentage and the superficial gas velocity were investigated. An Eulerian-Eulerian framework was used to solve the mass and momentum equations for three phases. Of different interphase forces, the drag force was applied for both solid and liquid with the modified Brucato model for the liquid-gas and Pinelli model for the liquid-solid interactions. For all the geometries tested in this study tetrahedral mesh scheme with the resolution of 600,000 to 700,800 cells was used. A converged solution was achieved with the residuals of all the equations less than 10^{-4} and the typical simulation time was 120 h on 16 nodes with 32 processors. The results for two phase flow showed an excellent agreement with the experimental data for the axial velocity, gas-holdup, and the solid concentration. Since there was no experimental data for the three phase system available, the CFD results for this section were described qualitatively with the critical impeller speed. The standard deviation of the solid concentration quantified the suspension in different operational and geometrical conditions which in turn defined the critical impeller speed. It was found that an increase in the impeller speed decreased the concentration of solid particles at the base of the tank and for the various impellers designs a good agreement between the critical impeller speeds and its experimental measurements were observed. A uniform suspension was seen for the finer particles while higher gas flow rate had dissimilar effects on the solid suspension quality. The comparison of the ring and pipe sparger

designs revealed that at a similar condition using ring sparger needed a lower critical impeller speed.

Scargiali et al., (Scargiali et al., 2007) simulated the gas holdup and gas distribution in a Rushton-turbine stirred tank with an Eulerian-Eulerian multiphase method. Half of the tank with a ring sparger was modelled using two grid resolutions: a coarse grid with 70, 596 cells and a fine one with 282,384 cells. The sliding mesh method with a large time step (equal to 60° of the impeller's rotation) ensured sufficient reduction in the mass residuals and having a constant gas holdup after around 100 revolutions of the impeller. The hybrid discretization scheme was used and source/sink terms were used for sparging and collecting the gas phase. The predicted gas holdup and the gas flow pattern with the coarse mesh showed good agreement with the literature data. The reduction of the angular velocity and the gas flow rate lowered the overall gas holdup, while using different bubble sizes did not affect the gas-liquid flow. Moreover, inclusion of lift, virtual mass and the turbulent dispersion interphase forces was found to be negligible and caused some convergence difficulties and additional computational demands. The authors claimed that the simulation of the gas cavity did not guarantee the accuracy of the CFD model and the prediction of the bubble size distribution can be decoupled from the flow equations.

Doroodchi et al., (Doroodchi et al., 2008) aimed to expand the applicability of the Lane proposed drag coefficient correlation by including the effect of turbulence intensity. In this experimental work, an oscillating turbulence creator generated the controlled levels of turbulence intensity to investigate the reduction in the ratio of slip velocity (U_S) over the particle terminal velocity (U_T) for a range of Stokes numbers. The measurements showed that the decrease in the settling velocity was a function of turbulence intensity and the particle characteristics (size and density). Comparison of the results with the Lane's model showed that the single proposed curve of Lane model (for U_S/U_T ratio as a function of St) should be modified by a family of curves for different particle size and density at various turbulence intensities. Furthermore, a plot of U_S/U_T as a function of Richardson number (Ri) showed that the maximum decrease in the particle settling velocity can be attributed to both inertial force (caused by turbulence) and gravity force (due to the particle weight). Therefore, the authors concluded that for different particles under various turbulence conditions the

Richardson number might be more practical to consider the particle settling velocity reduction.

Tabib and Schwarz (Tabib and Schwarz, 2011) performed LES simulations to study the addition of the sub-grid scale turbulent dispersion force (SGS-TDF) for gas-liquid and liquid-liquid flow inside a bubble column and pulp mixer. The magnitude of SGS-TDF was compared to the other interphase forces such as lift, virtual mass and drag for both cases. Besides, the numerical predictions of velocities and holdups were validated against the LDV and PIV measurements. For the bubble column the turbulent dispersion force was lower than the drag force; but for the pump mixer its scale was close to the drag force. Generally, it was observed that the influence of the TDF for the pump mixer was more pronounced than that of the bubble column. The presented results in this study pointed out one of the drawbacks for Eulerian-Eulerian multiphase method in conjunction with LES. They highlighted that when coarse mesh is applied the Eulerian-Eulerian with LES framework should be modified to include the SGS-TDF.

Recently, Buffo et al., (Buffo et al., 2012) combined a population balance model (PBS) and CFD to predict the bubble sizes inside gas-liquid stirred reactors. Using the PBS not only described the interaction between the continuous and dispersed phase, but also the coalescence and breakup effects of the air bubbles were included. For the CFD modelling Eulerian-Eulerian method with a $k-\epsilon$ mixture turbulence model was used. The drag force was modelled based on the terminal velocity of bubbles in a stagnant liquid. The extra equations for the PBS were added through a UDS in Fluent 12. The impeller was modelled using MRF and non-slip boundary conditions were applied for the walls. The sparger was modelled as porous media with the inlet velocity and tank's surface was opened to the atmosphere. The computed Sauter mean bubble diameter compared well with the bubble size distribution data from literature without modifying the model constants. The coupling of PBS with CFD for the gas-liquid modelling of stirred tanks showed promising results and the author recommended future studies on the predictions of the mass transfer.

2.5. Summary of gas-liquid simulations of stirred tanks

Section 2.4 reviews the previously published articles on the gas-liquid simulations of stirred tanks. Generally, the encountered complications for the turbulent flow of water and air bubbles within the tank have led researchers to apply some simplifying assumptions to resemble the flow field. Thus, no consensus on the methodology for the gas-liquid simulation of the stirred-tank has been proposed so far. However, there have been ranges of CFD methods introduced for the gas-liquid modelling of the stirred tanks. These methods have been improved over the years to approximate all the complexities within the domain as close to reality as possible with computationally affordable costs. As seen in the previous section, most of the studies applied an isotropic turbulence model, such as k- ϵ turbulence model, for the effects of turbulence on the continuous phase, while the turbulence induced by the air bubbles was assumed to be insignificant. Moreover, the impeller rotation was mostly modelled using the steady-state method of MRF which has been recognized to be less computationally intensive compared to the other alternatives. On the other hand, the higher computational power has lowered the number of simplifications in the modelling frameworks. For instance, different interfacial forces between the air bubbles and water have been tested and it was found that among the various forces the drag force had higher magnitude. Therefore, different drag coefficient equations have been formulated to include the influence of turbulence on the air bubbles. Another example that shows the enhancement of the gas-liquid modelling approach is implementing an additional transport equation for the bubble number density inside the tank. In addition to that, the accumulation of air bubbles behind the blades has also been assessed using CFD. For example in the study of Lane a modification was added for the drag coefficient correlation for the regions with high volume of gas phase. A summary of the reviewed articles is provided in Table 2-5. In the table, all the papers are itemized in terms of impeller type, multiphase approach, turbulence model, impeller modelling method, grid resolution, interphase forces, and the bubble size modelling approach. The table shows that the current study has an improvement compared to the previous ones. It includes a comprehensive comparison of different drag coefficient correlations under a range of operational conditions for three different volume stirred tanks. This study also suggests the optimized choice of the drag coefficient correlation for the gas-liquid modelling inside the Rushton-turbine tank.

Table 2-5 Summary of reviewed literature on gas-liquid simulations of stirred tanks

Reference	Impeller Type	Multiphase approach	Turbulence model	Impeller modelling	Grid resolution	Interphase forces	Bubble size modelling
(Gosman et al., 1992)	Rushton turbine	Eulerian-Eulerian	Modified k- ϵ	Black-box	27×20×15 (z, r, θ)	Added mass and drag	Constant
(Bakker and Akker, 1994)	PBT Disc turbine Lightnin A315	Eulerian-Eulerian	ASM	Black-box	40×25×25 52×27×17 50×25×20 (z, r, ϕ)	Drag with a modified Reynolds number	Bubble number density
(Morud and Hjertager, 1996)	Rushton turbine	Eulerian-Eulerian	Standard k- ϵ	Source/sink	47 × 24 (z, r)	Drag	Constant
(Ranade and Deshpande, 1999)	Rushton turbine	Eulerian-Eulerian	Standard k- ϵ	Snapshot	17×32×32 35×63×80 ($r \times \theta \times z$)	Drag	Constant
(Lane et al., 2000b)	Rushton-turbine	Eulerian-Eulerian	Standard k- ϵ	MRF		Drag: Ishii-Zuber Brucato Bakker Modified Brucato	Constant
(Venneker et al., 2002)	Rushton-turbine	Single-phase + PBE	RSM	Black-box			PBE
(Lane et al., 2002)	Rushton turbine	Eulerian-Eulerian	Standard k- ϵ	MRF	43,920	Drag: Ishii-Zuber Bakker Brucato	Bubble number density
(Lane et al., 2003)	Rushton turbine Lightnin A315	Eulerian-Eulerian	Standard k- ϵ	MRF SM	59,000 183,000	Drag (Lane model)	Constant
(Khopkar et al., 2005)	Rushton turbine	Eulerian-Eulerian	Standard k- ϵ	Snapshot	58×95×64 ($r \times \theta \times z$)	Drag (modified Brucato)	Constant
(Lane et al., 2005)	Rushton turbine Lightnin A315	Eulerian-Eulerian	Standard k- ϵ	MRF SM	59,000 183,000	Drag (Lane with gas cavity modification) Turbulent dispersion	Bubble number density
(Khopkar et al.,	Three down-	Eulerian-Eulerian	Standard k- ϵ	Snapshot	47×94×136	Drag (modified	Constant

2006)	pumping PBT				$(r \times \theta \times z)$	Brucato)	
(Khopkar and Ranade, 2006)	Rushton turbine	Eulerian-Eulerian	Standard k- ϵ	Snapshot	63×98×82 $(r \times \theta \times z)$	Virtual mass Drag: Bakker Modified Brucato	Constant
(Kerdouss et al., 2006)	Double turbine	Eulerian-Eulerian	Dispersed k- ϵ	MRF	280,000 tetrahedral elements	Drag (Modified standard drag)	Bubble number density
(Torré et al., 2007)	Three-bladed retreat curve impeller	Eulerian-Eulerian	Standard k- ϵ RSM	SM	958,000 832,000	Drag (standard)	Constant
(Murthy et al., 2007)	Rushton turbine Downward/upward PBT	Eulerian-Eulerian	Standard k- ϵ	MRF	600,000 700,800	Drag (Brucato)	Constant
(Scargiali et al., 2007)	Rushton turbine	Eulerian-Eulerian	Standard k- ϵ	SM	70, 596 282,384	Drag Lift Added mass Turbulent dispersion Sub-grid turbulence force	Constant
(Tabib and Schwarz, 2011)	Bubble column Pulp mixer (Lightnin R320)	Eulerian-Eulerian	LES (studied sub-grid turbulence force)	SM	400,000 587,000	Lift Drag Added mass	Constant
(Buffo et al., 2012)	Rushton turbine	Eulerian-Eulerian	Mixture k- ϵ	MRF	230,000	Drag Drag (Schiller-Naumann, Bakker,	PBS
Current study	Standard Rushton turbine (2.25 l, 10 l, 50 l)	Eulerian-Eulerian	Dispersed k- ϵ	MRF	235,872	Khopkar, Lane) under different operational and geometrical conditions	Constant per-simulation

2.6. Flotation

The flotation separation process has become the primary and preferable separation technology in the minerals industries. The reason lies for its prominence for treating of the complex and low grade ores where the required level of liberation is only achieved after several stages of comminution. According to King (King, 2001), although the fundamental principles of the separation process in the flotation are well-understood, deriving a general model which is fully capable of predicting the process responses is very difficult, if not impossible. The complexities of the modelling task can be looked at from various points of views. Hydrodynamically, the flotation process occurs in a fully turbulent flow field. The impeller rotation should provide a beneficial level of turbulence in the tank at which the solid particles remain suspended. However, the high turbulence intensity, caused by the impeller rotation, can be detrimental, as it detaches the valuable minerals from the air bubbles and prevent them from traveling to the froth phase. Technically, the separation involves several micro-processes. The air bubbles, induced from the sparger, rise up towards the surface of the tank and during their travel they meet and collide with the suspended particles (i.e., collision sub-process). The next sub-process to take place is the attachment of solid particles to the air bubbles (i.e., attachment sub-process) and it depends critically on the surface characteristics of the solid particles. If the particle surface is hydrophobic enough to adhere to the air bubbles and it has enough time to rupture the surrounding liquid around the air bubble, a stable bubble-particle aggregate is formed. The aggregates then continue their upward movement toward the tank's surface where they can be successfully skimmed from the froth phase. Nevertheless, the deformation of the bubble-particle aggregates (i.e., detachment sub-process) can happen due to their interactions with the large turbulent eddy or the entrainment² phenomenon.

King suggested that when establishing a successful predictive model for flotation, the separation process should be postulated as a first-order rate kinetic procedure (King, 2001). This modelling approach yields a flotation rate which can incorporate different aspects of the flotation separation process (hydrodynamics, technical, operational, geometrical and etc.). He has constructed a general structure

² Entrainment happens when gangue particles are dragged to the froth phase by the air bubbles.

for a flotation model based on the rate of transfer of particles from the slurry to the air bubble:

$$\begin{aligned} & \text{Rate of transfer} = \\ & \text{number of potential collisions} \times \text{number of bubbles per unit volume} \times \\ & \text{Efficiency of collection} \end{aligned} \quad \text{Eq. 2.2}$$

This formulation structure has been the premise for most of the flotation modelling research over the years. Various studies have tried to derive different quantitative expressions for the mentioned terms in Eq. 2.2. They have mostly divided the collection efficiency into three probabilities corresponding to the probabilities of collision, attachment and detachment and proposed different equations for each probability, while the other terms in Eq. 2.2 have been actively subjects of many flotation modelling studies. Sub-section 2.6.1 reviews the most important models presented for the flotation sub-processes. It also searches each paper to find out the significant operational and hydrodynamic factors of the flotation separation process.

2.6.1. Kinetic-based models for the flotation separation

One of the earliest models for the bubble particle collision efficiency was proposed by Gaudin, who assumed that for the Stokes flow ($Re_b < 1$) by ignoring the inertial force one can correlate the collision efficiency with the ratio of the particle size to the air bubble size (Gaudin, 1932). Another study aimed at formulating the number of collision of particles in a turbulent flow was performed by Abrahamson in 1975. He proposed an expression for the collision rate in a highly turbulent and isotropic fluid field (Abrahamson, 1975).

$$Z_{pb} = 5.0 N_p N_b \left(\frac{d_p + d_b}{2} \right)^2 \sqrt{\bar{U}_p^2 + \bar{U}_b^2} \quad \text{Eq. 2.3}$$

where Z_{pb} is the bubble-particle collision rate ($\text{m}^{-3} \text{s}^{-1}$), N_p and N_b are the particle and bubble number concentrations (m^{-3}), d_p and d_b are particle and bubble diameters (m), \bar{U}_p^2 and \bar{U}_b^2 are the average velocities of the particle and bubble relative to the liquid phase ($\text{m} \text{s}^{-1}$). The velocities were computed using:

$$\bar{U}_i^2 = \frac{\bar{U}^2}{1 + 1.5\tau_i\varepsilon/\bar{U}^2} \quad \text{Eq. 2.4}$$

In this equation τ_i is the particle/bubble relaxation time in fluid (s), ε is the energy dissipation rate per unit mass in $\text{m}^2 \text{s}^{-3}$ and \bar{U}^2 is the mean squared velocity

deviation of the fluid. The equation was based on the gas kinetic model and the distribution of the particle velocities in a turbulent flow. The author also limited the applicability of Eq. 2.3 for particle/bubble that follows the assumption of the independent velocity (Eq. 2.5).

$$d_p^2 > \frac{15\mu\bar{u}^2}{\rho_p\varepsilon} \quad \text{Eq. 2.5}$$

where μ is the fluid viscosity ($\text{kg s}^{-1} \text{ m}^{-1}$) and ρ_p is the particle density kg m^{-3} . The author stated that the main benefit of this equation was its applicability for a highly turbulent flow field.

Two years after Abrahamson, a hydrodynamic model was proposed by Anfruns and Kitchener (Anfruns and Kitchener, 1977) for collision, taking into account only gravitational and viscous forces and the drag and inertial forces were ignored. Their model was only valid for Stokes flow conditions and inertia-less flotation. They reported reasonable agreement with experimental data from quartz and with small bubble Reynolds numbers with $d_b = 0.5$ to 1 mm corresponding to with immobile surface. Schubert and Bischofberger (Schubert and Bischofberger, 1978) also experimentally investigated the influence of flotation hydrodynamics using dimensionless numbers (power and flow numbers). Changing the impeller speed and the air flow rate, cassiterite flotation tests were performed to explore the effects of the declared factors on the recovery and grade of *Sn*. The laboratory apparatus included a 6.6 l tank equipped with a double-finger-type impeller, whereas the industrial tests were conducted on 12-cell flotation series of 3 m³ volumes. At constant air flow rate (flow number), increasing the impeller speed had a positive effect on recovery. From the flotation hydrodynamics standpoint, it was proposed that the higher power number led to more collision of bubbles and particles and resulted in an increase in the recovery. Furthermore, at a constant impeller rotational speed the recovery showed a maximum at a certain air flow rate and after that it was reduced. This behaviour was attributed to the presence of more air bubbles available for attachment. The authors concluded that increasing the power input had a twofold effect. It increased the detachment forces yielding lower recovery and decreased the bubble sizes which made the buoyancy force impractical for the coarse particles to float.

Fallenius (Fallenius, 1987) derived an analytical equation for the turbulent fluctuating velocity in 1987. In his study it was assumed the flow field was single-

phase and the solid particles did not have any reduction effects on the turbulent fluctuating velocity. The equation was applied for various sets of experimental data from different types of industrial scale flotation cells (i.e., Outokumpo with volume range of 0.004 to 38 m³, Wemco with volume range of 0.028 to 28.3 m³, Denver with volume range of 0.011 to 36.1 m³, Minemet with volume range of 0.651 to 12.01 m³, Mekhanobre with volume range of 0.14 to 6.2 m³, and Sala with volume range of 2.69 to 3.34 m³). The findings, interestingly, showed that the fluctuating velocity was independent of the cell type and the volume. The only influential factor was found to be the rotor speed that slightly changed the velocity by increasing the cell size.

Another analytical expression established on the experimental and literature data was the work of Zhou et al., (Zhou et al., 1993) who addressed the impact of superficial gas velocity, liquid velocity, bubble size, gas holdup and frother concentration on the bubble rise velocity. Since they observed a good agreement between the model's predictions and the measurements, they inferred that the proposed model can be used to explore the effects of operational factors on the bubble rise velocity.

The interactions of the particulate phase including air bubbles and solid particles with the vortices for the turbulent flow were discussed by Crowe et al., (Crowe et al., 1995). They showed that the air bubbles usually go towards the centre of vortices, whereas the particles travel outward. This can be interpreted as the effect of the largest turbulent eddies for the detachment process. In other words, the particles will detach from a bubble-particle aggregate when it encounters a turbulent flow field.

In 1999, Bloom and Heindel (Bloom and Heindel, 1999, Heindel and Bloom, 1999) studied bubble-particle attachment and collision probabilities. Their study yielded different equations for the collision and attachment probabilities. The force balance between the effective forces, gravity, resistive force during film drainage, centrifugal force, flow force, lift force, and the drag force, on a particle led to form an analytical expression of the attachment probability. The presented equation was applicable for both Stokes and non-Stokes flow and it included different characteristics of the flotation such as fluid properties, bubble and particle diameters and velocities, and the ratio of initial-to-critical film thickness (h_0/h_{crit}) during the sliding motion of the particles over the bubbles. The proposed equation for the collision probability was also tested for both Stokes ($Re_p < 2$) and intermediate flow

($2 < Re_p < 500$) fields. The basis for deriving this equation was finding an expression for the capturing radius (R_c) which defines the maximum distance that a particle can collide with a bubble within this radius. In the new equations, three non-dimensional groups were applied including the particle settling velocity magnitude, the bubble Reynolds number, and the radius of particle over bubble. The obtained model computed the experimental data of the collision probabilities for different bubble and particle radii. The computations slightly overpredicted the measurements and it was attributed to the fact that the experimental information was represented as the collision efficiency rather than the exact collision probability. Further, the new model was compared with the available collision probability models and the comparison revealed the good capability of the proposed model with the previous equations.

In the experimental work of Dai et al. (Dai et al., 1999), they combined the experimental measurements of quartz flotation recoveries with Generalized Sutherland Equation (GSE) (Sutherland, 1948, Dukhin et al., 1995) to determine the attachment efficiency of quartz particles (with the size range of 7.5-70 μm) with nitrogen bubbles (of diameters 0.77, 1.00, 1.52 mm). The achieved attachment efficiencies were reduced with increasing the particle diameters, while an increase in attachment efficiency was observed by increasing the contact angle. In addition, decreasing the bubble size increased the attachment efficiency, although for the highly hydrophobic particles (large values of contact angles) the dependency on the bubble size was less pronounced. Later, they also reviewed the models for the bubble-particle collision step of the flotation separation process (Dai et al., 2000). Each model was elaborated in terms of the hydrodynamics and fluid flow regimes in which they were developed. Moreover, the experimental flotation data were used to compare the collision models. It was found that the Generalized Sutherland Equation (GSE) produced the closest results to the experiments. The authors stated that due to the inclusion of the inertial force in GSE this model was superior when compared to the others.

The next study of Bloom and Heindel in 2002 presented two new analytical expressions for the collision and detachment frequencies (Bloom and Heindel, 2002). They identified a critical bubble/particle diameter ratio for application of the models and assumed the turbulence should be in the inertial sub range. For the collision frequency model two formats were introduced with the influence of body forces and

without the effect of body forces. The collision frequency computations showed that the body forces increased the bubble-particle collision frequency by an order of 1.5. The detachment model was based on the bubble and particle sizes as well as the dissipation energy rate (i.e., application of Bond number). The authors also emphasized the importance of the bubble radius on the collision frequency. One year later, they combined their equations to predict the flotation efficiency in a semi-batch process (Bloom and Heindel, 2003). They proposed a new comprehensive model that accounted for collision, attachment and stabilization in the flotation process. In the new model a partial differential equation was solved for the concentration of free particles. Two rate constants for the attachment and detachment were added to reflect the appearance and disappearance of the free particles. These two rate constants covered the three probabilities for collision, attachment and detachment as well as the bubble-particle collision and detachment frequencies. The capability of the model was validated for the experimental measurements of the deinking flotation. It was found that for an ideal agreement between the experiments and the predictions the model was highly dependent on the stability parameter and the initial-to-critical film thickness.

Nguyen (Nguyen, 2003a, Nguyen-Van and Kmet', 1994, Nguyen et al., 1998, Nguyen, 1999) categorized the forces exerting on a particle attached to a large bubble as adhesive and detaching forces. The adhesive forces including capillary force, buoyancy, and pressure force, worked in favour of the attachment, while the detaching force such the weight of particle hindered a successful formation of bubble-particle aggregate. The force balance between the two groups of the forces yielded a new equation for the attachment tenacity. The determining parameters were the particle size, the surface tension between the gas and liquid and the particle contact angle. He also derived another equation for the maximum floatable particle size based on the particle contact angle, surface tension, particle density and the mean centrifugal acceleration of the turbulent eddies. Contrary to the works of Bloom and Heindel, they found the role of bubble size in the attachment efficiency was insignificant and for small particles encountered with big bubbles can be neglected. Also, the new expression for the maximum particle size for flotation was compared to the experimental data and even though simplifying assumptions were applied for the computations, a reasonable agreement with the experiments was observed. The

authors highlighted the role of turbulence on the detachment process and they suggested that better understanding of the turbulent dissipation rate will improve their proposed method.

Pyke (Pyke et al., 2003, Pyke, 2004) derived a fundamental equation for the calculation of the flotation rate constant. This equation accounted for the collision, attachment and detachment flotation sub-processes. The generalized Sutherland equation was applied to compute the collision efficiency, while the attachment rate was calculated based on the ratio of the adhesion angle to the maximum collision angle. The bubble-particle stability efficiency was also determined based on the adhesive and detaching forces with the aid of the dimensionless Bond number. In order to examine the new model, they performed flotation experiments with high-purity quartz in a Rushton turbine flotation tank. The bubble size and the velocities were also measured using a bubble size analyser and LDV. It was shown that the magnitude of the collision efficiency increased with particle size, though the other efficiencies showed contrary behaviour with the particle size. The turbulent dissipation rate reduction decreased the flotation rate constant. In addition, the role of bubble velocity was highlighted as it significantly influenced the attachment efficiency of the large particles. The predicted flotation rate constants with the new approach showed an acceptable agreement with the experimental data when certain values of bubble velocities and dissipation rates corresponded to the low turbulent regions, were applied³.

Bloom (Bloom, 2006) intended to enhance their semi-batch flotation model to a mathematical continuous model for flotation. Similar to his previous work on flotation, a first order equation for the number of free particles was introduced wherein the effects of the attachment and detachment were accounted for. Modifications were also applied to the previous methodology to remove the simplifying assumptions. For instance, a new term was introduced to take into account the average number of particles that can be attached to bubbles. This term had never been appeared in the previous modelling of the flotation sub-processes. Employing industrial scale experimental data, he validated the new model. The sensitivity analysis and the parametric study of the various terms in his new modelling approach

³ The proposed methodology of Pyke has been implemented in the CFD model to predict the flotation rate constant. In Chapter 5 the details of this set of equations and the results are discussed.

revealed wide variations in the final results. However, the author concluded that the proposed approach would be able to obtain the continuous flotation process efficiency and might be utilized for the optimization of the process.

Yianatos (Yianatos, 2007) reviewed the kinetic models of mechanical cells and flotation columns. Practically, the models for the conventional flotation cells were divided into two groups where the first group considered the recovery of minerals in the pulp and the second one focused on the froth recovery. For the column flotation the role of hydrodynamic factors such as terminal velocity and the bubble Reynolds number on the flotation performance were highlighted. This paper showed that despite the complex process of the flotation separation the knowledge of its kinetic behaviour would help to model this process.

Schubert (Schubert, 2008) investigated the influence of hydrodynamic factors on the flotation rate of fine particles. It was stated that the attachment sub-process mostly occurred in the impeller (high turbulent) region of the flotation tank. It was also advised that for the higher flotation rate of fine particles a high collision rate was required. In order to achieve this, four different parameters were suggested to be influential. First was the design of an efficient rotational system which resulted in an increase in the rotational speed of the impeller. In order to have better collision the dispersion of the slurry should be steady and finally the damping of the turbulence due to solid particle should be minimized to have optimum conditions for the fine particles flotation. Generally the author recommended that the ratio of the dissipation rate over kinematic viscosity of the fluid is required to be maximized for the fine particles and for a wide range of particle sizes an optimum hydrodynamic condition was impractical.

In most of the reviewed literature, the hydrodynamic factors have been treated as an average value. For example, the energy dissipation rate has been determined with dividing the power input by the mass of fluid and this single value has been applied for the entire flotation vessel. However, various studies showed that the turbulent properties around the rotational system are much higher than the bulk region. As a case in point, Schubert (Schubert, 2008) stated that the ratio of the average dissipation rate to the maximum dissipation rate can reach up to 200. Therefore, using an average value for the whole domain may cause serious uncertainties for the predictions of the flotation performance. Due to this reason and

the shortage of the analytical formulations to embody the effects of hydrodynamic parameters, the application of numerical methods, such as CFD, for modelling of the flotation process has become a demanding, yet challenging subject of research. The next sub-section elucidates the most important contributions of CFD models for enhancing the flotation modelling.

2.6.2. CFD-based models for the flotation separation

In all of the available equations for the flotation sub-processes, hydrodynamic parameters such as the volumetric gas flow rate, bubble diameter, energy dissipation rate and the bubble velocity have been included. These parameters are intended to assess the influence of flow hydrodynamics on the flotation performance. Using constant values for these factors throughout for the flotation tank has been the common way to cope with the hydrodynamic side of the flotation. However, the appearance of the CFD technique offers a substitute to the use of spatially-averaged values, since it can provide the local values of the hydrodynamically important terms in the sub-processes formulations. Therefore, using the numerical modelling of flotation not only offers an alternative to the empirical modelling approach but also provides local values of the hydrodynamic properties as inputs for the analytical expressions.

The CFD modelling of a fully turbulent multiphase flow inside the stirred tank faces many numerical challenges by itself and if one aims to combine it with other micro processes of the flotation separation to produce the overall separation performance the complexities would be multiple. Because of these complications encountered, the application of CFD for the flotation modelling has been mostly limited to the studies of Koh and Schwarz (Koh et al., 2000, Koh and Schwarz, 2003b, Koh et al., 2003, Koh and Schwarz, 2003a, Koh and Schwarz, 2006b, Koh and Schwarz, 2007, Koh and Schwarz, 2009, Koh and Smith, 2011). This sub-section reviews their published papers available on the open access resources.

As their first attempt in 2000 (Koh et al., 2000), they compared two different flotation cells namely the CSIRO cell and a standard Rushton turbine tank, in terms of the number of bubble-particle collision per time per volume. An Eulerian-Eulerian approach for the modelling of the gas-liquid within each tank was applied, where the turbulent features of the liquid phase was computed using the standard k- ϵ turbulence

model. The solid particles were implicitly introduced into the domain. In other words, the liquid phase was assumed to be a pulp with a certain solid percentage. The solid particles were homogeneously distributed within the tank. The bubbles and the particles were assumed to be uniformly distributed inside the tanks with constant diameters and Abrahamson equation (Eq. 2.3) computed the number of bubble-particle collision as a post-processing step. The results presented in this paper included the distribution of the gas phase and the turbulent dissipation rate. Applying the local values of the energy dissipation, the bubble-particle collision rates were also calculated for different zones inside the tanks. Three different regions were defined to cover the hydrodynamically important areas of the cells (i.e., impeller discharge, impeller surrounding and the bulk region). The distribution of the collision rate showed that the impeller discharge zone had the highest rate for both tanks; however, the CSIRO tank showed a higher collision rate per volume. The authors claimed that the obtained results could be used for design and modification of flotation cells.

In their next work in 2003, they compared only flow of water inside two flotation tanks namely the Metso Minerals and Outokumpu cells (Koh et al., 2003). To validate the CFD model, an LDV device measured the velocity components of the liquid phase within both tanks. The momentum and continuity equations in conjunction with the standard k- ϵ model for the turbulence quantities were solved. Two different techniques, sliding mesh and the multiple reference frames, were applied and compared for the modelling of impeller rotation via CFX4.4. The Metso Minerals cell was discretized into 156,820 cells, while the computational domain representing the Outokumpu tank had 146,912 cells. The obtained flow field for the Metso Minerals showed three vortices two below and above the impeller and the third one close to the surface. Further, the comparison of the velocity predictions with the LDV data illustrated a good agreement. The predicted flow pattern for the Outokumpu cell, however, provided two vortices below and above the impeller. The velocity predictions for this case also revealed close correspondence to the experimental information.

Koh and Schwarz in 2003 incorporated the bubble-particle collision rate and bubble-particle attachment rate in a CFD model to simulate a Denver-type flotation cell. In order to include the effects of fine particles the criterion defined by Eq. 2.5 was applied. The number of bubble-particle collision for the fine particles was

computed using the equation of Saffman and Turner (Saffman and Turner, 1956). The Yoon and Luttrell equation (Yoon and Luttrell, 1989) for the collision probability was also applied to account for those particles following the liquid streamlines. The Eulerian-Eulerian framework of CFX4.4 solved the conservation equations of mass and momentum in conjunction with turbulence quantities of the liquid phase. The impeller rotation was modelled using the MRF approach, while the froth layer was excluded in this study. The CFD predictions included the dissipation rate of turbulence, the volume fraction of each phase and the bubble-particle collision pattern. Using constant bubble and particle sizes the computed collision rate showed independency from the particle diameter, whereas collision probability increased with the particle size. The computed collection rate constant showed higher values than the typical industrial flotation rate constant and it was attributed to the differences in the transport times between the laboratory and the industrial scale tanks.

In 2006, they completed the flotation sub-processes modelling by including the detachment rate and the attachment probability into a CFD model (Koh and Schwarz, 2006a). The detachment rate was computed based on the relative velocity of a bubble-particle aggregate and the pulp phase. It was assumed that eddies with comparable size with the bubble-particle aggregate can cause detachment of solid particles from the air bubbles. This concept was first developed by Mika and Fuerstenau (Mika and Fuerstenau, 1968). A first order kinetic model was equipped with all the equations of sub-processes as source and sink terms that demonstrated the attachment and detachment phenomenon, respectively. CFX4.4 was used to solve the conservation equations for the liquid-gas system in an Eulerian-Eulerian structure. A similar approach was used for introduction of the solid particles (i.e., a new material as slurry with uniform distribution of single-size particle diameter). Two different geometries, a Rushton turbine tank and CSIRO Denver type flotation cell, were used in this study. The CFD predictions of the energy dissipation rate, volume fraction of gas phase, and the number of bubble-particle encounters were applied to calculate the sub-processes. The flotation rate constant was determined based on the half time reaction and it increased by increasing the particle diameter. It was also found that the initial attachment occurred close to the impeller while at the top part of the cell the bubbles experienced more stable conditions. The authors concluded that high attachment rates, close to the impeller, explained the fast formation of the bubble-

particle aggregate at this zone. However, the adequate bubble area flux was required to move the aggregates towards the froth layer.

In a follow-up study, they applied the previous CFD model for modelling of a self-aerated flotation cell (Koh and Schwarz, 2007). The only difference was that they included the influence of the gravitational force via adding a source term in the equation. An Eulerian-Eulerian approach was applied for a Denver type cell which was discretized into 103,000 grid points. Increasing the rotational speed increased the gas flow rates and the predicted results showed good agreement with the experimental information. The impact of the gravitational force increased the detachment rate due to the fact that it decreased the rise velocity of bubbles. It must be remembered that, since the Bond number was applied to reflect the ratio of the detachment to attachment forces, the inclusion of the gravitational force strengthened the overall detachment forces exerted on the air-bubble aggregate. Later, the proposed CFD model for the self-aerated Denver flotation cell was expanded one step further to investigate the influence of the bubble size distributions on the flotation rate constant (Koh and Schwarz, 2008). The Multi-Size-Group (MUSIG) feature of the CFX4.4 predicted the bubble size distribution by solving a transport equation for the bubble number density. Solving this equation resulted in a distribution of bubble diameters inside the tank which were taken as input for the kinetic modelling of the flotation sub-processes. Flotation simulations were performed for the observed bubble sizes at the previous step. The results showed that the flotation rate constant had a maximum with increasing the bubble diameter and after a certain bubble size it would decrease. The authors concluded that the CFD model can be used as an exploratory tool for the flotation performance study.

Evans et al., (Evans et al., 2008) combined the gas-liquid methodology of Lane for the gas dispersion modelling with the flotation modelling of Koh and Schwarz. The main aim of this study was to include the Lane's drag model for the flotation modelling. The governing equations involved the drag force and the turbulent dispersion force beside the conservation of mass and momentum. An extra PDE was also implemented for the bubble number density equation, while the gas cavity was modelled by modifying the drag expression. The gas dispersion model was tested for 5 different cases using different angular velocities and impeller systems (Rushton turbine and Lightin 315). The results comprised the gas volume fraction,

bubble diameter and the cavity formation which in all cases showed reasonable agreements with the experimental information. Further, Koh and Schwarz modelling technique was used to model the flotation sub-processes with extra source acting on the bubble-particle aggregate. The predicted bubble sizes from the solution of the bubble number density equation identified the bubble diameters for the sub-processes modelling. The predicted net rate of attachment in the flotation cell showed that both attachment and detachment occurred around the impeller. And the authors repeated the fact that CFD has the potential for the design and optimization of the flotation tanks.

Liu and Schwarz (Liu and Schwarz, 2009a) developed a multiscale modelling approach to investigate the turbulent influence on the bubble-particle collision efficiency. This work was based on their previous work in 2005 (Liu et al., 2005) where a methodology for the micro (bubble scale) and macro (cell scale) scale CFD modelling of the flotation was introduced. Micro-scale numerical tests were performed for the bubble-particle collision efficiency and investigation of the drag coefficients. The results were integrated into a macro scale model for the flotation cell. The predicted bubble-particle collision efficiencies were compared with the literature data which showed a good agreement. It was found that inclusion of the turbulence on the collision efficiency formulation resulted in an increase in this value. They continued the multi-scale modelling approach to investigate the influence of the bubble mobility and the turbulent environment on the collision performance (Liu and Schwarz, 2009b). The numerical results, obtained by solving the RANS equations and Lagrangian particle tracking method, were compared with the literature data to evaluate the model viability. The bubbles' walls and turbulence effects were also incorporated into the CFD model through the resistance function and using $k-\epsilon$ turbulence model, respectively. The effect of turbulence on the collision efficiency was found to be an improvement, while the fine particles resulted in a reduction in the collision efficiency. The proposed model was able to take into account the turbulent environment effects and the mobility of the bubble. Thus, the authors claimed that coupling it with the macro-scale flotation modelling could be applied to analyse and optimize the flotation rate in real situation.

Koh and Schwarz (Koh and Schwarz, 2009) applied their previous CFD-based model for the modelling of the Microcel column and Jameson flotation cell. Similar to

the previous studies an Eulerian-Eulerian multiphase approach was used for the pulp-gas modelling. An additional equation was also applied for the net rate of attachment which involved source and sink terms of attachment and detachment rates. The numerical predictions for the Microcel showed a circulating flow inside the column with the uniform distribution of gas phase within the column. The contour plots of detachment showed that there was a link between the dissipation rate of turbulence and the detachment rate. The higher dissipation rate regions around the sparger caused higher rate of detachment of particles from bubbles. Similar to Microcel, the dissipation rate contour plots for the Jameson cell revealed that near the air sparger system the maximum energy dissipation rate took place which in turn increased the detachment rate. The presented results in this study provided better insights for the column flotation hydrodynamics. Moreover, it was found that the cell performance can be improved by decreasing those regions with the maximum turbulent dissipation rate.

Koh and Smith (Koh and Smith, 2010) tried to validate the numerical prediction of flotation rate constants by batch flotation tests. The influence of different stirring speeds was investigated in a modified Denver flotation cell. The modelling framework involved the computation of mass, momentum and turbulence quantities for the multiphase flow of the gas-liquid within the CSIRO tank by means of Eulerian-Eulerian technique. The multiple reference frames was used for impeller modelling and the top surface of the tank was described by a degassing boundary condition. Further, the computation of net rate of attachment was added to the CFD model using an extra PDE in which two sources considered for the attachment and detachment rates of the bubbles and particles. The predicted profiles of the velocity and the gas holdup showed an increase with the impeller speed. The recovery-time graph demonstrated that the best agreement with the experimental recoveries of ballotini glass beads was achieved at 1200 rpm. In addition, the predicted flotation rate constant, determined from the remaining number of particles in the cell, showed reasonable agreement with the measurements. The authors, however, highlighted that the optimized conditions proposed in this study might require adjustment for other operational conditions. In 2011 in a follow-up study Koh and Smith investigated the influence of stirring speed and the induction time on the flotation performance. They verified the CFD predictions with the ballotini flotation tests. The CFD model

predicted the velocity components, the phase volume fractions, and the turbulence quantities. In addition, the flotation sub-processes were modelled via a transport equation wherein the attachment and detachment rates were included. A modified Denver flotation cell was discretized into 100,000 cells and a constant bubble diameter of 1 mm was applied in the modelling. Increasing the impeller speed yielded a more intense turbulent flow inside the tank with higher volume of the gas phase. The predicted flotation rate constant showed good agreement with the measurements and the predicted graph of recovery-time followed the trend of experimental data. The induction time results showed that a lower contact angle required more induction time. In other words, for the less hydrophobic particles one might reduce the angular velocity of the impeller to allow the particles to have longer time for the attachment. Table 2-6 provides a summary of CFD studies on flotation modelling. The table also shows how the current study simulates the flotation process using CFD derived data. This work, contrary to the CFD model of Koh and Schwarz, eliminates the need for solving an extra PDE for the number concentration of the free particles which results in a less computationally expensive CFD model. Moreover, it comprises the fluctuating behaviour of the flow variables in a kinetic model for the flotation process. This in turn enhances the predictive capability of the developed methodology for the flotation modelling.

Table 2-6 Summary of reviewed literature on the CFD modelling of flotation separation process

Reference	Type of flotation tank	Multiphase approach	Turbulence model	Solid treatment	Inclusion of PBE	Bubble size	Sub-process modelling	Mineral(s)
(Koh et al., 2000)	CSIRO Standard Rushton turbine	Eulerian-Eulerian	Standard k-ε	Pulp phase, monosized particles homogeneously distributed	No	Constant	Collision	Ballotini
(Koh et al., 2003)	Metso Minerals Outokumpu	Single-phase	Standard k-ε	N.A	N.A	N.A	N.A	N.A
(Koh and Schwarz, 2003a)	Denver cell	Eulerian-Eulerian	Standard k-ε	Pulp phase, monosized particles homogeneously distributed	No	Constant	Collision Attachment	Ballotini
(Koh and Schwarz, 2006b)	CSIRO Denver Standard Rushton turbine	Eulerian-Eulerian	Standard k-ε	Pulp phase, monosized particles homogeneously distributed	First-order rate kinetic model	Constant	Collision Attachment Detachment	Ballotini
(Koh and Schwarz, 2007)	Self-aerated Denver cell	Eulerian-Eulerian	Standard k-ε	Pulp phase, monosized particles homogeneously distributed	First-order rate kinetic model	Constant	Collision Attachment Detachment (with inclusion of gravitational force)	Ballotini
(Koh and Schwarz, 2008)	Denver cell	Eulerian-Eulerian	Standard k-ε	Pulp phase, monosized particles homogeneously distributed	First-order rate kinetic model	Multi-sized bubbles but constant per-simulation	Collision Attachment Detachment	Ballotini
(Evans et al., 2008)	Standard Rushton turbine Lightin 315 Denver cell	Eulerian-Eulerian	Standard k-ε	Pulp phase, monosized particles homogeneously distributed	First-order rate kinetic model	Constant per-simulation	Collision Attachment Detachment	Quartz

(Liu and Schwarz, 2009a)	Denver cell	Multi-scale approach	Standard k-ε	distributed N.A	First-order for bubble size	Variable	Collision rate Collision efficiency	Alumina
(Liu and Schwarz, 2009b)		Multi-scale Lagrangian	Standard k-ε	Lagrangian particles	N.A	Constant	Collision rate Collision efficiency	Quartz
(Koh and Schwarz, 2009)	Microcel column Jameson cell	Eulerian-Eulerian	Standard k-ε	Pulp phase, monosized particles homogeneously distributed	First-order rate kinetic model	Constant	Collision Attachment Detachment	Particle density 1520 kg/m ³
(Koh and Smith, 2010)	Denver cell	Eulerian-Eulerian	Standard k-ε	Pulp phase, monosized particles homogeneously distributed	First-order rate kinetic model	Constant	Collision Attachment Detachment	Ballotini
(Koh and Smith, 2011)	Denver cell	Eulerian-Eulerian	Standard k-ε	Pulp phase, monosized particles homogeneously distributed	First-order rate kinetic model	Constant	Collision Attachment Detachment	Ballotini
Current study	Standard Rushton turbine	Eulerian-Eulerian	Dispersed k-ε	Pulp phase, monosized particles homogeneously distributed Different sized particles per-simulation homogeneously distributed	Flotation rate constant was included	Constant per-simulation	Collision Attachment Detachment	Quartz Galena (for a wide range of hydrophobicities, agitation speeds and gas flow rates)

2.7. Conclusion

This section has reviewed the related articles about the applications of the CFD techniques for the stirred tank modelling. It starts with the simulations of water inside the stirred tank. The relevant CFD issues have been categorized based on the type of uncertainties that they can produce in the final solutions. The input uncertainties are mostly caused by the users' mistakes when they try to outline the problem for the CFD solver codes. For example, if the impeller's geometry does not adequately replicate the actual geometry of the impeller, the solution would suffer from a significant discrepancy with the reality. In the single-phase modelling of the stirred tanks different models implementations and formulations are the main sources of the model uncertainties, the second type of related uncertainty in the water-modelling of the agitated tanks. The reviewed articles has shown that adopting different turbulence models, impeller modelling approaches and various solvers assess the level of accuracy for the numerical predictions of the flow features. Most of the papers have highlighted the anisotropic nature of the turbulence in the vessel due to the rotation of the agitation system. However, using anisotropic turbulence models such as RSM and LES have shown to be computationally very expensive and they are only practical for the research purposes. Four different methods have been utilized for the impeller modelling, using experimental data (i.e., black box), snapshot approach, sliding mesh and multiple reference frames. Of these, the black box scheme is restricted by the availability of the experimental data corresponding to the impeller geometry. The snapshot approach has been merely seen in the studies of Ranade and the generality of this approach has not been tested by other researchers. Moreover, between the SM and MRF methods, which are available in most of the commercial CFD codes, the MRF is one tenth of the SM less time-consuming. Finally, the numerical uncertainties, the last type of inherent uncertainty in the single-phase modelling of the stirred tanks, are caused by the magnitude of the domain's discretization. It has been revealed that a relatively coarse mesh is able to predict the general flow patterns and the velocity components within the stirred tanks. Nevertheless, the predictions of the turbulent kinetic energy and the turbulent dissipation rate around the impeller require higher level of mesh refinement. Furthermore, many evidences in the literature have pointed out that the flow

characteristics around the rotating blades, such as the presence of vortices, need more elements in this region to be accurately captured.

Several important lessons relevant to the gas-liquid modelling of the mechanically agitated vessels have emerged from the extensive review of the previous studies on this field. This review shows that generally the high degree of complexities for the gas-liquid modelling has lowered the number of studies compared to the single-phase. Moreover, the different modelling strategies have appeared in the literature and researcher proclaimed that their methods provided an acceptable validation against the experimental data. Historically, the Lagrangian-Eulerian framework was the affordable option for the gas liquid modelling, where the low volume fraction of air bubbles allowed the researcher to track the trajectories of each droplet. The application of Eulerian-Eulerian multiphase method for the gas-liquid modelling has a parallel growth with the computational power. In that, the powerful computers enable the solvers to include a separate set of transport equations for the discrete phase (i.e., the gas phase) and the properties of the secondary phase (such as velocity components and volume fraction) are achievable at every point inside the domain. The turbulence properties including turbulent kinetic energy and its dissipation rate have also been dealt with in most of the previously published papers. Similar to the single-phase modelling, an isotropic turbulence model, the standard $k-\epsilon$, has been recommended to be a feasible choice. The definition of the interphase forces between the continuous liquid phase and the dispersed air bubbles has been another major concern in the literature. It has been shown that of the various forces: virtual mass, lift, and drag, the drag force is the dominant interphase force. Therefore, several formulations for the drag coefficient correlation have come into view in the previous studies. In addition, only few investigations have been conducted to predict the bubble size distribution inside the tank. Overall, the reported predictions of the bubble diameters have showed a reasonable correspondence with the reality, yet some researcher have suggested that further investigations would improve the description of the air bubbles inside the tank. It is worth noting that before having the capability of adding one set of transport equation for the bubble number density function, the bubble size was assumed to be constant. Currently, multiphase CFD studies of flotation still use the constant bubble size approximation inside the domain to achieve acceptable computational time for gas-liquid modelling.

Finally, the last sub-section of this review has specified two methods (the kinetic and the numerical approaches) for the flotation modelling. The first conventional way is based upon the premise of King's formulation (Eq. 2.2) where the transfer rate of particles to bubbles is defined by the number of effective collisions between the solid particles and the air bubbles. In order to improve this basis, many experimental and analytical studies have been carried out to frame the flotation sub-processes (i.e., collision, attachment, and detachment). As a result, there have been many equations for the sub-processes in which different aspects of the flotation were addressed. In the empirical expressions, the turbulence characteristics of the flow have been averaged over the entire domain and a constant value has been used for the computations of the flotation responses. This has led to the appearance of the second strategy for modelling flotation cells. This approach is founded on the application of CFD for capturing all the details of the flow variables inside the flotation tank. However, limited articles have been published showing the applicability of the CFD for the sub-processes modelling. Koh and Schwarz have developed and applied a general CFD framework for the modelling of flotation process. In their strategy, an additional equation for the number concentration of free particles is implemented into the solver. The flotation sub-processes have been introduced, in this equation, via proper source and sink terms. Using the local values of the turbulent properties, the source and sink terms results in the net rate of attachment after considering the detachment impacts. An Eulerian-Eulerian multiphase approach with the standard k- ϵ turbulence model has been the general method to solve the governing equations of pulp and air bubbles inside the tank. Koh and Schwarz also used a simplifying assumption for the bubble size inside the flotation tank. It was postulated that the air bubbles were ideal spheres with constant diameters homogeneously distributed within the tank. This methodology has been subjected to validation studies as well and it has exhibited its predictive capability for the flotation sub-processes modelling.

Chapter 3 Development of a CFD methodology for single-phase flow in stirred tanks

3.1. Introduction

This chapter describes the process of developing a CFD methodology for water modelling inside two types of stirred tanks. The first geometry is adopted from the study of Armenante (Armenante et al., 1997) where they measured the velocity components and the turbulent properties using LDV. The second vessel is a standard Rushton turbine flotation tank for which Newell experimentally obtained the velocities and turbulent characteristics (Newell, 2006). As mentioned previously, in order to develop a CFD-based model for the flotation process, it is crucial to first gain insights about the flow of water and its relevant phenomenon within the vessel. This will serve as a basis to expand the modelling approach for the gas-liquid and the flotation sub-processes modelling in later chapters.

In this chapter the different factors causing uncertainties in the computational results of single-phase modelling are discussed. The input uncertainty is minimized with specifications of the input constants with a high level of accuracy. The impacts of the model uncertainties for both geometries are investigated by performing a turbulence model study, and comparing different implementations of the impeller modelling via Fluent CFD code (ANSYS, 2011a). Moreover, the numerical uncertainties are evaluated using various mesh resolutions. Also the Grid Convergence Index (GCI) method proposed by Roach (Roache, 1994) is applied to bound the numerical uncertainties in simulations. It must be noted that during the development of the CFD methodology two criteria, including the required computational time and the level of agreement with the experimental measurements, have been chosen to assess the practicality and accuracy of the numerical predictions.

3.2. Governing equations

Computational Fluid Dynamics or CFD for short is a numerical process which solves the mathematical equations describing the underlying physics of the fluid motion (Blazek, 2001). Before derivation of the governing equations, it is worth noting that the general convention for CFD methods is that the fluid is assumed to be a “continuum”. In other words, even the smallest elements of the fluid can have mean velocity and turbulent energy. For the case of stirred tanks, the continuous and turbulent movement of water inside the stirred tank can be explained by two conservation laws: the conservation of mass and the conservation of momentum. In the conservative form the continuity, or the mass conservation equation, is written as follow (Wendt and Anderson, 2009, Batchelor, 2000):

$$\frac{\partial \rho}{\partial t} + \nabla \cdot (\rho \vec{v}) = S_m \quad \text{Eq. 3.1}$$

where ρ is the fluid density, t is time, and \vec{v} is the velocity vector. The S_m term in Eq. 3.1 denotes the added source term of the secondary phase that can be introduced to the continuous phase (e.g. the air bubbles).

The conservation of momentum equation (referred to as the Navier-Stokes equation) is defined as (Wendt and Anderson, 2009, Batchelor, 2000):

$$\frac{\partial}{\partial t} (\rho \vec{v}) + \nabla \cdot (\rho \vec{v} \vec{v}) = -\nabla p + \nabla \cdot \left[\mu \left((\nabla \vec{v} + \nabla \vec{v}^T) - \frac{2}{3} \nabla \cdot \vec{v} I \right) \right] + \rho \vec{g} + \vec{F} \quad \text{Eq. 3.2}$$

where the static pressure, laminar viscosity, unit tensor, gravitational acceleration and external body force of the fluid are denoted by p , μ , I , \vec{g} , and \vec{F} .

The solutions to Eq. 3.1 and Eq. 3.2 provide a complete description of the flow fields for all types of laminar single-phase flows. Furthermore, if the required computational power is accessible to perform Direct Numerical Simulation (DNS), the solutions to the mentioned equations can explain even the turbulent flow field for agitated vessels. However, computational resources are not yet powerful enough to broadly apply the DNS method. Hence, Eq. 3.1 and Eq. 3.2 are required to be modified and approximated for practical simulations of the turbulent flow inside stirred tanks. Typical approximation of the equations is called Reynolds averaging (Fletcher, 1991, ANSYS, 2011a). In this procedure the solution variables such as the

velocity components, u_i , are separated into summation of a mean (\bar{u}_i) and an instantaneous (u'_i) component:

$$\mathbf{u}_i = \bar{\mathbf{u}}_i + \mathbf{u}'_i \quad \text{Eq. 3.3}$$

The Reynolds averaged forms of Eq. 3.1 and Eq. 3.2 are derived by replacing the new form of the flow variables (i.e., Eq. 3.3) into the continuity and momentum balance equations:

$$\frac{\partial \rho}{\partial t} + \frac{\partial}{\partial x_i} (\rho \mathbf{u}_i) = 0 \quad \text{Eq. 3.4}$$

$$\frac{\partial}{\partial t} (\rho \mathbf{u}_i) + \frac{\partial}{\partial x_j} (\rho \mathbf{u}_i \mathbf{u}_j) = -\frac{\partial p}{\partial x_i} + \frac{\partial}{\partial x_j} \left[\mu \left(\frac{\partial u_i}{\partial x_j} + \frac{\partial u_j}{\partial x_i} - \frac{2}{3} \delta_{ij} \frac{\partial u_l}{\partial x_l} \right) \right] + \frac{\partial}{\partial x_j} (-\rho \overline{u'_i u'_j}) \quad \text{Eq. 3.5}$$

Eq. 3.4 and Eq. 3.5 are known as Reynolds-averaged Navier-Stokes or RANS equations. As can be seen, an additional term, $-\rho \overline{u'_i u'_j}$, has appeared in the averaged version of the momentum balance equation. This term is called Reynolds stress and signifies the effects of the turbulence eddy on the momentum transport. In order to solve the set of equations (Eq. 3.4 and Eq. 3.5) a closure expression for the Reynolds stress tensor should be specified which leads to the introduction of different turbulence models.

In this study the standard k- ϵ turbulence model (Launder and Spalding, 1972) is utilized to compute the Reynolds stress term in Eq. 3.5. Other categories of turbulence models have been compared with the standard k- ϵ model elsewhere (Patel et al., 1985, Shih et al., 1994, Wilcox, 1994, Karimi et al., 2012).

The k- ϵ turbulence model takes advantages of the Boussinesq hypothesis to determine the Reynolds stress tensor (ANSYS, 2011a). In this method the Reynolds stress is formulated based on the turbulent viscosity, μ_t , and the mean velocity gradient as follow:

$$-\rho \overline{u'_i u'_j} = \mu_t \left(\frac{\partial u_i}{\partial x_j} + \frac{\partial u_j}{\partial x_i} \right) - \frac{2}{3} \left(\rho k + \mu_t \frac{\partial u_k}{\partial x_k} \right) \delta_{ij} \quad \text{Eq. 3.6}$$

where k is the turbulent kinetic energy. The main advantage of the Boussinesq hypothesis is that it is a fairly inexpensive computational method due to the fact that it presumes turbulence is isotropic in the flow field. Therefore, it can be recognized by the fluctuating components of the velocity. The k- ϵ turbulence model falls within the

two-equation turbulence models class in which two separate conservation equations for the turbulent kinetic energy (k) and turbulent dissipation energy rate (ε) are solved.

$$\frac{\partial}{\partial t}(\rho k) + \frac{\partial}{\partial x_i}(\rho k u_i) = \frac{\partial}{\partial x_j} \left[\left(\mu + \frac{\mu_t}{\sigma_k} \right) \frac{\partial k}{\partial x_j} \right] + G_k + G_b - \rho \varepsilon + S_k \quad \text{Eq. 3.7}$$

$$\frac{\partial}{\partial t}(\rho \varepsilon) + \frac{\partial}{\partial x_i}(\rho \varepsilon u_i) = \frac{\partial}{\partial x_j} \left[\left(\mu + \frac{\mu_t}{\sigma_\varepsilon} \right) \frac{\partial \varepsilon}{\partial x_j} \right] + C_{1\varepsilon} \frac{\varepsilon}{k} G_k - C_{2\varepsilon} \rho \frac{\varepsilon^2}{k} + S_\varepsilon \quad \text{Eq. 3.8}$$

In Eq. 3.7 and Eq. 3.8, two generation terms have emerged, G_k and G_b , which represent the production of k due to the mean velocity gradient and the buoyancy, respectively. G_k is written as:

$$G_k = -\overline{\rho u'_i u'_j} \frac{\partial u_j}{\partial x_i} \quad \text{Eq. 3.9}$$

The G_b term relates to the temperature gradient inside the domain. So, for stirred tanks case where the temperature is constant this term can be neglected. The recommended model constants of Launder and Spalding (Launder and Spalding, 1972) are employed for the single-phase modelling of the stirred tank (Table 3-1).

Table 3-1 Model constants for Eq. 3.7 and Eq. 3.8

Constant	Value
$C_{1\varepsilon}$	1.44
$C_{2\varepsilon}$	1.92
C_μ	0.09
σ_k	1.0
σ_ε	1.3

In Eq. 3.6, the turbulent viscosity, μ_t , is calculated via Eq. 3.10:

$$\mu_t = \rho C_\mu \frac{k^2}{\varepsilon} \quad \text{Eq. 3.10}$$

In Eq. 3.7 and Eq. 3.8, the S_k and S_ε terms are the customized source terms for the turbulent kinetic energy and its dissipation rate, and can be manipulated via user defined subroutines.

The turbulent flow of water inside the stirred tank is bounded by the outer walls. The presence of walls creates boundary layers very close to the walls where the flow's state can alter from the laminar to the fully turbulent regimes. Typically, three layers are distinguished near the walls; the first one is called the viscous sub-layer in which the flow is laminar. Turbulence is in the outer layer. The intermediate layer connects the viscous sub-layer to the fully-turbulent zone. In this region the importance of the molecular viscosity and the turbulent eddies are similarly

significant. Using wall functions, one can link the solution variables of the inner region to the fully-turbulent layer. The wall functions include a formulation for the mean velocity and equations for the turbulent quantities near the wall. The standard wall function, adopted in this study, applies Eq. 3.11 for the mean velocity (ANSYS, 2011a):

$$U^* = \frac{1}{\kappa} \ln(Ey^*) \quad \text{Eq. 3.11}$$

where U^* and y^* are the dimensionless velocity and the dimensionless distance from the wall. They are expressed as follows:

$$U^* \equiv \frac{U_P C_\mu^{1/4} k_P^{1/2}}{\tau_w / \rho} \quad \text{Eq. 3.12}$$

$$y^* \equiv \frac{\rho C_\mu^{1/4} k_P^{1/2} y_P}{\mu} \quad \text{Eq. 3.13}$$

where κ is the von Karman constant ($=9.793$), E is a constant ($=0.4187$), U_P is the mean velocity of the fluid at the near-wall node P , k_P is the turbulence kinetic energy at the near-wall node P , y_P is the distance from point P to the wall, and μ is the dynamic viscosity of the water. The overall Reynolds number of the flow determines the lower and upper limits of y^* .

In the k - ε turbulence model, the transport equation for k is computed for the entire domain regardless of the near-wall regions. The boundary condition at the wall is:

$$\frac{\partial k}{\partial n} = 0 \quad \text{Eq. 3.14}$$

In Eq. 3.14 n denotes the coordinate normal to the wall. For near-wall control volumes, the kinetic energy production, G_k , (see: Eqs. 3.7 and 3.8) is calculated according to the logarithmic law:

$$G_k \approx \tau_w \frac{\partial U}{\partial y} = \tau_w \frac{\tau_w}{\kappa \rho C_\mu^{1/4} k_P^{1/2} y_P} \quad \text{Eq. 3.15}$$

Finally, Eq. 3.16 is the expression for the turbulent dissipation rate for the cells adjacent to the wall:

$$\varepsilon_P = \frac{C_\mu^{3/4} k_P^{3/2}}{\kappa y_P} \quad \text{Eq. 3.16}$$

The governing equations derived thus far can be applied for a broad range of turbulent flow. The RANS equations along with the standard k- ε turbulence model are known for their capabilities in modelling of the industrial flows. They can provide numerical predictions of the flow field with an acceptable level of agreement, while the computational requirements are affordable (Ranade, 2002). However, for stirred tank modelling, these equations should be solved in a moving reference frame to consider the impeller rotation. The multiple reference frame model (Luo et al., 1994) is applied in this study where the domain is divided into two regions: the rotational zone and the stationary zone. The governing equations of the flow in the rotational zone are solved in a rotating reference frame. A stationary reference frame is, however, utilized to resolve the fluid flow equations outside the rotational zone (i.e., rest of the tank). For the stationary subdomain Eq. 3.4 and Eq. 3.5 are computed to find the fluid flow variables. For the rotating reference frame with a linear velocity of \vec{v}_t and an angular velocity of $\vec{\omega}$ the conservation of mass and momentum can be re-written as:

$$\frac{\partial \rho}{\partial t} + \frac{\partial}{\partial x_i} (\rho \vec{v}_r) = 0 \quad \text{Eq. 3.17}$$

$$\frac{\partial}{\partial t} (\rho \vec{v}_r) + \nabla \cdot (\rho \vec{v}_r \vec{v}_r) + \rho (2\vec{\omega} \times \vec{v}_r + \vec{\omega} \times \vec{\omega} \times \vec{r} + \vec{a} \times \vec{r} + \vec{a}) = -\nabla p + \nabla \cdot \left\{ \mu \left[(\nabla \vec{v}_r + \nabla \vec{v}_r^T) - \frac{2}{3} \nabla \cdot \vec{v}_r I \right] \right\} + \vec{F} \quad \text{Eq. 3.18}$$

where $\vec{a} = \frac{d\vec{\omega}}{dt}$ and $\vec{a} = \frac{d\vec{v}_r}{dt}$. In Eq. 3.18 the term $(2\vec{\omega} \times \vec{v}_r)$ is the Coriolis acceleration and $(\vec{\omega} \times \vec{\omega} \times \vec{r})$ is the centripetal acceleration.

The governing equations derived in this sub-section are the premise of the single-phase modelling inside the stirred tanks. The Fluent CFD solver solves the equations to obtain the velocity components as well as pressure distribution. In addition, the various sources of the uncertainties in the numerical solutions of the governing equations are investigated. For example, in implementation of the MRF, the rotational zone dimensions, where the equations are solved in the moving reference frame, can influence the final solutions. The detailed descriptions of the diagnostic tests for finding and minimizing the uncertainties are presented later in this chapter.

3.3. Results and discussion

In order to develop a CFD methodology that is quantitatively capable of predicting the flow inside stirred tanks, various issues related to the single-phase modelling of stirred vessels have been explored. In this section, the main challenges encountered during the process of establishing a CFD model for the single-phase simulations of the stirred tanks are reported. Since the typical stirred vessels in the chemical industries include unbaffled vessels and for the flotation modelling the application of Rushton turbine agitation systems are confirmed in minerals industries, two types of vessels, an unbaffled mixer and a standard Rushton turbine, have been tested. The first sub-section elaborates the findings from the unbaffled vessels, while the second sub-section concentrates on the numerical approaches applied to model the flow of water inside a standard Rushton turbine flotation tank.

3.3.1. Simulations of single-phase flow inside an unbaffled mixer

The first tank configuration used is a 6-bladed, cylindrical, flat-bottom unbaffled vessel. The tank diameter, T , is 293 mm and for all the simulations the tank is filled with water. The impeller with diameter, D , of 98 mm is mounted at 73 mm off the tank's base (i.e., clearance = 73 mm). The six equally spaced vertical blades have a width of 19.6 mm and the angular velocities of 450 rpm and 700 rpm corresponding to Reynolds number of 7.1×10^4 and 11.1×10^4 have been tested. Armenante (Armenante et al., 1997) measured the velocity components and the turbulent properties for a mixer almost similar to this one. Therefore, the numerical predictions at each step are validated against the experimental information of Armenante. The geometrical details of the first computational domain for the entire tank are tabulated in Table 3-2.

Table 3-2 Geometrical details of the unbaffled mixer

Parameter	Symbol	Dimension (mm)
Tank diameter	T	293
Tank height	$H = T$	293
Impeller diameter	$D = T/3$	98
Blade height	$BH = D/7$	14
Blade length	$BL = D/2$	49
Impeller clearance	$IC = T/4$	73

At the first stage, in order to perform the preliminary tests, the entire tank is chosen. It is intended to comprise all the 3D effects and investigate the flow features at every location in the tank. Figure 3-1 displays the schematic design of the unbaffled

mixer created with the help of ANSYS Design Modeller (ANSYS, 2011b). The figure also shows five different planes at 53, 71, 88, 160 and 233 mm from the bottom of the tank on which Armenante reported the radial distribution of the velocities and the turbulence properties.

The numerical solutions of the governing equations at the centre of each control volume are obtained with Fluent code. The transient tests are carried out with the k- ϵ turbulence model at the rotational speed of 450 rpm. The second order discretization scheme computed the momentum and the turbulent features of the flow. Additionally, the SIMPLE algorithm coupled the continuity and momentum equations to derive the pressure field inside the tank (Petrila and Trif, 2005).

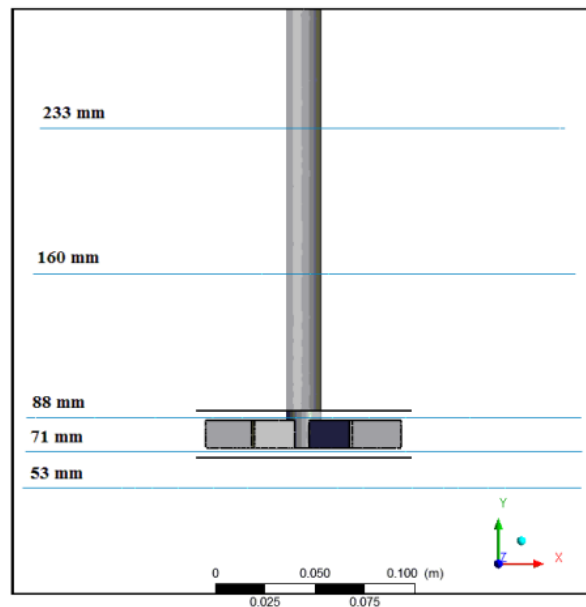


Figure 3-1 Schematic of the entire un baffled mixer tank.

3.3.1.1. Dimensions of the rotational zone

The first step for successful modelling of water inside the tank is finding the extent of the rotational zone around the impeller, as there is no general agreement in the previous works reviewed in Chapter 2. It also reduces the uncertainties related to the model's implementation for the impeller modelling. The main criterion for the optimized size of the rotational zone is that it should provide the closest agreement with the experimental measurements while the CPU time is affordable. Four different dimensions are allocated with 1, 2, 5, and 7 mm distance from all sides of blades (i.e., four cylinders with height and length of 16×100 mm, 18×102 mm, 24×108 mm, and

28×112 mm). It is worth noting that the continuity and momentum balance equations inside these cylinders are being solved in a rotating reference frame, whereas for the rest of the tank a stationary reference frame is adopted. Figure 3-2 exemplifies two instances of the rotational zone dimensions for the unbaffled mixer. The left hand side image is the smallest extents for the rotational zone where the rotating cylinder is only a tablet encompassing the blades with 1 mm distance from them. The right hand side image, however, is the largest extents of the spinning zone with 7 mm distance from the blades. The simulations for four different cases are conducted to predict the velocity components and the turbulent properties. All the simulations are started from zero velocity field and they are stopped when the normalized continuity residuals are below 10^{-3} .

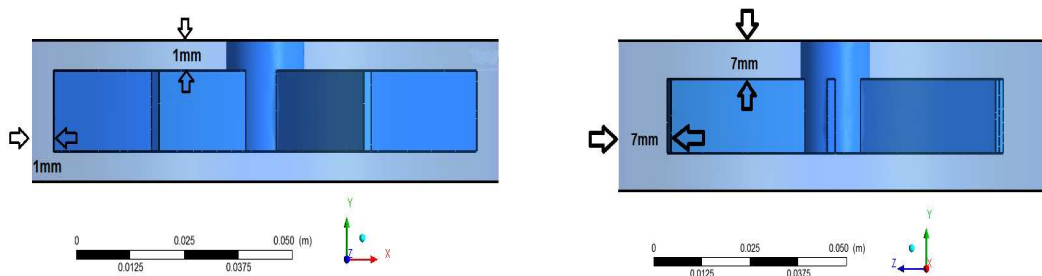
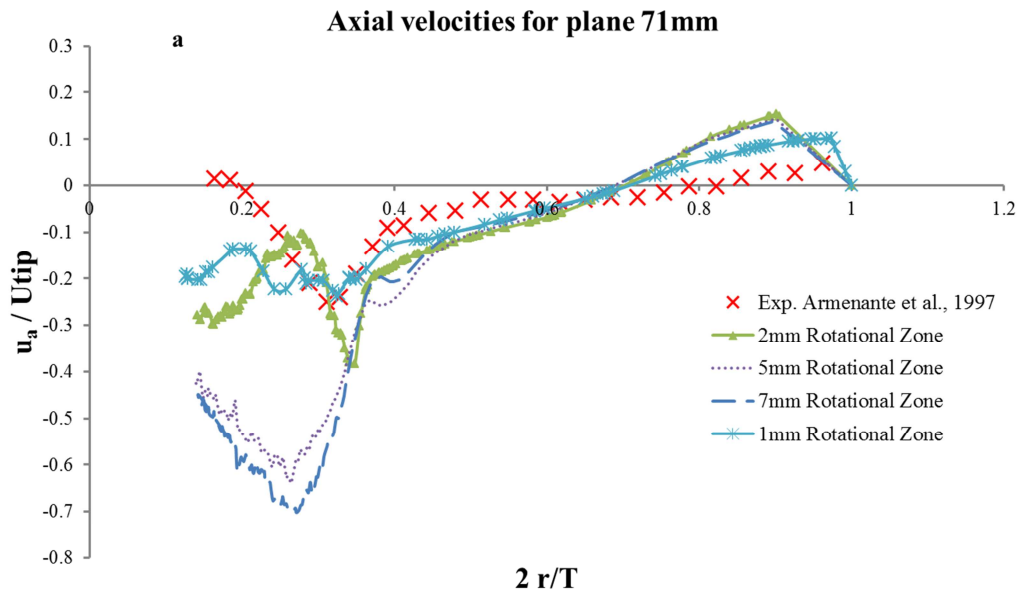


Figure 3-2 Two examples of the rotational zone dimensions for the unbaffled mixer

Figure 3-3 shows the numerical predictions of two velocity components, a: the axial velocity (u_a), and b: the tangential velocity (u_t) as a function of radial distance from the shaft (r) on a plane 71 mm from the tank's base. The X and Y axes are non-dimensionalized with the impeller tip velocity and the tank diameter, respectively. In this figure the symbols indicate the experimental measurements of Armenante and the different line styles correspond to the various rotational zone dimensions. The numerical predictions of axial velocity show that all the selected cylinders for the rotational zone predict a negative peak for the axial velocity close to the blade's tip ($2r/T = 0.311$), then the values of the velocity are rising towards the outer walls of the tank. The experimental data also illustrate a negative maximum axial velocity at the tip. This value increases close to the wall. Hence, all the rotational zones tested are able to capture the trend of axial velocity. However, the quantitative comparison of the CFD results with the measurements reveals that for the larger rotational zones (i.e., 5 and 7 mm) the predicted maximum axial velocities have been underpredicted with more than 50% error. The smaller extents of the rotation zones (i.e., 1 and 2

mm), on the other hand, not only captured the location of maximum axial velocity correctly but also they quantitatively match the experiments reasonably well (to within average differences of 16.10% and 7.98% for the 2 mm and 1 mm rotational zones, respectively). The tangential velocity predictions in Figure 3-3 (b) show that the trend of experimental velocity is captured with different dimensions of the rotational zone. The location of the maximum tangential velocity ($0.26 < 2r/T < 0.34$), which occurred near the tip of the blade, is also predicted with a reasonable degree of accuracy (with error $< 4\%$). However, far from the impeller ($0.5 < 2r/T < 1$) the numerical predictions of the tangential velocity are below the mentioned values (with an average difference of 36.93%). Comparing the numerical predictions of the other velocity components as well as the turbulent kinetic energy and its dissipation rate, one can draw a general conclusion which confirms that the smaller rotational zones around the impeller enhance the precision of the CFD data. According to the findings of this test for future simulations of the entire tank a rotational zone with 1 mm distance from all sides of the blade has been chosen.



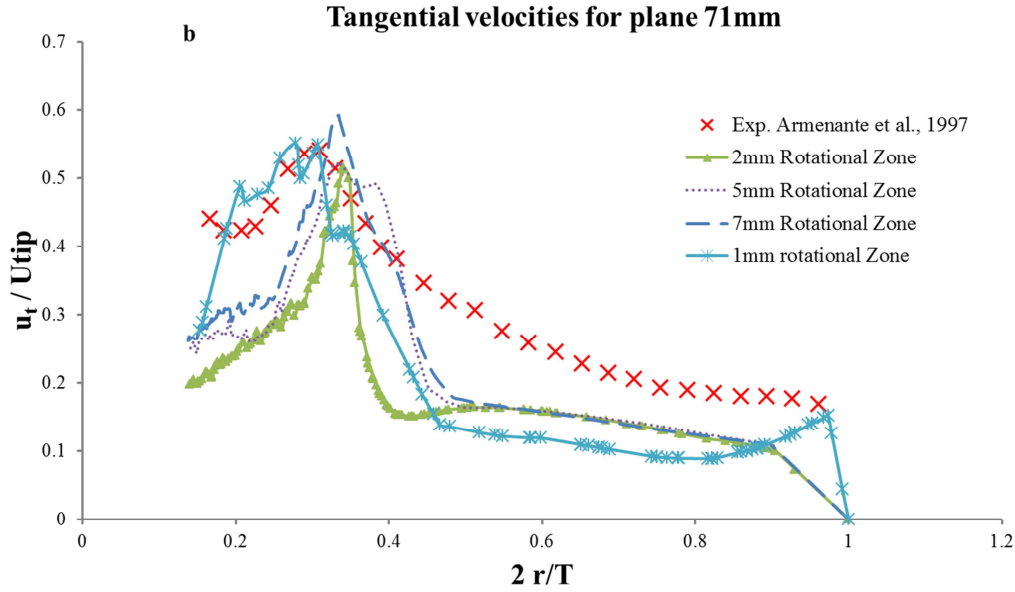


Figure 3-3 Numerical predictions of the dimensionless velocity components as a function of non-dimensional distance from the shaft on plane 71: (a) axial velocity, (b) tangential velocity

3.3.1.2. Time step size

The second preliminary test is to investigate how specifying a practical time step can change the quality of the numerical predictions. A time step is the incremental change in time over which the governing equations are being solved and the flow variables are advancing toward the steady-state situation. Therefore, this incremental progress in time can significantly affect the numerical solutions. The time step sizes are chosen for the initial tests based on the rotational angle of the impeller. Figure 3-4 displays two states of the impeller at two different times. The left hand side image is the position of the impeller at time step equal to zero and by progressing the time for only one time step, the right hand side image shows the new location of the blades with respect to the time marching. The different time step sizes corresponding to 5° , 10° , 12° and 15° of the impeller rotation are simulated to explore the influence of this factor on the predictions of the flow field.

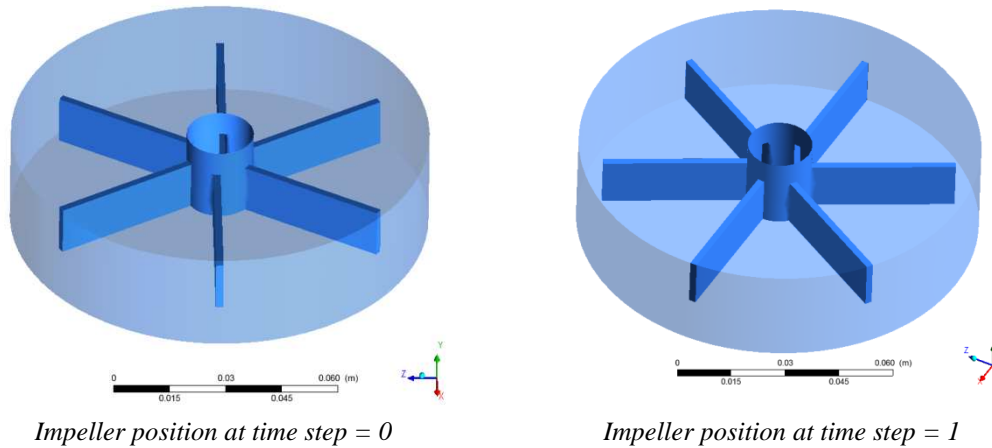


Figure 3-4 The impeller positions at time step=0 and time step=1

To verify the effects of the model uncertainties associated with the practical time step size, the numerical predictions of the velocity components and turbulent characterizations are compared to the experimental data of Armenante (Armenante et al., 1997). Figure 3-5 shows two examples of the predictions of the tangential velocity, non-dimensionalized by the impeller tip velocity, and the turbulent kinetic energy, non-dimensionalized by the impeller tip velocity squared, as a function of non-dimensional distance from the shaft. The symbols indicate the experimental measurements and the four line styles represent the predictions for the different time step sizes on plane 71 mm from the base of the tank. For both tangential velocity and the turbulent kinetic energy the numerical predictions have indicated a maximum value before gradually decreasing towards the wall. At the wall ($2r/T=1$), the velocity becomes zero due to the application of the non-slip boundary condition. This observation is in agreement with the measurements. Moreover, the four different time step sizes predict the location of peak tangential velocity ($0.26 < 2r/T < 0.34$) with an acceptable precision and the quantitative comparison with the experimental data determines the absolute average differences of 18.96%, 5.30%, 8.48% and 24.37% for 5° , 10° , 12° , and 15° of the rotation of impeller. However, the location of the maximum turbulent kinetic energy predicted with different time step sizes falls within the range of $0.24 < 2r/T < 0.36$ whereas the experimental equivalence occurs at $0.35 < 2r/T < 0.47$. The quantitative comparison also shows the error of more than 50% due to the incorrect predictions of the peak's location. Other velocity components as well as the turbulent energy dissipation rate for all the planes are validated with the available experimental data. It is observed that the numerical predictions obtained by the time step size equal to 12° have less discrepancy with the experimental data. Thus,

for the later simulations this time step size is selected, along with the 1 mm rotational zone for the impeller modelling to minimize the uncertainties of the CFD predictions.

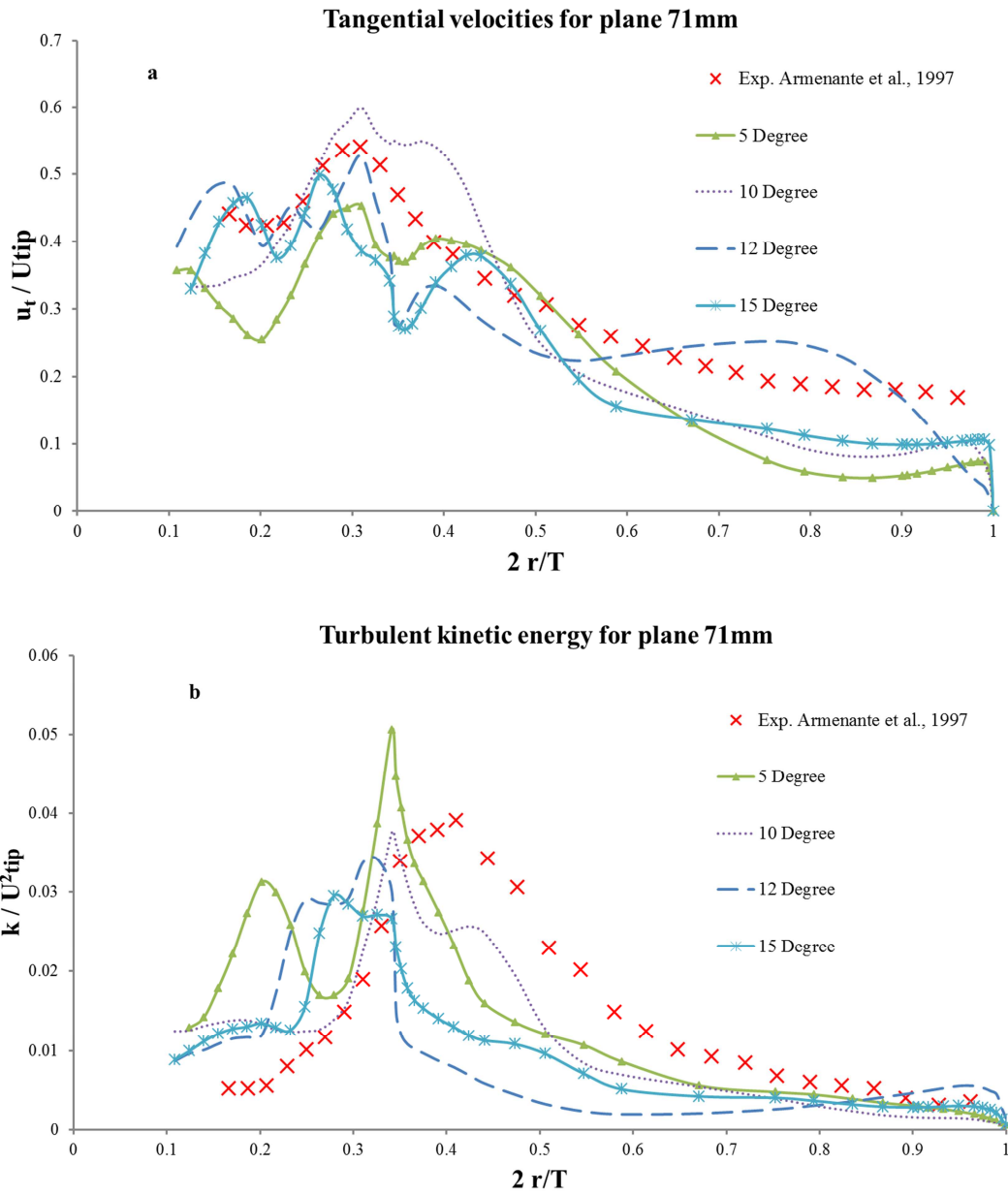


Figure 3-5 Numerical predictions of non-dimensional tangential velocity (a) and turbulent kinetic energy (b) as a function of non-dimensional distance from the shaft

3.3.1.3. Grid study

One of the primary sources of the numerical uncertainty is the spatial discretization level of the computational domain in x , y and z directions (i.e., meshing the geometry). A typical definition for the grid or mesh is that a meshed geometry is the outcome of discretizing the computational domain into a number of control

volumes. These cells then define discrete points (i.e., cell centres) on which the flow variables are calculated. Therefore, the density of the grid points determines how accurate the gradients of the flow variables are being appraised. An ideal degree of the mesh refinement must be able to capture even the smallest size of the turbulent eddies with the order of Kolmogorov turbulent length scale. However, the cell counts for such a grid resolution would inhibit simulations due to the huge computational expense. Hence, a practical solution is finding an optimized mesh resolution which is fine enough to resolve the major details of the flow structures, while the demanded CPU time is not prohibitive.

In addition, the quality of the generated grid directly influences the rate of convergence of the solution and the numerical uncertainties inherited with the accuracy of the solutions. The typical criterion to evaluate the quality of the mesh is its skewness. This non-dimensional parameter quantifies how much deformed a cell is when it is compared to an optimal cell shape. For the hexahedral elements, used in this study, Eq. 3.19 is applied to calculate the skewness of the generated mesh.

$$\text{Skewness} = \max \left[\frac{\theta_{max}-90}{90}, \frac{90-\theta_{min}}{90} \right] \quad \text{Eq. 3.19}$$

where θ_{max} is the largest angle in the cell, and θ_{min} is the smallest angle in the cell.

The following mesh skewness spectrum (Table 3-3) is suggested by ANSYS Fluent (ANSYS, 2011a) to examine the mesh quality before importing it to the CFD solver (i.e., Fluent). The same scale is also applied in this research to examine the mesh quality.

Table 3-3 Recommended skewness scale to evaluate the mesh quality

Excellent	Very good	Good	Acceptable	Bad	Unacceptable
0.00 – 0.25	0.25 – 0.50	0.50 – 0.80	0.80 – 0.94	0.95 – 0.97	0.98 – 1.00

In order to study the effects of grid resolution on the numerical predictions of the flow field various mesh densities are built up. The Mesher Application of ANSYS Workbench package was used to create the different mesh schemes. The geometry was divided into different zones and using the edge sizing feature of the software enabled us to control the number of elements in different parts of the tank. It was observed from the previous tests that the flow field inside the mixer is rotationally symmetric. Therefore, the geometry for a 60° sector of the entire vessel including only one blade is created and meshed. The slice modelling allows us to explore very fine

grids, since the overall CPU time would be a few orders of magnitudes lower than for modelling of the whole vessel. Figure 3-6 displays the created geometry for the slice modelling. The boundary conditions applied for the simulations are also shown. The vessel is assumed to be closed at the top (A) and the wall boundary condition is prescribed for the lid of the tank. The shaft (D) has also been treated as a stationary wall. The blade (E) is, however, defined to be a moving wall with the same angular velocity of zero relative to the rotational zone (F). In other words, the rotational velocity of the blade is identical to the rotational speed of the moving zone. In order to obtain a uniform mesh, it was assumed that the thicknesses of the shaft and blade are negligible, the same assumption was also used by Armenante and he also confirmed that the zero thickness walls did not significantly influence the numerical predictions. (Armenante et al., 1997). The previous observations showed that the flow solution is expected to have a periodical nature in the computational domain. Thus, the periodic boundary condition is applied for the two opposite planes or side-walls (B and C) in the computational model. The remaining boundaries including the tank walls are set as no-slip velocity boundary conditions. The multiple reference frames (MRF) method is implemented to model the impeller rotation. In addition, for all the simulations of the 60° slice, the pressure field inside the tank is derived with the SIMPLE algorithm, while a second order upwind discretization method is used to compute the convective terms in the flow equations (Ferziger and Perić, 1996). Similar to the previous simulations, the domain is initialized with a zero velocity field and the converged solution is achieved when the normalized residuals for the continuity equation drops below 10^{-3} .

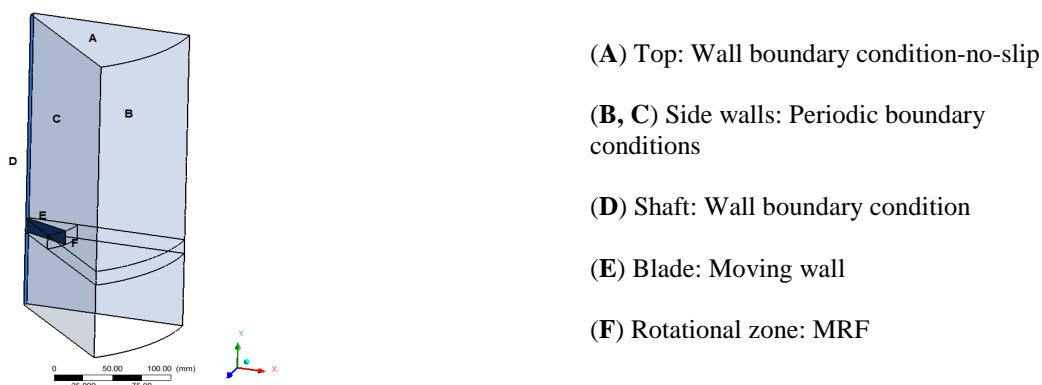


Figure 3-6 Schematic illustration of the boundary conditions for the slice modelling

Seven different grid densities were constructed to quantify the numerical uncertainties related to the discretization of the domain. In each case, the mesh

resolution for the rotational zone is maintained finer compared to the bulk zone, due to the fact that the flow fluctuations are higher in this part of the vessel. Details of each grid system in terms of the number of elements in the rotational zone and the bulk zone in conjunction with the mesh qualities are summarized in Table 3-4.

Table 3-4 Mesh details for the slice modelling

Case#	Bulk region			Rotational zone			No. Cells		Skewness		
	<i>r</i>	θ	<i>z</i>	<i>r</i>	θ	<i>z</i>	Original	Adapted	Min	Max	Ave
C1	31	20	65	11	20	5	40,300	59,375	0.0125	0.1086	0.0242
C2	40	24	78	14	24	6	74,880	110,762	0.0104	0.1429	0.0190
C3	48	29	94	17	29	8	130,848	176,306	0.0050	0.0990	0.0211
C4	58	35	113	20	35	10	229,390	296,478	0.0041	0.1077	0.0168
C5	70	42	126	24	42	12	370,440	472,129	0.0034	0.1260	0.0210
C6	84	50	139	29	50	14	583,800	704,818	0.0029	0.1436	0.0208
C7	92	60	154	35	60	17	850,080	1,024,317	0.0015	0.1606	0.0309

* The numbers in the *r*, θ , and *z* columns represent the number of elements in each direction of the cylindrical coordinate system.

The first test that is carried out for each mesh density concentrates on the accuracy of the solution close to the walls. As discussed earlier, the formation of the boundary layers adjacent to the solid surfaces is required to be mathematically described for the *k*- ϵ turbulence model. The *y*⁺ value is used as a measure to account for the temporal fluctuations of the turbulence inside the boundary layer. This parameter is defined as the dimensionless distance from the wall to the first grid point:

$$y^+ = \frac{u^* y}{\nu} \quad \text{Eq. 3.20}$$

where *y* is the distance to the wall, ν is the kinematic viscosity, and *u*^{*}, the friction velocity is defined as:

$$u^* = \sqrt{\frac{\tau_w}{\rho}} \quad \text{Eq. 3.21}$$

in Eq. 3.21, τ_w is the wall shear stress and ρ is the fluid density.

The boundary cells with high values of *y*⁺ should undergo the refinement process. It is recommended (Bartels et al., 2002, ANSYS, 2011a) that for using the standard wall function the value of *y*⁺ in the first cell should be within the logarithmic law layer $11 < y^+ < 300$, whereas enhanced wall treatment requires *y*⁺ as low as possible ($y^+ < 5$). The *y*⁺ contour plot for all the surfaces with the wall boundary conditions reveals that the maximum *y*⁺ value occurs at the blade region.

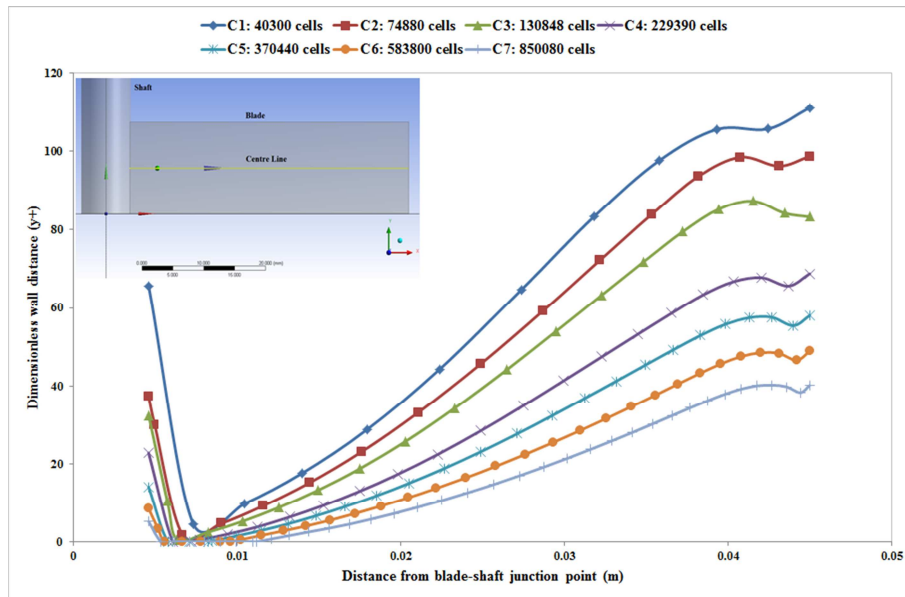


Figure 3-7 Values of y^+ for seven different mesh schemes on the centre line of the blade

Figure 3-7 is a plot showing the values of y^+ on the centre line of the blade as a function of distance from the blade-shaft junction point. The different cases from Table 3-4 are illustrated with different line styles. As can be seen, the y^+ value is continuously increasing toward the tip of the blade. In order to reduce the y^+ values at the tip, the solution-adaptive mesh refinement feature of the solver is applied. This option allows us to increase the density of the control volumes based on the user-defined criteria. The criteria can be drawn according to the geometrical constraints or the numerical solution data. Mesh refinement then takes place on those regions that meet the adaptation functions. The main advantage of this method is that one can locally increase the number of cells based on the solution data and analyse the impacts of the supplementary cells on the results without regenerating the entire mesh. For the case of the stirred tank in this study, the adaptation function is set up for the high value of the y^+ . Different mesh refinements methods are performed for the problematic area (i.e., on the blade). Figure 3-8 replicates the same graph as Figure 3-7 for the y^+ value as a function of distance from the shaft, except the values are derived after the mesh refinement. The total number of cells after the adaptation is also shown in Table 3-4. The first case with the coarsest mesh (i.e., 59,375) is not significantly influenced by the refinement procedure. Conversely, all the other cases indicate a noticeable reduction in the values of the y^+ at the centre line of the blade. It is also clear from Figure 3-8 that the y^+ graphs for the two finest mesh schemes (i.e., with 704,818 and 1,024,317 number of cells) are overlapped. Hence, increasing the

number of cells beyond one million elements does not lead to further improvement in the y^+ value.

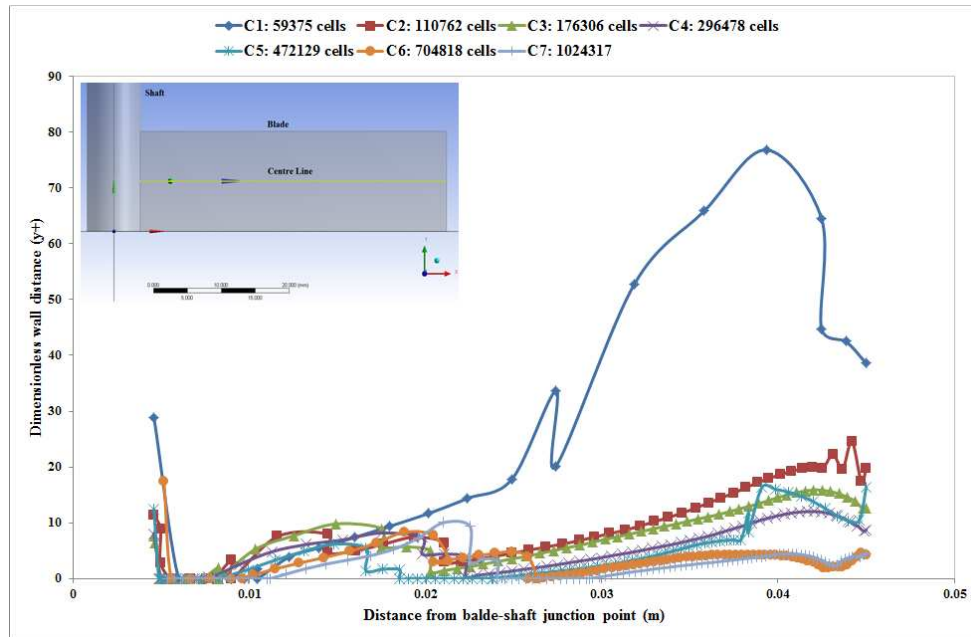


Figure 3-8 Values of y^+ for seven different mesh schemes on the centre line of the blade after mesh refinement

In Figure 3-9 the maximum value of y^+ on the centre line of the blade is plotted as a function of cell numbers. For the first three cases on Table 3-4 (C1: 59,375, C2: 110,762, and C3: 176,306) a substantial reduction in the maximum y^+ value is observed. However, the same reduction rate is not continued for the other cases. Comparison of the CPU times for the different grid resolutions, however, demonstrates a high computational demand for a slight decrease on the y^+ value beyond a certain number of cells. The increase in computational time resulting from increasing the mesh resolution seems to follow a linear trend. Also, an extreme case with 2 million cells is examined and the effect on the y^+ is found to be insignificant while the computational time is increased from 27 hours (for a case with 1 million cells) to 48 hours.

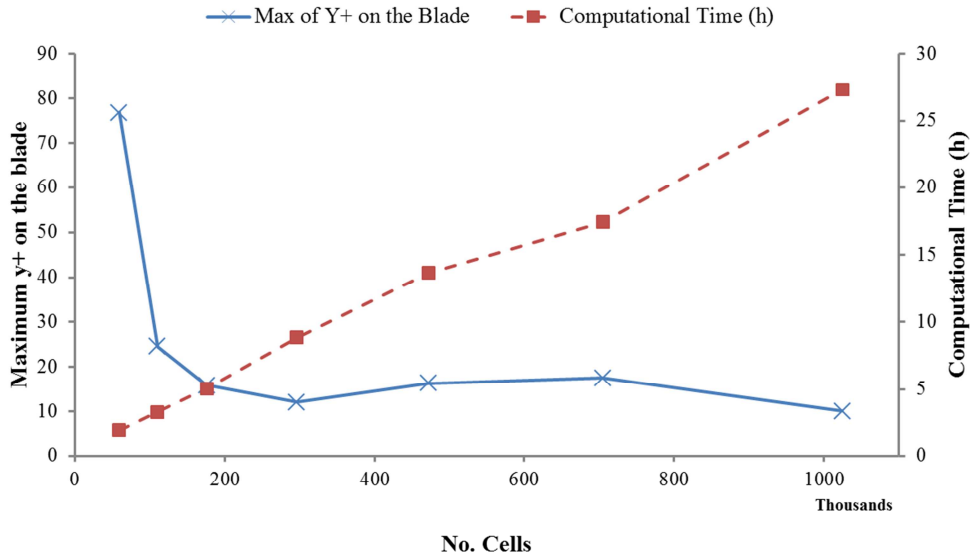


Figure 3-9 Maximum value of y^+ as a function of number of cells and CPU time for seven cases tested for slice modelling

This systematic study of y^+ , as a scale to assess the mesh quality near the walls, suggests that the temporal turbulent fluctuations close to the walls can be captured by a grid density between 500,000 to 700,000 numbers of cells. Figure 3-10 illustrates the final contour plot of y^+ values for case 6 in Table 3-4 after mesh refinement. It is also zoomed to designate the adapted surface mesh on the blade. This figure clearly shows that having more elements at the tip of the blade has decreased the value of y^+ at this zone. It can be concluded therefore that the refined mesh on the blade is able to resolve the fluctuations of the turbulence with a satisfactory level of accuracy.

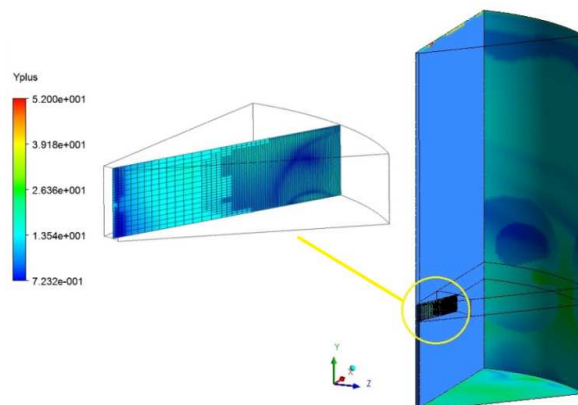


Figure 3-10 Contour plots of the y^+ value for the case with 704,818 cells

The methodical study of y^+ evaluates the dependency of the solution data on the quality of the mesh elements for the near the wall regions. Another common

practice for developing a CFD model is distinguishing a mesh resolution beyond which the solutions of the governing equations do not vary significantly. This test can be performed by running a set of simulations on a sequence of grid systems that usually begins with a coarse mesh and gradually refine it until negligible variations on the flow field parameters are observed. The grid independent solution thus minimizes the numerical uncertainties caused by the spatial discretization of the computational domain. It is worth pointing out that there must be a compromise between the number of cells and the computational time, since the solutions of the partial differential equations would approach the exact values if infinite number of cells covered the computational domain.

In order to achieve the grid independent solution, four points on five planes at different parts of the computational domain are defined to investigate the deviations of the flow variables. The locations of the planes are selected in such a way that the numerical predictions can be validated by the experimental measurements. The points are also placed to cover the hydrodynamically significant zones in the vessel (e.g. close to the shaft, walls and the blade).

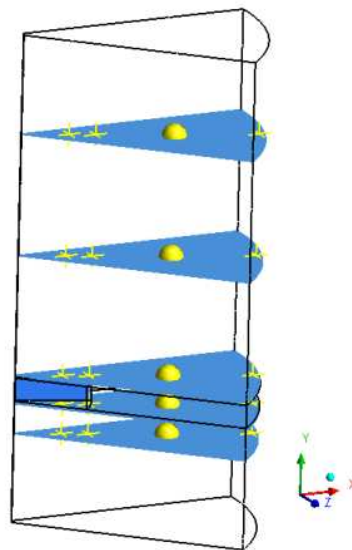


Figure 3-11 Locations of the selected points for the grid sensitivity test in the slice modelling

Having run the simulations for the different grid resolutions (see: Table 3-4), the velocity components (i.e., axial, radial, and tangential) and the turbulent properties (i.e., kinetic energy, and the dissipation rate) are extracted for all the illustrated points in Figure 3-11. The changes of the solution data as a function of number of cells are plotted for all the points on five different planes. The graphs are then used to

determine the dependency of the CFD results on the number of cells. For the sake of brevity, the results for the tangential velocity component and the turbulent kinetic energy in the middle of each plane, depicted by the yellow balls in Figure 3-11, are shown here. Figure 3-12 is a set of graphs showing the non-dimensional tangential velocity (non-dimensionalized by the tip velocity) as a function of cell numbers for five different planes. Significant variations of the tangential velocity are shown for the first four grid densities on all the planes. However, further mesh refinement has led the solution to approach to its asymptotic range. In other words, additional grid points will not yield any improvements in the numerical predictions of the velocity or the solution is independent of the cell numbers.

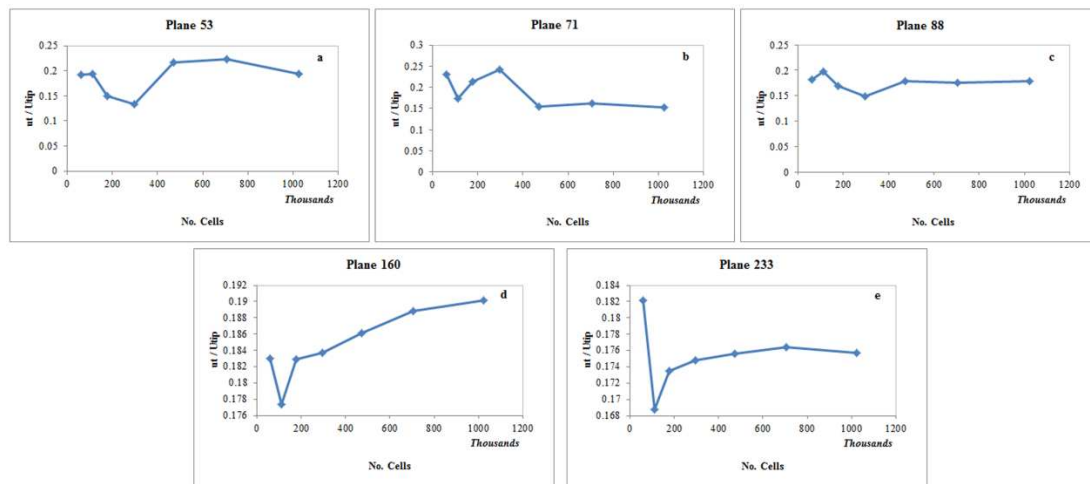


Figure 3-12 Tangential velocity as a function of cell number for the depicted points on Figure 3-11

Figure 3-13 is another instance that shows the sensitivity of the turbulent kinetic energy predictions on the mesh resolution. In this figure, the non-dimensional turbulent kinetic energy, non-dimensionalized by the square of the tip velocity, is plotted against the different number of cells for the nominated points illustrated in Figure 3-11. Comparable to the tangential component of the velocity, for the first four grid schemes the turbulent kinetic energy also fluctuates noticeably with gradual refinement of the mesh. However, the numerical solutions have become more consistent and stable when the cell count is higher than 450 thousands elements. The observations from this figure validate that the converged solution no longer depends on the number of grid points. Further discretization of the domain, therefore, only increases the solution time without improving the quality of the CFD results.

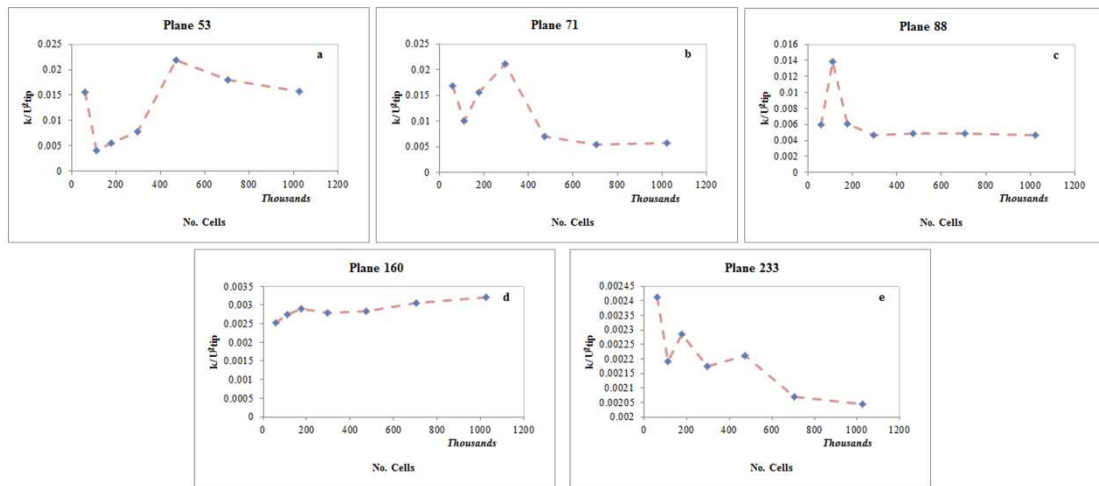


Figure 3-13 Turbulent kinetic energy as a function of cell number for the depicted points on Figure 3-11

Besides examining these two flow properties, specific efforts are made to compare the sensitivity of the other flow variables (including axial and radial velocities as well as the turbulent dissipation rate) to the level of discretization. Inspections of the CFD predictions for four points on five different planes produce a similar result further supporting the claim of a grid-independent solution. It was found that a grid system with more than 450,000 elements for a 60° sector of the stirred tank is a computationally affordable mesh scheme where the solution data are independent of the grid spacing.

The grid independence and y^+ tests discussed above were aimed to minimize the numerical uncertainties and errors related to the spatial discretization. The y^+ study estimates the quality of the grids near the wall and it determines how accurately the boundary layers near the walls can be resolved. Moreover, the grid independent study shows that although the exact solutions of the governing equations can only be obtained when the distances between each grid point tends to zero, the solutions achieved from a gradual mesh refinement process can be the possible way of controlling the uncertainties arising from the discretization. It also shows that a grid independent solution defines a cell count limitation beyond that the flow simulations are only practical if the powerful computational tools are available and the minor flow features are the focal point of the research.

3.3.1.4. Turbulence model study

Reviewing the published literature on the single-phase modelling of the stirred tanks in Chapter 2 reveals that the closure of the governing equations (i.e., choice of turbulence model) has been obtained with different numerical approaches. Consequently, there have been a range of different turbulence models in the literature to cope with the unsteady and fluctuating characteristics of the turbulence inside the stirred tank. Each turbulence model adds a sufficient number of equations to the typical mass and momentum equations for computations of the unknowns. Moreover, the efficiency of different models has been validated by comparing the predictions with experimental data. The validation has been reported either qualitatively or quantitatively by quantifying the percentage of difference between the predictions and measurements.

In this study the conservative forms of the continuity and the momentum balance equations are time-averaged to account for both the mean and instantaneous components of the flow variables (see sub-section 3.2. Governing equations). The time-averaged forms of the governing equations (RANS equations) have introduced a new unknown term, Reynolds stress, $(-\overline{\rho u'_i u'_j})$ shown in Eq. 3.5. The formulation of the new unknown term based on the known factors and empirical expressions creates some level of approximations and uncertainties in the solutions. Thus, to confirm that the model uncertainties caused by the choice of the turbulence model are minimized a turbulence model study is carried out. The turbulence models are categorized into two groups. The first group is the RANS-based turbulence models that have been divided into one-equation model, two-equation models, three-equation models, and the Reynolds Stress Model (RSM). Except the latter one, the others formulate the Reynolds stress according to the Boussinesq hypothesis. The second group, Large Eddy Simulation, applies a filtering operation to the Navier-Stokes equations which separates the turbulent eddies into large and small scale eddies. In this method, the movements of large eddies are directly resolved, whereas sub-grid scale models are used for the small size eddies. It is not the purpose of this sub-section to articulate the details of each turbulence model, since the original references on the turbulence models theory are available e.g., (Tennekes and Lumley, 1972, Batchelor, 1982, Stanisic, 1985, Menter, 1994).

Three members of the RANS-based turbulence models including: the one-equation model of Spalart-Allmaras (SPALART and ALLMARAS, 1992), standard $k-\epsilon$ (Launder and Spalding, 1972) and the transition Shear-Stress Transport (SST) from the two-equation models (Menter, 1994), and the $k-\kappa-\omega$ (Walters and Cokljat, 2008) with three additional equations were compared. It should be mentioned that the RSM turbulence model has resulted in a diverged solution. Attempts to remedy this by decreasing the under-relaxation factors, initializing with the other turbulence models, gradually increasing the angular velocity and varying the time step were unable to achieve a converged solution.

The numerical predictions of the velocity components and turbulent properties computed with each turbulence model are compared with the experimental measurements of Armenante to evaluate the influence of the choice of turbulence models on the solution data.

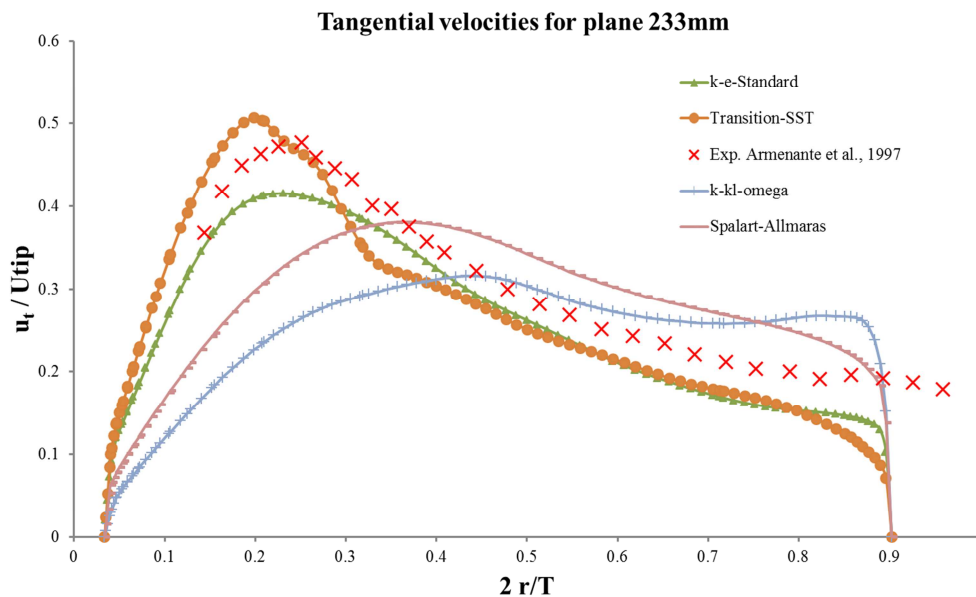


Figure 3-14 Numerical predictions of the tangential velocity with the RANS-based turbulence models for plane 233 mm from the bottom of the unbaffled mixer

Figure 3-14 shows an instance of the application of different turbulence models for the prediction of the velocity component. This figure displays tangential velocity (u_t) on plane 233 mm from the tank's base, non-dimensionalized with the tip velocity of impeller (U_{tip}), as a function of radial distance (r) non-dimensionalized with the tank's diameter (T). The symbols indicate the experimental measurements of Armenante whilst the four line styles correspond to the turbulence models applied.

The numerical predictions show a significant difference between the various turbulence models investigated. The two-equation models, standard k- ϵ and transition SST, generally predict the velocity profiles better than the remaining three choices. The k-k1- ω turbulence model has failed to capture the trend of experiments, while the Spalart-Allmaras turbulence model has clearly located the maximum tangential velocity outside its experimental range. However, the results from the standard k- ϵ and the transition SST turbulence models show that the location of peak velocity (i.e., $0.185 < 2r/T < 0.288$) and the trend of the tangential velocity on plane 233 mm have been correctly captured. The transition SST turbulence model slightly overpredicts the maximum tangential velocity on plane 233 mm with an average difference of 8.82%, while the standard k- ϵ underpredicts this quantity with an average difference of 8.67%. Both models have underpredicted the tangential velocity on the middle section of the tank (i.e., $0.288 < 2r/T < 1$) to within an average difference of 12.06% and 14.43% for the standard k- ϵ and transition SST, respectively. Overall comparison of the numerical predictions reveals that among the models with the scalar assumption of the turbulent viscosity (i.e., RANS-based models) the standard k- ϵ and transition SST provide a closer match with the measurements of Armenante (Armenante et al., 1997) (Appendix A).

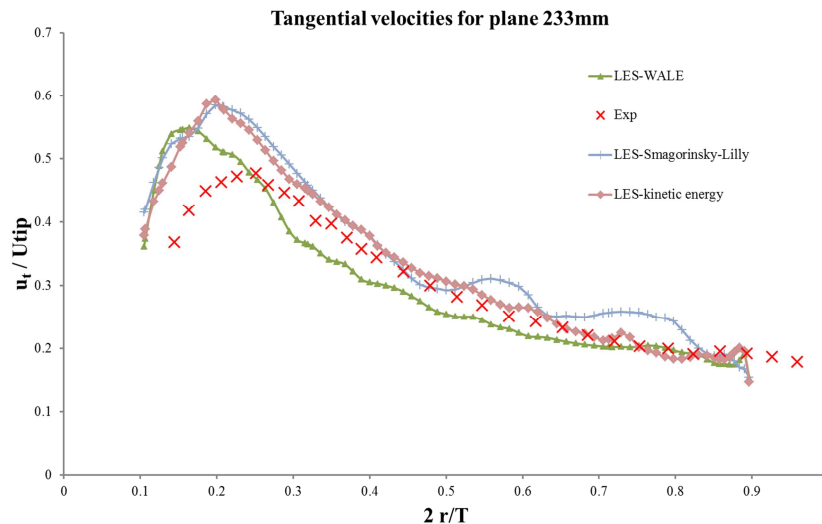


Figure 3-15 LES predictions of the tangential velocity for plane 233 mm from the bottom of the unbaffled mixer

For the LES simulations three sub-grid scale models entailing: Smagorinsky-Lilly (Smagorinsky, 1963), WALE model (Nicoud and Ducros, 1999), and dynamic

kinetic energy (Kim and Menon, 1997) are compared to predict the unsteady behaviour of the water inside the stirred tank. The tangential velocity profiles on plane 233 mm from the tank's base, predicted by various sub-grid scale models, are depicted in Figure 3-15. In this plot the symbols represent the LDV measurements of Armenante and the different styles for the solid lines correspond to the LES predictions of the tangential velocities. The simulated trend of the tangential velocity with all the sub-grid models indicates a maximum at $0.13 < 2r/T < 0.25$ which reduces toward the outer walls of the vessel. The predicted trend is in line with the experimental data, yet close to the wall, the model is not able to capture the velocity. The disagreement close to the wall can be attributed to the fact that the LES model for the single-phase modelling necessitates a more refined mesh resolution compared to the required level of mesh resolution for the RANS-based turbulence models. The three sub grid scale models overpredict the maximum tangential velocity on plane 233 mm to within an average difference of 20.24%, 13.56%, and 19.34% for the Smagorinsky, WALE and kinetic energy models, respectively. However, the numerical predictions of the tangential velocity at the middle of the tank (i.e., $0.288 < 2r/T < 1$) show an acceptable agreement with the experiments with an average difference of 11.33%, 9.63% and 5.74% for the Smagorinsky, WALE and kinetic energy models respectively. The predictive capabilities of the sub-grid scale models are assessed for the other velocity components and the turbulent characteristics. The global comparison shows that the three different sub-grid models of the LES did not reveal a noticeable difference. It must be mentioned that of these three models, one may select the "kinetic energy" method for having both adequate agreement with experimental data and a reasonable computational cost (Appendix A).

Thus far, the members of the two turbulence model categories have been applied for the flow predictions inside the unbaffled mixer. It has been shown that the choice of the turbulence models, even formulated with a similar hypothesis, can lead to significant model uncertainties in the predictions. So, it is necessary to investigate the influence of the turbulence models with the structural differences in their formulations. In order to do that, the standard k- ϵ , from the RANS-based turbulence model group, is compared with the LES predictions with the kinetic energy sub-grid scale model. Figure 3-16 is a plot that displays the comparison of the two turbulence models for the prediction of the tangential velocity profile on plane 233 mm. The

symbols represent the measurements of Armenante and the two different line styles indicate the numerical predictions of the standard k- ϵ and LES/kinetic-energy. The comparison shows that both models are successful in predicting the trend of the velocity profile. They show that the maximum velocity occurs at $0.185 < 2r/T < 0.288$ which is comparable with the location of the peak tangential velocity on the experimental data of Armenante. However, the LES/kinetic-energy overpredicts the maximum tangential velocity with an average difference of 19.34%, while the standard k- ϵ turbulence model underpredicts the peak velocity with an average difference of 8.67%. Looking at the bulk region of the flow at $0.288 < 2r/T < 1$, both models yield a very good agreement with the experimental data. Comparison of the velocity profiles at the middle section of the tank indicates that the quality of the tangential velocity predictions with the LES/kinetic-energy is slightly better than those predicted with the standard k- ϵ (the average difference of 5.74% for the LES/kinetic-energy compared to 12.06% of standard k- ϵ). Besides the level of agreement between the numerical predictions and the experiments, the two turbulence models are evaluated in terms of the computational expenses. Although the LES predictions for the middle section of the tank for the tangential velocity match the measurements marginally better, it comes at the expense of 68 hours CPU time compared to 53 hours for the standard k- ϵ model. It is important to keep in mind that the simulations for the turbulence model study are performed on an Intel Corei7 CPU 1.6 GHz workstation with 4GB RAM.

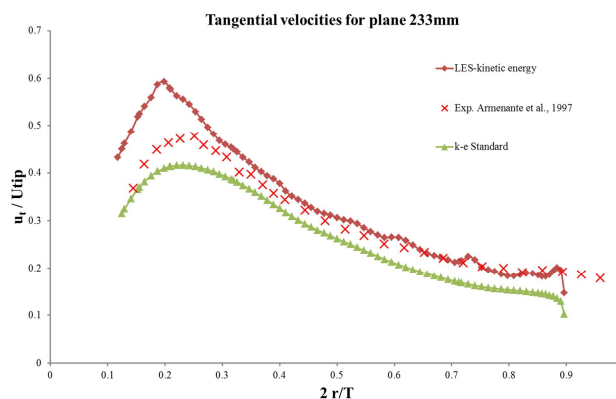


Figure 3-16 Numerical predictions of the tangential velocity on plane 233 mm from the bottom of the unbaffled mixer with k- ϵ standard and LES-kinetic energy

The CFD predictions for the other components of the velocity as well as the turbulent kinetic energy and its dissipation rate on the other planes are also validated

with the experimental measurements (e.g., Appendix A.1). It was found that the overall predictions of the turbulent features with the LES model provide a slightly better agreement compared to the RANS-based turbulence models. This finding can be explained by the fact that LES separates the different scale of the turbulent eddies rather than the isotropic turbulence field assumption for the RANS-based turbulence model. However, the standard k- ϵ turbulence model can yield a better agreement for the overall flow field characteristics inside the unbaffled mixer. This is also observed in previous studies on the water modelling of stirred tanks, such as the works of (Oshinowo et al., 2000, Lane et al., 2000a, Coroneo et al., 2011, Joshi et al., 2011b).

In conclusion, the first group of models take advantage of the isometric turbulence field and therefore they are sensible choices when the computational resource is the limiting factor. The second group (i.e., LES), however, divides the turbulent scales into large and small clusters. The large scales are simulated while the small scales are treated with a sub-grid scale model. This procedure results in better prediction of the turbulence characteristics in the stirred tank. However, compared to the RANS-based turbulence models, the LES requires more cell numbers for the accurate prediction of the flow field and consequently its computational demand is generally higher than the first group of turbulence models. As a general recommendation, one should implement the LES model for the stirred tank if the research is intended to provide details of the turbulence field for fundamental analysis. On the other hand, the RANS-based turbulence models, specifically the standard k- ϵ model, yield a low ratio of cost over benefit for engineering modelling and optimization purposes. As mentioned before, the main aim of this study is to yield accurate predictions of the flow variables for flotation modelling and due to the complexities of the flotation process a low cost approach would be more beneficial in this research.

3.3.2. Simulations of single-phase flow inside a standard Rushton turbine

CFD analysis of the unbaffled mixer shed some light on the general CFD issues related to the modelling of water inside a vessel with an agitation system. The second geometry that has been investigated in this study is a Rushton turbine flotation tank (Rushton, 1952). The geometry is adopted from the work of Newell (Newell, 2006) who experimentally measured the velocity profiles and the turbulent characteristics inside the tank. The computational domain for the water modelling

includes a fully baffled cylindrical tank with a diameter (T) and height (H) of 145 mm. The four baffles are extended for the entire length of the tank and they are attached to the wall with equal spacing. The Rushton turbine with diameter (D) equal to $T/3$ is mounted at the 48.3 mm from the tank's flat bottom (i.e., clearance). A central hub at this clearance carries six equally-spaced vertical blades with a blade height of $W=D/5$.

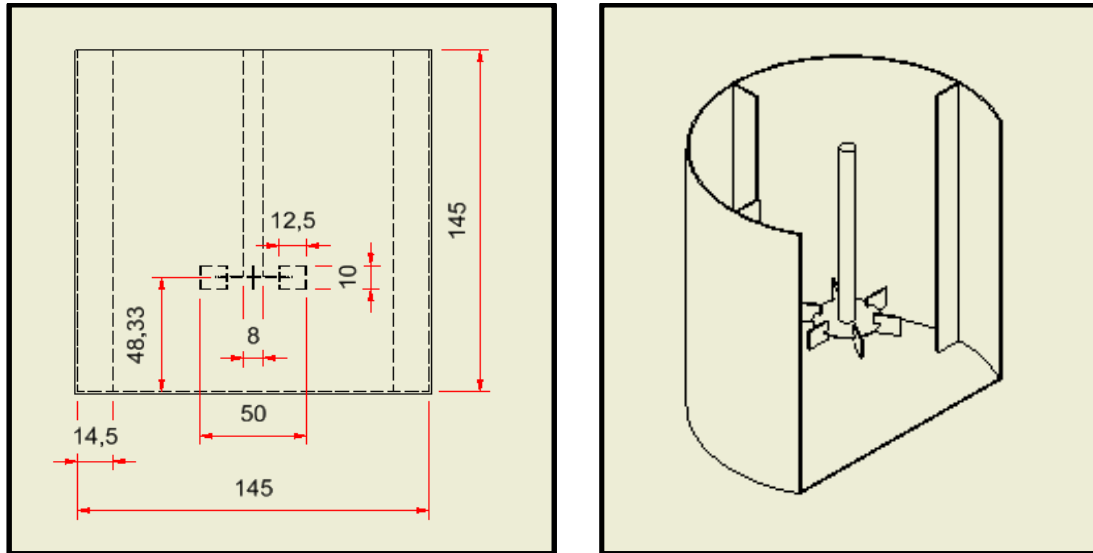


Figure 3-17 The schematic illustration of the Rushton turbine tank used for the water modelling

Figure 3-17 displays the Rushton turbine tank applied in this research. Table 3-5 also summarizes the geometrical details of the tank along with the mathematical relations with the tank's height and the impeller's diameter.

Table 3-5 Geometrical details of the standard Rushton turbine tank

Parameter	Symbol	Dimension (mm)
Tank diameter	T	145.
Tank height	$H = T$	145.
Impeller diameter	$D = T/3$	48.3
Blade height	$W = D/5$	9.67
Blade length	$L = D/4$	12.1
Blade thickness	$BT = D/30$	1.61
Baffle width	$BW = T/10$	14.5
Baffle thickness	$FT = T/30$	4.83
Impeller clearance	$IC = T/3$	48.3

Newell (Newell, 2006) used Laser Doppler Velocimetry to measure the flow characteristics in three radial positions inside the tank. The measurement points were selected to encompass the three hydrodynamically important zones inside the vessel. The first radial distance was near the impeller to handle the high turbulent region within the vessel, whereas the other two corresponded to the intermediate and low

turbulent zones at the bulk and near the wall areas, respectively. Figure 3-18 depicts the 2D and iso-view locations of the LDV data in the computational domain. The three yellow lines, on which 9 vertical positions for the measurements were appointed, denote the high, intermediate and low turbulence regions inside the tank. The experiments were performed for three different angular velocities of the impeller: 470 rpm, 650 rpm, and 800 rpm. The preliminary unsteady CFD tests are carried out for the impeller speed of 470 rpm; however the effects of increasing the angular velocity on the flow field are also explored. To simplify the simulations somewhat, the thicknesses of the baffles, blades, and the central disk are presumed to be negligible (i.e., zero thickness walls). This is a common assumption for the CFD modelling of Rushton turbine tank and it is widely applied by previous researcher in this field for example (Lane and Koh, 1997, Bakker and Van den Akker, 1994, Ranade, 1997). The rotating shaft is also extended for the full height of the tank to prevent difficulties during the meshing of the domain. Since the 3D computational domain used in this study is rotationally symmetric it is therefore limited to only half of the vessel and the periodic boundary conditions are applied for the side walls. The blades inside the rotational zone have the moving boundary conditions, while the top part and the baffles are treated as stationary walls (Figure 3-18).

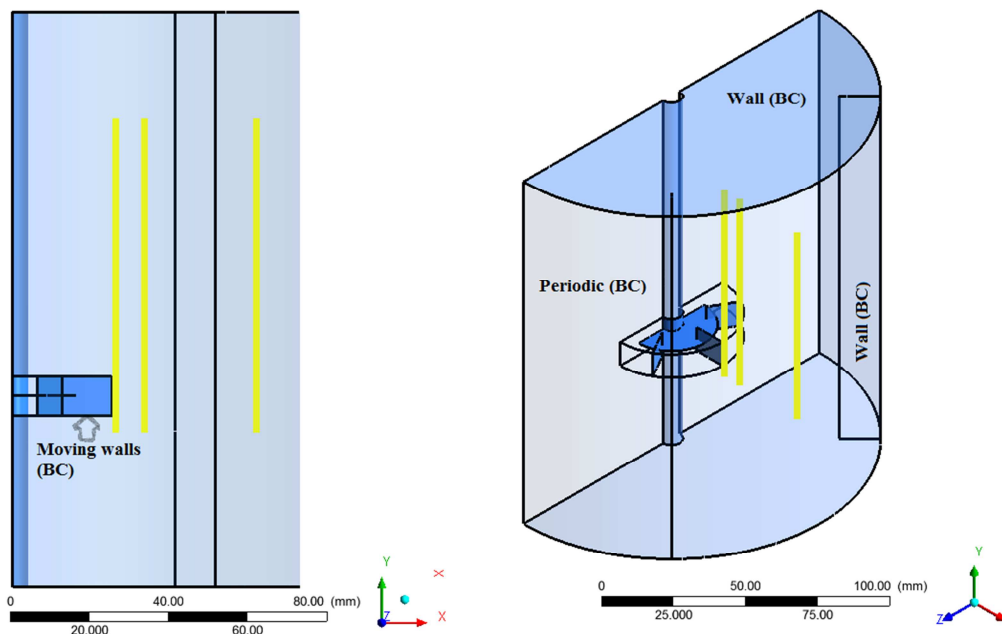


Figure 3-18 Measurement locations of Newell for the standard Rushton turbine tank

To account for the rotation of impeller, the multiple reference frames (MRF) method is implemented. The application of MRF method begins with separating the

rotating impeller region from its stationary surrounding. Adequate extensions of the rotational zone, where the equations are calculated in a rotating reference frame, can minimize the numerical uncertainties. The findings for the unbaffled mixer have suggested that a rotating zone adjacent to the blades provide a better solution. Hence, four different cases for the rotational zone, mostly created close to the turbine, are investigated with the dimensions of $1.5 W \times 0.5 D$, $0.75 W \times 0.25 D$, $0.376 W \times 0.125 D$, and $0 W \times 0 D$ (W : blade height, and D : impeller diameter). Figure 3-19 shows the numerical predictions of the tangential velocity component as a function of non-dimensional distance from the top of the tank (h : height, H : tank height). The numerical predictions are at the high turbulent region on the radial distance of $r/R = 0.36$ (r : radial distance, R : tank radius). The symbols indicate the experimental measurements of Newell and four different lines are representing the various extents for the rotating zone. The origin $(0, 0)$ in the graph defines where the impeller is mounted, so positions below the impeller have negative values.

Qualitative comparison reveals that all the applied rotational zone dimensions are able to follow the trend of experimental data. The peak tangential velocity at the impeller tip has been correctly captured by all the cases. However, the rotational zone attached to the blades ($0 W \times 0 D$) overpredicts the maximum velocity with an average difference of 26.62%. The validations are also performed for the other components of the velocity plus the turbulent properties. The CFD shows that a zone with dimensions of $0.376 W \times 0.125 D$ would give the best agreement with the experiments of Newell.

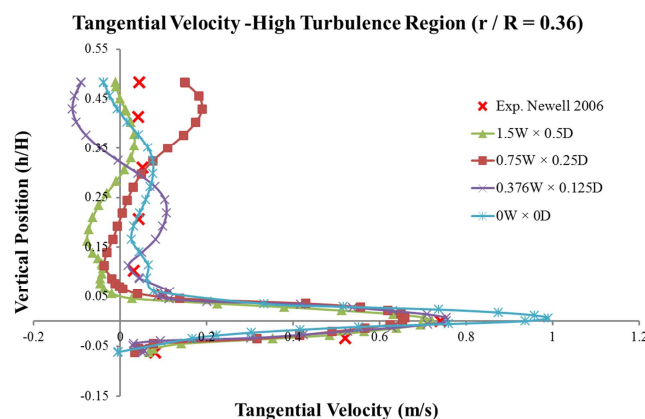


Figure 3-19 Numerical predictions of the tangential velocity as a function of vertical position for four different rotational zone dimensions in the standard Rushton turbine tank

In all the simulations, ANSYS Fluent was used as the CFD solver and similar to the unbaffled mixer the SIMPLE scheme coupled the continuity and momentum

equations, while the second order discretization method was used for the mass and momentum equations. Once the normalized residuals of the continuity equation were reduced to 1×10^{-3} the computations were stopped and the solutions were considered as the final converged solutions.

Finding the optimized dimensions for the rotational zone allows us to evaluate the other origins of uncertainties and errors in the CFD data. The next two subsections concentrate on the influence of the spatial discretization and the impact of the various turbulence models on the quality of the numerical predictions.

3.3.2.1. Numerical uncertainties associated with the single-phase modelling of the standard Rushton turbine tank

Previous literature on the single-phase modelling of stirred tanks has shown that the level of discretization of the computational domain may induce serious uncertainties on the predictions. The accuracy level of the numerical predictions for different mesh resolutions has been solely determined with the comparison of the CFD data with experimental measurements. However, the first drawback of this approach is that it always requires performing experiments and more importantly, the comparison with the experiments does not account for the inherent errors and uncertainties presented in the numerical methods. Previous work did not quantify these inaccuracies due to the lack of an accepted method for reporting the numerical uncertainties for the CFD modelling of stirred tanks.

However, in other engineering fields where the required level of accuracy in the predictions is very strict and the experimental measurements are very expensive, such as aerospace, the quantification of numerical uncertainties has been actively investigated. As results, several approaches have been suggested to relate the numerical uncertainties with the discretization levels (Roache, 1994, Karniadakis, 1995, Roache, 1997, Oberkampf et al., 1998, Freitas, 2002, Celik et al., 2008). The various methods presented in the literature are studied and of these, the well-established method of Roache is applied for the case of stirred tank. Roache proposed a method for uniform reporting of the numerical errors using the Grid Convergence Index (GCI). The GCI method is established on the generalized theory of Richardson extrapolation (Richardson, 1911, Richardson and Gaunt, 1927). The GCI evaluates

the discretization and iterative convergence errors on the numerical solutions computed for the two different grid spacings.

The GCI test starts by performing three simulations with three different grid spacings, namely, h_1 , h_2 , and h_3 . These spacings represent the discrete solutions for the fine, medium, and coarse mesh resolutions. A flow variable, $f(x,y,z,t)$, can be expressed with the grid spacing (h) in the form of series expansion:

$$f(x, y, z, t) = f(x, y, z, t)_{exact} + g_1 h + g_2 h^2 + g_3 h^3 + \dots \quad \text{Eq. 3.22}$$

where the functions g_1 , g_2 , and g_3 are defined in the continuum (i.e., they are independent of discretization) and $f(x,y,z,t)_{exact}$ is the continuum value at zero grid spacing. Note that for infinitely differentiable solutions, these functions are related to all orders of the solution derivatives through the elementary Taylor series expansions, but this is not a necessary assumption for Richardson extrapolation. Roache suggested it is only required that Eq. 3.22 be a valid definition for the order of the discretization.

For a second order solution (i.e., $g_1 = 0$), with two separate solutions such as, f_1 and f_2 which are solved for the fine and coarse grid spacings (i.e., h_1 and h_2), the leading-order error terms in the error expansion can be eliminated (i.e., by solving for g_2 at the grid points in Eq. 3.22 and by substituting this value into Eq. 3.22 to obtain a more accurate estimate of $f(x,y,z,t)_{exact}$. This yields in:

$$f(x, y, z, t) = f(x, y, z, t)_{exact} + \frac{(h_2^2 f_1 - h_1^2 f_2)}{(h_2^2 - h_1^2)} + \text{High. Order. Terms} \quad \text{Eq. 3.23}$$

The grid refinement ratio, r , can be expressed as h_2/h_1 and if one assumes that h is small, which allows the high order terms to be neglected, Eq. 3.23 can be simplified to approximate an equation for f_{exact} :

$$f(x, y, z, t)_{exact} \cong f_1 + \frac{(f_1 - f_2)}{(r^2 - 1)} \quad \text{Eq. 3.24}$$

The Richardson extrapolation method has been traditionally applied to approximate the exact value of a flow variable (i.e., $f(x,y,z,t)_{exact}$) when a grid is doubled or halved. It is written as follows:

$$f(x, y, z, t)_{exact} \cong \frac{4}{3} f_1 + \frac{1}{3} f_2 \quad \text{Eq. 3.25}$$

The GCI approach proposed by Roache (Roache, 1997) is founded on the premise of the generalized theory of Richardson extrapolation defined above. The first

step in computing the GCI is to calculate the fractional error inherited in the solution for the fine mesh, f_1 , as follows:

$$E_1^{fine} = \frac{\varepsilon}{1-r^p} \quad \text{Eq. 3.26}$$

where the relative error $\varepsilon = f_2 - f_1$ and p is the formal order of accuracy of the algorithm defined as:

$$p = \frac{\ln(\frac{f_3-f_2}{f_2-f_1})}{\ln(r)} \quad \text{Eq. 3.27}$$

Similarly, the solution for the coarse grid has an error that can be approximated by:

$$E_2^{coarse} = \frac{r^p \varepsilon}{1-r^p} \quad \text{Eq. 3.28}$$

In order to carry out the GCI test, Roache recommended generating at least three grid densities representing the fine, medium, and coarse solutions. Having three mesh resolutions, the order of convergence can be estimated to allow the user to select a grid spacing ensured the numerical predictions are in asymptotic range (Roache, 1994).

To assess the numerical uncertainty and report the grid convergence studies on a standard basis, a safety factor, F_s , is incorporated into Eq. 3.26 and Eq. 3.28. This results into two expressions for the GCI for fine and coarse grids:

$$GCI_1^{fine} = F_s |E_1| \quad \text{Eq. 3.29}$$

$$GCI_1^{coarse} = F_s |E_2| \quad \text{Eq. 3.30}$$

Setting F_s equal to unity leads to a too optimistic estimation of error. However, Roache suggested a more conservative range of $1.25 \leq F_s \leq 3$ for practical simulations. Indicating the level of this term depends on the intended accuracy. A large value for safety factor can be chosen if a higher level of confidence in the CFD predictions is desired. It is worthwhile to point out that the value of GCI is an indicator that examines how much the computed value for a flow variable is away from its asymptotic range. In this way, it specifies an error band on the solutions that depicts the bias of the numerical predictions from the exact values. A small value of GCI signifies that the solution is within the asymptotic range. GCI can also be used to gauge how much further grid refinement would change the numerical solution.

The GCI tool, outlined above, quantifies the numerical uncertainties inherited for the single-phase modelling of the laboratory scale Rushton turbine tank applied in this study. Three structured hexagonal mesh schemes with a constant grid refinement ratio of two ($r = 2$) are generated to perform the GCI test. The edge sizing feature of the meshing software (ANSYS Workbench Mesher Application) controls the grid refinement ratio by dividing each edge into certain number of segments. In each of the grid systems efforts are made to keep the skewness ratio as low as possible. In this way the errors that are triggered by the bad-quality elements will be minimized. Moreover, to capture the temporal turbulent fluctuations in the boundary layer the maximum y^+ (i.e., the dimensionless wall distance) is maintained within the logarithmic law layer in all cases (i.e., $30 < y^+ < 300$). Table 3-6 shows the coarse, medium, and fine mesh details with the required CPU time for each case.

Table 3-6 Mesh details used for the GCI test on the standard Rushton turbine tank

Mesh	Type	Size interval (mm)	No. of cells	% of cells with skewness < 0.2	CPU time (h)
Coarse	Hex	4	65,723	92.24	0.2
Medium	Hex	2	476,010	96.61	2.1
Fine	Hex	1	3,744,472	94.90	77.6

Figure 3-20 displays the numerical predictions of three velocity components as a function of non-dimensional distance from the top of the tank (h : height, H : tank height) for the high turbulence region inside the tank (see: Figure 3-18). The red crosses in this figure demonstrate the experimental measurements of Newell, the solid lines represent the CFD results and the shaded regions correspond to the values of GCI computed with the above explained method using $p = 1.75$ and $F_s = 1.25$. The figure shows that for all the velocity components there exist a maximum at the impeller's level (i.e., $h/H = 0$). The numerical predictions show that the trends of velocities, a sudden maximum at the tip of the impeller, have been correctly captured. In addition, the results show that the CFD methodology applied is capable of predicting the velocity components in the high turbulence region (i.e., close to the impeller). The overall average percentage of difference between the predictions and measurements, 26.79% for the axial velocity, 9.13% for the tangential velocity, and 13.29% for the radial velocity, ensures that the CFD predictions match the experimental data reasonably well. The slightly poor quantitative agreement for the axial velocity in the high-turbulent region can be attributed to the position of impeller,

since at this region rotation of the impeller generates a lot of instabilities. The shaded region in the figure illustrates the results of the GCI test, which defines an error band for the results. It indicates the effects of numerical uncertainty, caused by the mesh refinement, on the solutions. The overall average of the GCI value for the velocity components in the high-turbulent region at axial, tangential, and radial directions are 13.12%, 12.54%, and 6.80%, respectively. The overall averages reveal that the values of GCI at the high-turbulent region are relatively small. This suggests that the numerical uncertainty due to the discretization for the velocity predictions at the high-turbulent region has been minimized.

Figure 3-21 displays the numerical predictions of axial, tangential, and radial velocities in the medium turbulent region (see: Figure 3-18) as a function of non-dimensional distance from the tank's top. Similar to Figure 3-20 the symbols depicts the experiments, the solid line corresponds to the CFD solutions and the shaded region demonstrate the error band quantified by the GCI test. The figure shows very good qualitative agreement between the CFD results and the measurements of Newell, since the solid lines follow the trend of the symbols. In addition, the maximum tangential and radial velocities at the impeller's tip have been suitably predicted. The average difference of 16.30% for the axial velocity, 10.61% for the tangential velocity, and 22.78% for the radial velocity shows a good quantitative agreement with the experimental data in the medium turbulent zone (i.e., bulk flow). It is also important to notice by increasing the distance from the impeller and approaching the medium turbulent region the experimental maximum velocities are reduced. This observation is captured with the numerical predictions, too. For instance the prediction of maximum tangential velocity in the high turbulent region is 0.73 m/s (experiment: 0.74 m/s) and its equivalence for the medium turbulent region is decreased to 0.44 m/s (experiments: 0.51 m/s). The shaded region in Figure 3-21 computed by the GCI characterizes an error band on how far the numerical solutions are from the asymptotic values. In the medium turbulent region the total average of GCI values for axial, tangential and radial velocities are 8.19%, 15.86%, and 13.59%, respectively. Since in all the three-dimensional directions the average value of GCI is relatively small, the numerical uncertainty due to the mesh refinement level does not significantly contribute to the slight disagreement between the CFD data and the experimental data. For all the velocity predictions shown in Figure 3-20 and Figure 3-21,

the computed values of GCI are small. Therefore, the current CFD methodology is capable of successfully predicting the hydrodynamics of water flow inside the standard Rushton turbine tank. However, the local GCI values for the peak velocity in the tangential and radial directions in the medium turbulent region (Figure 3-21 e & f) are fairly large ($GCI < 22.19\%$ for tangential direction and $GCI < 26.12\%$), indicating that the predictions and simulations in this region could be improved by local mesh refinement.

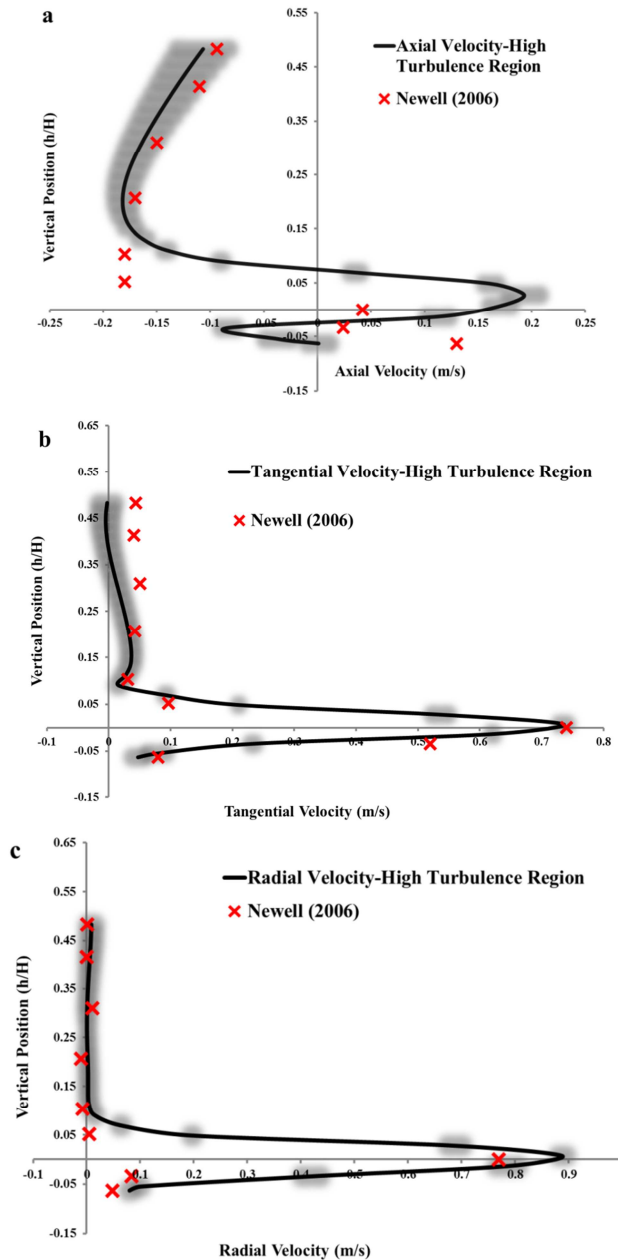


Figure 3-20 Numerical predictions of velocity components as a function of non-dimensional distance from top of the tank in the high-turbulent region: (a) axial, (b) tangential, (c) radial

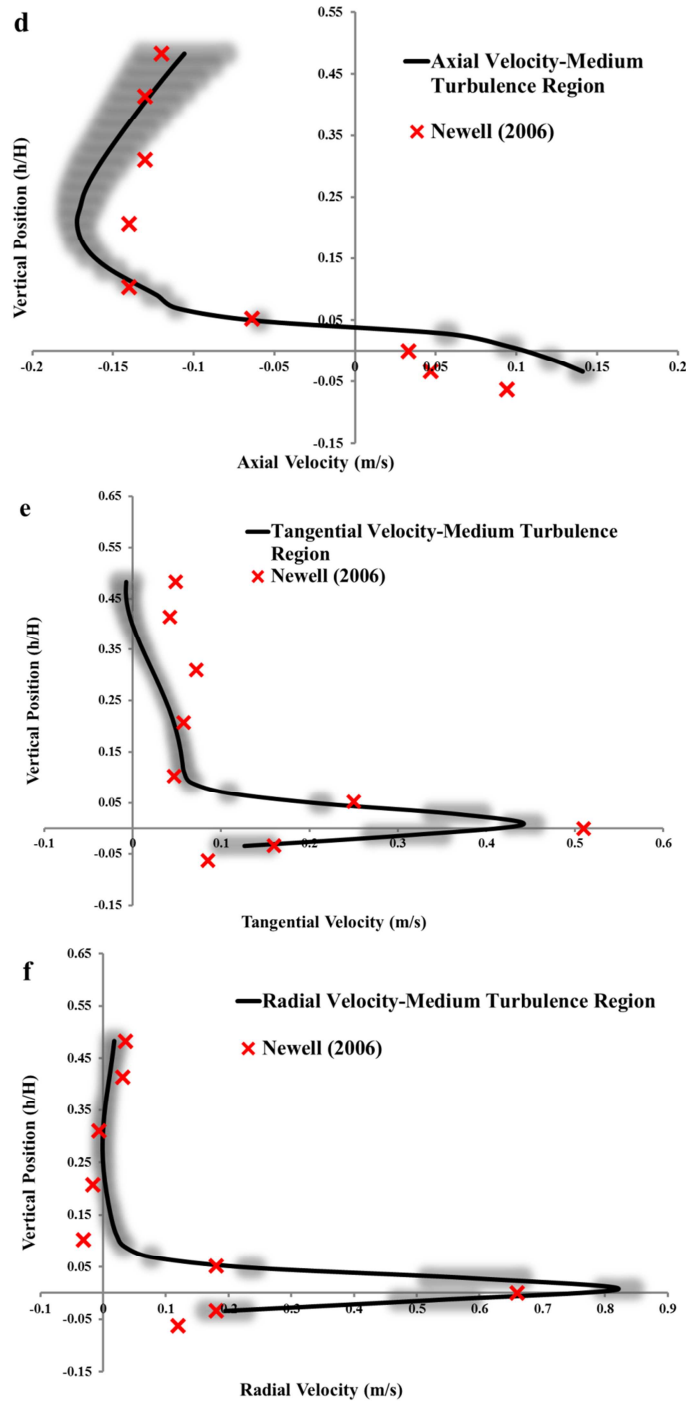


Figure 3-21 Numerical predictions of velocity components as a function of non-dimensional distance from top of the tank in the medium-turbulent region (d) axial, (e) tangential, (f) radial

In the previous works on the CFD modelling of water inside stirred tanks, described in Chapter 2, there was a general agreement on the underprediction of the turbulent quantities. This finding was attributed to the lack of a sufficiently fine mesh, especially around the impeller, to accurately resolve the turbulent flow inside the tank

(Bartels et al., 2002, Deglon and Meyer, 2006, Coroneo et al., 2011). In order to assess the validity of this argument and to evaluate the effect of discretization on the numerical predictions of the turbulent properties, Figure 3-22 validates the numerical predictions of turbulent quantities with Newell data for the high and medium turbulent regions. In the figure the solid lines display the CFD predictions, while the symbols correspond to the measurements and the shaded regions are the GCI computations. Qualitatively, the numerical solutions have correctly captured the trend of the turbulence field, showing a maximum at the impeller level. The maximum turbulent kinetic energy and dissipation rate at the impeller tip are also in acceptable agreement with the experimental data (to within an average difference of 29.67% for k and 17.58% for ε). Yet, the GCI results reveal slightly high values for this zone ($GCI < 13.9\%$ for k and $GCI < 17.1\%$ for ε). This implies that the local mesh refinement at the rotational zone and near the impeller tip could improve the agreement between the CFD outcomes and experimental data. The numerical predictions of k and ε in the medium turbulent region (i.e., bulk flow) show significant underprediction of the maximum turbulent properties, although an extremely fine mesh with 3.7 million cells has been utilized for half of the tank. The local average values of GCI at this zone are small, $GCI < 5.4\%$ for k and $GCI < 5.2\%$ for ε . These diagnostic values of GCI for this area highlight that the discrepancy between the maximum predictions and the measurements for both k and ε cannot be improved by using a more refined mesh. In other words, the quantification of numerical uncertainties stresses that the discretization error does not significantly contribute to the underprediction of maximum turbulent kinetic energy and the maximum turbulent dissipation rate at the medium turbulent region. Therefore, it may be concluded that the isotropic turbulence assumption used in the standard k - ε turbulence model does not hold for the simulation of anisotropic turbulence field inside the stirred tank. This problem might be tackled by application of Large Eddy Simulation (LES) where the large eddies are explicitly calculated and the sub-grid scale models are applied for the small scale eddies.

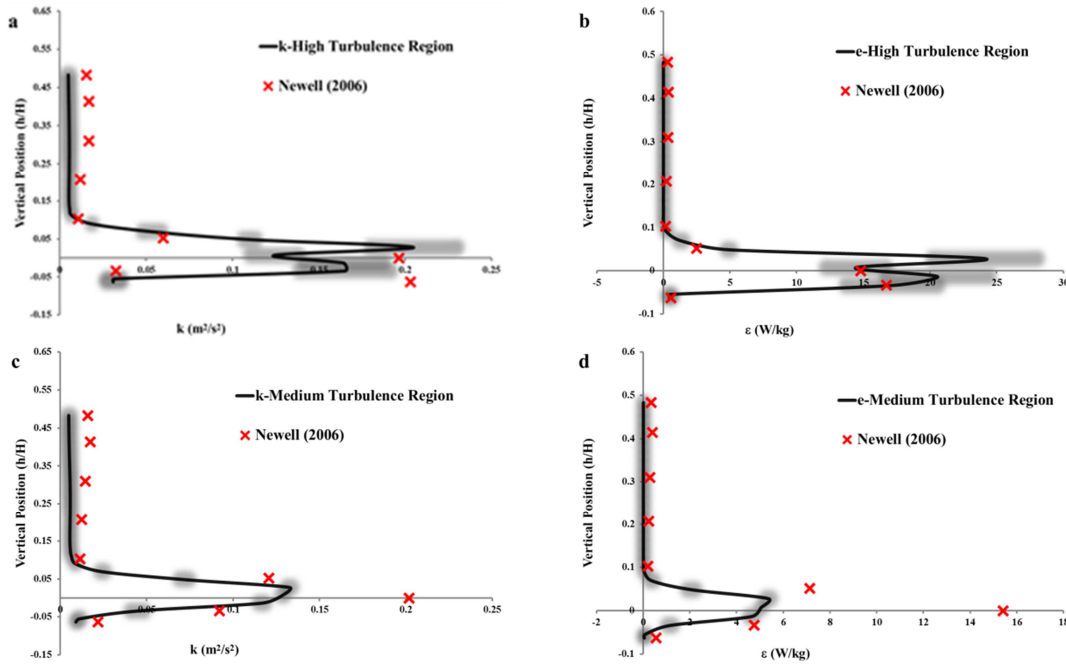


Figure 3-22 Numerical predictions of turbulent kinetic energy (k) and turbulent dissipation rate (ϵ) as a function of non-dimensional distance from top of the tank (a and b) high turbulent region, (c and d) medium turbulent region

The extremely fine mesh with 3.7 million cells that has been used for the GCI test cannot be an economical choice for future simulations. Besides, an optimized number of control volumes should be determined for which not only the solution is grid-independent but also the required CPU time is affordable. The optimized mesh is intended to eliminate or at least minimize the numerical uncertainties related to the discretization level. Therefore, seven different structured hexagonal mesh resolutions were constructed to systematically assess the grid sensitivity of the predictions. In each case, the number of elements around the impeller was higher compared to its surrounding. Further, while generating the grid, care was taken to exclude the cells with maximum skewness ratio higher than 0.9. Table 3-7 specifies the number of elements in each zone (i.e., bulk region and rotational zone), the total number of cells, and the corresponding CPU time for running the simulations on an Intel Corei7 1.6 GHz CPU. Similar to the previous runs, the MRF method handled the rotation of impeller inside the domain and the converged solution was achieved once the normalized continuity residuals dropped below 10^{-3} .

Table 3-7 Mesh details for the grid independence study of the standard Rushton turbine tank

Case#	Bulk region			Rotational zone			No. Cells	Skewness			CPU Time (h)
	r	θ	z	r	θ	z		Min	Max	Ave	
C1	74	48	31	32	48	9	71,040	2.1E-2	0.76	2.7E-2	5.4
C2	86	60	43	38	60	10	110,940	1.7E-2	0.85	2.3E-2	9.7
C3	102	72	52	48	72	12	190,944	1.4E-2	0.86	2.8E-2	18.3
C4	116	80	67	52	80	15	310,880	1.2E-2	0.88	2.5E-2	42.8
C5	148	96	82	72	96	20	582,528	6.4E-3	0.90	3.2E-2	53.1
C6	172	104	92	84	104	24	822,848	3.8E-3	0.85	3.4E-4	71.0
C7	220	112	102	116	112	30	1,256,640	3.6E-3	0.87	3.9E-2	95.2

The grid sensitivity analysis was performed based on the variations of the flow quantities at certain locations inside the domain. Nine different points were used to examine the fluctuations of the CFD outcomes with refining the number of cells. The placements of the examining spots covered the high, medium and low turbulent areas inside the tank at different vertical heights. Figure 3-23 displays the spatial positions of the selected points on which the deviations of the flow variables were investigated. However, for the sake of brevity the results only for the points illustrated by the yellow balls are discussed here.

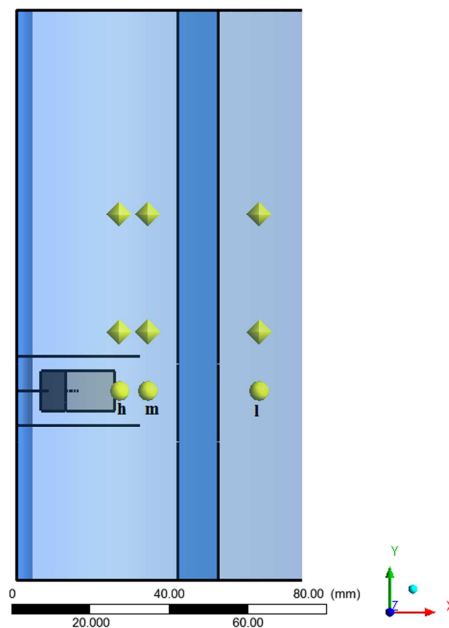


Figure 3-23 Locations of the examining points for the grid independence study in the standard Rushton turbine tank

Figure 3-24 is a set of plots showing the fluctuations of the axial velocity (a-c) and turbulent kinetic energy (d-f) as a function of cell numbers for the high (h), medium (m), and low (l) turbulent regions depicted by yellow balls on Figure 3-23. As seen, the changes in axial velocity at the high and medium turbulent zones (Figure

3-24 a and b) are negligible when the numbers of cells is more than 800,000 cells. As expected in at the low turbulent area even a relatively coarse mesh with more than 310,000 cells can result in independent solutions. The numerical predictions of the turbulent kinetic energy for the high and medium turbulent zones (Figure 3-24 d-e) show similar behaviour for the axial velocity component, where the numerical values of these quantities do not significantly differ after 800,000 control volumes. In the low turbulent region the turbulent kinetic energy becomes independent of the grid density after 310,000 cells. As expected, near the walls the grid-independent solution is obtained for both axial velocity and turbulent kinetic energy with coarser mesh schemes compared to the high and medium turbulent zones. This can be attributed to the low gradients of both velocity components and the turbulent properties at this zone. Thus, even a coarse mesh resolution is capable of capturing the flow field in this region. However, for the aim of minimizing the numerical uncertainty and obtaining greater detail in the impeller region the mesh scheme applied in case 6 (i.e., with 822,848 cells) is selected for the future simulations.

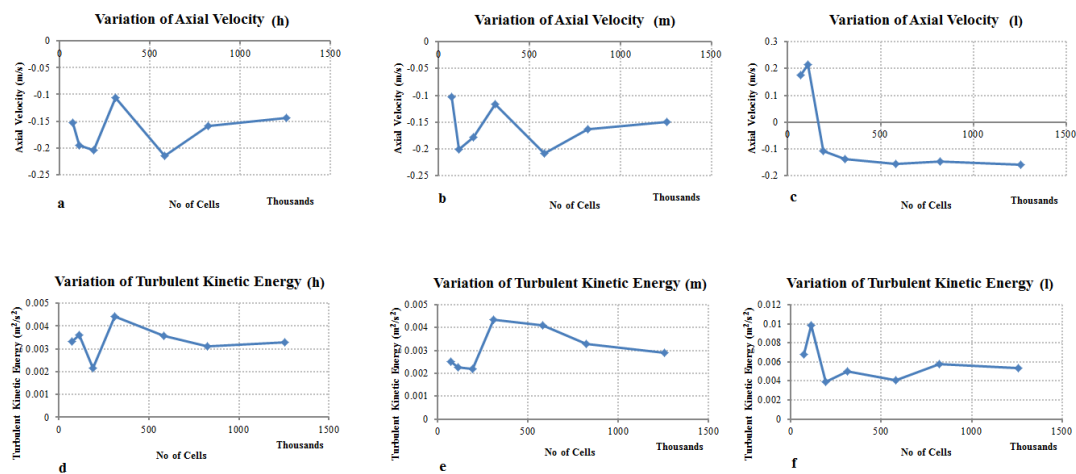


Figure 3-24 Numerical variations of the axial velocity (a-c) and the turbulent kinetic energy (d-f) as a function of cell numbers for the standard Rushton turbine tank

In addition to the mentioned flow properties, the other components of the velocity as well as the turbulent dissipation rate on all the arranged points are checked to evaluate their variations with the cell count. The findings are similar to those discussed above.

From the GCI and grid-independent study, one may draw the conclusion that firstly the numerical uncertainty for the single-phase modelling of the standard Rushton turbine tank cannot be completely eliminated. Nevertheless, diagnostic tools

such as the GCI and the sequential grid refinement aid in limiting numerical errors in the predictions. For the case of the standard Rushton turbine tank studied here, it is found that the commonly seen underprediction of the turbulent properties will not be improved only by mesh refinement and one should account for the drawbacks of the isotropic turbulence assumption in the standard k- ϵ turbulence model formulation. Moreover, the grid independent study reveals that a coarse mesh resolution is adequate enough for the regions inside the tank where the flow gradients are low, while for the high turbulent zones (e.g. around the turbine) a somewhat intense mesh resolution is required to resolve all the flow features.

3.3.2.2. Model uncertainties associated with the single-phase modelling of the standard Rushton turbine tank

In developing a CFD model for the single-phase simulation of the Rushton turbine flotation tank, the model uncertainty arises from the alternative model formulations and implementations such as the application of MRF versus sliding mesh method for the impeller modelling or how the turbulence field is modelled inside the tank and etc. Previous literature, specifically works of Lane (Lane et al., 2000a, Lane, 2006), have shown the computational superiority of the MRF approach both in the accuracy of the predictions and the computational demand (MRF time \approx 10 SM time). Hence, it is assumed in this study that the choice of MRF will attain the minimized model uncertainty and focus is solely made on the other major origin of the model uncertainty, which is the turbulence formulation.

The turbulence model study for the unbaffled mixer in sub-section 3.3.1.4 demonstrates that the k- ϵ model provides acceptable results for the single-phase modelling, while the application of LES was avoided due the higher CPU time, even though the level of agreement with the measurements was comparable with the k- ϵ model. For the case of standard Rushton turbine tank, three members of the k- ϵ group including: standard k- ϵ (Launder and Spalding, 1972), Renormalization Group k- ϵ (or RNG k- ϵ) (Orszag et al., 1993), and Realizable k- ϵ model (Shih et al., 1994) are compared. The common assumptions in the above models are that they all postulate the turbulence field is isotropic and they solve two transport equations for k and ϵ .

Figure 3-25 is a semi non-dimensional plot showing the numerical predictions of the resultant velocity at the high turbulent region as a function of vertical distance

(h) from the top of the tank, non-dimensionalized with the tank height (H). The symbols in this graph display the experimental measurements of Newell, while the three line styles correspond to the different turbulence models investigated. The numerical predictions show a negligible difference between different turbulence models. All the three turbulence formulations have correctly captured the trend of velocity, which shows a maximum at the impeller tip. The RNG k- ϵ , however, shows a slight fluctuation at the vertical position with a range of $0.14 < h/H < 0.38$. This can be attributed to the implemented formula for the turbulent Prandtl number where the standard k- ϵ constant values are used. The three turbulence models applied match the maximum resultant velocity occurred at the impeller level (i.e., $h/H=0$) very well to within an average difference of 8.01% for standard k- ϵ , 6.64% for realizable k- ϵ , and 4.64% for RNG k- ϵ turbulence model. The numerical predictions of the resultant velocity for the bulk flow region at $0.207 < h/H < 0.483$ also show a reasonable conformity with the experiments with an average different of 7.52%, 13.41%, and 34.78% for the standard, realizable and RNG members of the k- ϵ family, respectively.

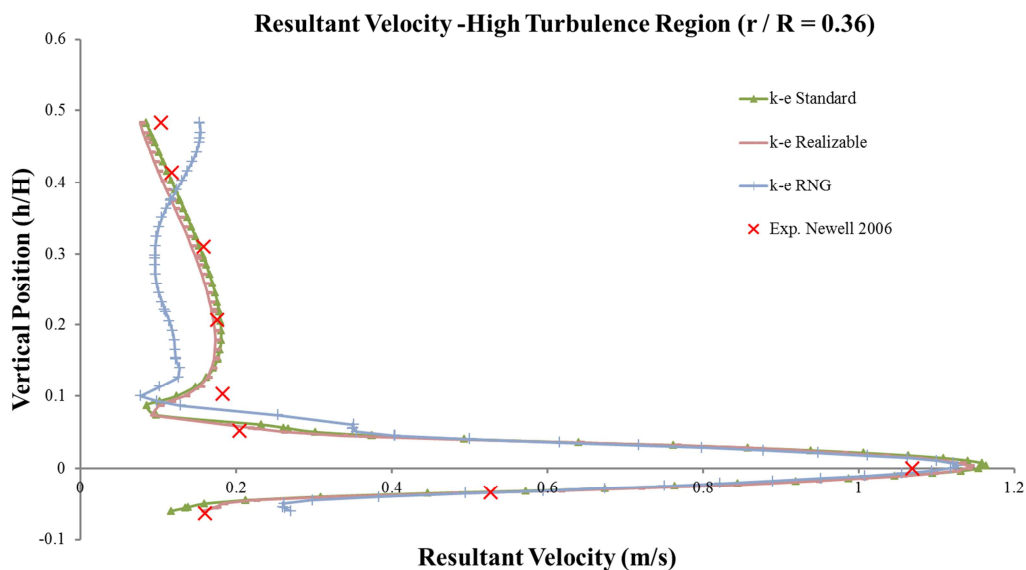


Figure 3-25 Numerical predictions of resultant velocity as a function of non-dimensional distance from the top of the tank with different RANS-based turbulence model for standard Rushton turbine tank

The second group of turbulence models investigated is the three different sub-grid scale models for the LES. As discussed previously, the LES formulation, contrary to the k- ϵ family, utilizes a filtering operation to divide turbulent eddies into large and small scales. The motion of the large-scale eddies in the flow are resolved, whereas

the sub-grid scale models implicitly model the small eddies. The sub-grid scale models apply the Boussinesq hypothesis to compute the small-scale turbulent stresses. Three different sub-grid scale models, Smagorinsky-Lilly (Smagorinsky, 1963), kinetic energy (Kim and Menon, 1997), and WALE (Nicoud and Ducros, 1999) are checked to explore the related model uncertainties in their numerical predictions.

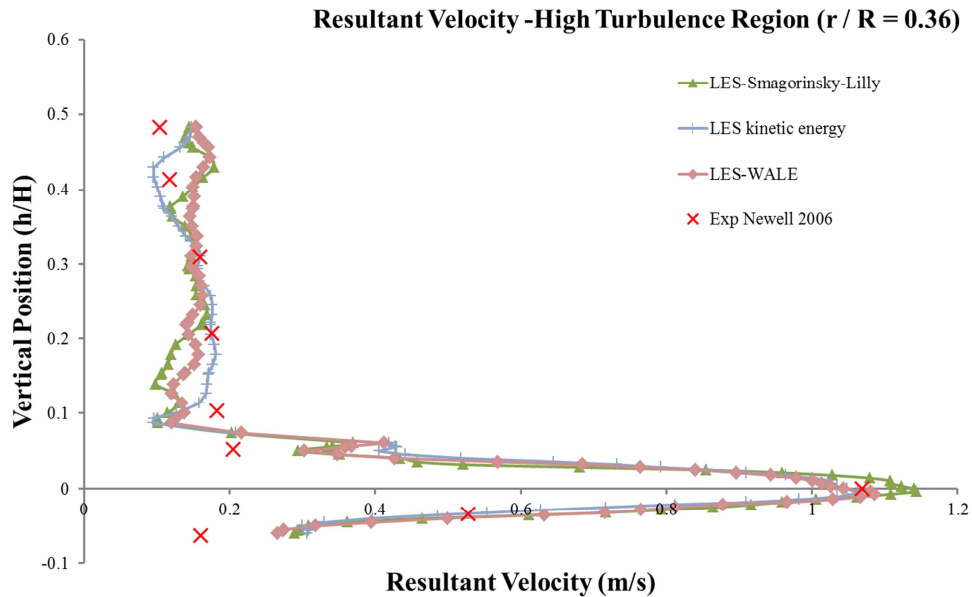


Figure 3-26 LES predictions of resultant velocity as a function of non-dimensional distance from the top of the tank with sub-grid scale models for standard Rushton turbine tank

To gauge the impacts of the model uncertainty on the numerical outcomes, the predictions by three sub-grid scale turbulence models for the high turbulent region inside the tank are compared in Figure 3-26. The figure shows the resultant velocity predictions as a function of vertical distance (h) from the top of the tank, non-dimensionalized by the tank height (H). The symbols indicate the experimental data from Newell and the solid lines correspond to predictions of the various sub-grid scale models. The results show that the locations of the peak, and the trend in the resultant velocity, have been correctly simulated. The three sub-grid scale models match the maximum resultant velocity with an average difference of 6.66% for Smagorinsky-Lilly, 1.92% for kinetic energy model, and 2.40% for WALE. However, slightly higher inconsistencies are observed at the bulk flow region (i.e., $0.207 < h/H < 0.483$). The kinetic energy model provides the best agreement with the measurements in this zone with an average difference of 15.87%. However, the computed resultant velocities with the Smagorinsky-Lilly and WALE sub-grid scale models show greater

of discrepancies with the experimental data with an average difference of 26.00% and 26.23% for Smagorinsky-Lilly and WALE models, respectively.

The final step in investigation of the model uncertainty for the water-modelling inside the stirred tank is to evaluate which group of turbulence models, i.e. those with the isotropic turbulence theory or the LES approach with a range of turbulence eddies, provide more accurate predictions, yet still remaining computationally feasible. In order to achieve that, Figure 3-27 compares the numerical predictions of the resultant velocity at the high turbulence region with the standard k- ϵ and LES with kinetic-energy sub-grid scale model as a function of non-dimensionalized distance from the top (h : height, H : tank height). In the figure the symbols represent the Newell experimental data and the two different line styles correspond to two turbulence models compared. The trend of LDV data for the resultant velocity shows a maximum at the impeller level ($h/H=0$); this phenomenon has been accurately captured with both turbulence models. Quantitative comparison of the turbulence models reveals that the standard k- ϵ turbulence model overpredicts the maximum resultant velocity with an average difference of 8.01%, while the LES/kinetic-energy underpredicts it with only 1.93% of difference. In addition, at the bulk flow zone in the vertical distance range of $0.207 < h/H < 0.483$ the standard k- ϵ turbulence model produce higher level of accuracy in the numerical predictions of the resultant velocity with an average difference of 7.52% compared to 15.87% for the LES/kinetic-energy. Apart from the resultant velocity at the high turbulence region, the numerical predictions of other velocity components and the turbulent properties for high, medium, and low turbulent zones are compared (For example Appendix A reports the numerical predictions of tangential velocity). Comprehensive comparison reveals that the CFD results with the standard k- ϵ turbulence model produce slightly better agreement with the experiments. Nonetheless, the LES predictions for all the flow variables are still comparable to the Newell measurements with an average difference of between 10 to 20%. From the computational time standpoint, the standard k- ϵ takes almost 35 hours to obtain the converged solution, while for the same mesh resolution the LES computational demand is approximately twice this time.

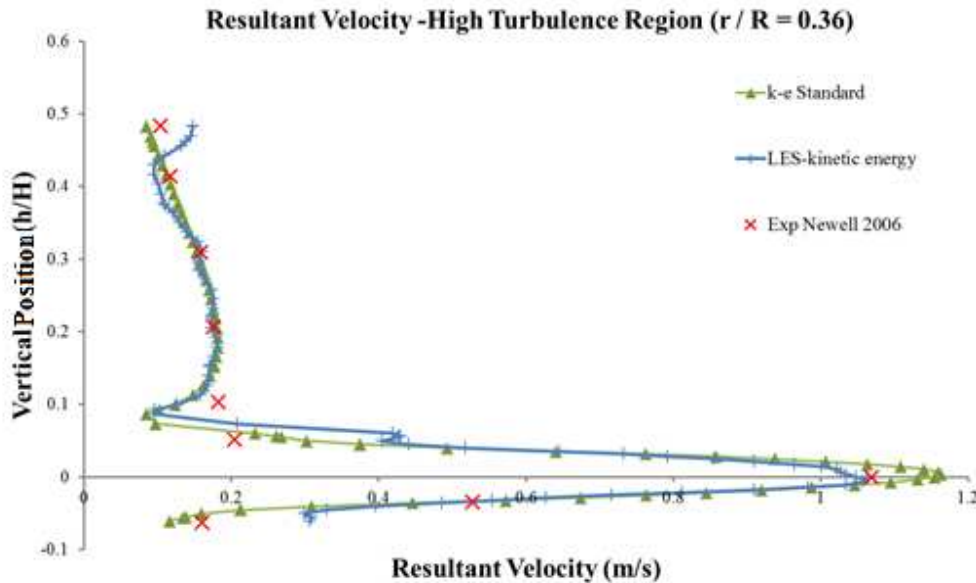


Figure 3-27 Numerical predictions of the resultant velocity; comparison of the k- ϵ standard turbulence model and LES with kinetic-energy subgrid scale model for the standard Rushton turbine tank

In summary, investigation of the model uncertainty for the single-phase modelling of the standard Rushton turbine tank shows that even though the standard k- ϵ employs the isotropic turbulence assumption inside the tank it appears to be the most practical option for the modelling of water velocity components and turbulence characteristics. The LES choice, however, comes with additional computational expenses but with approximately similar confidence in the CFD results. Nevertheless, discrepancies between the simulations and experiments are observed for the choice of standard k- ϵ turbulence model. This can be remedied by the application of Direct Numerical Simulation (DNS) where the Navier-Stokes equations are solved on an extremely fine mesh to resolve all the turbulent scales in the flow. In this way the approximations and empirical constants implemented in the turbulence formulations will be avoided and therefore the model uncertainty related to the choice of turbulence model is thoroughly eliminated. However, for the fully turbulent flow inside the stirred tank the computational requirements of DNS are beyond the range of our accessible computational power. Thus, the two-equation k- ϵ turbulence model will be used and special effort will be made to minimize input and numerical uncertainties in the modelling procedure, since the model uncertainty caused by the turbulence model formulations cannot be entirely excluded.

3.3.2.3. Simulations of single-phase flow for different angular velocities

Thus far, various aspects of a practical CFD model for the single-phase modelling of stirred tanks are explored. Efforts have been made on reducing or eliminating the uncertainties and errors in the solutions and the developed conceptual CFD model is intended to replicate the actual flow behaviour with a reasonable similarity. Moreover, the accuracy of the constructed CFD methodology is determined with the validation against the experimental data.

Additional simulations have been carried out in this sub-section to assess the predictive capability of the model outside the operational range in which it has been established. Three different angular velocities for the Rushton turbine have been tested including 470 rpm, 650 rpm and 800 rpm. The goal of the simulations is to study different features of the flow field for the entire tank and on another level, understand the detailed flow characteristics around the impeller blades. The capability to numerically model and analyse all the flow features in different scales allows us to describe some of the phenomenon that occurs in the gas-liquid flow field and flotation process. Therefore, this investigation has focused on the influence of increasing the rotational speed on general flow features such as the flow pattern, and turbulent properties. It also answers the question whether or not the established CFD approach is able to capture the details of the trailing vortices around the blades.

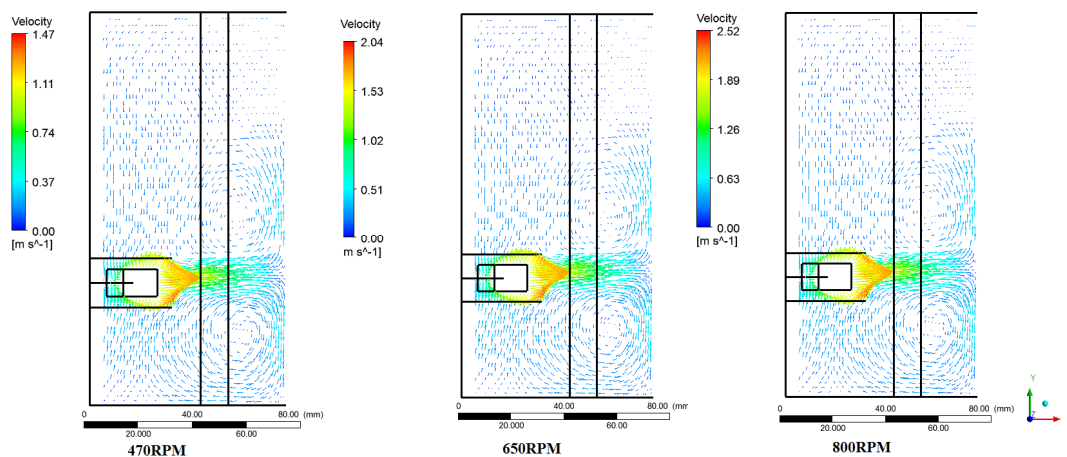


Figure 3-28 The predicted flow pattern for three different angular velocities of the Rushton turbine tank

Figure 3-28 shows the vector plots of the predicted flow pattern for the three different angular velocities of the impeller inside the standard Rushton turbine tank. The vectors are drawn in a vertical plane (x-y direction) at the centre of the tank and

the lengths of the arrows specify the velocity magnitude. The figure depicts that for all cases investigated the water is ejected in a radial direction from the blades towards the periphery of the tank. This is where the water is redirected due to the impact with the wall and two separate upward and downward flow streams are formed. The flow separation eventually creates two recirculation zones at the bottom and top parts of the tank. The fluid then returns to the Rushton turbine in an axial direction from below and above the turbine, thus maintaining the circulation loops. The lengths of the arrows in the bottom loop are typically larger than those in the upper loop which points out that the fluid velocity is higher at the lower circulation zone. The formation of the circulation areas for the Rushton turbine has been repeatedly reported in previous studies (Ranade, 1997, Lane and Koh, 1997). As seen in Figure 3-28, increasing the rotational speed does not vary the general pattern of water flow inside the tank, as in all cases the jet-like flow of water is discharged from the blades and providing two circulation zones. However, the velocity magnitudes at the discharge streams are different and the increase in the angular velocity increases the maximum velocity at the impeller tip from 1.22 m/s for 470 rpm to 1.76 m/s for 650 rpm and further to 2.18 m/s for the 800 rpm. As shown, increasing the impeller speed from 470 rpm to 800 rpm enhances the maximum velocity approximately 56%. This increase, from a flotation point of view, translates into a higher chance of bubbles and particles to collide and attach. Since the velocity levels in the bulk region for various rpms are similar (0.13 m/s for 470 rpm, 0.15 m/s for 650 rpm, and 0.18 m/s for 800 rpm), it infers that increasing the angular velocity of the impeller yields higher probabilities of collision and attachment, while the nearly similar conditions for the bulk region guarantees the stabilization of the bubble-particle aggregates in the flotation tank.

Sub-section 3.3.2.2 shows that the developed CFD model can successfully predict the turbulent properties inside the tank. Hence, the influence of the impeller speed on the turbulent quantities has been also explored as the second important feature of the flow field.

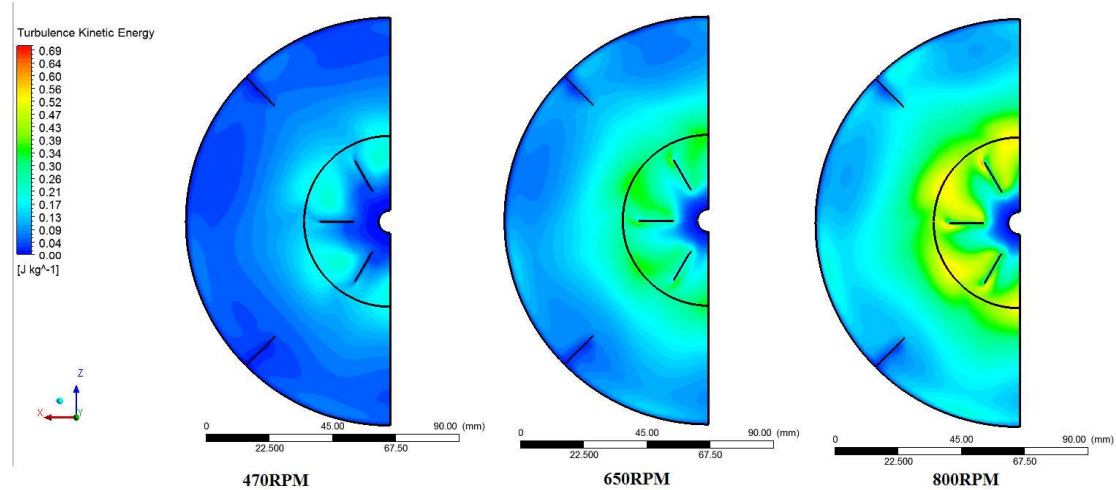


Figure 3-29 The predicted contour plots of the turbulent kinetic energy for three different angular velocities of Rushton turbine tank

The contour plots of the predicted turbulent kinetic energy (k) at three tested rpms are depicted in Figure 3-29. The figure displays the turbulent kinetic energy gradients on a horizontal cross-section of the tank located at the impeller level. The contour plots show that the turbulent kinetic energy around the impeller has a higher level for all cases considered; and further away from the blades the magnitude of the kinetic energy in the tank is decreased. The maximum turbulent kinetic energy takes place behind the blades as can be seen in the figure. Newell has explained this phenomenon by the occurrence of the trailing vortices in this area generated by the separation flow over the impeller blades (Newell, 2006). Increasing the rotational speed of the impeller significantly changes the turbulent kinetic energy. The numerical predictions of the maximum turbulent kinetic energy show an increase with increasing impeller speed. To verify this phenomenon and evaluate the predictive capability of the CFD model, the numerical predictions of maximum turbulent kinetic energy as a function of angular velocity are illustrated in Figure 3-30. In this figure the symbols represent the maximum turbulent kinetic energy measured by Newell and the solid line corresponds to the CFD simulations. A linear increase between the maximum turbulent kinetic energy and the impeller speed has been reported by the experimental data for which the CFD results demonstrate a similar behaviour. Moreover, the quantitative comparison reveals that the predicted maximum turbulent kinetic energies match the experimental data very well with an average difference of 0.36%, 2.17%, and 1.44% for 470 rpm, 650 rpm and 800 rpm, respectively.

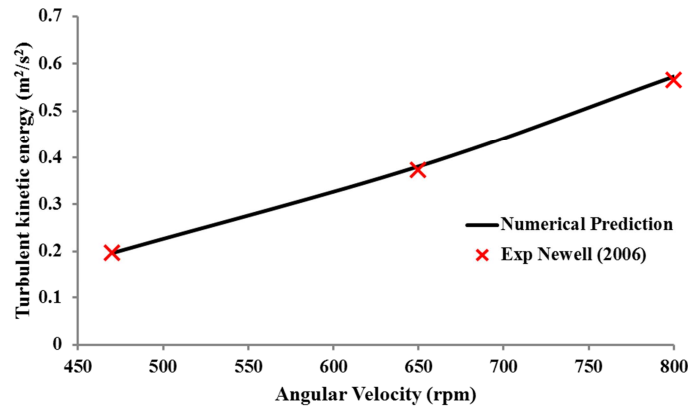


Figure 3-30 Numerical predictions of maximum turbulent kinetic energy as a function of angular velocity for the standard Rushton turbine tank

In addition to the turbulent kinetic energy the influence of increasing the impeller speed on the turbulent energy dissipation rate (ϵ), has been also studied. Figure 3-31 illustrates the simulation results of the turbulent energy dissipation rates experienced on a horizontal plane with a distance equal to the clearance of the standard Rushton turbine tank. As seen, far from the impeller and close to the baffles the magnitude of ϵ is very low compared to the rotational zone. The maximum turbulent dissipation rate has occurred behind the impeller blades for all the angular velocities and its value increases with increasing impeller speed. The turbulent dissipation rate gradients experienced behind the impeller blades are due to the dissipation of the larger eddies into smaller eddies, which is expected due to the presence of high turbulent shear stresses created by the wake region and the fluid surrounding it.

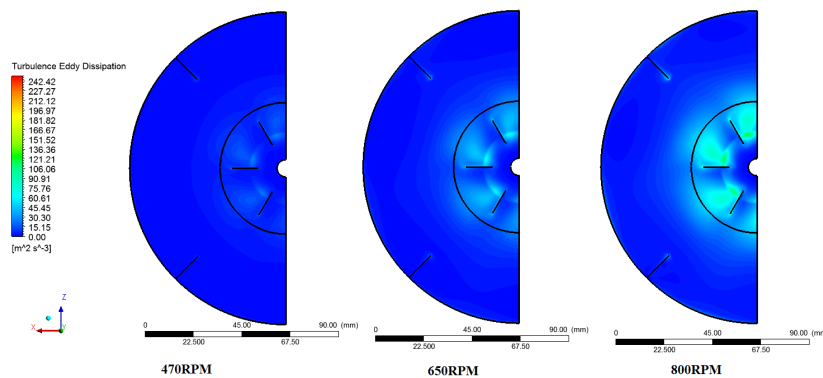


Figure 3-31 Predicted contour plots of the turbulent energy dissipation rate for three different angular velocities of Rushton turbine

The validation of maximum turbulent dissipation rate has been shown in Figure 3-32. This figure shows the experimental measurements of Newell (symbols);

while the numerical predictions are depicted by a solid line. It is observed that the maximum ε increases with the impeller speed and this trend for the maximum dissipation energy has been correctly captured by the numerical predictions. Further, the CFD predictions of the maximum dissipation rates are in acceptable agreement with the measurements, within an average difference of 11.97% for 470 rpm, 8.16% for 650 rpm and 5.81% for 800 rpm.

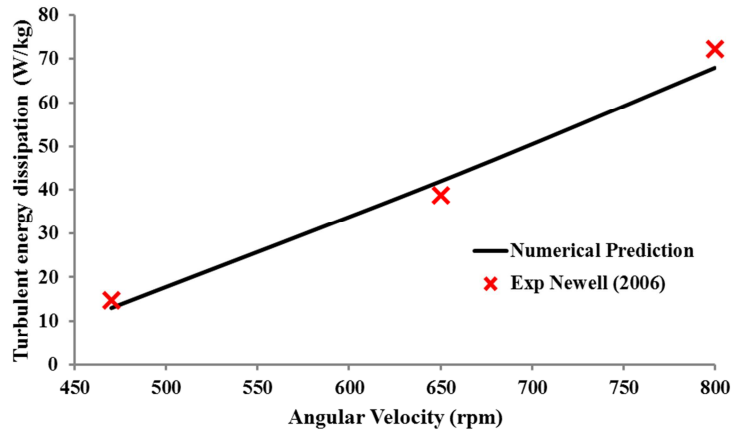


Figure 3-32 Numerical predictions of maximum turbulent energy dissipation rate as a function of angular velocity for the standard Rushton turbine tank

This investigation about the two turbulent quantities inside the stirred tank shows that first of all the developed CFD model can predict the turbulent kinetic energy and its dissipation rate with an acceptable degree of accuracy. Secondly, the CFD approach is able to capture the flow behaviours in different impeller speeds. Accurate prediction of the turbulent quantities inside the stirred tank is of great importance, since they transfer the momentum and energy across the tank which is crucial in the mixing applications. Moreover, for the gas-liquid flow inside the tank the bubble break-up and coalescence are often formulated as a function of k and ε . Therefore, accurate predictions of these values will lead to greater accuracy for the simulation of the dispersed gas within a continuum fluid. From the flotation modelling standpoint, the mathematical equations of the flotation sub-processes involve correlations in which the hydrodynamic properties of the slurry are represented with the turbulent properties. Hence, accurate predictions of the k and ε not only yields precision for the simulation of the air bubbles motions, but also the flotation sub-processes models that employ these factors will be benefited.

The third crucial aspect of the flow field that has been studied by varying the impeller speed is the presence of trailing vortices. The existence of the trailing vortex pair behind the blades in stirred tanks has been experimentally shown by Van't Riet and Smith (Van't Riet and Smith, 1975). Ranade et al., (Ranade et al., 2001) have highlighted the importance of modelling of this phenomenon. They emphasized that the ability to model the trailing vortices behind the impeller blades enhances the confidence in the design and scale-up processes of stirred tanks.

The trailing vortices are formed behind each rotating blade owing to the fact that the fluid elements are separated at the trailing sides of the blades. Trailing vortices can be considered as low pressure structures with high swirling motions at the back of each blade. Ranade (Ranade et al., 2001) stated that trailing vortices have the main role in the dissipation of energy at the impeller region. Moreover, Van't Riet and Smith (Van't Riet and Smith, 1975) showed that in the core of each vortex the pressure is lower than its surrounding, so for multiphase flows the dispersed phase (i.e., air bubbles or solid particles) can be drawn into the vortices. For the case of a gas-liquid system, the accumulation of air bubbles behind each blade is known as the ventilated cavities. Therefore, the CFD model developed in this study has been examined to check whether it is able to capture this flow characteristic inside the Rushton turbine tank. In order to capture the trailing vortices in the single-phase flow of water inside the standard Rushton turbine tank, Figure 3-33 illustrates the contour plots of velocities and iso-surfaces of vorticity magnitude around the blades. The vorticity is a vector quantity measuring the local rotation of the fluid elements. In that, it quantifies the strength of the fluid rotation around the impeller blades. The vorticity can be written as the curl of velocity vector:

$$\xi = \nabla \times \vec{V} \quad \text{Eq. 3.31}$$

As mentioned, the trailing vortices have shown strong swirling motions. Therefore, the vorticity magnitude of the fluid around the impeller blades can be a representative indicator of the presence of trailing vortices at this region. Also, the contour plots of velocity characterize how the water elements are moving around the blades. The velocity contour plots for all the rpms investigated show a similar flow pattern. Two vortices have been formed behind each of the rotating blades in which the velocity magnitude is reducing by approaching to the core of each vortex. This type of velocity distribution at the rear of blades clearly demonstrates that the fluid

elements are experiencing rotational motions. Moreover, increasing the angular velocity of the impeller does not vary the flow pattern. Though, the velocity magnitudes at the loci of vortices are appreciably increased from 0.41 m/s for 470 rpm to 0.58 m/s for 650 rpm and further to 0.63 m/s for 800 rpm. This indicates a growth in the swirling motion of the trailing vortices by increasing the angular velocity.

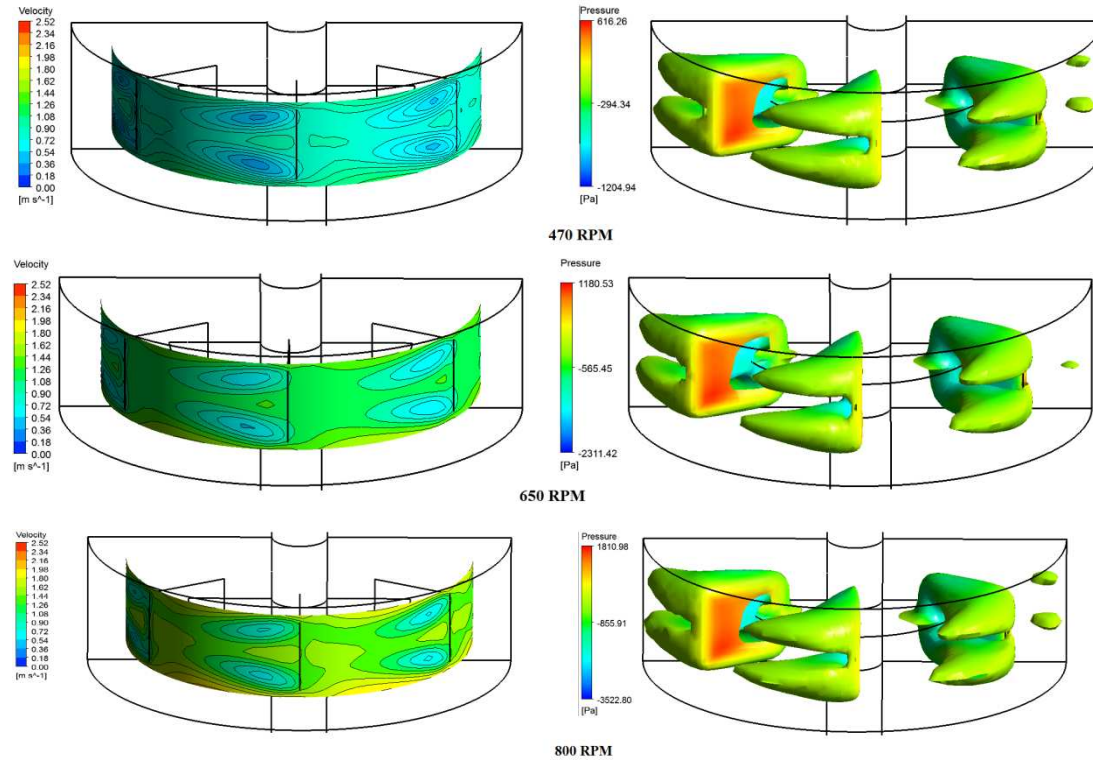


Figure 3-33 Contour plots of velocity distribution and iso-surfaces of vorticity around the blades at three different impeller speeds for the standard Rushton turbine tank

Van't Riet and Smith (Van't Riet and Smith, 1975) have defined the trailing vortex pair as the low pressure rotating structure behind the blades. Thus, further insights into the trailing vortices structure can be gained by considering the iso-surfaces of the vorticity around the blades when they are coloured by the pressure distribution. The right hand side images in Figure 3-33 depict the areas behind the blades with constant values of vorticity. The interface at each zone are coloured with the numerical predictions of the pressure distribution. As seen, there are two deformed conical shapes at the top and bottom edges of each blade signifying the trailing vortices. They show that the fluid at this zone has rotational motions which also correspond to the contour plots of velocity. Regarding the pressure distribution, there exist a strong pressure gradient at the front and back sides of the blades. For instance, at 470 rpm, the pressure at the front side of the blade falls into the red range of the

legend (i.e., < 616 Pa), whereas the numerical predictions of the pressure distribution on the outer surface of the deformed cones (i.e., trailing vortices behind the blade) are within the range of $-300 < P < -85$ Pascal. Increasing the angular velocity has negligible impact on the shape of the iso-surfaces; however the vorticity magnitude for maintaining the deformed conical shape (i.e., trailing vortex pair) behind the blade is required to increase from 270 l/s for 470 rpm to 400 l/s for 650 rpm and further to 450 l/s for 800 rpm. In other words, increasing the rotational speed of the impeller has strengthened the local rotation of the fluid behind the blades. In addition, comparison of the pressure level at the back and front sides of the blade reveals an increase in the pressure gradient with the impeller speed. Quantitatively, the maximum pressure in front of the blade is increased from 450 Pa to 1390 Pa when the impeller speed is varied from 470 rpm to 800 rpm. Accordingly, the minimum pressure level is decreased from -95 Pa for 470 rpm to -250 Pa for 800 rpm.

As shown in this study, the CFD model in conjunction with a grid density of more than $800,000$ cells is capable of simulating the rotating motion of the trailing vortices. The potential to numerically model this phenomenon is of great importance in the gas-liquid flow and the flotation separation process. For the gas-liquid flow, the low pressure regions with high centrifugal forces at the centre of each vortex will suck the air bubbles into these zones behind the blades. It is found that increasing the impeller speed causes an increase in both the pressure gradient and swirling motion of the trailing vortices. This will result in more gas accumulation behind the blade that in turn increases the air bubble size due to the dominance of the coalescence phenomenon. In the flotation process, having larger air bubble diameters reduces the available interfacial area for the particles to collide and attach to. Therefore, the probability for collision and attachment will be decreased which eventually has a diminishing effect on the flotation separation efficiency. In other words, for an efficient flotation process to occur an optimum rotational speed for the impeller should be chosen to simultaneously increase the turbulent intensity while minimising the gas accumulation behind each blade.

3.4. Conclusion

This chapter has discussed the development of a CFD-based approach for modelling of water inside the stirred tanks. The major goal was to determine the sources of inherent inaccuracies in the CFD modelling of water inside the mechanically stirred tank. Having recognized the origins of errors, attention was given to the development of a numerical method that is capable of predicting both the macro and micro fluid flow phenomena inside the tanks. The model uncertainties in the numerical approach, caused by the model implementations and formulations, have been minimized by investigating the optimized dimensions for the rotational zone around the impeller and obtaining the economical choice of turbulence model. In all tests, validations against experimental measurements show that the influences of the model uncertainties on the numerical predictions are decreased to a reasonable level. The second source of uncertainties, numerical uncertainty, in the single-phase modelling of stirred tanks has been also assessed. The previous literature in this field suggested that the typical grid independence study was the sole way of evaluating the discretization errors on the CFD outcomes. However, in this study in addition to the common sequential grid refinement study, the Grid Convergence Index (GCI) test has been applied for reporting the inherent uncertainties in the CFD modelling. In this way, confidence can be built on the CFD results by drawing an error bar for the predictions which shows how far the numerical predictions are from the asymptotic range. Moreover, the performance of the developed CFD method has been tested under different angular velocities of the impeller and the CFD model shows its capability in capturing the different flow features such as the general flow patterns, turbulent properties and the trailing vortices.

To summarize, the main findings of this chapter are articulated here:

- Even though the MRF method for the impeller modelling has been verified to account for both results accuracy and the computational time, care should be taken on defining the rotational zone dimensions around the impeller. It is found that a rotational zone close to the impeller blades, yet not attached to them, yields better agreement with the measurements.

- The time marching for the calculation of the governing equations can be chosen with regard to the degree of rotation of impeller. It was found that short time steps (e.g. between 10 to 15 degrees of rotation of blades) are adequate choices for the single-phase modelling.
- The numerical uncertainty due to the discretization errors can cause numerical predictions to deviate significantly from experimentally determined values. Discretization errors can be studied by a grid independence study and the grid convergence index (GCI). It was found that a fairly coarse mesh scheme for a laboratory scale vessel (2.25 l) with 200,000 to 300,000 cells results in an acceptable predictions of the flow pattern and the velocity components inside the tank. However, accurate predictions of the turbulent quantities require denser grid resolution with between 700,000 to 800,000 computational cells.
- The grid convergence index, applied for the first time to study the numerical uncertainties in the CFD modelling of stirred tanks, has revealed that, contrary to previous studies, the underprediction of turbulent properties cannot be improved with only refining the mesh, as the computed GCI values for these properties of the flow are fairly small.
- The turbulence model study has been also carried out to reduce the model uncertainties in the results. The comparison between the RANS based turbulence models with the isotropic assumption for the turbulent field and the LES, where the turbulent field is divided into large and small scales, showed that both models are capable of predicting the flow field behaviours within the stirred tanks. The standard k- ϵ from the RANS group and the LES with kinetic energy subgrid scale model both predicts the flow properties with reasonable accuracy. However, the required computational time for the LES/kinetic energy is more demanding than the standard k- ϵ model. Thus, for multiphase modelling where the fluid flow includes significant modelling detail, the use of the standard k- ϵ turbulence model is most practical.

- The potential of the established CFD model has been demonstrated by simulating the flow fields for different impeller speeds. For all the angular velocities investigated it was found that the model can predict the flow patterns and the turbulent properties as well as the trailing vortices behind the blades. Increasing the impeller rotational speed linearly increases the maximum turbulent properties (both k and ε). Moreover, an increase in impeller speed increases the pressure gradient between the back and front side of each blade that in turn results in a more powerful swirling motion inside the trailing vortices.

Chapter 4 Development of a CFD methodology for gas-liquid flow in stirred tanks

4.1. Introduction

A large number of flows encountered in the mineral processing industries and chemical engineering are typically a mixture of different phases. Often, there exist a medium (e.g. water in mineral processing) that carries and disperses the secondary particulate phase (e.g. air bubbles or solid particles). The particulate phase can interact with the continuous phase due to its inertial reaction with the motion of this phase. In the same way, the liquid phase resists the movement of the particulate phase through various forces such as the drag force. Moreover, the multiphase processes function under different flow regimes, which can be identified by the operational and geometrical conditions under which the processes occur. The principle hydrodynamics of multiphase flow significantly differ with the changes in the vessel's configurations and operating conditions. For instance, for the gas-liquid flow within stirred tanks, different sparger designs will lead to completely different gas flow patterns inside the tank. Moreover, for the same design of the sparger, operation under various angular impeller velocities might affect the gas holdup and distribution of the secondary phase inside the tank. Therefore, a modelling tool for the multiphase processes should encompass most of the possible fluid flow details while the different reactor configurations and operating conditions are accounted for.

One of the important aspects of multiphase modelling that needs to be addressed beforehand is whether the different phases presented are separated or dispersed. In separated or stratified form, the different phases flow in semi-continuous mode in which the significant feature of the flow is the interfaces between the phases (e.g., film flow and jet flow). The second type of multiphase flow regime is dispersed flow. In this case, the secondary phases flow in the form of particles or droplets within the continuous phase. There also exists the mixed multiphase flow regime in which

both the dispersed and the semi-continuous interfaces are present simultaneously. For instance, if the gas bubbles flow over a circular-shape liquid film, this can be thought of as mixed multiphase flow. The gas-liquid behaviour inside stirred tanks can be classified in the dispersed multiphase flow group, as the discrete gaseous phase distributes into a continuous phase. In ANSYS Fluent CFD solver there are two major schools of thoughts for modelling dispersed multiphase flow.

The Lagrangian-Eulerian strategy employs the Navier-Stokes equations to simulate the continuous fluid, while the Lagrangian particle tracking method monitors the motion of the dispersed phase. It is recommended (ANSYS, 2011a) that the application of this method should be limited to multiphase flows where the volume fraction of the secondary phase is low (e.g. $< 10\%$). The Eulerian-Eulerian approach for multiphase modelling, however, considers different phases as interpenetrating continua and introduces conservation equations for each phase. The volume fraction of each phase varies with respect to time and spatial location and in every computational control volume the sum of these continuous values must be unity. In ANSYS Fluent three different options are available that employ the Eulerian-Eulerian concept for the multiphase modelling, including Volume of Fluid (VOF), the Mixture model and the Eulerian model. The VOF, the simplest of the three, is applicable when capturing the interface between immiscible liquids is the aim of simulations. The Mixture model solves the Navier-Stokes equations for the primary phase (i.e., mixture) and computing an algebraic equation for the relative, or slip, velocity between the phases treats the secondary phase. The last modelling technique, Eulerian model, treats each of the available phases in the domain as a continuum and solves a set of continuity and momentum equations for each phase. This method is only limited by the availability of the memory space and the computational power. In other words, n number of different phases can be described by the Eulerian model, if the required computational resources are accessible. The coupling between different phases is achieved through adding exchange terms in the momentum equation. It is also feasible to modify the exchange terms by implementing user-defined functions for certain multiphase flows.

The next step in the modelling of dispersed multiphase flow is to evaluate the level of coupling, or the interaction, between the continuous phase and the dispersed phase. Elghobashi (Elghobashi, 1994) proposed three different ways of coupling when

a particulate phase disperses within a continuous phase. One-way coupling is defined for multiphase flows in which the dispersed phase is affected by the continuous phase. In this case only the continuous phase can transfer momentum to the dispersed phase through drag and turbulence. In the framework of the applied CFD solver in this study (i.e., ANSYS Fluent), one-way coupling can be handled with Discrete Particle Model (DPM), Mixture, and Eulerian models. The second method is called two-way coupling, which can be used when there is either an intermediate loading of the particulate phase or the dispersed phase has a Stokes number larger than unity. In this method, the impact of the dispersed phase on the continuous phase cannot be neglected. The particulate phase, therefore, reduces the mean momentum and turbulence level of the continuous phase, whereas it is affected by the carrier phase through drag and turbulence. The two-way coupling can be implemented via DPM, Mixture and Eulerian multiphase models in ANSYS Fluent. It is worth remembering that, apart from the level of coupling between the phases, one should consider other factors for an efficient CFD model. For example, the application of DPM for the multiphase modelling is limited to the volume fractions of the secondary phase below 10%. The last and most complete method of coupling for high loading of the particulate phase is called four-way coupling. This coupling approach takes into consideration the interactions between the dispersed phases by themselves (i.e. particle-particle or bubble-bubble). In ANSYS Fluent framework this can be marginally achieved for solid-liquid multiphase flows by incorporating the particle pressure and viscous stresses exerted on particles into the two-way coupling method. Thus, only the Eulerian approach for the granular phase modelling can be used for the four-way coupling. These limitations of the CFD solver can be augmented by integrating a Discrete Element Method (DEM) model with the CFD data. In this way, the DEM solver can handle the inter-particulate interactions (i.e. the locations and velocities of the dispersed phase), while the CFD solver calculates the local velocity of the liquid phase. This modelling strategy is, however, outside the scope of this work. Thus, in this study the available Eulerian-Eulerian approach of ANSYS Fluent was applied for the gas-liquid modelling. As discussed due to high volume fraction of gas phase in some cases simulated the DPM method was not the method of choice. Moreover, combination of MRF for the impeller modelling and the DPM for the discrete phase modelling, will lead to unrealistic predictions of the particulate phase trajectories (ANSYS, 2011a). However, using Eulerian-Eulerian method enables us to

apply the one-way coupling between the continuous phase and the dispersed phase. In other words, the liquid phase can influence the air bubble. In order to include the effect of turbulence eddies on the air bubbles movements the drag coefficient correlation was modified using UDF. The proposed model of Lane for the drag coefficient was implemented into the Eulerian-Eulerian framework to manipulate the exchange coefficient for the coupling between the two phases available in the computational domain.

This chapter explains the process of developing a CFD model for gas-liquid modelling inside stirred tanks. The geometry, similar to the single-phase modelling, is adopted from the work of Newell who has experimentally measured the gas holdup inside the tank (Newell, 2006). As mentioned previously, the main aim of this study is to establish a CFD approach for the flotation sub-process modelling. The gas-liquid modelling is therefore the second prerequisite step toward the successful flotation modelling. The findings from this section can be the premise for the simulation of the flotation separation, as the efficiency of the flotation sub-processes are strongly influenced by the distribution of the injected air from the sparger and its total holdup. It should be remembered that a constant bubble size was prescribed at the sparger for each simulation following the common practice as applied by previous studies (Khopkar et al., 2006, Khopkar et al., 2005, Ranade and Van den Akker, 1994). They showed that the application of uniform sized air bubbles within stirred tanks resulted in the practical prediction of the gas-liquid flow inside stirred tanks. Not only the computational requirements were practical but also an acceptable agreement level between the numerical predictions and experimental values of gas hold up was reported. The values for the bubble diameters in the current study were adopted from the experimental data of Newell who measured the bubble size for the similar Rushton turbine tank under different operational conditions. This section starts with the required governing equations for the gas-liquid modelling with the Eulerian-Eulerian framework and continues with the investigation of different sparger configurations for the accurate prediction of the gas holdup inside the tank. Of the various interphase forces between the liquid and air phase, the effect of drag force is also explored by comparing different drag coefficient correlations. The optimized expression for the drag coefficient is then tested under different conditions to evaluate the predictive capability of the founded model.

4.2. Governing equations

The fundamental physics of the gas-liquid flow inside a laboratory scale Rushton turbine tank is attained by the solutions of Eulerian-Eulerian two-fluid equations. The Eulerian approach allows us to solve the mass and momentum balance equations for both the liquid and gas phases. The turbulence inside the primary phase is accounted for with the standard k- ϵ turbulence model. In addition, the concept of volume fraction for phase q , α_q , which varies in time, is introduced as the volume in each cell in the computational domain being occupied by phase q . This volume, V_q , can be written as:

$$V_q = \int_V \alpha_q dV \quad \text{Eq. 4.1}$$

for two different phases in the stirred tank, we have:

$$\sum_{q=1}^2 \alpha_q = 1 \rightarrow \alpha_1 + \alpha_2 = 1 \quad \text{Eq. 4.2}$$

where α_l denotes the volume fraction of the primary phase (i.e., water), and α_2 represents the volume fraction of the gas phase in each cell.

The governing continuity equation which is solved for phase, q , can be expressed as follows:

$$\frac{\partial}{\partial t} (\alpha_q \rho_q) + \nabla \cdot (\alpha_q \rho_q \vec{U}_q) = \sum_{p=1}^n (\dot{m}_{pq} - \dot{m}_{qp}) + S_q \quad \text{Eq. 4.3}$$

where α_q is the volume fraction of phase q , ρ_q is the density, \vec{U}_q is the mean velocity vector, S_q is the mass source term (e.g. a source of air at the sparger). In Eq. 4.3, \dot{m}_{pq} and \dot{m}_{qp} indicate the mass transfer rate from the p^{th} phase to the q^{th} phase and the mass transfer rate from q^{th} phase to the p^{th} phase, respectively. Since for the gas-liquid modelling of the stirred tanks there is no mass transfer between the different phases, the first term on the right-hand side of Eq. 4.3 is set to zero.

The momentum balance equation for phase q can be expressed as:

$$\frac{\partial}{\partial t} (\alpha_q \rho_q \vec{U}_q) + \nabla \cdot (\alpha_q \rho_q \vec{U}_q \vec{U}_q) = -\alpha_q \nabla p + \alpha_q \rho_q \vec{g} + \nabla \cdot (\alpha_q \mu_q (\nabla \vec{v}_q + \nabla \vec{v}_q^T)) + \alpha_q \left(\mu_T - \frac{2}{3} \mu_q \right) \nabla \cdot \vec{v}_q \mathbf{I} + \sum_{p=1}^n \vec{R}_{pq} + \vec{F}_q + \vec{F}_{lift} + \vec{F}_{vm} \quad \text{Eq. 4.4}$$

where p is the pressure, \vec{g} is the gravity vector, μ_q is the laminar viscosity, μ_T is the turbulent viscosity, \mathbf{I} is the unit vector, v is the phase velocity, \vec{R}_{pq} is the interfacial

force, \vec{F}_q is the external body force (e.g. the Coriolis and the centrifugal force caused by rotation of impeller), \vec{F}_{lift} is the lift force, and \vec{F}_{vm} is the virtual mass force. Reviewing the previous literature for gas-liquid modelling has shown that the influence of the virtual mass force and the lift force on the air bubbles inside the stirred tank is negligible (Lane et al., 2002, Khopkar and Ranade, 2006). Therefore, these two terms in the momentum balance equation are fixed as zero.

In order to formulate the effects of turbulence on the velocity components and the other flow variables, the dispersed mode of the standard k- ϵ turbulence model, available in ANSYS Fluent, is utilized. It is worth remembering that the single-phase modelling results have suggested the application of this model due to its accuracy and inexpensiveness. The dispersed version of the standard k- ϵ model solves a set of transport equation for the turbulent kinetic energy (k) and turbulent dissipation rate (ϵ) for only the primary phase as follows:

$$\frac{\partial}{\partial t} (\alpha_q \rho_q k_q) + \nabla \cdot (\alpha_q \rho_q \vec{U}_q k_q) = \nabla \cdot \left[\alpha_q \frac{\mu_t}{\sigma_k} \nabla k_q \right] + \alpha_q G_{k,q} - \alpha_q \rho_q \epsilon_q + \alpha_q \rho_q \Pi_{kq}$$

Eq. 4.5

$$\frac{\partial}{\partial t} (\alpha_q \rho_q \epsilon_q) + \nabla \cdot (\alpha_q \rho_q \vec{U}_q \epsilon_q) = \nabla \cdot \left[\alpha_q \frac{\mu_t}{\sigma_\epsilon} \nabla \epsilon_q \right] + \alpha_q \frac{\epsilon_q}{k_q} (C_{1\epsilon} G_{k,q} - C_{2\epsilon} \rho_q \epsilon_q) + \alpha_q \rho_q \Pi_{\epsilon q}$$

Eq. 4.6

where Π_{kq} and $\Pi_{\epsilon q}$ shows the impact of air bubbles on the primary phase, q and $G_{k,q}$ is the turbulent kinetic energy production represented by Eq. 3.9. The constants in Eq. 4.5 and Eq. 4.6 including $C_{1\epsilon}$, $C_{2\epsilon}$, σ_k , and σ_ϵ are identical with the model constants for the governing equations of k and ϵ for the single phase modelling (see: Table 3-1).

The term Π_{kq} defines the generation of turbulent kinetic for the liquid phase due to the velocity gradient and it is written as:

$$\Pi_{kq} = \sum_{p=1}^2 \frac{K_{pq}}{\alpha_q \rho_q} (k_{pq} - 2k_q + \vec{v}_{pq} \cdot \vec{v}_{dr})$$

Eq. 4.7

where k_{iq} is the covariance of the velocities for the water phase (q), and the dispersed air bubbles (p), \vec{v}_{pq} is the relative velocity and \vec{v}_{dr} is the drift velocity. For the second unknown term in Eq. 4.6, $\Pi_{\epsilon q}$, the proposed model of Elghobashi (Elghobashi and Abou-Arab, 1983) is applied as follow:

$$\Pi_{\varepsilon q} = C_{3\varepsilon} \frac{\varepsilon_q}{k_q} \Pi_{kq} \quad \text{Eq. 4.8}$$

where $C_{3\varepsilon} = 1.2$. Having closed the transport equations for k and ε , now the turbulent viscosity, μ_T , in the primary phase for Eq. 4.4 can be derived from the following:

$$\mu_T = \rho_q C_\mu \frac{k_q^2}{\varepsilon_q} \quad \text{Eq. 4.9}$$

where the energy dissipation rate for the primary phase is denoted by ε_q and C_μ is a constant equal to 0.09 (ANSYS, 2011a).

As mentioned, using the Eulerian-Eulerian multiphase framework allows users to incorporate the momentum exchange between various phases presented in the computational domain. For the case of gas-liquid modelling inside the stirred tank this is facilitated with an interphase force term in the momentum balance equation (i.e., \vec{R}_{pq} in Eq. 4.4). ANSYS Fluent correlates the interphase force term with the slip velocity between the liquid and gas phases via a fluid-fluid momentum exchange coefficient (K_{pq}) as follows:

$$\sum_{p=1}^2 \vec{R}_{pq} = \sum_{p=1}^2 K_{pq} (\vec{v}_p - \vec{v}_q) \quad \text{Eq. 4.10}$$

where K_{pq} denotes the interphase momentum exchange coefficient, \vec{v}_p and \vec{v}_q are the velocity vectors of the gas and liquid phases, respectively.

The fluid-fluid exchange coefficient can be computed as:

$$K_{pq} = \frac{\alpha_q \alpha_p \rho_p f}{\tau_p} \quad \text{Eq. 4.11}$$

where the volume fraction of the liquid phase, volume fraction of gas phase, density of the gas phase, the drag function and the particulate relaxation time are denoted by α_q , α_p , ρ_p , f , and τ_p respectively. The relaxation time for the air bubbles is computed using Eq. 4.12:

$$\tau_p = \frac{\rho_p d_p^2}{18\mu_q} \quad \text{Eq. 4.12}$$

where d_p is the diameter of the air bubbles in the domain.

The drag function, f , in Eq. 4.11 is usually formulated using a correlation for the drag coefficient (C_D) in conjunction with the relative Reynolds number (Re). The default option in ANSYS Fluent provides the Schiller-Naumann (Schiller and Naumann, 1935) model for the drag function as follow:

$$f = \frac{C_D Re}{24} \quad \text{Eq. 4.13}$$

Schiller and Naumann proposed the following expressions for the drag coefficient correlation:

$$C_D = \begin{cases} \frac{24(1+0.15Re^{0.687})}{Re} & Re \leq 1000 \\ 0.44 & Re > 1000 \end{cases} \quad \text{Eq. 4.14}$$

$$Re = \frac{\rho_q |\vec{v}_p - \vec{v}_q| d_p}{\mu_q} \quad \text{Eq. 4.15}$$

Surveying the previous literature in Chapter 2 for gas-liquid modelling in stirred tanks revealed that firstly the choice of the drag coefficient correlation can significantly vary the numerical predictions for the stirred tank and secondly the Schiller-Naumann model did not necessarily provide the best representation of the drag force between the air bubbles and their surrounding liquid. This can be attributed to the fact that Schiller-Naumann model has been developed for a single spherical object moving in an infinite pool that exhibits a laminar flow regime. However, the gas-liquid inside the stirred tank is experiencing a fully turbulent flow due to the rotating action of the impeller.

In order to enhance the potential of the numerical modelling approaches, various researchers have tried to embody the effect of turbulence eddies on the air bubbles inside the stirred tank via modifying the drag coefficient correlation. This results in several new equations for the drag coefficient. In this study, all the available equations for the drag coefficient correlations are tested to find out the optimized option for developing a CFD based model for the gas-liquid modelling of the standard Rushton turbine flotation tank.

The first expression was introduced by Bakker (Bakker and Akker, 1994), who modified the relative Reynolds number in Eq. 4.15 to entail the turbulence impacts on the dispersed phase within the stirred tank. They added an adjustable fraction of the turbulent viscosity to render a new drag coefficient correlation:

$$Re = \frac{\rho_q |\vec{v}_p - \vec{v}_q| d_p}{\mu_q + C_* \times \mu_T} \quad \text{Eq. 4.16}$$

In Eq. 4.16, C_* is a fixed value which accounts for the decrease in the relative velocity of the dispersed phase when the air bubbles flow in the turbulent flow field of the stirred tank. Bakker applied $C_* = 0.02$ for his numerical simulations; however, this

value can differ based on the conditions simulated to give a better fit to the experimental data.

The third drag coefficient correlation evaluated in this study is induced from the work of Brucato in 1998 (Brucato et al., 1998b). The Brucato expression is based on experimental measurements of the average particle settling velocity under turbulent flow conditions. He included the Kolmogorov length scale to encompass the effect of turbulence on the particles and derived a correlation for the drag coefficient established on the particle/bubble size as follow:

$$\frac{C_D - C_{D0}}{C_{D0}} = K \left(\frac{d_p}{\lambda} \right)^3 \quad \text{Eq. 4.17}$$

where C_{D0} is the drag coefficient in the stagnant liquid, and K is the correlation constant. The Kolmogorov length scale (λ) in Eq. 4.17 can be expressed as:

$$\lambda = \left(\frac{v^3}{\varepsilon} \right)^{1/4} \quad \text{Eq. 4.18}$$

where ε is the turbulent dissipation rate and v is the kinematic viscosity.

Brucato reported the constant to be 8.76×10^{-4} in his study. However, Khopkar in 2006 (Khopkar and Ranade, 2006) suggested a new modification of the Brucato model by reducing the constant to 6.5×10^{-6} .

Lane in 2006 introduced another correlation for the drag coefficient based on the ratio of the slip velocity (U_S) to the particle terminal velocity (U_T). He constructed his model based on the curve fitting of the available experimental stirred tank drag coefficient data from literature. Lane drag coefficient equation is defined as follows:

$$\frac{\overline{C_D}}{C_{D,0}} = \left(\frac{U_S}{U_T} \right)^{-2} \quad \text{Eq. 4.19}$$

where the ratio of U_S/U_T depends on the Stokes number:

$$\frac{U_S}{U_T} = 1 - 1.4Stk^{0.7} \exp(-0.6Stk) \quad \text{Eq. 4.20}$$

The Stokes number can be defined as:

$$St = \frac{\tau_p}{T_L} \quad \text{Eq. 4.21}$$

where τ_p represents the relaxation time for the dispersed phase and T_L is the integral time scale. The particle relaxation time τ_p is calculated by the proposed equation of Bel F'dhila and Simonin (Fdhila and Simonin, 1992):

$$\tau_P = \frac{\rho_p/\rho_q + C_A}{(3/4)(C_{D,0}/d_b)U_T} \quad \text{Eq. 4.22}$$

In Eq. 4.22, C_A is the added mass coefficient with value of 0.5. Due to the large difference between the densities of the liquid phase and the gas phase, Lane assumed $\rho_p \approx 0$ and simplified Eq. 4.22 to the following expression for the relaxation time (Spelt and Biesheuvel, 1997):

$$\tau_P = \frac{U_T}{2g} \quad \text{Eq. 4.23}$$

The turbulent characteristics of the flow field are accounted for with the term T_L in the Stokes number equation. In the Lane proposed equation, this term is calculated based on the ratio of the turbulent kinetic energy (k) over the turbulent dissipation rate (ε) (Fdhila and Simonin, 1992):

$$T_L = 0.135 \frac{k}{\varepsilon} \quad \text{Eq. 4.24}$$

In order to determine the integral time scale, Lane (2006) computed the average value of ε based on the power input for the tank applied in his study. The average value of the turbulent kinetic energy is also calculated based on the average turbulent integral length scale. Hence, the term T_L was based on the mean values of k and ε for the entire tank, in his study. However, a modification is carried out in this study to derive the local values of k and ε for every control volume in the domain at each time step. Therefore, the computed value of the integral time scale in this study may be interpreted as the local turbulent conditions being integrated into the Lane model.

4.3. Results and discussion

The governing equations derived in the previous section are solved to explore the different CFD related issues for the gas-liquid modelling within the standard Rushton turbine tank. The relatively unknown nature of the underlying physics of the flow makes the model's development task an iterative process. The model developer should take into account all the resources of the uncertainties in the model predictions and seek to minimize or eliminate them with the validation against experimental measurements. Therefore, in this section the solutions of the governing equations are compared when different sparger designs implemented for the tank. Moreover, the comparison of the various expressions for the drag coefficient is performed to

determine the equation which exhibits the closest agreement with the experiments. The optimized drag coefficient correlation is then utilized to investigate its potential for the gas-liquid simulations of the stirred tank flow field in a diverse range of operational conditions.

4.3.1. Sparger design

The influence of the sparger configurations for the stirred tank has been solely considered experimentally. For instance the experimental works of Rewatkar et al., (Rewatkar and Joshi, 1991a, Rewatkar and Joshi, 1991b, Rewatkar and Joshi, 1993) where they studied the impact of the geometrical properties of the sparger and its location with respect to the impeller on the liquid mixing time and power consumption. However, the previous works on the numerical modelling of the stirred tank have shown that none of the numerical studies have taken this matter into considerations (see: Chapter 2). Numerically, two methods have been reported for injection of the dispersed gas phase into the computational domain. The first technique utilizes a velocity inlet boundary condition for a certain surface, usually on the shaft, which acts as the sparger. The second procedure uses a solid wall, sometimes mimics the exact geometry of the sparger, inside the domain as the sparger and this wall is usually placed at the mid clearance (i.e., the vertical distance from the impeller to the tank base). A source term of air bubbles (including mass equal to the gas flow rate and three components of momentum) with constant diameter is then prescribed for a zone with one cell-distance from the sparger inside the solution domain. In this way, a pertinent volume of gas phase with 3-dimensional velocity and momentum that corresponds to the gas flow rate and superficial gas velocity is assigned for this region. This method also requires the definition of a sink term to collect the purged gas from the sparger. The sink term is regularly situated at the top of the tank to mimic the atmospheric pressure at this region. The second approach for the gas induction shows more popularity for gas-liquid modelling in the stirred tank due to its solution stability. This strategy is also employed in this section to investigate different sparger systems. It must be remembered that the various sparger assemblies might increase the model uncertainties in the numerical solutions. The sparger design study is therefore intended to minimize the inherent uncertainty and develop a CFD methodology for gas-liquid modelling in stirred tanks that is able to correctly predict the gas behaviour inside the tank.

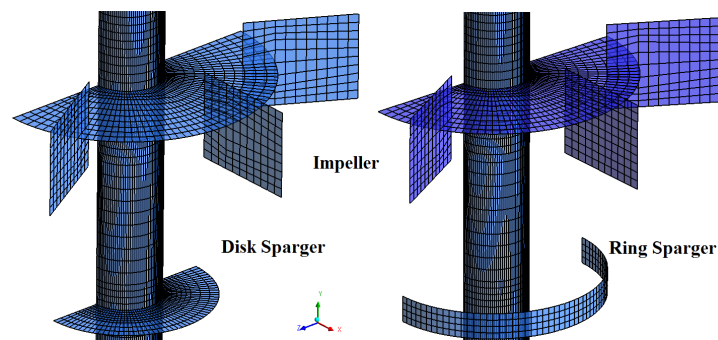


Figure 4-1 Schematic diagram of the ring and disk spargers

In order to achieve this aim, two sparger designs with three different diameters (d_s) with respect to the impeller diameter (D) are explored. Two different angular velocities of the impeller representing the laminar (0 rpm) and turbulent (350 rpm) flow regimes are also investigated. The location of the sparger can be of significant importance. For example, the air bubbles injected from a sparger located close to the impeller might be significantly affected by the centrifugal force of the impeller rotation. The air bubbles, therefore, may not have a chance to be distributed properly in the lower part of the tank. Thus, three different impeller locations including, close to the bottom, at the middle of clearance, and close to the impeller are investigated in this study. Figure 4-1 depicts the typical ring and disk spargers studied located at the mid-clearance. Twelve different cases have tabulated in Table 4-1 where those cases with the ring sparger are named with CR and the disk sparger with CD. The base sparger diameter, $d_s/D = 0.75$, was adopted from the previous literature on the numerical modelling of the gas-liquid inside the standard Rushton turbine tank (Joshi et al., 2011b). However, changes are made to cover different diameters for both types of the sparger configurations.

It is worth noting that in the experimental setup of Newell (Newell, 2006) a 3 mm thickness porous (porosity = 40%) stainless steel plate at the bottom of the tank sparged air bubbles into the flotation vessel. Using this type of sparger for the numerical experiments, however, led to a diverged solution. The divergent behaviour can be explained by the fact that for the simulation of this type of sparger the entire bottom surface of the tank was designated as the source, without the porosity consideration. Hence, to keep the gas flow rate identical to the experiments, the value of the gas velocity was reduced. The small value of the velocity at the inlet (i.e., plate sparger) can therefore be affected significantly by the velocity fluctuations, when it is compared with the designated velocities for the ring or disk sparger with the smaller

surface areas. In other words, a small change in the velocity during the solution of the governing equations generated a significant source of error in the numerical solution of the continuity equation, which eventually resulted in the diverged solution. Attempts to mitigate this problem by using smaller time step size did not show significant improvement.

According to this study, it is however recommended to start the sparger design procedure with the calculation of the total area of sparger on which the air bubbles are being injected. For instance, as Newell applied a plate sparger with 40% porosity and mean pore size of 13 μm , a first practical estimation of the sparger diameter might be derived based on the total available area for the air bubbles on the plate sparger with 40% porosity. This would suggest a diameter ratio of 0.6326. This area can then be used as the basis for constructing various sparger systems for the computational domain.

Table 4-1 Different sparger designs tested in this study

Case No.	Sparger type	ds / D	Angular velocity (rpm)
CR1	Ring	0.50	350.
CR2	Ring	0.50	0.00
CR3	Ring	0.75	350.
CR4	Ring	0.75	0.00
CR5	Ring	1.00	350.
CR6	Ring	1.00	0.00
CD1	Disk	0.40	350.
CD2	Disk	0.40	0.00
CD3	Disk	0.50	350.
CD4	Disk	0.50	0.00
CD5	Disk	0.75	350.
CD6	Disk	0.75	0.00

For testing different sparger designs the MRF method was applied for the impeller modelling. The adequate extensions of the rotational zone to minimize the model uncertainties were obtained from the single-phase modelling findings (see: Chapter 3, sub-section 3-3). The impeller blades were modelled as the moving walls boundary conditions with the relative velocity of zero with regard to the rotational zone angular velocity. However, for the case of laminar flow simulations (i.e., 0 rpm) the stationary wall boundary conditions were prescribed for the blades. The sparger was also assumed to be a wall boundary condition (i.e., no-slip) on which a mass source of air with constant bubble size was located. In order to inject the gas phase through different sparger geometries, bubbles of constant size, taken from the experimentally measured data of Newell, were defined for two different flow regimes

(i.e., $d_b = 1.57$ mm for the turbulent flow and $d_b = 1.70$ mm for the laminar flow). Similar to the single-phase modelling, the symmetrical flow behaviour allowed us to model only half of the tank by using periodic boundary conditions for the side walls. The other boundaries such as the baffles and the tank walls were defined as no slip velocity. The boundary conditions applied are depicted in Figure 4-2.

The solution of the Eulerian-Eulerian framework was started by modelling only water inside the tank. The developed flow of water was then employed as the initialized case for the gas-liquid modelling. Further, for computing the turbulence for the liquid phase, the dispersed k- ϵ turbulence model was selected. ANSYS Fluent was performed on a High Performance Computer (HPC) cluster with 8 nodes and an installed capacity of 2.83GHz processors per node with 16GB of RAM, to solve the governing equations. The SIMPLE scheme coupled the mass and momentum balance equations. Moreover, the discretization of the conservation equations was performed using a second order upwind method, while for the volume fraction equation the QUICK scheme yielded the closest agreement with the experimental data. The iterative process of solving the equations was stopped when the following convergence criteria were satisfied:

- Normalized continuity residuals $< 1 \times 10^{-3}$
- A difference of less than 1% between the final gas holdup value and the average value for the last five seconds of the flow time.

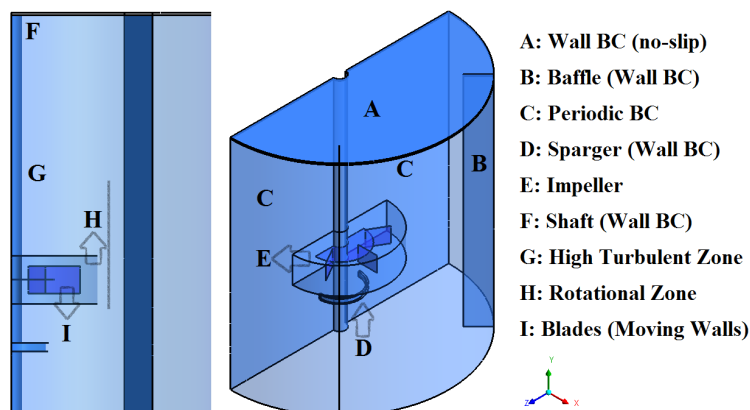


Figure 4-2 Schematic illustration of the laboratory-scale Rushton-turbine flotation tank showing the boundary conditions used in all simulations.

In order to explore the influence of sparger designs on the numerical predictions of the gas holdup, Figure 4-3 displays the CFD results for the (a) ring and (b) disk assemblies. In this figure, the dashed lines represent the predictions for the

ring sparger and the solid lines correspond to the disk sparger. The CFD results have clearly shown that the different sparger designs can noticeably affect the gas holdup predictions. However, this aspect of the gas-liquid modelling has not been addressed in the previous literature. Increasing the diameter of the ring, while the volumetric gas flow rate was held constant, increases the volume average of the gas inside the tank approximately linearly, regardless of the flow regime. However, for the disk sparger arrangements, the increase in the gas holdup predictions reveals a non-linear growth that increases with the impeller speed. This observation can be interpreted by the fact that the gas velocity is reduced to maintain a constant gas flow rate when the cross sectional area of the sparger is increased. Therefore, the lower gas velocity for the air bubbles allows them to remain behind the blades and baffles for more time, thereby increasing the overall volume fraction of gas in the tank.

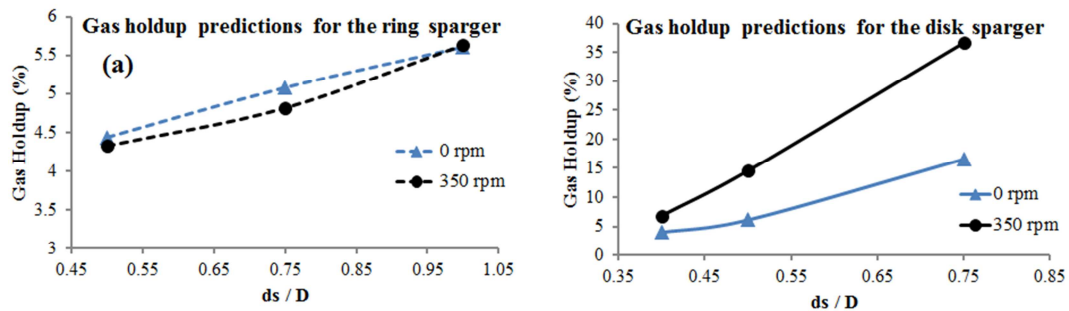


Figure 4-3 Numerical predictions of the gas holdup for different sparger designs (a) ring sparger, (b) disk sparger, under laminar and turbulent flow

The quantitative comparison of the gas holdup predictions with the experimental measurements of Newell (5.2% for 350rpm and 3.7% for 0rpm) shows that the ring sparger with $ds/D = 0.5$ and the disk sparger with $ds/D = 0.4$ match the experiments reasonably well with average difference of 18.4% and 20.1%, respectively. Hence, these two configurations are explored at three different locations comprising close to the tank bottom, mid-clearance and close to the impeller. Table 4-2 summarizes the numerical experiments for two types of sparger systems at different placements with regard to the impeller position. Similar to the previous set of simulations, two different angular velocities of impeller corresponding to the laminar and turbulent flow conditions have been investigated. For both disk and ring spargers the numerical predictions of gas holdup decrease when the sparger placed close to the impeller. This observation was similar for the laminar and turbulent flow regimes. This phenomenon can be explained by the fact that locating the spargers at

the bottom of the tank increases the probability of the air bubbles remaining in the circulation loop at the bottom of the tank, while as the spargers are placed further from the base, the presence of the gas in the lower circulation loop is reduced which decreases the gas holdup values. The percentage of difference between simulated cases and the experimental data demonstrates that the disk sparger generally characterizes the dispersed gas phase better than the ring sparger. In addition, the disk sparger located at the mid-clearance and adjacent to the impeller results in a reasonably good agreement with the measurements. Even though the close-to-impeller disk sparger design seems to produce the lowest percentage of difference with the experiments, the placement of the sparger may reduce the probability of the gas distribution at the lower section of the tank. Therefore, for the future simulations the disk sparger with $ds/D = 0.4$ positioned at the mid-clearance has been chosen.

Table 4-2 Numerical predictions of the gas holdup for two sparger configurations at three different positions

Sparger type	ds / D	Location	Simulations		Experiments		Error (%)
			Angular velocity (rpm)	Gas holdup (%)	Angular velocity (rpm)	Gas holdup (%)	
Ring	0.5	Bottom	350.	4.33	350.	5.20	-16.79
			0.00	4.44	0.00	3.70	19.94
		Mid-clearance	350.	2.55	350.	5.20	-50.99
			0.00	2.62	0.00	3.70	-29.24
			350.	2.24	350.	5.20	-56.92
Close to impeller	0.00	1.80	0.00	3.70	-51.22		
	350.	6.86	350.	5.20	32.00		
Disk	0.4	Bottom	0.00	4.00	0.00	3.70	8.18
			350.	6.41	350.	5.20	23.32
		Mid-clearance	0.00	3.81	0.00	3.70	3.04
			350.	5.28	350.	5.20	1.52
			0.00	3.05	0.00	3.70	-17.63

Two main conclusions can be drawn from the investigation of the different sparger designs for the gas-liquid modelling of the standard Rushton turbine tank. The first findings is that for developing a multiphase CFD methodology the strategy by which the secondary dispersed phase is being injected into the continuous phase will generate uncertainties in the predictions. Hence, one should take into consideration the various possible approaches to distinguish and reduce the model uncertainties caused by the introduction of the second phase in the computational domain. Moreover, for the specific case of laboratory scale Rushton turbine tank investigated in this section, it is found that the disk sparger with the diameter 40% of the impeller

diameter can provide the minimum uncertainties in the predictions of the gas holdup when it is located at the mid-clearance.

4.3.2. Comparison of different drag coefficient correlations

The governing equations derived in sub-section 4.2 have indicated that the continuous phase (i.e., water) and the dispersed phase (i.e., air bubbles) interact through incorporation of the lift, virtual mass and drag forces into the momentum balance equation. As discussed, previous researchers have found that the influences of the first two forces are negligible on the numerical predictions of the multiphase flow, whereas special attention has been concentrated on how to associate the turbulent effects on the air bubbles via modifications of the drag force (Brucato et al., 1998b, Bakker and Akker, 1994, Khopkar and Ranade, 2006, Kerdouss et al., 2006, Lane, 2006, Doroodchi et al., 2008). As a result, new drag coefficient equations have been introduced for the gas-liquid modelling inside stirred tanks. The implementations of the various expressions for the drag coefficient create model uncertainties and cause instabilities in the solutions. Thus, as an important step for developing a comprehensive methodology for the gas-liquid modelling inside the stirred tank, the performance of five different drag coefficient correlations including the standard Schiller-Naumann, Bakker (Bakker and Akker, 1994), Brucato (Brucato et al., 1998b), Khopkar (Khopkar et al., 2006) and Lane (Lane, 2006) at two different impeller velocities, 0 rpm and 350 rpm (corresponding to the laminar and the turbulent flow regimes) are compared. The formulation details and the differences of each drag expressions are articulated in sub-section 4-2. The reason that these formulations have been selected is that they incorporate the effects of turbulence on the air bubbles movements in different methods. Thus, a successful approach for gas-liquid modelling within stirred tanks should be able to capture the influence of turbulent eddies through the manipulation of the drag force.

Figure 4-4 compares the gas holdup predictions, at the laminar flow regime, from four different drag equations as a function of flow time. The symbols in this graph represent the experimental measurements of Newell (Newell, 2006), the dotted line corresponds to the predictions for the Schiller-Naumann model, the solid line to the predictions from the Khopkar model, the dashed-dotted line to the Lane model and the dashed line to the Bakker model. It must be noted that the solution from the Brucato drag coefficient at 0 rpm did not meet the first convergence criteria (i.e., the

normalized continuity residuals $< 10^{-3}$). The CFD results illustrate that the inclusion of the different drag coefficients can significantly vary the gas holdup values. The values of gas holdup predicted by Khopkar drag model (the solid line in Figure 4-4) evidently demonstrate severe fluctuations in the solutions which does not seem to converge to a constant point by advancing the flow time. Hence, the second criterion emphasizing on the trivial variations of the flow variables is not satisfied using this model. This is explainable by the description of the turbulent dissipation rate (ε) in the model. Both Brucato and Khopkar models apply the Kolmogorov length scale to encompass the effect of turbulence on the air bubbles (Eq. 4.17 and Eq. 4.18). An overall average for ε was used to compute the Kolmogorov turbulent scale by Brucato and Khopkar, while in the current study the implemented User Defined Function (UDF) utilizes the local values of the dissipation rates at each grid point to calculate the Kolmogorov length scale. The UDF is also modified to compute the volume average of the turbulent dissipation rate at every time step and import the calculated values for the computation of the Kolmogorov turbulent scale. Simulations of the gas-liquid flow with this method from both the Brucato and Khopkar drag equations did not lead to converged solutions for the laminar flow condition. It infers that using drag coefficient correlations with incorporation of the Kolmogorov turbulent length scale may not be the best representation of turbulence in gas-liquid modelling of the Rushton turbine tank.

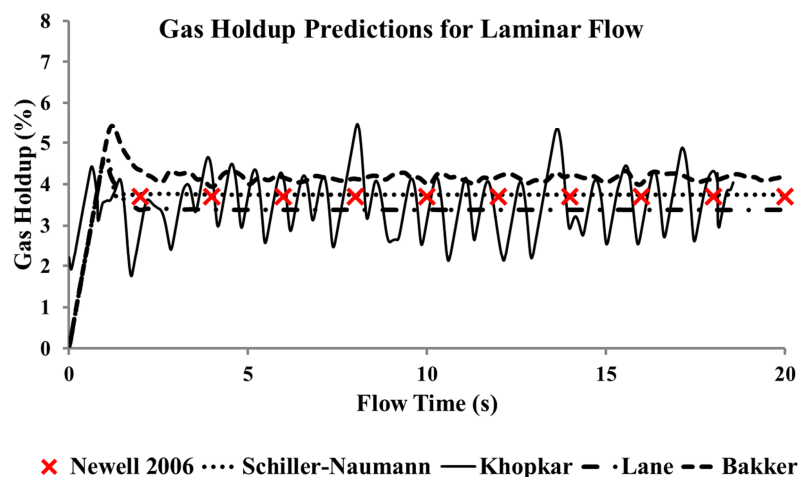


Figure 4-4 Numerical predictions of gas holdup with four different drag coefficient correlations for laminar flow regime inside the standard Rushton turbine tank

However, the other drag coefficient equations with integrating the turbulence impact yield a fair agreement with the experiments. The Bakker model results in an

overprediction of the gas holdup by an average difference of less than 14.9%. Lane drag coefficient correlation, on the other hand, underpredicts the gas holdup only by less than 8.7% difference with the experimental data. The gas-holdup predicted by the standard Schiller-Naumann correlation, however, matches the experimental data very closely, with an average difference of 1.4%. This observation is consistent with the expectation, since, of the various drag coefficient correlations examined, the standard Schiller-Naumann is the only model that has been established for the laminar regime. Therefore, from the comparison of the different drag coefficient correlations for the laminar multiphase regime inside the standard Rushton turbine tank, one may draw this conclusion that the only drag expression without association of the turbulence effect (i.e., Schiller-Naumann) can regulate the drag force between the dispersed air bubbles and the continuous water phase.

As the fluid flow inside the Rushton turbine tank often falls into the turbulent regime, the second set of simulations has focused on the comparison of the mentioned drag coefficient equations when the 350 rpm velocity of the impeller produces a fully turbulent flow inside the tank. Figure 4-5 compares the numerical predictions of the gas holdup as a function of flow time for the turbulent flow of gas-liquid inside the tank. In this figure the symbols show the experimental data of Newell, the dotted line corresponds to the predictions of Schiller-Naumann model, the solid line corresponds to the gas holdup predictions of Khopkar model, the double-parallel lines to the predictions of Brucato, the dashed line to the predictions of Bakker model and the dashed-dotted line to the Lane model. The first implication from this graph is that the predictions from both Brucato and Khopkar models did not show insignificant variations in the value of gas holdup (as seen in the laminar regime). Thus, the solutions from these two models cannot be assumed as converged solutions. The Schiller-Naumann model results in the overprediction of the gas holdup and a poor agreement with 68.7% difference with the experiments is observed. This can be simply attributed to formulation of this drag coefficient correlation, since there is no indication of turbulence in the equations (see: Eq. 4.14 and Eq. 4.15). It is worth pointing out that the choice of Schiller-Naumann model for the drag force was often seen in the previous literatures. Yet, the disagreements with the experiments were interpreted as the lack of either finer mesh or more sophisticated formulations for turbulence model. The CFD predictions of the gas holdup using Bakker and Lane

models demonstrate a fair agreement with the measurements of Newell to within an average difference of less than 48.1% and 25.2% for the Bakker and Lane models, respectively. It can be inferred from the comparison that the influence of turbulent eddies on the drag force should be taken into account for a successful CFD method capable of simulating the gas-liquid flow inside the stirred tank. Of the tested correlations for the drag coefficient the Brucato and Khopkar model resulted in diverged solutions for both laminar and turbulent flow conditions. Thus, these two models should be excluded for the future investigations. The Schiller-Naumann model matched the experimental data for the laminar case; however for the turbulent flow it did not show promising results. The Bakker and Lane models, on the other hand, have performed fairly well for both laminar and turbulent conditions. The proposed drag coefficient equation of Lane has exhibited the best conformity with the experimental measurements of the gas holdup.

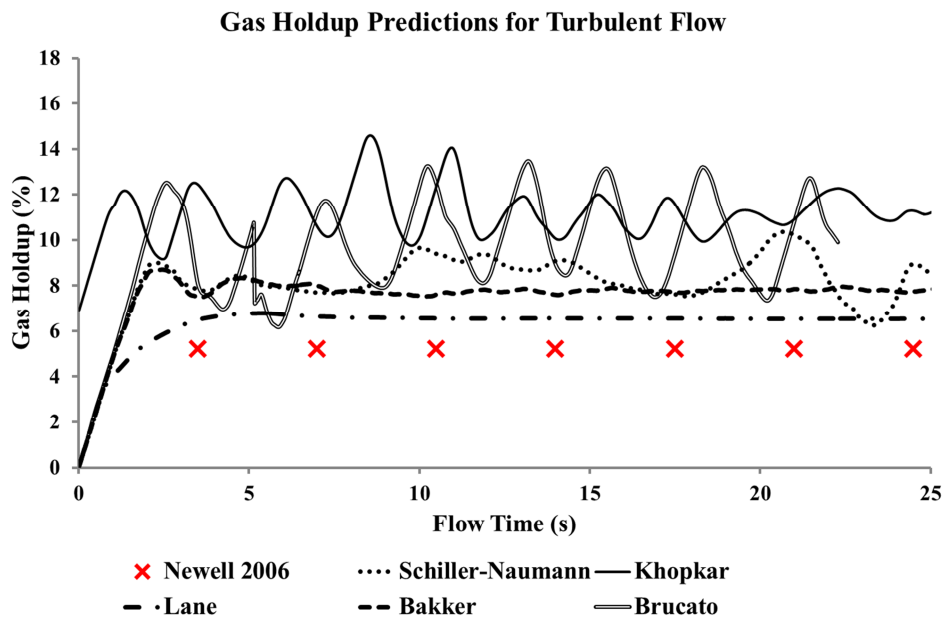


Figure 4-5 Numerical predictions of gas holdup with five different drag coefficient correlations for turbulent flow regime inside the standard Rushton turbine tank

In addition to the prediction of gas holdup value, an effective CFD methodology should be able to simulate the gas flow features inside the tank. In order to gain further insight into the dispersed phase hydrodynamics Figure 4-6 shows the vector plots of the air velocity on a vertical cross-section through the tank produced by the three most stable drag coefficient correlations for the turbulent flow (impeller angular velocity of 350 rpm). Due to the diverged solutions the predictions of Brucato

and Bakker for the air velocity are not included in the figure. In this figure h and r indicate the spatial height and radius of the grid points inside the tank while H and R correspond to the tank height and radius.

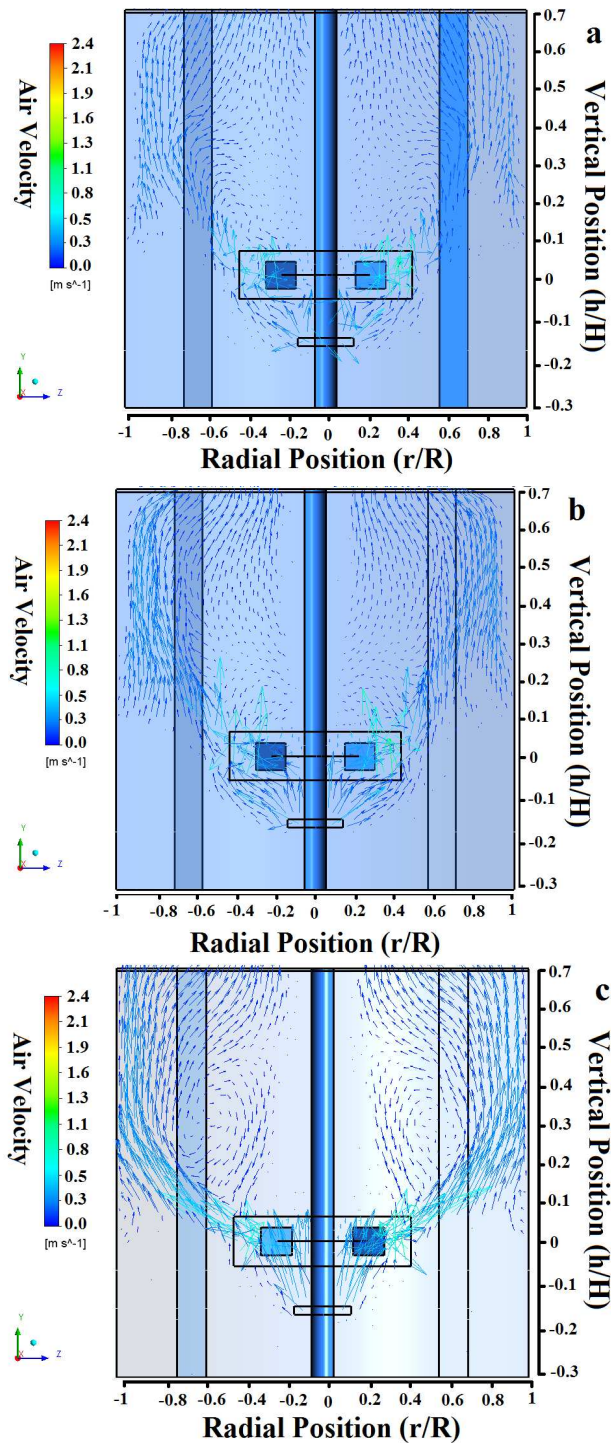


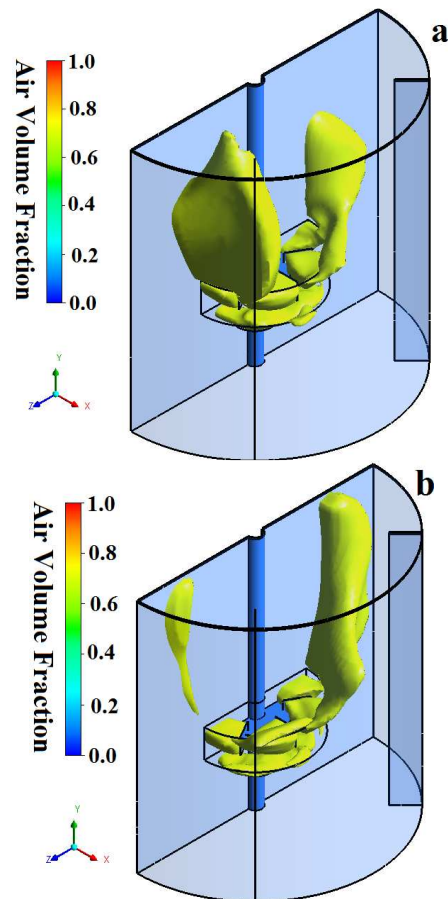
Figure 4-6 Comparison of the air velocity vectors for the drag coefficient correlations at 350 rpm (a) Schiller-Naumann, (b) Bakker, and (c) Lane.

The applied drag coefficients are able to simulate the movement of dispersed air bubbles inside the tank shown in Figure 4-6. For all cases the gas is injected from

the sparger located at the mid-clearance underneath the impeller with a constant bubble diameter (i.e., $d_b = 1.57$ mm). The air bubbles gain an upward movement toward the impeller. Once they enter the rotational zone the turbine rotation forces the air bubbles to accelerate at this zone ($-0.4 < r/R < 0.4$, $-0.05 < h/H < 0.05$). Due to the buoyancy and inertial forces of the gas phase and the exerted centrifugal force from the impeller, the air bubbles eventually leave the rotational zone with a balanced pattern including an inclined path with respect to the impeller blades. The distribution of the air bubbles occurs symmetrically in a zone slightly higher than the rotational zone with the coordination $0.45 < r/R < 0.65$ and $0.05 < h/H < 0.3$. In the bulk flow region ($-1.0 < r/R < 1.0$, $0.2 < h/H < 0.7$), the air bubbles rise up toward the top of the tank mostly due to the buoyancy force and the low impact of the centrifugal force causes the air bubbles to decelerate at this area. It is found that the velocity magnitude predicted by Schiller-Naumann and Bakker model in the bulk flow ($-1.0 < r/R < 1.0$, $0.2 < h/H < 0.7$) are somewhat similar, whereas the Lane's predictions of the velocity at this zone illustrate slightly higher level. Moreover, the air flow pattern confirms the presence of a symmetrical vortex arrangement which is formed near the top of the impeller. The distribution of this vortex varies slightly depending on the drag coefficient correlation used. The Schiller-Naumann and Bakker models capture this vortex pattern close to the rotational zone (within the range $0.3 < r/R < 0.5$, $0 < h/H < 0.15$ for the Schiller-Naumann and $0.2 < r/R < 0.4$, $0.1 < h/H < 0.25$ for the Bakker model), while from the Lane model's predictions, the vortex occurs near the bulk region of the tank (within the range $0.4 < r/R < 0.8$, $0.2 < h/H < 0.4$).

There are no available visual experimental data (such as the gas flow pattern images or PIV data) to validate the simulated fluid flow of the gas phase inside the standard Rushton turbine tank. However, the previously confirmed phenomena for the gas-liquid flow within stirred tanks can be employed to evaluate the performance of the various drag coefficient correlations. The formation of air cavity or the accumulation of the air bubbles behind each impeller blades, for instance, is one of the well-known examples (Bombač et al., 1997, Lane, 2006, Rigby and Evans, 1998). As discussed in Chapter 3, the substantial pressure gradient and the presence of the trailing vortices in this region draw the air bubbles into this zone and form the air cavity. Therefore, in the current study, the correct prediction of the location of gas cavity is selected as a criterion to assess the performance of the different drag

coefficient equations. It should be mentioned that typically there are two methods of accounting for the gas cavity. The first one includes a modification in the drag force formulation for the regions with a critical volume fraction of the gas phase. This method is elaborated by Lane (Lane, 2006), who altered the drag coefficient correlation for the regions within the computational domain with the gas volume fraction higher than the critical value ($> 50\%$). The second approach is based on the computed void fraction inside the domain. In that, the grid cells with the volume fraction of the secondary phase higher than a certain value imply the presence of the accumulated gas. In this study, it is assumed that the regions inside the tank with the air volume fraction equal to or greater than 80% mimic the formation of the ventilated cavity. In order to discern these zones the iso-surfaces of the air phase in which the air volume fraction is equal to or greater than 0.8 are extracted in Figure 4-7.



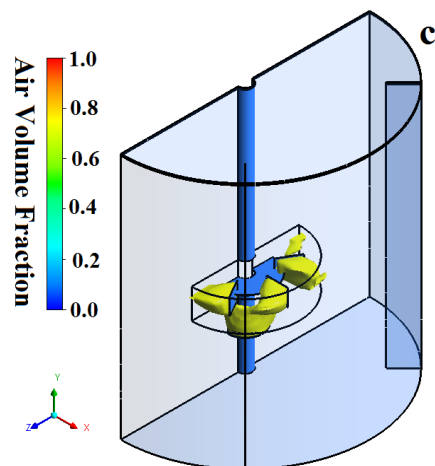


Figure 4-7 Comparison of the air cavity locations for the different drag coefficients at 350 rpm (a) Schiller-Naumann, (b) Bakker, and (c) Lane.

This figure shows that the application of different drag coefficients can significantly affect the simulation of the gas phase. As can be seen, both the distribution of air bubbles and the location of the gas cavity predicted by the various drag equations show different behaviours for different drag coefficient implementations. The high volume fraction of the gas predicted by Schiller-Naumann and Bakker drag coefficient models is found to be in the bulk region of the tank. The Schiller-Naumann drag model predicts, to a certain extent, symmetrical gas accumulation at the bulk region. However, the location of the high volume fraction of the gas phase for the Bakker model is slightly biased to the right side of the tank. In contrast to Schiller-Naumann and Bakker model, under the same conditions, applying the proposed model of Lane for the drag coefficient correlation has led to the accumulation of the gas phase behind the blades. This observation is in line with the expectation and the previously reported results (Ranade and Deshpande, 1999, Lane et al., 2005, Lane, 2006). The results presented here reveal that the drag coefficient correlation of Lane not only yields the closest agreement of the predicted gas holdup with the measurements but also results in an accurate prediction of the location of the gas cavity and the distribution of the air bubbles. The success of this model compared to the alternatives can be described by its more sophisticated formulation to include the effect of turbulent eddies on the air bubble dispersion, as it includes the ratio of the slip to terminal velocity of the particulate phase correlated by the Stokes number.

Further understanding of the observed gas dispersion inside the stirred tank can be obtained by comparison of the vorticity contour plots computed with the different drag coefficient correlations. Figure 4-8 provides the contour plots of the

vorticity magnitude (i.e., the measure of local rotation in the fluid) for the turbulent flow inside the Rushton turbine tank obtained by three drag coefficients. The figure illustrates that the magnitude of the vorticity is changed by the application of various formulations for the drag coefficient. It is also clear that, for all the cases tested, the maximum rotation of the fluid elements occurs in the rotational zone due to the impeller motion. The Schiller-Naumann model reveals a symmetrical vorticity pattern in the bulk flow region. Comparison of Figure 4-7-a and Figure 4-8-a shows a comparable pattern between the gas cavity and the vorticity magnitude at the bulk flow region. From this, it can be concluded that the inaccurate gas accumulation in the bulk region predicted by the Schiller-Naumann model may be associated with the prediction of the vorticity magnitude in the water phase. In other words, the air phase does not have enough kinetic energy to scatter in the liquid phase as rapidly as it does in a well-mixed (turbulent) stirred tank. The contour plots of vorticity predicted by Bakker's model, however, show an asymmetric distribution of vorticity inside the tank. This observation is also comparable with the predicted zones with high volume fraction of the gas phase in Figure 4-7-b. From this comparison one can imply that the uneven distribution of the vorticity on one side of the tank leads to an asymmetric accumulation of the air in the bulk flow region of the tank. This finding suggests that the formulation of Bakker model for the drag coefficient may not adequately represent the influence of the turbulent eddies on the air bubbles. In that, the modification of Reynolds number by including a fraction of turbulent viscosity in Bakker's equation (Eq. 4.16) cannot lead to a precise simulation of the dispersed gas phase hydrodynamics. Comparison of the location of the air cavity in Figure 4-7-c and the vorticity magnitude distribution in Figure 4-8-c, predicted by Lane drag model, follow a very similar symmetrical pattern. The magnitude of the predicted vorticity by Lane model is 43% greater than predicted by the Schiller-Naumann and Bakker models. This high value of vorticity in the vicinity of the impeller blades promotes the rapid dispersion of air at this region and thereby it prevents the formation of air cavities in the bulk region of the Rushton turbine tank which is consistent with the observations reported in previous studies (Ranade and Deshpande, 1999, Lane, 2006).

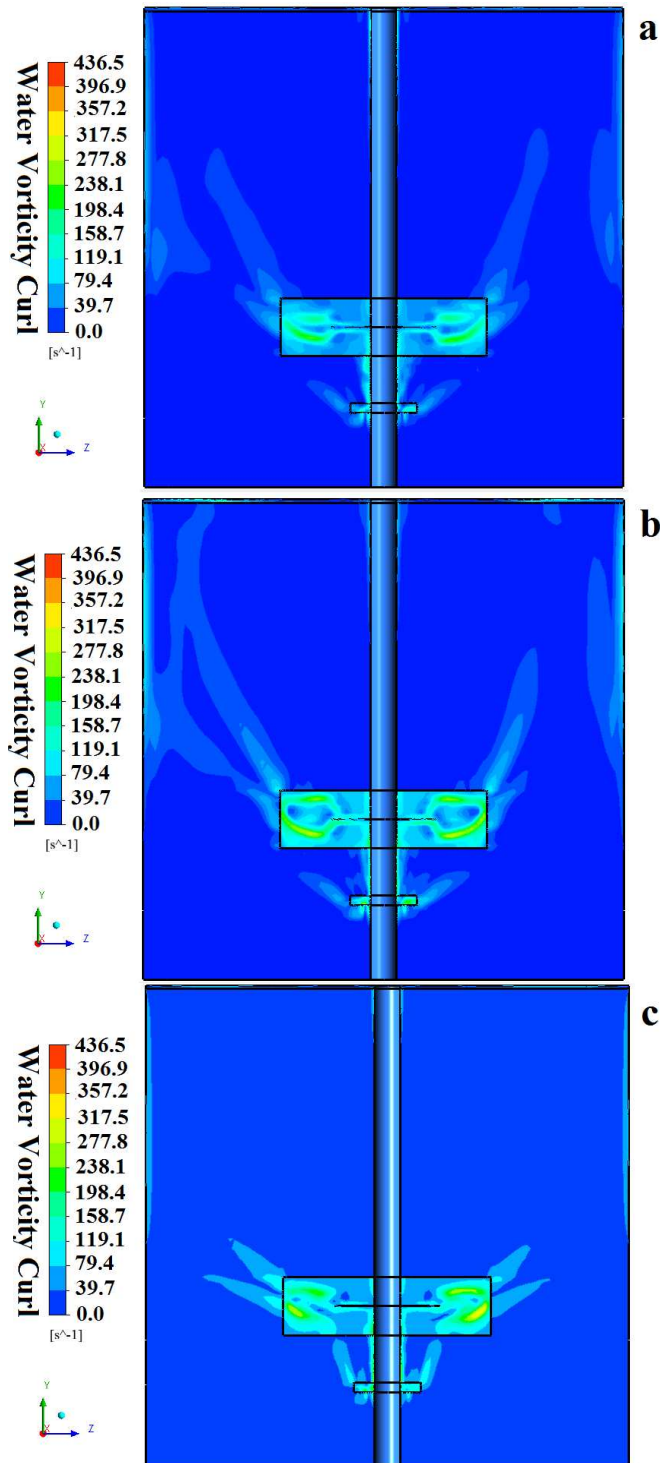


Figure 4-8 Comparison of the vorticity contours for the drag coefficient correlations at 350 rpm (a) Schiller-Naumann, (b) Bakker, and (c) Lane.

4.3.3. Simulations of the gas-liquid flow for different operational and geometrical conditions

The previous section compared five different correlations for the drag coefficient in the gas-liquid modelling of a standard Rushton turbine tank at a constant

gas flow rate and two angular velocities of the impeller. The comparison included the gas holdup, gas flow pattern and the location of the gas cavity inside the tank. The CFD results demonstrate that of the different drag models, the formulation of Lane for the drag coefficient can successfully account for the influence of turbulence on the air bubbles. This correlation, in conjunction with Eulerian-Eulerian framework, leads to the most accurate predictions of the dispersed phase behaviour inside the tank. Lane applied his model for only two different impeller speeds for a tank agitated with a Rushton turbine system. He also applied his drag model for a Lightin 315 impeller type at a constant angular velocity. For both cases very good agreement between the gas holdup predictions and measurements were reported (Lane et al., 2003). It is evident that, although the proposed drag coefficient correlation seems to be successful for the gas-liquid modelling in stirred tanks, there is a lack of numerical experiments to explore the capability of this model under different operational and geometrical conditions. This section is therefore intended to tackle this problem and investigate the application of Lane's drag model for different scales of stirred tanks operating under various impeller speeds and superficial gas velocities. In order to achieve this aim, three different scales Rushton turbine flotation tanks including 2.5 l, 10 l and 50 l tanks are adopted from Newell's work (Newell, 2006), in which he measured the overall gas holdup and bubble sizes under various conditions. The geometrical details of the different domains tested are summarized in Table 4-3.

Table 4-3 Geometrical details of the three different Rushton turbine tanks

Dimension (mm)	Cell Volume (l)		
	2.25	10.0	50.0
Tank diameter (T)	145.	235.	400.
Tank height (H)	145.	235.	400.
Impeller diameter (D)	50.0	80.0	133.
Blade height (D/5)	10.0	16.0	27.0
Blade width (D/4)	12.0	20.0	33.0

The first step to commence the simulations of the gas-liquid inside these stirred tanks is finding the grid independent solution for each of them. For the laboratory scale flotation tank with 2.25 l volume the independent solution from the numbers of cells was achieved in section 3.3.2 in Chapter 3.

The medium tank (i.e., 10 l) was discretized into 170016, 450560, and 838656 cells corresponding to coarse, medium and fine mesh resolutions, while the same grid densities as well as a finer mesh scheme with 1,552,320 cells were applied for the

large tank (i.e., 50 l). For both cases the variations of the solutions were negligible when the cell count reached more than 800,000. Therefore, the fine grid system is used for the gas-liquid modelling of the medium and large tanks. The numerical approach developed in the previous sections (4.3.1 and 4.3.2), including the application of a disk sparger with the diameter equal to 40% of the impeller diameter, along with the Lane drag coefficient is implemented to predict the overall gas holdup inside the tanks. Moreover, the bubble size for all the cases simulated is assumed to be constant over the entire domain, as discussed in section 4.1. The bubble diameters for each simulation are adopted from the measurements of Newell and reported in the last column of Table 4-4. It should be pointed out that for the medium size tank at the angular velocity of 470 rpm the bubble size was assumed to be 0.3 mm.

The gas-liquid flow within the laboratory scale Rushton turbine tank was simulated for four different angular velocities of the impeller, while a range of superficial gas velocities indicating three gas flow rates at the sparger were simulated. The same magnitude of the gas velocity is also used for the medium tank; however three different angular velocities are prescribed for the rotational zone for the medium tank. Finally, the variation of gas holdup inside the large tank is tested with two different rotational speeds and three different gas velocities (Table 4-4).

Table 4-4 Description of the different operational and geometrical conditions tested for the gas-liquid modelling

Case no.	Tank volume (l)	Impeller speed (rpm)	Superficial gas velocity (cm/s)	Bubble diameter (mm)
S1	2.25	350	0.35	1.57
S2		350	0.45	1.69
S3		350	0.55	1.74
S4		450	0.35	1.68
S5		450	0.45	1.74
S6		450	0.55	1.83
S7		550	0.35	1.66
S8		550	0.45	1.75
S9		550	0.55	1.83
S10		800	0.35	1.59
S11		800	0.45	1.71
S12		800	0.55	1.80
M1	10	300	0.35	0.37
M2		300	0.45	0.37
M3		300	0.55	0.38
M4		380	0.35	0.33
M5		380	0.45	0.34
M6		380	0.55	0.35
M7		470	0.35	Not reported
M8		470	0.45	Not reported
M9		470	0.55	Not reported

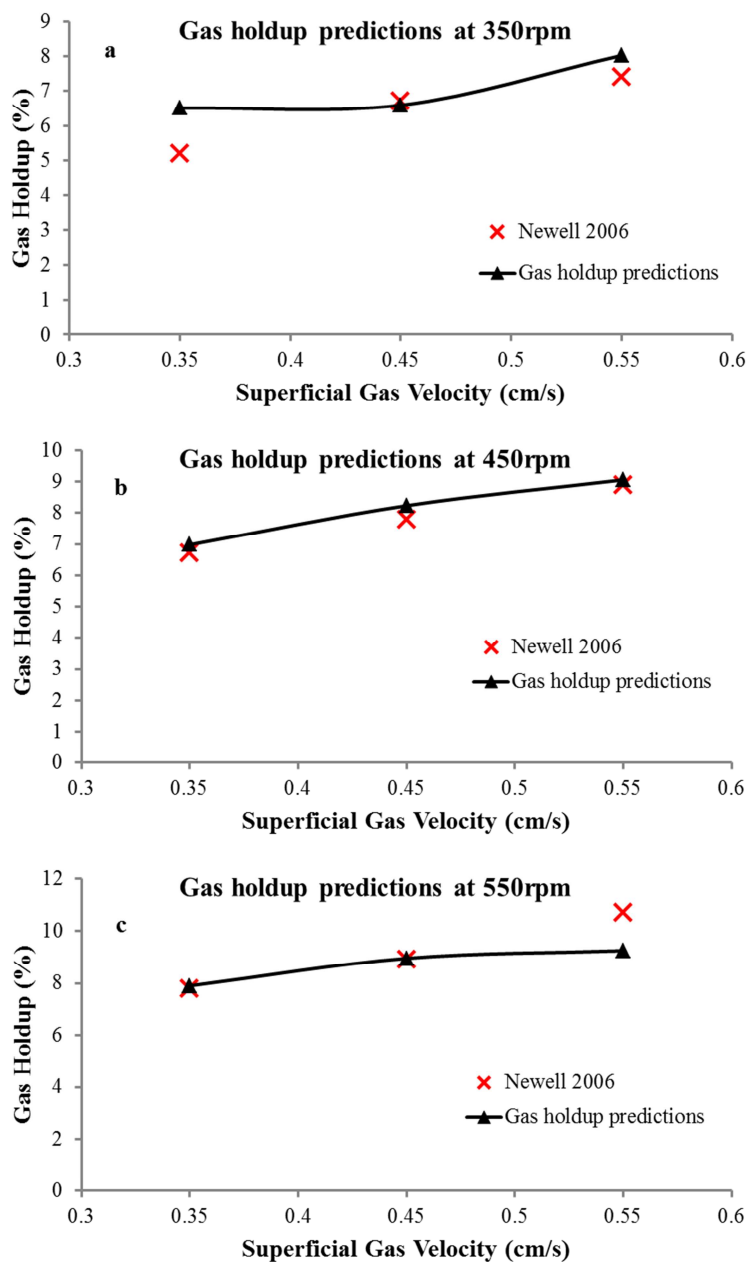
L1		255	0.10	0.38
L2		255	0.17	0.41
L3	50	255	0.35	0.38
L4		330	0.10	0.40
L5		330	0.17	0.41
L6		330	0.35	0.38

The numerical approach that is adopted for the parametric study is identical to the developed methodology whose efficiency was confirmed in sub-sections 4.3.1 and 4.3.2. The established CFD strategy for the gas-liquid modelling is bulleted here:

- Eulerian-Eulerian approach for the multiphase modelling.
- Dispersed k- ϵ model for the turbulence modelling.
- MRF technique for the impeller modelling.
- Lane's drag coefficient correlation for the drag force.
- Uniform air bubbles with constant diameters throughout the domain.
- Source/sink terms for injection/collection of the gas into the domain.
- Periodic boundary conditions to reduce the computational efforts.
- Second order discretization scheme for the momentum equation.
- QUICK discretization scheme for the VOF equation.
- Initialization of the gas-liquid solution with developed flow of water.

The effects of impeller speed on the gas holdup are shown in Figure 4-9. This figure displays the numerical predictions of the gas holdup as a function of superficial gas velocity for the 2.25 l volume tank. The symbols indicate the gas holdup measurements from Newell (Newell, 2006), whereas the solid lines correspond to the CFD results at different impeller speeds. Newell's measurements have shown that increasing the flow rate through the superficial gas velocity increases the gas holdup. For all the impeller speeds, the numerical predictions of the gas holdup demonstrate behaviour similar to the experimental data in that the predicted gas holdup increases with the superficial gas velocity. Quantitative comparison of the computed gas holdup at 350 rpm (Figure 4-9-a) shows that for the low velocity of the gas phase at the sparger, the gas holdup is overpredicted with an average difference of 25.17%. This might be explained by the fact that the lower velocity of the air bubbles may increase their chances of being trapped in the gas cavity, resulting in the overprediction. However, increasing the superficial gas velocity has led to better predictions of the gas holdup value and good agreements with the experiments are found for the gas velocities of 0.45 cm/s and 0.55 cm/s with an average difference of 1.58% and 8.46%,

respectively. Moreover, the overall Root Mean Squared Deviation (RMSD) for the numerical predictions of gas holdup for a range of superficial gas velocities is low enough (i.e., RMSD = 0.84) to establish the credibility of the CFD method. At an angular velocity of 450 rpm the correlation between the experimental gas holdup values and the superficial gas velocity has been correctly captured. Moreover, the numerical predictions match the experimental data very closely to within an average difference of 4.16%, 5.56%, and 1.78% for the gas velocities of 0.35 cm/s, 0.45 cm/s and 0.55 cm/s, respectively and the RMSD = 0.31 for different gas velocities confirms the trustworthiness of the results.



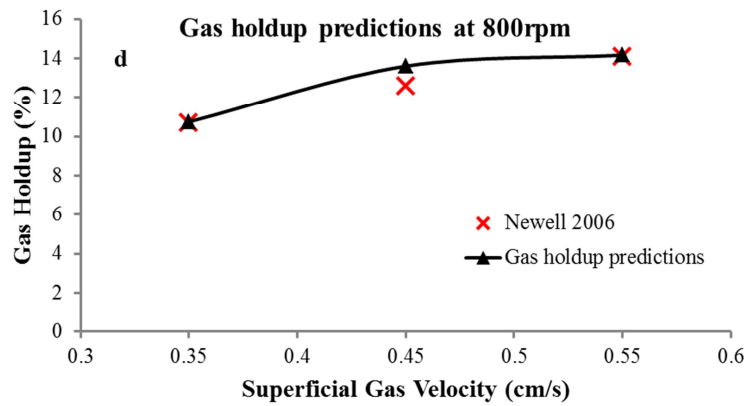
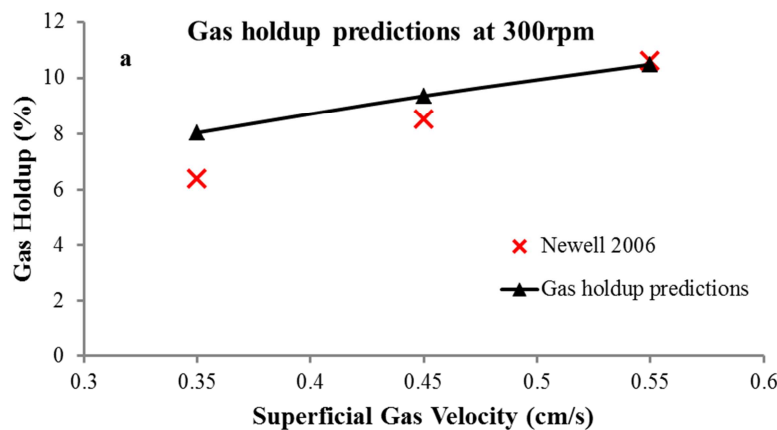


Figure 4-9 Numerical predictions of the gas holdup for the 2.5 l tank at four different impeller speeds (a) 350 rpm (b) 450 rpm (c) 550 rpm (d) 800 rpm as a function of superficial gas velocity

Figure 4-9-c depicts the computed gas holdup for the impeller velocity of 550 rpm. Although for the highest superficial gas velocity (i.e., 0.55 cm/s) the gas holdup has been underpredicted with an average difference of 13.50%, the computed gas holdups for the first two superficial gas velocities (i.e., 0.35 cm/s and 0.45 cm/s) show an almost perfect fit with the measurements, with the error percentage of 1.31% and 0.71% and the overall RMSD of 0.84. The CFD predictions of the gas holdup for the highest angular velocity (Figure 4-9-d) also indicate a satisfactory quantitative agreement with the measurements (with an average difference of 0.46% for the gas velocity of 0.35 cm/s, 7.99% for the gas velocity of 0.45 cm/s and 0.51% for the gas velocity of 0.55 cm/s and overall RMSD of 0.58). Further implications from this set of plots can be extracted by comparing the predicted gas holdup values at a constant superficial gas velocity while the impeller speed is increased. It is evident that the gas holdup increases with increasing angular velocity of the impeller. This means that a higher gas holdup at a constant superficial gas velocity can be obtained by increasing the impeller rotational speed. For instance, at the superficial gas velocity of 0.35 cm/s, as the impeller speed is increased from 350 rpm to 450 rpm and further from 450 rpm to 550 rpm, the computed gas holdup value is escalated from 6.51% to 6.98% and further to 7.90% which is in line with the experiments, too. Increasing the impeller speed from 550 rpm to 800 rpm also results in a 36% growth in the predicted value of gas holdup in the tank. Similarly, the measurements of Newell exhibit a 37% increase in the gas holdup when the impeller speed is altered from 550 rpm to 800 rpm. In addition, the other two superficial gas velocities (i.e., 0.45 cm/s and 0.55 cm/s) have

illustrated a similar behaviour between the gas holdup and the angular velocity of the impeller for both Newell's measurements and the numerical predictions.

Figure 4-10 is a set of plots illustrating the numerical predictions of the gas holdup as a function of superficial gas velocity at three different rotational speeds for the 10 l volume tank. In this figure the symbols display the gas holdup measurements of Newell for the medium tank and the solid lines represent the numerical predictions of the gas holdup predicted by Lane drag coefficient. The measurements show a slight increase in the gas holdup at different impeller speeds when the air flowrate is increased. This increasing trend has been reasonably simulated by the CFD model. It is also observed that increasing the level of turbulence due to increasing both the gas velocity and the angular velocity of the impeller might result in the numerical predictions deviating from the experimental data. This is specifically apparent for Figure 4-10-c. This can be explained by the fact that the application of Lane drag coefficient correlation requires certain level of turbulence to be successful and therefore for a higher gas velocity the influence of the turbulence induced by the gas phase should be introduced using source terms for turbulent kinetic energy and turbulent dissipation rate of the gas phase. In order to confirm this effect, simulations with the gas velocities lower (0.1 cm/s) and higher (0.75 cm/s) than the experimental range, reported by Newell, were also performed. These showed that without inclusion of the source terms for turbulent properties, the model is not able to take into account the correlation between the gas holdup predictions and the superficial gas velocity at the sparger. In other words, the observed disagreement between the numerical predictions and experiments at the highest impeller speed and gas velocity can be improved by including source terms of turbulent characteristics for the Lane model.



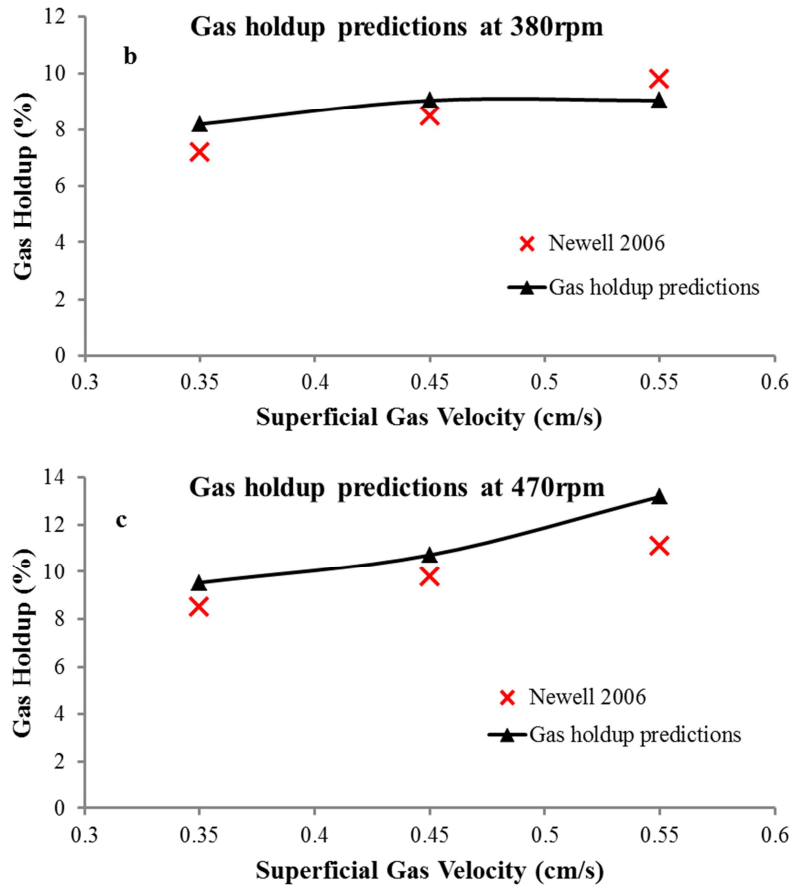


Figure 4-10 Numerical predictions of the gas holdup for the 10 l tank at three different impeller speeds (a) 300 rpm (b) 380 rpm (c) 470 rpm as a function of superficial gas velocity

The quantitative comparison of the gas holdup obtained with the Lane model and the measurements of Newell at 300 rpm shows that increasing the superficial gas velocity enhances the agreement between the predictions and measurements in such a way that the error percentage for the gas velocity of 0.35 cm/s reduces from 25.62% to 10.12% when the gas velocity rises to 0.45 cm/s. The improvement in the accuracy of the numerical predictions continues with increasing superficial gas velocity; at 0.55 cm/s the difference between simulated holdup and measurement reduces to only 1.03%. This observation also shows that a certain level of turbulence is required for the accurate prediction of the gas holdup. In other words, if the gas velocity is low, the level of turbulence induced by the particulate phase is low and the Lane correlation might be less successful. The marginally high RMSD of 1.07 for these predictions can be explained by the level of disagreement for the first gas holdup prediction (computed value at the gas velocity of 0.35 cm/s). The gas holdup computations at 380 rpm, shown in Figure 4-10-b, show a slight increase with the superficial gas velocity. The CFD predictions demonstrate a reasonable similarity with the

measurements, as the computed percentage of differences are 13.86% for the gas velocity of 0.35 cm/s, 6.47% for the gas velocity of 0.45 cm/s and 7.62% for the gas velocity of 0.55 cm/s and the overall RMSD is 0.79. Further, Figure 4-10-c validates the gas holdup predictions computed with the Lane model with the experimental data of Newell at 470 rpm. An acceptable agreement for the different superficial gas velocities is observed which shows average differences of 12.12% for the gas velocity of 0.35 cm/s, 9.29% for the gas velocity of 0.45 cm/s and 18.74% for the gas velocity of 0.55 cm/s. Considering the influence of angular velocity on a constant superficial gas velocity, for example at 0.45 cm/s, it is clear from the experimental data that increasing the impeller speed from 300 rpm to 380 rpm did not significantly vary the value of gas holdup. Further increase from 380 rpm to 470 rpm, however, increases the gas holdup by 15.29% and a similar growth is also observed in the numerical prediction (i.e., 18.34%). The slight disagreement for the higher gas velocity at the highest impeller speed can be explained by the fact that increasing the impeller speed increases the turbulent dissipation level in the tank, which in turn amplifies the Stokes number around the impeller. Taking into account the formulation of Lane drag coefficient (Eq. 4.19 and Eq. 4.20), the drag force will be reduced around the rotational zone, which allows the air bubbles to move toward the sink term with less resistant force in the domain. Therefore, the computed value of gas holdup is less than the expectation.

The predicted gas holdup for the large tank, with 50 l volume, as a function of superficial gas velocity, is displayed in Figure 4-11 for two different impeller speeds. In the figure the symbols represent the experimental measurements of Newell and the solid lines correspond to the CFD computations. Newell's results show that at a constant impeller speed, increasing the superficial gas velocity has led to having higher volume of gas inside the flotation tank. The same qualitative trend has been also observed in the numerical predictions of the gas holdup. The quantitative comparison at 225 rpm, on the other hand, shows only a fair agreement with the experiments to within an average difference of 38.35% for gas velocity of 0.1 cm/s, 26.05% for gas velocity of 0.17 cm/s and 22.99% for gas velocity of 0.35 cm/s. As described, this level of disagreement can be remedied using sources of turbulent kinetic energy and turbulent dissipation rate for application of Lane drag coefficient correlation. This is a potential improving point for Lane drag coefficient that future

work can concentrate on. The agreement between the numerical predictions and the experiments improved for an impeller speed of 330 rpm. It is also found that at 330 rpm the percentage difference between the predictions and measurements is reduced when the flow rate of injected air is increased. The observed percentage of differences are 26.38% for the gas velocity of 0.1 cm/s, 17.57% for gas velocity of 0.17 cm/s and 8.44% for 0.35 cm/s. It is also found that for the large scale tank, increasing the angular velocity of the impeller decreases the overall root mean squared deviation values from 1.61 at 225 rpm to 0.89 at 330 rpm.

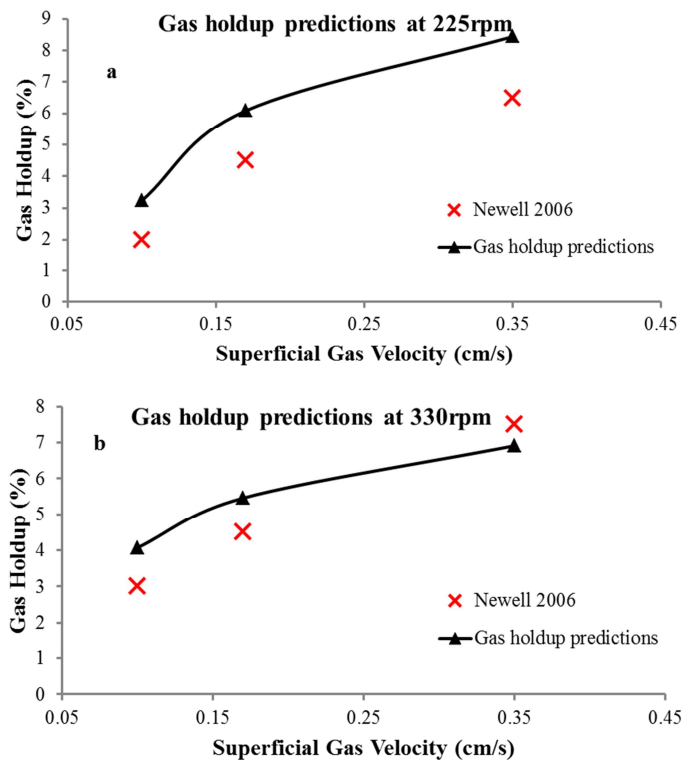


Figure 4-11 Numerical predictions of the gas holdup for the 50 l tank at two different impeller speeds (a) 225 rpm (b) 330 rpm as a function of superficial gas velocity

In summary, the parametric study carried out above has shown that regardless of the size of the flotation tank, the overall amount of the gas phase within the tank increases with the air flow rate and the rotational speed of the impeller. The numerical predictions of the gas holdup facilitated with the Lane drag coefficient correlation have also demonstrated a promising potential for the gas-liquid modelling inside the stirred tanks but with current limitations (see: Appendix B). The CFD outcomes for the small-scale agitated tank exhibit a highly linear correlation between the gas holdup and the impeller speed. This linearity is slightly reduced by increasing the tank's scale, for which the CFD model correctly captures the behaviour. Moreover,

between the operational and geometrical factors, the latter has higher influence on the CFD predictions, since it has been found that increasing the tank's volume results in more discrepancies between the gas holdup predictions and measurements. However, for the small and medium scale tanks the confidence level of the obtained CFD results ensures the engineer to apply the developed CFD methodology and expect to simulate the gas-liquid flow acceptably close to the reality. The simulation of gas-liquid behaviour inside the larger scale flotation tank reveals a fair agreement with the experimental works of Newell. It is worthwhile recalling that simulation of multiphase flows for large scale domains always involves a compromise between the available computational resources and the level of grid refinement. In other words, use of greater computational resources would enable us to use finer mesh resolutions for the large flotation tank, which would improve the CFD prediction of the gas holdup when using the Lane drag coefficient equation. Moreover, it should be noted that the application of Lane drag coefficient correlation for the gas-liquid modelling of stirred tanks at very low or high levels of turbulence might force the user to implement sources of turbulence to regulate the turbulence level inside the tank to enhance the agreement level between the predictions and experiments.

4.4. Conclusion

This chapter has accomplished the development of a multiphase CFD methodology for gas-liquid modelling in stirred tanks. The main aim was to establish a CFD approach which is simultaneously economical and provides accurate insights into the gas-liquid flow features inside the tank. The model was constructed by expanding the single-phase methodology developed in Chapter 3. An Eulerian-Eulerian multiphase model, along with the dispersed k- ϵ turbulence model, was applied to solve the governing equations for the liquid and gas phase. The geometrical changes in the domain included adding a sparger to purge the air bubbles into the tank and a sink region to collect the injected gas. In order to minimize the uncertainties caused by the sparger, two types of sparger configurations (i.e., ring and disk sparger) at various locations with respect to the impeller clearance were implemented in the model. The results showed that the simulated air sparging method can significantly affect the convergence of the numerical solution. However, this aspect of the gas-liquid modelling of stirred tanks has not been reported previously in the literature.

Currently, trial and error is still required to calibrate the sparger effects on the numerical predictions. Also, amongst different methods of introducing the gas phase into the domain the current study has shown that the source/sink method via disk/ring would lead to better representation of the air bubbles behaviours inside the tank compared to using the velocity inlet boundary condition for the gas injection.

Having included the secondary dispersed phase into the computational domain, the Eulerian-Eulerian framework adds the interphase forces to incorporate the interactions between the air bubbles and the liquid phase. Of the various interphase forces, the drag force has been confirmed in literature to be the most influential one for the stirred tank modelling and this finding was accepted in this work. In addition, the turbulent impacts on the air bubbles should be incorporated through the modification of the drag coefficient equations. Therefore, the available drag coefficients with different methods for integration of the turbulence on the air bubbles were compared. Five different drag coefficient correlations, namely the Schiller-Naumann, Bakker, Brucato, Khopkar and Lane models, were implemented via user defined functions in the CFD solver to estimate the gas holdup under laminar and turbulent conditions. The gas holdup predictions for the laminar flow showed that, expectedly, the drag coefficient formulated for the laminar regime in liquid resulted in the best agreement with the experimental data. However, for the turbulent flow regime, only the Lane drag model with a sophisticated methodology to include the turbulence effects on the air bubbles led to an acceptably low discrepancy between the gas holdup predictions and measurements. It also correctly captured the gas flow pattern inside the tank illustrating the formation of the gas cavity behind the impeller blades.

The applicability of the proposed drag coefficient correlation by Lane was evaluated in this chapter when it has been utilized for gas-liquid modelling of 2.5 l, 10 l, and 50 l volume Rushton turbine tanks. A range of operational conditions covering different angular velocities and superficial gas velocities was tested for each tank to investigate the predictive capability of this drag coefficient expression for gas holdup predictions. The results showed that the predicted gas holdup values using the Lane drag model match the experimental data both qualitatively and quantitatively. The modelling of the gas holdup for the small and medium tanks produced good agreement with the experiments, while the fair agreement was observed for the large

scale tank, which can possibly be enhanced by using denser grid resolution. Another possible solution to resolve the disagreement is the application of source terms for the turbulence characteristics. As seen in section 4.3.3 a certain level of turbulence was required for the Lane drag coefficient to successfully predict the gas holdup inside the tank. It should be remembered that for all the simulations performed the air bubble sizes were constant on a per-simulation basis. In this way, even though the air bubbles diameter were constant for the entire computational domain, different operating conditions necessitate the application of various bubble sizes, and these were obtained from Newell's experimental measurements. If experimental data for the bubble sizes are not available, the inclusion of one extra partial differential equation for the bubble number density can provide the predictions of bubble sizes for further simulations. However, this method has not been conducted in the current study due to the computational costs and the availability of Newell's measurements.

Overall, the validated CFD methodology developed in this chapter for gas-liquid dispersion within the stirred tank can provide a practical tool for the primary stages of stirred tanks design. It can also provide reasonably accurate gas holdup predictions (less than 6%, 13%, and 23% for laboratory, pilot and industrial scale Rushton turbine tanks, respectively) under different operational conditions and can generate detailed 3D features of the gas distribution inside the tank. It should be also noted that the supplementary experimental data can be applied to calibrate the CFD model for the specific applications. Moreover, this methodology can serve as the basis to deliver accurate data (including both velocity components and the turbulence properties) for the flotation modelling. In this way, the flotation sub-processes equations can take advantage of the local flow properties from this approach and lead to an advanced modelling technology for the flotation modelling.

Chapter 5 CFD modelling of the flotation sub-processes

5.1. Introduction

In mineral processing industries, flotation has been applied for many years to separate valuable minerals from the gangue based on the differences in the hydrophobicity of the solid particles. In this process, air bubbles collect the hydrophobic particles and transport them to the froth phase where they are skimmed and recovered in a launder. The surface of the valuable minerals can be naturally hydrophobic or gain this characteristic through usage of different chemical reagents (i.e., collectors, regulators and depressant). Either way, an appropriate chemical environment inside the flotation tank is the first step for separation to occur. Once the selective chemical environment for the valuable species has been established, the flotation rate or the rate of removal of the solid particles from the slurry only depends on the hydrodynamic properties of the flotation cell and the mechanical properties of the particles. Of the different hydrodynamic factors inside the flotation cells Arbiter (Arbiter and Harris, 1969) have pointed out that the rotational speed of the impeller and the air flow rate can dictate the dominant hydrodynamics of the flow inside the tank. Moreover, Gorain et al. (Gorain et al., 1995a, Gorain et al., 1995b, Gorain et al., 1996, Gorain et al., 1997) emphasized the effects of the mentioned parameters on the hydrodynamic responses of a flotation cell such as gas holdup, bubble size, superficial gas velocity, and the bubble surface area flux. Having the chemical and hydrodynamic conditions prepared in a flotation cell, the collection of solid particles with air bubbles involves three mechanisms, the bubble-particle collision, bubble-particle attachment, and formation of the bubble-particle aggregate. Detachment of the solid particles and the air bubbles might also take place, a mechanism in which the solid particles detaches from the air bubbles and moves downward to the tank's base reducing the flotation performance.

Initially the solid particles are suspended in the slurry due to the impeller rotation and after purging the dispersed gas phase they approach very closely until the

liquid film surrounding the air bubble reaches its critical thickness, which leads to the drainage and rupture of the liquid around the bubble. The solid-liquid-gas contact line will slide upon the air bubble surface toward the lower section of the air bubble. This sequence is known as the attachment phenomenon between the hydrophobic particles and the dispersed air bubbles. As a result of the attachment process, the bubble-particle aggregate will be formed and if the aggregate contains enough buoyancy energy, it will rise up toward the froth phase. Detachment can happen during the path due to the high turbulence in the bulk flow region of the tank.

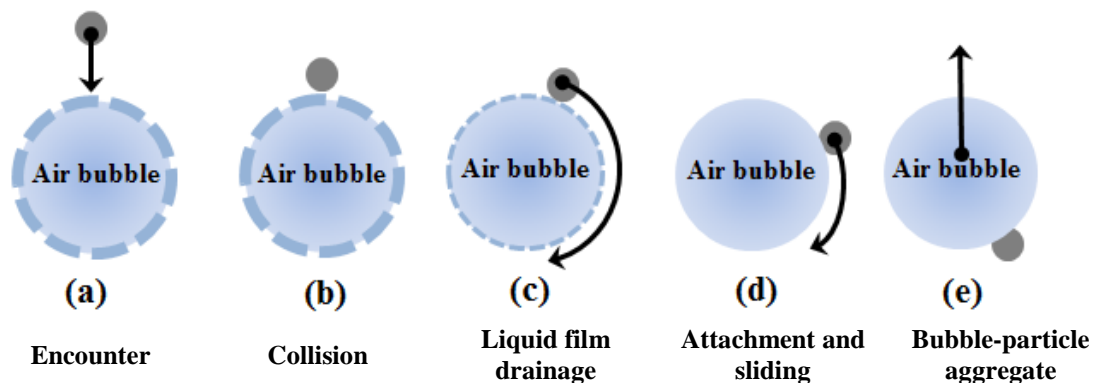


Figure 5-1 Schematic representation of the flotation sub-processes

The schematic illustration of the flotation sub-processes is depicted in Figure 5-1 where the light blue circle represents the air bubble, the thick dashed line corresponds to the liquid film encompassing the air bubble and the small dark circle displays the solid particle. As described, at the first stage they approach (a) until the collision occurs (b). The intervening liquid film commences to thin out leading to the film rupture, while the solid particle slides over the bubble's surface (c). The solid-liquid-gas interface moves on the surface of the air bubble and at a stable position they establish a bubble-particle aggregate (d and e).

Because of the various micro scale phenomena occurring in a flotation cell, King (King, 2001) emphasised the difficulties in the modelling of the flotation process. He has, however, suggested that a successful predictive model for the flotation separation should be initiated based on the theory that assumes the separation in the flotation cell is a first order rate kinetic process. Hence, he recommended a general format for the transfer rate of particles from the slurry to the bubble phase (see: Eq. 2.2).

The conservative form of the macro scale kinetic model for flotation separation is written as (Jameson et al., 1977, Duan et al., 2003):

$$\frac{dN_p}{dt} = kN_p = -Z_{pb}E_{coll} \quad \text{Eq. 5.1}$$

where k is the flotation rate constant, N_p is the number of particles, Z_{pb} is the number of bubble-particle collisions and E_{coll} is the performance of collection of particles with the air bubbles.

In order to integrate the influence of the micro scale occurrences in the flotation model (i.e., collision, attachment, and detachment) Derjaguin and Dukhin (Dukhin et al., 1974, Derjaguin and Dukhin, 1993, Dukhin et al., 1995) have separated the collection efficiency in Eq. 5.1 (i.e., E_{coll}) into three probability functions evaluating the collision, attachment and detachment efficacies.

$$E_{coll} = E_c \times E_a \times E_s \quad \text{Eq. 5.2}$$

In this equation the performance of the bubble-particle collision, attachment and stability are represented by E_c , E_a , and E_s , respectively. Thus, a successful quantitative model for the flotation separation process should follow Eq. 5.1 to describe the kinetic aspects of the flotation (i.e., macro-modelling), while at the same time the efficiency of the bubble-particle collection in the cell should be comprised by pertinent equations for the flotation sub-processes (i.e., micro-modelling). According to this principle, a considerable amount of research has been carried out to derive formulations in which the three flotation sub-processes are correlated with the cell hydrodynamics and operational conditions inside the cell. The most influential studies in this field have been reviewed in sub-section 2.6 in Chapter 2. However, one might argue that in all of these modelling approaches the fluctuating hydrodynamic characteristics of the flow have been simplified by use of either correlations or spatially invariant flow parameters. This might lead to uncertainties on the representation of a varying phenomenon such as flotation by the assumption of constant values for the hydrodynamic properties of the fluid flow.

Since during this chapter a property-based flotation model due to Pyke (Pyke, 2004) for the flotation rate constant has been applied and incorporated with the CFD data, the next sub-section summarizes the mathematical background of this model. Nevertheless, the aim of the current study is not to replicate the details of all the

various expressions for the flotation sub-processes on which other references have already reported (Dai, 1998, Dai et al., 2000, Pyke, 2004).

The fundamental flotation model as implemented by Pyke is applied into an Eulerian-Eulerian multiphase framework in order to develop a CFD approach that is able to predict the flotation rate constant. The predictive capability of the CFD-kinetic model is then verified by an exploratory study on the impact of the hydrodynamic parameters such as the impeller speed, superficial gas velocity, and the air bubble velocity on the computed values of the flotation rate constant.

5.2. Fundamental flotation model due to Pyke

The basis for the derivation of model used by Pyke starts from the expression of Schulze and Amand for the rate of particle transfer (Schulze, 1989, Julien Saint Amand, 1999) where the removal rate of particles relates to the flotation rate constant:

$$\frac{dN_p}{dt} = -zN_pN_bE_{coll} = -kN_p \quad \text{Eq. 5.3}$$

N_p and N_b are the numbers of particles and bubbles in the cell and z , which is known as the bubble-particle collision kernel, can be specified as:

$$z = \frac{Z_{pb}}{N_pN_b} \quad \text{Eq. 5.4}$$

By substituting Eq. 5.4 into Eq. 5.3 we can derive an expression for the flotation rate constant based on the number of bubble-particle collision rate per unit volume per unit time:

$$k = \frac{Z_{pb}}{N_p} E_{coll} \quad \text{Eq. 5.5}$$

Pyke applied Abrahamson's equation for the bubble-particle collision rate, which appeared as Eq. 2.3 in Chapter 2 and is repeated here for convenience:

$$Z_{pb} = 5.0N_pN_b \left(\frac{d_p+d_b}{2} \right)^2 \sqrt{\bar{U}_p^2 + \bar{U}_b^2} \quad \text{Eq. 5.6}$$

where Z_{pb} is the bubble-particle collision rate ($\text{m}^{-3} \text{s}^{-1}$), N_p and N_b are the particle and bubble number concentrations (m^{-3}), d_p and d_b are particle and bubble diameters (m), \bar{U}_p^2 and \bar{U}_b^2 are the average velocities of particle and bubble relative to water (m s^{-1}).

Schubert (Schubert and Bischofberger, 1998) suggested Eq. 5.7 to compute the root mean squared velocity of particles and bubbles relative to the liquid phase:

$$\sqrt{\bar{U}_i^2} = \frac{0.33\varepsilon^{4/9}d_i^{7/9}}{\nu^{1/3}} \left(\frac{\rho_i - \rho_f}{\rho_f} \right)^{2/3} \quad \text{Eq. 5.7}$$

where ε is the energy dissipation rate, d_i is the bubble/particle diameter, ρ_i is the bubble/particle density, ρ_f is the fluid density and ν is the fluid kinematic viscosity.

In the derivation of a property-based model, Pyke assumed that in a flotation cell the magnitude of the bubble diameters are significantly greater than those of the particle diameters (i.e., $d_b \gg d_p$ which is less applicable for the flotation of coarse particles). Hence, he neglected the effect of the two terms representing the particle conditions in Eq. 5.6 and Eq. 5.7 entailing the particle diameter (d_p) and the root mean squared velocity of the particle relative to the water (i.e., \bar{U}_p^2). The final equation for the bubble-particle collision rate is, consequently, written as:

$$Z_{pb} = 5N_p N_b \left(\frac{d_b}{2} \right)^2 \left[\frac{0.33\varepsilon^{4/9}d_i^{7/9}}{\nu^{1/3}} \left(\frac{\rho_p - \rho_f}{\rho_f} \right)^{2/3} \right] \quad \text{Eq. 5.8}$$

Replacing the bubble-particle collision rate in Eq. 5.5 with Eq. 5.8, the flotation rate constant may be revised in the form of:

$$k = 5N_b \left(\frac{d_b}{2} \right)^2 \left[\frac{0.33\varepsilon^{4/9}d_i^{7/9}}{\nu^{1/3}} \left(\frac{\rho_p - \rho_f}{\rho_f} \right)^{2/3} \right] E_{coll} \quad \text{Eq. 5.9}$$

Pyke presumed that all the air bubbles have spherical shape with a uniform diameter in a cell and for a given gas flow rate (G_{fr}), the number of bubbles per unit time and volume can be computed by:

$$N_b = \frac{6G_{fr}}{\pi d_b^3 \cdot V_r} \quad \text{Eq. 5.10}$$

where V_r is the reference volume.

In order to include the residence time (t_r) in the cell, a turbulent velocity factor (u_i) was added in Eq. 5.9 based on the works of Amand, and Jordan and Spears (Julien Saint Amand, 1999, Jordan and Spears, 1990):

$$t_r = \frac{1}{u_i} \quad \text{Eq. 5.11}$$

Thus, the final format of the fundamental flotation model derived by Pyke for the flotation rate constant may be written as:

$$k = \frac{7.5}{\pi} \frac{G_{fr}}{d_b V_r} \left[\frac{0.33 \varepsilon^{4/9} d_b^{7/9}}{v^{1/3}} \left(\frac{\rho_p - \rho_f}{\rho_f} \right)^{2/3} \frac{1}{u_i} \right] E_c \cdot E_a \cdot E_s \quad \text{Eq. 5.12}$$

In this equation, the bubble-particle collision, attachment and stability efficiencies are denoted by E_c , E_a , and E_s , respectively. The benefit of this equation is that the flotation rate constant is the product of three factors. The first factor, $\frac{7.5}{\pi} \frac{G_{fr}}{d_b V_r}$, takes into account the mechanical features of the flotation cell by having the gas flow rate and the volume of the apparatus. The second term, $\left[\frac{0.33 \varepsilon^{4/9} d_b^{7/9}}{v^{1/3}} \left(\frac{\rho_p - \rho_f}{\rho_f} \right)^{2/3} \frac{1}{u_i} \right]$, acts as a turbulence indicator within the tank. The turbulent dissipation rate, ε , demonstrates a rate at which the smallest turbulent eddies convert the kinetic energy inside the cell into the thermal energy, while the residence time is expressed by the average velocity of bubble in the turbulent flow. The last term, $E_{coll} = E_c \times E_a \times E_s$, comprises the micro processes occurring between the solid particles and air bubbles in the tank. In other words, the derived model for the flotation rate constant as implemented by Pyke embodies macro and micro scale phenomena inside a flotation tank. The closure for this model can be achieved by formulating the flotation sub-processes. Pyke closed the fundamental equation with the Generalized Sutherland Equation (GSE) for the collision efficiency (Dai, 1998), Dobby and Finch model (Dobby and Finch, 1987) for the attachment efficiency and the proposed model of Schulze for the stability of the bubble-particle aggregates (Schulze and Dobias, 1993). The current study uses the same combination of the equations for the sub-processes modelling, similar to the works of Pyke and Newell, since they showed that this combination produced an acceptable prediction of their experimental data (Pyke et al., 2003, Pyke, 2004, Newell, 2006).

The Generalized Sutherland Equation (GSE) is used to compute the collision efficiency between the air bubbles and solid particles. This equation is developed by incorporating the interception and inertial forces exerted on the solid particles. Dai (Dai, 1998) reported a good agreement with experiments when the GSE was used to determine the collection efficiency for the individual bubble of diameter 0.77mm under pH = 5.6 with bubble velocity of 31.6 cm/s. However, Pyke added a cautionary note when this equation is used for the turbulent flow. The Generalized Sutherland Equation can be expressed as:

$$\frac{E_{c-GSE}}{E_{c-SU}} = \sin^2 \theta_t \exp \left[3K_3 \cos \theta_t \left(\ln \frac{3}{E_{c-SU}} - 1.8 \right) - \frac{9K_3 \left(\frac{2}{3} + \frac{\cos^3 \theta_t}{3} - \cos \theta_t \right)}{2E_{c-SU} \sin^2 \theta_t} \right] \text{Eq. 5.13}$$

$$E_{c-SU} = \frac{3d_p}{d_b} \text{Eq. 5.14}$$

The maximum collision angle, θ_t , can be calculated from:

$$\theta_t = \sin^{-1} \left[2\beta \left(\sqrt{1 + \beta^2} - \beta \right) \right]^{\frac{1}{2}} \text{Eq. 5.15}$$

where β shows the significance of interception and inertial forces on the collision rate, which can be written as:

$$\beta = \frac{4 \times E_{c-SU}}{9K_3} \text{Eq. 5.16}$$

and K_3 is calculated by:

$$K_3 = \frac{4v_b(\rho_p - \rho_f)}{9\eta d_b} \text{Eq. 5.17}$$

where η is the dynamic viscosity and v_b is the velocity of bubble.

The second flotation sub-process in Eq. 5.12, the attachment efficiency, E_a , is formulated based on the work of Dobby and Finch (Dobby and Finch, 1987). They introduced a collision angle, θ_a , for which the sliding time (i.e., the time that particle slides over the bubble surface) and the induction time (i.e., the required time for attachment) are identical. Dobby and Finch suggested that the ratio of the collision angle over the maximum collision angle can interpret the efficiency of the attachment:

$$E_{a-DF} = \frac{\sin^2 \theta_a}{\sin^2 \theta_c} \text{Eq. 5.18}$$

The collision angle can be obtained by:

$$\theta_a = 2 \arctan \exp \left[-t_{ind} \frac{2(v_p + v_b) + (v_p + v_b) \left(\frac{d_b}{d_p + d_b} \right)^3}{d_p + d_b} \right] \text{Eq. 5.19}$$

where t_{ind} is the induction time, v_p is the particle velocity and v_b is the bubble velocity. Since in a flotation cell the bubble diameter is often larger than the particle diameter and due to the exerted buoyancy force, the magnitude of the bubble rising velocity is greater than the particle velocity, one can simplify Eq. 5.19 by ignoring the velocity of the particle inside the vessel. Further, the induction time has been experimentally correlated with the particle size as follow:

$$t_{ind} = Ad_p^\beta \quad \text{Eq. 5.20}$$

where the constants A and β can be attained using curve fitting to the available experimental data. The value of $\beta = 0.6$ has been recommended by Dai (Dai et al., 1999). He also showed that this value is less sensitive to the particle size. The A value, on the other hand, showed dependency on the contact angle of the solid particle to the air bubble (i.e., θ), Eq. 5.21 has been applied by Pyke to calculate this term:

$$A = 0.028 \left(1 + \frac{1}{\sin \theta_r} \right) \quad \text{Eq. 5.21}$$

The final term in Eq. 5.12, the bubble-particle stability efficiency, E_s , is expressed as the ratio of the attachment forces over the detachment forces. A particle remains attached to the bubble if the sum of all the stress forces exerted on the particle is lesser than the attachment forces. Schulze (Schulze and Dobias, 1993) has formulated this force balance with the help of Bond number:

$$E_s = 1 - \exp \left(1 - \frac{1}{B_o} \right) \quad \text{Eq. 5.22}$$

where the Bond number can be calculated by:

$$B_o = \frac{d_p^2(\Delta\rho g + \rho_p a) + 1.5d_p(\sin 2\omega)f(d_b)}{|6\sigma \sin \omega \sin(\omega + \theta)|} \quad \text{Eq. 5.23}$$

and

$$f(d_b) = \left(\frac{4\sigma}{d_b} - d_b\rho_f g \right) \quad \text{Eq. 5.24}$$

In this equation σ is the surface tension and ω can be determined from the contact angle:

$$\omega = \left(180 - \frac{\theta_t}{2} \right) \quad \text{Eq. 5.25}$$

The only term in the Bond equation that relates to the turbulent characteristics of the flow is a defining the detachment forces as follows (Hui, 2000):

$$a = 29.6 \frac{\varepsilon^{2/3}}{\left(\frac{d_b + d_p}{2} \right)^{1/3}} \quad \text{Eq. 5.26}$$

The property-based model used by Pyke for calculating the flotation rate constant utilizes the above equations for modelling of the flotation sub-processes. In this way a system of closed equations is achieved by which the transfer rate of the solid particles within a flotation tank is correlated with the three underlying

characteristics of the flotation separation involving the mechanical aspects of the cell, the hydrodynamic features of the turbulent flow, and finally the micro phenomenon between the solid particles and the air bubbles inside the tank. Although the capability of this set of equations has been verified and it has also been used to explore the influence of the different factors on the flotation performance (e.g. Pyke (2004) and Newell (2006) works), there exist potential enhancement points where the modelling method can take advantage of the detailed information of the fluid flow to deliver a better description of the flotation separation process. As discussed, CFD techniques elucidate the fluid flow in temporal and spatial scales. In that, the flow variables from the turbulent flow inside the flotation tank can be attained and then implemented into the kinetic-based flotation model due to Pyke to improve the overall predictive capability of the modelling approach. Scrutinizing the set of equations proposed by Pyke, one may recognize that the hydrodynamic indicator of the fluid flow in Eq. 5.12 (i.e., $\left[\frac{0.33 \varepsilon^{4/9} d_b^{7/9}}{\nu^{1/3}} \left(\frac{\rho_p - \rho_f}{\rho_f} \right)^{2/3} \frac{1}{u_i} \right]$) as well as the sub-processes' equations can be benefited from the local values obtained by CFD. Therefore, the main scope of this chapter is to equip the CFD solver for the calculation of the fundamental equation of Pyke for the flotation rate constant, while the local values of the hydrodynamically significant parameters are being implemented in the flotation modelling equations.

5.2.1. Limitations and simplifying assumptions in the fundamental flotation model due to Pyke

The fundamental flotation model used by Pyke for the flotation rate constant has been derived in the previous sub-section. In this equation the rate constant is a function of collision frequency, and probabilities of attachment and detachment. In Eq. 5.12, E_c considers the hydrodynamic effects during the impact of solid particles to air bubbles, E_a takes into account whether the collisions result in successful attachments and E_s is an inverse probability of detachment. The reminder of Eq. 5.12 is a form of collision frequency which relates the number of bubble-particle collision to mechanical features of the tank as well as the turbulent characteristics of the slurry phase. As mentioned in the previous section, Pyke applied the GSE, Dobby and Finch, and Schulze models for the probabilities of collision, attachment and detachment, respectively. This sub-section is, thus, intended to discuss and address the limitations and assumptions of the flotation model used by Pyke for the flotation rate constant.

Gaudin (Gaudin, 1932) initiated the collision theory for encountering the hydrophobic particles with bubbles inside the flotation vessel. Supporting evidence for this theory was also provided later (Bogdanov and Filanovski, 1940, Sutherland, 1948). Sutherland (Sutherland, 1948) suggested that due to the level of complexities involved in the collision process only essential features should be comprised in a mathematical expression for the bubble-particle encounter. He proposed three simplifying assumptions for the collision modelling including:

- The particles are massless and their velocities are identical to the fluid velocity (i.e., the particles follow the streamlines of the fluid phase).
- The solid particles and air bubbles are assumed to be rigid spheres.
- The air bubble Reynolds number is larger than 1 (i.e., potential flow).

According to Sutherland, if the distance between the particles and air bubbles is reduced to a critical collision radius, R_c , the collision is more likely to occur. The basis for R_c is founded on the critical streamlines of a fluid past from a line of motion of the spherical air bubble.

$$R_c = \left(\frac{3d_b d_p}{4}\right)^{1/2} \quad \text{Eq. 5.27}$$

Therefore, the collision efficiency depends on the geometrical characteristics of the solid particles and air bubbles and it is defined by Eq. 5.14 (or Sutherland collision efficiency). Although the applicability of Eq. 5.14 is straightforward and only necessitates the diameters of particle and bubble to compute the collision efficiency, Dai et al., (Dai et al., 1998) showed the importance of the particle inertia on the collision. They suggested that the particle inertia can decrease the collision efficiency below a critical Stokes number. Thus, for coarse particles where the influence of the particle inertia is more evident, the Sutherland equation tends to overestimate the collision efficiency. In addition, Yoon (Yoon and Luttrell, 1989, Yoon and Jordan, 1991) limited the application of Eq. 5.14 for flotation systems in which the air bubble diameter is smaller than 100 μm . Furthermore, in Sutherland equation it was assumed that once the bubble-particle distance is below R_c the collision takes place, regardless of how the solid particle approaches to the air bubble. However, later this assumption was modified by introducing of a maximum collision angle to account for the non-uniform collisions of the solid particles on the air bubbles (Dai et al., 1998, Nguyen-Van, 1994).

The bubble surface mobility and the particle inertia effects on the bubble-particle collision were further discussed by Dai (Dai, 1998). As mentioned, these two factors were neglected in the work of Sutherland. Nevertheless, experimental measurements of bubble rising velocities showed higher terminal velocity of the air bubble in clean water compared to the contaminated water demonstrating the influence of surfactant or water impurities on the mobility of bubble surface (Leja, 1982, Dai, 1998). Dai showed that for the potential flow in a laboratory scale flotation tank, where the bubble size is in the range of $0.5 \text{ mm} < d_b < 2 \text{ mm}$, the mobile bubble surface is a valid assumption and it also enhances the collision efficiency. Moreover, he argued that the mobilization of the air bubble surface increases the bubble-particle attachment due to the increasing impact on the film drainage rate for this type of air bubbles. Regarding the inertial force of the particles, a critical Stokes number of 0.08 was defined (Dai, 1998). For Stokes number $\ll 0.08$ the impact of inertial forces on the collision efficiency is insignificant. However, for the other extreme (i.e., Stokes number $\gg 0.08$) the collision efficiency can be obtained using Stokes number (Langmuir and Blodgett, 1946). For the intermediate particle size where Stokes number ≈ 0.08 , the collision efficiency is a function of both Stokes number and the particle size. Dai in establishing the Generalized Sutherland Equation, based on Dukhin work (Dukhin, 1982), concentrated on the conditions which are most probable for the practical flotation (i.e., Stokes $\ll 0.08$, and Stokes ≈ 0.08).

Dai derived the Generalized Sutherland Equation by solving the particle trajectory equation of Basset-Boussinesq-Oseen, (BBO) (Soo, 1967, Boothroyd, 1971, Thomas, 1992). He also introduced three levels of approximation to formulate a solution for BBO equation.

- First: particles move in the same path as the fluid elements. Therefore, the velocity and acceleration of particles and liquid phases are equal.
- Second: weak inertia force is prescribed for the particle but not enough to alter the particle acceleration from that of fluid. In this condition, particle and fluid velocities can be different.
- Third: particles have large Stokes numbers and therefore the velocity and acceleration of the fluid and particles vary independently.

Eq. 5.13 is the solution to the BBO equation under the second level of approximation. It is the ratio of Dukhin over Sutherland collision efficiencies, known

as the Generalized Sutherland Equation, which takes into account the collisions due to interception. The effect of inertial force of particles is also included in this formulation. The magnitude of the inertial forces was determined by dividing the liquid streamline into two sections, namely, the distant part of the streamline and the near part. At the distant part, the particle is being moved toward the air bubble by the particle inertial force which increases the collision probability. In the near part of the air bubble, however, the fluid velocity is divided into two components including the tangential and normal velocities. The variation of the fluid velocity can generate two force components near the bubble surface. The hydrodynamic pressing force which works in favour of collision (Derjaguin et al., 1984) and the centrifugal force, caused by the tangential velocity, acts against the solid particle deposition. Balancing the forces, one might assess a certain angle of collision on the air bubble for which the summation of the pressing force and the centrifugal force is zero. Thus, if a particle approaches a bubble with a smaller angle the pressing force is dominant, whereas the higher angle of collision will lead to dominant of the centrifugal force.

It is worth pointing out that the β factor in GSE (see Eq. 5.16) quantifies the importance level of the interception mechanism over inertial forces for the bubble-particle collision, since β is the ratio of Sutherland collision efficiency to the Stokes number. Considering β as the indicator of the collision mechanism, two scenarios might be implied:

- $\beta \gg 1$: the interception mechanism controls the collision efficiency and the inertial force of particles is negligible. In this case, Sutherland equation can be applied.
- $\beta \ll 1$: the inertial force prevails and its negative influence on the collision is important.

As expected, by increasing the particle size in a constant bubble size, the inertial forces increase and it has a decreasing impact on the collision efficiency. Dai (Dai, 1998) also showed that for two different bubble diameters ($d_b = 0.77$ mm and $d_b = 1.52$ mm) at the Stokes number close to the critical Stokes number (≈ 0.08), overestimation of the collision efficiency by Sutherland equation is only due to excluding the inertia effect. Thus, it can be safely said that the Generalized Sutherland Equation couples the decreasing influence of the inertia with the interception

mechanism to predict the collision efficiency. Dai (Dai, 1998) also suggested that the application of GSE is justified for the Stokes numbers of either below the critical value or close to it. However, for higher Stokes numbers, where there exist extensive inertial forces, the third level approximation should be used (Derjaguin and Dukhin, 1993).

The second flotation sub-process involved in the derived equation by Pyke is the bubble-particle attachment. The attachment probability between the solid particles and air bubbles is modelled using the proposed model of Dobby and Finch (Dobby and Finch, 1987). The premise of almost all the attachment models available for the flotation process is that attachment occurs when the contact time between the solid particle and the air bubble is longer than the induction time (Sutherland, 1948). The induction is defined as the required time for the liquid film around the air bubble to reach a critical thickness and then rupture (Sven-Nilsson, 1934). More details on the theoretical and experimental studies on the induction time and critical thickness of the liquid film can be found elsewhere (Crawford and Ralston, 1988, Schulze, 1989, Nguyen et al., 1998, Yoon and Luttrell, 1989, Trahar, 1981, Ye and Miller, 1988, Read and Kitchener, 1969, Schulze and Birzer, 1987, Yoon and Yordan, 1991, Jowett, 1980). However, we concentrated here on the attachment model proposed by Dobby and Finch, since it has been applied for the property-based flotation model due to Pyke. Dobby and Finch hypothesized that there is a certain contact or adhesion angle (θ_a in Eq. 5.18) at which the sliding time equals the induction time. In order to derive a formulation for the sliding time, they modified the particle sliding velocity equation of Sutherland (Sutherland, 1948) for potential flow:

$$v_{p\theta} = v_b \sin \theta \cdot \left(1 + \frac{r_b}{2(r_p+r_b)}\right) \quad \text{Eq. 5.28}$$

By approximating that the particle velocity, v_p , is smaller than the bubble velocity, v_b , they derived Eq. 5.29 for sliding time:

$$t_{sl}^p = \frac{2(r_p+r_b)}{2(v_p+v_b)+(v_p+v_b)\left(\frac{r_b}{r_p+r_b}\right)^3} \times \ln \left(\cot \frac{\theta}{2}\right) \quad \text{Eq. 5.29}$$

This equation can be seen as part of Eq. 5.19 for the computation of the collision angle. Dobby and Finch (1986), however, contradicted the potential flow condition assumed by Sutherland. They compared the tangential velocity of the fluid with experimental data under potential flow theory and concluded that the flow

conditions in the flotation with bubble sizes smaller than 1.2 mm is between Stokes and potential flow (i.e., intermediate). However, later this assumption also contradicted by Dai when he computed the attachment efficiency for both potential and intermediate conditions using Dobby and Finch model.

In order to compute the maximum collision angle, θ_c in Eq. 5.18, Dobby and Finch correlated the experimental data of Jowett (Jowett, 1980) with the bubble Reynolds number and three empirical expressions were introduced:

$$\theta_c = \begin{cases} 78.1 - 7.37 \log Re_b \rightarrow 20 < Re_b < 400 \\ 85.5 - 12.49 \log Re_b \rightarrow 1 < Re_b < 20 \\ 85.0 - 2.5 \log Re_b \rightarrow 0.1 < Re_b < 1 \end{cases} \quad \text{Eq. 5.30}$$

However, following the work of Dai for the collision model, Pyke applied Eq. 5.15 and Eq. 5.16 to calculate the maximum collision angle. The reason might be explained by the application β factor taking into consideration both interception and inertia effects for evaluating the maximum collision angle. Pyke analysed the experimental data of Dai (Dai, 1998) with assuming that there is no detachment occurring (i.e. $E_s = 1$). He argued that the attachment efficiency increases with both particle size and contact angle. Dai et al., (Dai et al., 1999) also used their previous experimental data to assess the capability of the modified Dobby and Finch model for the attachment efficiency. They reported, for the potential flow conditions (contrary to the intermediate flow condition for which the Dobby and Finch model was developed), the comparison between the attachment efficiency measurements and the calculated ones with the modified Dobby and Finch model yielded a reasonable agreement level.

The bubble-particle detachment (or the probability of stability) is the last micro phenomenon integrated into the flotation model due to Pyke. The formulation of the detachment sub-process is based on the forces acting on the bubble-particle aggregate. The stability of the aggregate has been studied both theoretically and experimentally (Schulze, 1977, Crawford and Ralston, 1988). These studies lead to a definition for the maximum floatable particle size (d_{pmax}). For example, Trahar and Warren (Trahar and Warren, 1976) reported a decrease in the flotation recovery of base metal sulphides for the particles with diameters larger than 100 μm . In 1984 Schulze formulated an upper limit for the particle size in quiescent conditions (Schulze and Hecker, 1984). He assumed for the typical flotation vessel only the

gravity and capillary force are important; using force balance Eq. 5.31 was proposed for the maximum floatable particle size as follow:

$$d_{pmax} = 2 \left[\frac{3\gamma_{lg}}{2(\rho_p - \rho_f)g} \right]^{1/2} \sin \left(180 - \frac{\theta_t}{2} \right) \quad \text{Eq. 5.31}$$

In this equation γ_{lg} is the surface energy between the liquid phase and the gas phase. On the other hand, under turbulent conditions which is more feasible in the flotation tank, Schulze described the stability of a bubble-particle aggregate based on the kinetic energy of the particle and the detachment energy (Schulze, 1977, Schulze and Hecker, 1984). For a spherical particle with the radius of R_p , an air bubble of radius R_b and considering the forces such as capillary, buoyancy, hydrostatic pressure and acceleration force due the rotation impeller, Eq. 5.32 formulates the maximum floatable particle size under turbulent condition (Schulze and Dobias, 1993):

$$d_{pmax} = 2 \left[\frac{3}{2\pi\rho_p v_t^2} \int_{h_{eq}}^{h_{crit}} \left\{ \frac{2}{3} \pi R_p^3 \rho_g \times \left(1 - \frac{2\rho_p}{\rho_f} - \cos^3 \omega + \frac{3h}{2R_p} \sin^2 \omega - \frac{3}{a^2 R_p^2} \sin \omega \sin(\omega + \theta) \right) - \pi (R_p \sin \omega)^2 \left(\frac{2\gamma_{lg}}{R_b} - 2R_b \rho_f g \right) \right\} dh \right]^{1/3} \quad \text{Eq. 5.32}$$

In this equation v_t represents the relative velocity of particle, while h_{eq} and h_{crit} are the particle equilibrium position and its critical position for the detachment to occur. Schulze (Schulze and Dobias, 1993) and Crawford (Crawford and Ralston, 1988) showed that this equation can explain the detachment of a spherical particle from a liquid-gas interface.

Schulze developed the stability model based on the force balance between the attachment forces and the detachment forces due to the external stresses in the flotation cell. Table 5-1 summarizes the forces exerting on a solid particle in the liquid-gas interface, it also categorizes the forces into the constructive or destructive for the bubble-particle aggregates.

Table 5-1 Summary of forces exerted on a solid particle.

Force	Equation	Attaching/Detaching
Gravity	$F_g = \pi d_p^3 \rho_p g / 6$	Detaching force
Static buoyancy	$F_b = \frac{\pi}{24} d_p^3 \rho_f g [(1 - \cos \omega)^2 (2 + \cos \omega)]$	Detaching force
Hydrostatic pressure	$F_{hyd} = \pi \frac{d_p^2}{4} (\sin^2 \omega) \rho_f g z_0$	Attaching force
Capillary	$F_{ca} = -\pi d_p \sin \omega \sin(\omega + \theta)$	Attaching force

Drag			Detaching force
Capillary pressure	—	—	Detaching force

The ratio of the detaching forces over the attaching forces results in the Bond number (see Eq. 5.23) that has been used in Eq. 5.22 to calculate the stability efficiency. Application of Bond number for the detachment exhibits limitations on the flotation modelling. Theoretically, there is no maximum value for the Bond number and it can increase to higher than unity. The Bond number of higher than one leads to negative rate for E_s implying that the solid particles is being created in the flotation tank. From the flotation perspective, however, $Bo > 1$ indicates that the bubble and particle cannot remain attached. In order to study this matter, the Bond numbers under different rotational speeds at a constant superficial gas velocity have been calculated. The aim is to investigate that whether the theoretical termination of flotation can occur under the conditions tested in this study. Figure 5-2 shows the calculated Bond numbers as a function of particle size for four different angular velocities of the impeller. As seen, there is a linear increase in the Bond number value by increasing the particle size which is expected due to the formulation of Bond number. Moreover, the increasing influence of the impeller speed on the Bond number is more pronounced for coarser particles ($d_p > 40 \mu\text{m}$). However, it is interesting to point out that for the cases simulated in this study the maximum average Bond number is below 0.3, even for the coarsest particle size at the highest impeller speed.

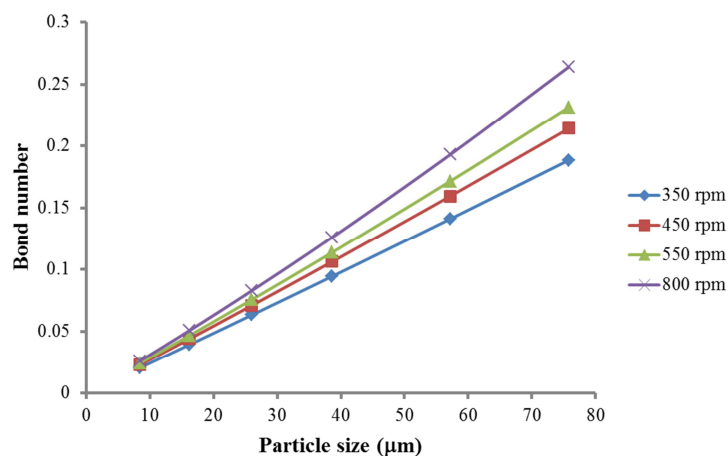


Figure 5-2 Bond number as a function of particle size for different impeller speed.

It can be implied from Figure 5-2 that the critical Bond number of higher than 1 may occur by simultaneous increase of the impeller speed and particle size.

Application of local hydrodynamic values (i.e., turbulent dissipation rate) allows us to calculate the Bond number for different zones inside the tank. As a case in point, the computational domain has been divided in the post-processing step into 14 slices of similar heights and the Bond number has been computed for each slice as a post-processing step (Figure 5-3). The high rate of dissipation rate around the rotational system (zone 5 and zone 6) resulted in the Bond number of higher than unity. Thus, one can conclude that these two zones in the vicinity of the impeller are more disposed to the detachment process.

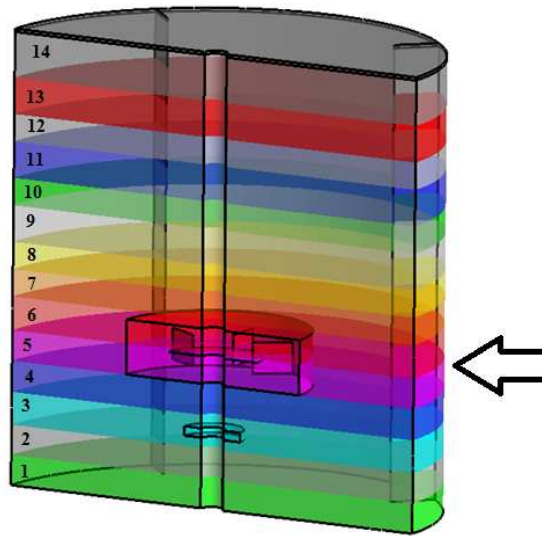


Figure 5-3 Different slices inside the domain for the local investigation of the Bond number.

It is worth indicating that the additional acceleration term, a , in Eq. 5.23 depends on the turbulent characteristics of the flow field. In a flotation tank the size of the turbulent eddies can be smaller than the bubble-particle aggregate size; in that they do not have enough energy to break the bubble-particle aggregate (Hui, 2000). However, there are turbulent eddies much larger than the typical bubble-particle aggregate size. They can trap the bubble-particle aggregate and due to the centrifugal force produced on the particle, the detachment is most probable. For the situation of having comparable sized bubble-particle aggregate and turbulent eddies, the dynamic interaction between the air bubble and the turbulent eddies generates detaching forces between the air bubble and the attached particle. This is assumed to be the controlling eddy size that interacts with bubble-particle aggregate. Hui also suggested calculating the acceleration factor of the attached particles in Eq. 5.23 based on the mean dissipation rate of the energy (see Eq. 5.26).

In addition to the calculation of Bond number, the stability efficiency has been also computed for four different impeller speeds. The stability probability as a function of particle size for various angular velocities of the impeller is given in Figure 5-4. This figure shows that, similar to the calculation of Bond number, for $d_p < 40 \mu\text{m}$ the stability efficiency is 1 and hence the collisions will lead to attachment. On the other hand, for particles with $d_p > 40 \mu\text{m}$ a drop in stability efficiency is observed which increases by increasing the impeller speed. Comparing Figure 5-4 with the experimental flotation performance reported by Trahar and Warren (Trahar and Warren, 1976) reveals similarities in the flotation behaviours when it is correlated with the particle size. They also reported a comparable drop in the flotation performance of the coarse particles. The experimental results of Trahar and Warren are shown in Pyke's PhD dissertation as Figure 2.10 (Pyke, 2004).

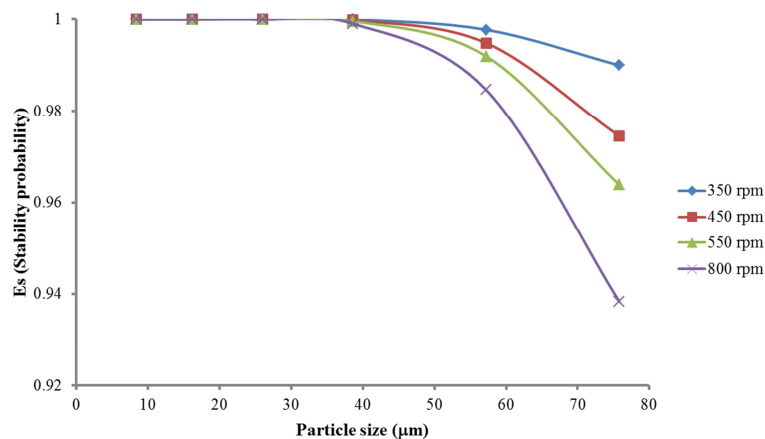


Figure 5-4 Stability probability as a function of particle size for four different impeller speeds

It can be inferred that not only is the efficiency of the bubble-particle aggregate stability, as a micro-process, decreased by particle size, but also the flotation recovery, as the macro response of the process, is also decreased after a certain particle diameter. Moreover, one might note that the decreasing impact of the flotation recovery on the Trahar and Warren experiments can be explained by the decrease in the stability probability of the coarse particles.

The only flotation modelling study explicitly focused on the uncertainty of the application of Schulze model for the stability is the study of Bloom (Bloom, 2006). He added a multiplying factor, α the so-called stability parameter, to modify the formulation of Schulze. However, he showed that the flotation efficiency significantly depends on the α factor (See Figures 1 to 5 in his article). The stability parameter

itself is dependent on both particle size and bubble size. Therefore, even though a modification of stability probability equation was carried out by Bloom, the final outcome of the modelling strategy (i.e., the flotation efficiency) was determined by the stability parameter.

To summarize, the application of Bond number in both conservative and the modified forms might lead to uncertainties on the numerical predictions. Thus, the accurate prediction of the stability efficiency necessitates the zoning of the tank. In that, for regions with high energy dissipation rate (i.e., $Bo > 1$) breakup of the bubble-particle aggregate is dominant, while for the bulk region of the vessel where $Bo < 1$, the E_s value falls in the range of $0 < E_s < 1$. Future work can, therefore, concentrate on finding the height and radius of a cylinder in which the Bond number is higher than 1 (e.g., around the rotational zone) and hence in this zone the couplet must break up. However, this requires the modifications of the UDF for the implementation of the flotation model due to Pyke. The code should be altered in a manner that within a region of $Bo > 1$ the bubble-particle breakup is prevailing, while outside of this zone the stability probability should be accounted for.

The last discussion in this sub-section focuses on the applied method of Pyke to account for the collision frequency of solid particles and air bubbles. The collision was first modelled by von Smoluchowski (Smoluchowski, 1917) who formulated this phenomenon by multiplying a collision kernel with the number concentration of two particle types:

$$Z_{pb} = \frac{4}{3} N_1 N_2 \left(\frac{d_1 + d_2}{2} \right)^3 G \quad \text{Eq. 5.33}$$

G is the velocity gradient perpendicular to the direction of particle motion and this equation is derived for laminar flow. The first model for the turbulent collision is proposed by Camp and Stein (Camp and Stein, 1943) who correlated the G factor in Eq. 5.34 with the turbulent properties of the fluid.

$$Z_{pb} = \frac{4}{3} N_1 N_2 \left(\frac{d_1 + d_2}{2} \right)^3 \sqrt{\frac{\varepsilon}{\nu}} \quad \text{Eq. 5.34}$$

Later, Saffman and Turner (Saffman and Turner, 1956) modified the constant in Eq. 5.34 and derived a new equation which is valid for the small particles that follow the fluid streamlines.

$$Z_{pb} = \sqrt{\frac{8\pi}{15}} N_1 N_2 \left(\frac{d_1+d_2}{2}\right)^3 \sqrt{\frac{\varepsilon}{\nu}} \quad \text{Eq. 5.35}$$

The Abrahamson equation (Eq. 5.6), however, was derived for a high turbulent dissipation rate and isotropic turbulent field. In this equation the G term of Eq. 5.33 was correlated by the mean squared velocities of the bubble and particle (Eq. 5.7). As mentioned previously to calculate the mean squared velocities Schubert equation (Schubert and Bischofberger, 1998), Eq. 5.7, was applied for $30 < Re < 300$. It should be pointed out that there are restrictions for the application of Abrahamson equation. First the particle diameter should be greater than the critical diameter defined by Eq. 5.36:

$$d_i^2 > d_{crit}^2 = \frac{15\mu_f U_f^2}{\rho_i \varepsilon} \quad \text{Eq. 5.36}$$

where U_f^2 is the mean squared velocity of the fluid. It is also recommended that for the application of Abrahamson expression one of the particulate phases diameters (i.e., solid particle or air bubble) should be larger than 100 μm . In practical flotation, most of the time air bubble diameters are larger than this limit. Moreover, for the small particles that can be affected by Kolmogorov scale fluid movements, the expression for the mean squared velocity may be erroneous and Abrahamson suggested a more general equation with an arbitrary function to link the inertial subrange with viscous range. Therefore, taking into account the above mentioned approximation and considering the fact that in flotation $d_b \gg d_p$, Eq. 5.8 can be applied for the estimation of the bubble-particle collision frequency in the derived equation for flotation by Pyke.

This sub-section shows that there are certain restrictions and assumptions on the derivation of Pyke equation for the flotation rate constant. As a case in point, Newell (Newell, 2006) applied this model for the predictions of flotation rate constant of quartz. In his study, the bubble velocity term was treated as a fitting factor to yield a better agreement with the experimental data. Nevertheless, the flotation model derived by Pyke offers a model for the flotation rate constant that not only covers the mechanical features, turbulence characteristics and sub-processes in a flotation tank, but also has the potential to be enhanced by the implementation of the local hydrodynamics values of the turbulent flow field inside the flotation vessel. Thus, accepting the simplifying assumptions of the model, the current study incorporates the model with a CFD solver to develop a CFD-kinetic model and investigate the new

approach for the predictions of the flotation rate constants of quartz and galena under different conditions.

5.3. Results and discussion

This section discusses the development and validation of a CFD method for the prediction of the flotation rate constant in a standard Rushton turbine flotation tank. The model development has been premised on the previous findings from the single-phase and multiphase methodologies developed in Chapter 3 and Chapter 4. In order to simulate the flotation separation process, fundamental flotation model due to Pyke has been implemented into the CFD solver via supplementary user-defined subroutines. Special efforts were made to employ the local values of the turbulent flow components from the CFD simulations in the fundamental flotation model while retaining its major structure unchanged. Moreover, simulations have been performed to explore the optimized range of the CFD modelling options for which a stable model capable of estimation of the flow variables and the computation of the flotation rate constant will be achieved. The model is also validated against the experimental data of Pyke and the computations of Newell using the fundamental model of Pyke (Pyke, 2004, Newell, 2006), but using spatially-uniform and empirically correlated hydrodynamic parameters. To gain more insights into the predictive capability of the CFD-kinetic model the flotation rate constants for two different minerals, quartz and galena, floating at different gas flow rates, hydrophobicity levels, and impeller speeds, have been investigated in the current study. This section aims to answer the following questions for the application of the CFD-kinetic method for the flotation modelling:

- Is it appropriate to incorporate the CFD flow-field data into a property-based flotation model to develop a CFD-based model for flotation modelling?
- Will the CFD-kinetic model improve the current state of art for flotation modelling?
- Can the new methodology for flotation modelling be applied to conduct a parametric study for the flotation separation process?

This section commences with a description of the numerical approach evolved in this study for the flotation modelling. Then the model is validated against the experimental measurements of flotation rate constants for two different minerals,

namely quartz and galena. The comparison is also made with the theoretical computations of Newell to indicate whether the CFD data improve the analytical results. Moreover, the model is subjected to the different operating conditions to evaluate the predictive reliability of the model when it is applied to a broader range of conditions experienced in flotation circuits.

5.3.1. Numerical approach

The turbulent flow of slurry (i.e., the solid particles and liquid water) and air bubbles inside the laboratory scale Rushton turbine flotation tank is simulated. The geometry and the average bubble diameters are adopted from the studies of Pyke and Newell (Pyke, 2004, Newell, 2006), where the experimental data for flotation rate constants for quartz and galena minerals under different operating conditions are reported. The Eulerian-Eulerian approach is applied to solve the governing continuity and momentum equations for the dispersed gas phase and the continuous slurry phase within the tank. The presence of the solid particles inside the computational domain was defined using the pulp concept. In other words, it was assumed that a pulp with a certain solid percentage was formed with spherical solid particles of constant diameters. It was also mentioned in sub-section 1.3 that the alternative to the introduction of the solid particle as the pulp is defining different phases corresponding to the available particle sizes in the domain. This requires additional set of continuity and momentum equations for each particle sizes. Besides, the interphase forces between the continuous liquid phase and all the dispersed phases should be taken into account as well as the interactions between the dispersed phases (i.e., air bubbles and solid particles, and solid particles of different sizes with each other). This approach would intensively increase the required computational resources leading to an impractical CFD model. However, introducing the solid particles in a homogeneous pulp phase would simplify the calculation of the micro processes between the air bubbles and solid particles. As an example, Appendix C shows a UDF that has been applied in this study to compute the rate of collision between the solid particles and air bubbles. In order to define the pulp phase for the flotation modelling, the slurry properties need to be defined for the CFD solver, since the available database of Fluent does not offer any fluid materials representing slurries. The procedure for specifying a new material for the solver includes determining the hydrodynamic properties of the new fluid (e.g., the density and the viscosity). This part has been

performed experimentally by preparing different solid percentages of quartz pulps for the rheometer experiments. The sample was pulverized to reach to the particle size distribution of $d_{100} < 106 \mu\text{m}$, since the same particle size distribution was used by Pyke and Newell. Pulps with solid percentages in the range of 5% to 35% by weight were then prepared for the rheometer experiments. The apparatus offers the measurements of viscosity profile through controlled stress measurements. It was equipped with two types of rotational systems namely cone/plate and plate/plate configurations. A PC interface was also connected to the device enabling the online plotting of the viscosity profiles by RHEOPLUS/32 V2.81 software. The final results are shown in Figure 5-5, where the relative viscosity of the pulp is plotted against the angular velocity and the different symbols correspond to the different solid percentages of the pulp. Each experiment was replicated twice to assure the minimum variations in the final viscosity results. The following graph is then used as a guideline to introduce different pulps into the computational domain.

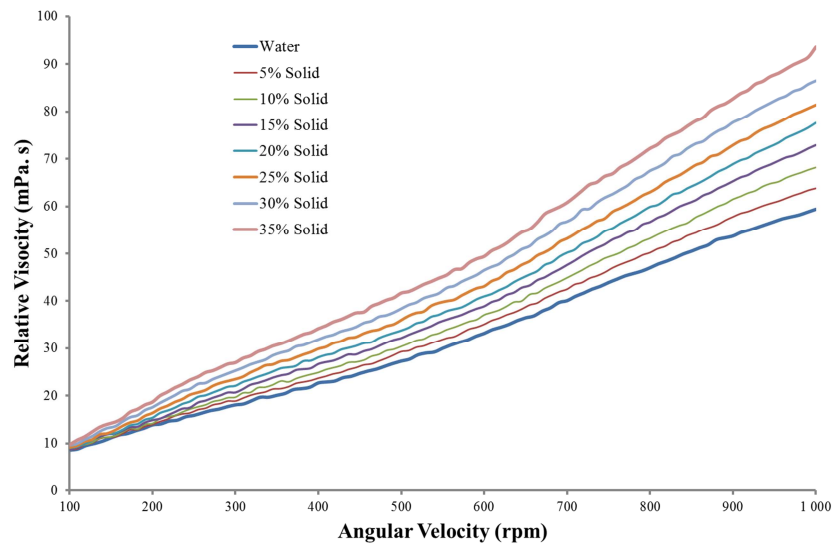


Figure 5-5 Rheometer measurements of relative viscosity as a function of angular velocity for different weight solid percentages of pulp

The second step of model development was to specify the underlying equations of the fluid flow. The governing equations for the gas-slurry are similar to the framework developed for the gas-liquid modelling in Chapter 4 (see: Eq. 4.3 & 4.4). As discussed in Chapter 4, the drag force between the liquid phase and the gas bubbles is the dominant interfacial force for the two-phase simulations of the stirred tanks. Thus, for the flotation modelling only the influence of the drag force on the air bubbles was considered. The comparison of the various drag coefficient correlations

for modelling of the turbulent multiphase flow inside the agitated tank in Chapter 4 has demonstrated that the expression of Lane for this coefficient provides the best match to experimental data for conditions appropriate in this study. Further, the proposed model of Lane for the drag coefficient has been shown to work reasonably well for different angular velocities and gas flow rates. Therefore, this drag model was implemented into the solver for the flotation modelling. The MRF method has been shown to be the best method for simulating the rotation of the impeller inside the computational domain. Hence, the flotation tank was divided into stationary and rotating zones to apply the MRF technique. Note that the extent of the rotational zone, in order to minimize the associated uncertainties, was determined from the findings of the single-phase modelling of stirred tanks. In addition, the boundary conditions for the blades were set as the moving walls with the relative velocity of zero compared to the rotational zone's angular velocity. The shaft and outer walls of the vessel were, however, defined as solid walls with no-slip velocity boundary conditions. Moreover, periodic boundary conditions were employed to halve the computational domain and reduce the overall CPU time. As the investigation of the various sparger designs has pointed out, the disk sparger with the diameter equal 40% of the impeller diameter, located at the mid-clearance, can be safely used to sparger air bubbles with a constant diameter into the flotation tank. The source term, a 3 mm thickness zone with mass and momentum for the air phase, was placed over the sparger, while a sink term at the top of the tank collected the injected gas. The diameters of air bubbles were held constant during the simulations and the experimental measurements of Newell were used to select the corresponding air bubble diameter for the different flotation conditions. Similar to the previous studies in this field e.g. (Koh and Schwarz, 2006b, Koh and Schwarz, 2007), the shapes of the air bubbles were assumed to be perfect spheres to eliminate the difficulties on the calculation of the flotation sub-processes for the non-ideal shape air bubbles. However, this might not be the case, as high speed video footage shows that the air bubbles can significantly deform on entering in highly turbulent regions.

Within the Fluent solver the SIMPLE scheme was implemented to couple the mass and momentum equations and derived the pressure field inside the tank. The discretization of the momentum equations was performed with a second order upwind method, whereas the QUICK scheme was used for the volume fraction equation. The

convergence criteria were defined similar to those used for gas-liquid modelling as well as an additional criterion for the flotation rate constant. In this way, a negligible variation for the gas holdup predictions (< 1% for the last 5 seconds of flow time), a stable overall flotation rate constant (< 3% variations for the last 3 seconds of flow time), and the normalized continuity residuals values below 10^{-3} were required to stop the computation of the governing equations.

In order to incorporate the fundamental model of the flotation rate constant, it is vital to recall the three main components of equation 5.12. The first part, $\frac{7.5}{\pi} \frac{G_{fr}}{d_b V_r}$, is dictated by the operational conditions and the mechanical features of the tank. The second term, $\left[\frac{0.33 \varepsilon^{4/9} d_b^{7/9}}{v^{1/3}} \left(\frac{\rho_p - \rho_f}{\rho_f} \right)^{2/3} \frac{1}{u_i} \right]$, involves two hydrodynamic parameters, the turbulent dissipation rate and the turbulent velocity of the fluid. In the studies of Pyke and Newell the turbulent energy dissipation rate, ε , has been measured as a single value using LDV, and torque turntable and this individual value was then applied for the entire volume of the tank. This single value was used in the fundamental property based model for the computation of the flotation rate constant. However, using CFD enables us to capture this quantity at every spatial point inside the tank and thereby the computation of the flotation rate constant can benefit from the local values of the energy dissipation rate instead of using an overall average. It has also been shown that the magnitude of the dissipation rate can be 10-100 times higher in the vicinity of the rotational zone compared to the total average (Schulze, 1977, Schubert and Bischofberger, 1998). Thus, using a mean value may not be a viable representative of the turbulent eddies conditions in the cell.

The second hydrodynamic term, u_i , in the fundamental equation of Pyke determines the turbulent fluctuation of the fluid velocity and in the computations performed by Pyke and Newell this term was assumed to have a single value computed by:

$$u_i = \sqrt{V_x^2 + V_y^2 + V_z^2} \quad \text{Eq. 5.37}$$

where the V_x , V_y and V_z are velocities in x , y and z directions obtained by LDV measurements at varying heights, weighted towards the zone around the impeller. The resultant average velocity computed by Eq. 5.27 may not be a suitable representation of the flow of pulp inside the tank, since the findings of the single-phase modelling

have confirmed that the velocity varies across the tank (e.g. see: Figure 3-25). The CFD method, however, computes the magnitude of the fluid velocity at the centre of each grid point within the domain. The flotation rate computation can thus take advantage of the local values obtained by CFD to represent more accurately the continual changes of the velocity components in the flotation tank.

The third part of Eq. 5.12, the product of E_c , E_a , E_s , representing the flotation sub-processes, can also be improved using the CFD calculations. The Generalized Sutherland Equation (GSE) applied in the fundamental model, derived by Pyke, for the estimation of the collision efficiency uses the bubble velocity. Pyke (Pyke, 2004) assumed that this term is analogous to the fluid velocity calculated by Eq. 5.27. Newell (2006), on the other hand, measured the bubble velocity for the different operational conditions using a video camera. He reported that the bubble velocity is a function of the cell height. Even though he experimentally measured the bubble velocity inside the laboratory scale Rushton turbine flotation tank, for the computation of the flotation rate constants, the measured values of the bubble velocity did not provide a close fit with the experimental measurements of the flotation rate constants. Therefore, this quantity was treated as a fitting factor to produce the best fit with the measurements. In all cases, he found that reducing the magnitude of the bubble velocity resulted in closer predictions of the flotation rate constants. This observation was attributed to the lack of understanding of the bubble velocity in the turbulent systems. As can be seen, the specification of bubble velocity was approximated in the calculation of E_c in the methods used by both Pyke and Newell. The uncertainty in the specification of bubble velocity can be indeed minimized by using the CFD solutions of the air velocity components in the flotation cell, where the local values of the gas velocity can be entered into the collision efficiency equation. This is another point indicating that the application of CFD can improve the property-based models for the flotation separation process. The efficiency of the second flotation sub-process, attachment efficiency (i.e., E_a), can similarly be aided by the local calculation of the air bubble velocity inside the flotation cell. Finally the expression of Schulze for the stability efficiency, E_s , applies the energy dissipation rate in the form of Eq. 5.26 to compute the Bond number. Similar to the second hydrodynamic term in Eq. 5.12, the local values of turbulent dissipation rate can also be applied here instead of an overall average.

As discussed, even though the fundamental flotation model due to Pyke has been confirmed to be reasonably accurate for the prediction of the flotation rate constant, there exist potential points in the formulations where, instead of using a single spatially-averaged value, the transient magnitudes of the flow variables can be implemented in the model to represent the flotation separation process more accurately (see sub-section 5.2.1). Therefore, the gas-slurry CFD methodology was supplemented by interconnected UDFs to compute the flotation rate constant using the model derived by Pyke whereas the computations take advantage of the local flow variables.

It must be remembered that the implemented UDF for the computation of the flotation rate constant is executed every iteration during the simulation. Thus, it calculates the flotation rate constant of each control volume inside the tank using the flow field local values such as the liquid and gas velocities as well as the turbulent kinetic energy and its dissipation rate. In order to compare the numerical predictions of the flotation rate constants with the experimental data, obtained as the overall rate constants for the flotation tank, it is required that an averaging technique will be applied for the computed values at each grid point. Therefore, the volume-weighted average of k is computed by dividing the summation of the product of the flotation rate constants and cell volumes by the total volume of the flotation tank (Eq. 5.38):

$$k = \frac{1}{V_{tank}} \sum_{i=1}^n k_i |V_{i-cell}| \quad \text{Eq. 5.38}$$

In Eq. 5.38, V_{tank} represents the total volume of the vessel, k_i is the computed value of the flotation rate constant at i^{th} grid point, and V_{i-cell} is the volume of the i^{th} cell in the computational domain. The volume averaging procedure starts after 1 second of the flow time and it continuous until a negligible variation is observed for the final value of the flotation rate constant. In other words, the data files are extracted based on a 1 second incremental step of the flow time and the overall volume-weighted average of the k_s are recorded. The final value of k with insignificant variations is, then, compared with the experimental data that were reported for the entire flotation tank.

5.3.2. Limitations of the numerical approach

The numerical approach applied in this study has been outlined in the previous subsection. Nonetheless, there are limitations and simplifying assumptions for the

application of this CFD-based methodology that must be pointed out for future development of this work.

When different phases (i.e., a continuous or carrier liquid phase and different dispersed phases) are available in a computational domain, it is essential to gauge the extent of the interaction or coupling between the continuous and the dispersed phase. For the case of mechanically agitated vessel, where the flow is fully turbulent, the complexities are manifold. The commonly used diagnostic test to determine the coupling level between the various phases is to obtain the relevant time and length scale. As discussed in Chapter 4, Elghobashi (Elghobashi, 1994) categorized 3 strategies for coupling between the different phases. Short descriptions of each method as well as how they can be implemented into the ANSYS Fluent CFD solver are tabulated in Table 5-2.

Table 5-2 Different methods of coupling between the dispersed phase and the continuous phase and ANSYS Fluent implementation.

Coupling method	Definition	Implementation	ANSYS Fluent multiphase model available
One-way	The continuous phase only affects the dispersed phase.	Using particle tracking as the post-processing step	DPM, Mixture, Eulerian
Two-way	Both the continuous phase and dispersed phase can sense each other.	The governing equation of the fluid phase will be modified due to the particulate phase	DPM, Mixture, Eulerian
Four-way	Interaction of dispersed phase is comprised.	An extra model for particle-particle interactions should be included.	Limited to Eulerian for granular phase by including shear viscosity from particle momentum exchange because of collision and translation

In order to provide a guideline on how to couple the different phases, Elghobashi (Elghobashi, 1991) categorized the methods of coupling based on the volume fraction of the particulate phase, α_p , and three different ratios corresponding to the length and time scales of the turbulent flow. For the length scale the distance between the centres of two adjacent particles, S , was normalized by the average particle size, d_p , as follow:

Furthermore, the particle response time, τ_p , was used to represent the turbulent time scale when it was divided by either Kolmogorov time scale, τ_k , or the turnover time of large eddy, τ_e .

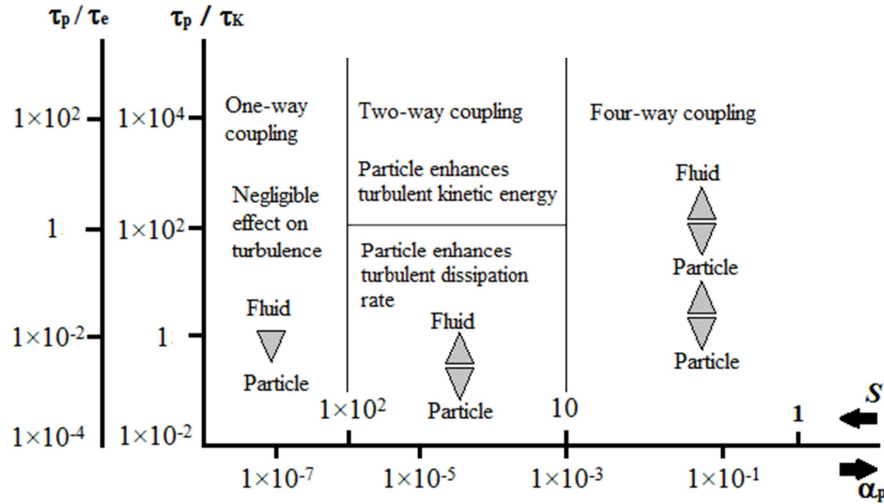


Figure 5-6 Guideline for coupling between phases in multiphase flows adopted from Elghobashi (Elghobashi, 1991)

Figure 5-6 displays the proposed regime map by Elghobashi. In this figure the dilute suspension was categorized as $\alpha_p < 10^{-3}$ where one-way or two-way coupling can model the interactions between the carrier and the dispersed phase. The S factor, denoting the relative distance between the particulate phases, determines the sufficient level of interactions between particles. According to this figure if the distance between the two neighbouring particles is large enough ($S > 100$), the dispersed phase impact on the liquid phase is insignificant and one-way coupling can handle the interactions between various phases. However, for the multiphase flows where $10^{-6} < \alpha_p < 10^{-3}$ and $100 < S < 10$, one should take into account the influence of the dispersed phase on the continuous phase through two-way coupling and depending on the particle relaxation time (i.e., τ_p) the particles can enhance the turbulent kinetic energy or the dissipation rate of the primary phase. Increasing the volumetric fraction of the dispersed phase further (i.e., $\alpha_p > 10^{-3}$) alters the multiphase regime into a dense suspension in which the effect of particle-particle interactions should be incorporated via four-way coupling approach.

In order to numerically couple the various phases in a multiphase flow field, the dispersed phase can be treated with two different methods. The first one assumes the dispersed phase to be an interpenetrating continuum and solves a set of continuity and momentum equations for it (Gidaspow et al., 1991) Within the ANSYS Fluent structure this method can be executed using an Eulerian-Eulerian model. The difficulties lie in the fact that for the different sizes of the particles/bubbles new phases are required to be defined. Thus, the number of governing equations would increase, which consequently might turn the numerical approach into an impractical numerical model (with regard to the available computational resources). The second approach of dealing with the particulate phase is to formulate them as discrete entities within a Lagrangian framework and quantify the particle-particle collision through a collision kernel e.g. (Goniva et al., 2010). The Discrete Element Method, (DEM), is the ubiquitous and relatively computationally intensive method to compute the motion of discrete particles (Cundall and Strack, 1979). Using DEM one can solve the equation of motion for the particles. This equation (Eq. 5.40) originates from Newton's Second Law, accounting for all the forces exerted on a particle, and its conservative form is as follow (Maxey and Riley, 1983):

$$m_p \frac{dU_{i,p}}{dt} = F_{i,drag} + F_{i,press} + F_{i,Virt} + F_{i,History} + F_{i,Bouy} + F_{i,Lift} + F_{i,Turb} + F_{i,Brown} \quad \text{Eq. 5.40}$$

In this equation, m_p is the mass of the particle, $U_{i,p}$ is the linear velocity of the particle, $F_{i,Drag}$ is the drag force, $F_{i,Press}$ is the pressure force due to the pressure gradient, $F_{i,Virt}$ is the virtual mass force due to acceleration of the surrounding fluid, $F_{i,History}$ is the history or Basset force due to changes in the boundary layer, $F_{i,Bouy}$ denotes forces due to gravity, $F_{i,Lift}$ is the Saffman and Magnus lift force due to the velocity gradient and particle rotation, $F_{i,Turb}$ denotes forces due to turbulent fluctuations and $F_{i,Brown}$ is the Brownian force due to molecular collisions. The details of the significant forces can be found elsewhere (Crowe et al., 1998). As shown in Table 5-2 four-way coupling requires a model for the particle-particle interactions. Hence, a potential method of obtaining the four-way coupling between the continuous and the dispersed phase can be proposed by integrating the DEM and CFD methods. In other words, the particle positions and velocities within the domain are computed by DEM and based upon these data the CFD solver computes the momentum exchange between the phases. Moreover, the primary phase velocity components can

be computed using the CFD solver with respect to the volume fraction of the dispersed phase and momentum exchange (Wierink, 2012).

As seen in Figure 5-6, for intermediate particle loading in a turbulent multiphase flow, the influence of the dispersed phase on the turbulent properties of the liquid phase should be accounted for. Although the continuous phase might be modelled using RANS, LES or, if the computational power allows DNS, the turbulent energy generated due to the particulate phase movement can alter the flow hydrodynamics. There have been numerous fundamental studies on how the dispersed phase modifies the turbulent nature of the carrier phase. Most of these studies were performed for channel flow; nonetheless the results would have the same implications for other types of turbulent multiphase flows. For example, Elghobashi and Truesdell (Elghobashi and Truesdell, 1992) computed a 3D velocity field of a homogenous turbulence using DNS. The impact of three kinds of solid particles on the turbulent field was investigated by integrating the complete equation of particle motion. They showed that the dispersion statistics of a solid particle were different from the surrounding fluid elements and the particulate phase intended to remain longer in a turbulence eddy when the gravity force is negligible. The effect of the different size particles on the turbulent characteristics was also addressed by Pan and Banerjee (Pan and Banerjee, 1996, Pan and Banerjee, 1997). They showed that particles smaller than the Kolmogorov length scale suppressed the turbulence intensity and Reynolds stress, whereas larger particles increased intensity. They also showed that the large particles can enhance the turbulent properties specifically near the wall and this increase was proportional to the size, Reynolds number and loading rate. The physical phenomena responsible for the alteration of the turbulent properties was described by Ahmed and Elghobashi (Ahmed and Elghobashi, 2001). Using DNS to evaluate the two-way coupling between the phases, they indicated that the dispersed phase changes the production rate of the turbulent energy through applying changes on the vorticity dynamics. They explained that the dispersed phase increases the alignment of the vorticity vector which increases the production rate of turbulence. They also showed the particles intended to accumulate in the low vorticity regions which in turn increase the velocity gradient leading to the change of the vorticity dynamics. They further studied this phenomenon (Ferrante and Elghobashi, 2003) and introduced a new group of particles (i.e., ghost particles) with $\tau_p / \tau_k = 0.25$ which modified the turbulence

kinetic energy and dissipation rate similar to the particle-free turbulence flow. Moreover, Geurts and Vreman (Geurts and Vreman, 2006) showed that in a turbulent flow and for the modest particle volume fraction of about 1.5% the inelastic collisions between particles should be coupled with the liquid phase via four-way coupling approach. The results of the two-way coupling, however, indicated that, even though it was computationally more preferable, it led to unphysical predictions of “centre-channel-jet” phenomena which were not recorded experimentally. Later, they (Vreman et al., 2009) also highlighted the importance of the four-way coupling when the volume fraction of the particle phase is about 1.3%. They suggested that for the volumetric solid percentage of higher than 1% the particle-particle interaction should be included.

Although the above mentioned articles emphasized on the importance of the inter-particle interactions within a turbulent flow field, the numbers of studies on the numerical modelling of flotation vessels in which, specifically, the two-way or four-way coupling approaches have been utilized are limited. As stated in sub-section 2.6.2 the CFD-based models are restricted to the works of Koh and Schwarz where they applied a pulp concept to introduce the solid particles. In this approach the particle movement is dictated by the liquid phase behaviour. In other words, the only interaction between the phases takes place between the pulp and air bubbles. However, Wierink and Heiskanen (Wierink and Heiskanen, 2008) showed that the flotation process should be modelled using higher order coupling between the different phases. Wierink et al., (Wierink et al., 2009) mapped the bubble-particle collision by mean of the bubble pressure fluctuation during the collision process. The bubble pressure during the collision was experimentally measured and used as a momentum coupling method. The theory behind this study was that a particle requires a minimum of kinetic energy to collide with the air bubble. The source of kinetic energy for a particle depends on its relative velocity which itself is a function of pressure gradient. Thus, the experimental data of the critical pressure ($= 0.28 \text{ Pa}$) would acts as the indicator of the successful collision. This theory was combined with a mixture two-fluid model to couple velocity, pressure and momentum. They also included the effect of dynamic surface tension for the bubble-particle modelling (Wierink and Heiskanen, 2010). Contrary to the typical flotation models where the surface tension is a constant value, they performed a tangential force balance and

included the Marangoni effect due to the varying surface tension (Clift et al., 1978). The influence of turbulence also included on the surface tension, while the interaction between particles at the bubble surface was accounted for by the lateral capillary force. Through his PhD work Wierink (Wierink, 2012) completed this methodology and formulated a computational model for three-phase systems in which both physical momentum coupling and the coupling between physic-chemical forces in the momentum exchange was considered. In this work the air bubble was defined as the interface between the liquid and gas phase and the particles motion (1000 particles in a Lagrangian framework) was modelled using DEM. Two open source codes, OpenFoam as the CFD solver and LIGGGHTS as the DEM solver, were coupled together to model the three-phase interactions. The capability of the CFD-DEM model was tested for one case where a cloud of particles falls on an individual air bubble. This test showed the full momentum coupling along with the physic-chemical coupling yielded promising results. However, the author emphasized the need for further validation studies. A similar approach was used by Goniva et al., (Goniva et al., 2012) for modelling of three phase flow including droplets, particles and a fluid phase. They applied the CFD-DEM approach for a rotating drum coater. Calculating the volume fraction of the dispersed phase throughout the domain, they were able to determine the effect of each particle for the momentum exchange. The authors suggested that the same strategy can be used for the other three-phase metallurgical processes.

As discussed above, a few studies for modelling of the flotation process are disposed toward incorporation of the particulate phase with DEM method, whereas the carrier phase hydrodynamics are modelled using CFD. This strategy is more focused on the micro-level phenomenon by treating a cloud of particles via Lagrangian framework, while the conventional Eulerian is applied for the continuous phase. Even though the computational expense of this methodology might hinder the day-to-day application of CFD-DEM integration (for instance Wierink (Wierink, 2012) reported 1332 hours of CPU time for his case study on a 2.83 GHz CPU), the high level of coupling between the three phases makes this approach very close to reality. The current study is, however, intended to develop a CFD-based model for the flotation process. Also, it is only bounded to the application of ANSYS Fluent CFD solver. Within the structure of this solver, the Eulerian-Lagrangian approach can be

conducted using DPM. This method tracks the trajectories of a large number of particles, bubbles, or droplets, while the continuous phase is modelled by solving the Reynolds-averaged Navier-Stokes equations. The trajectories of the particles are predicted by a simpler form of the particle motion equation (Eq. 5.40) in which the drag force and the virtual mass force due to the relative acceleration are included. The other forces such as Brownian or lift are optional and user can enable them depending on the problem. Therefore, for the low volume fraction of the secondary phase i.e., solid/air volume fraction $<10\%$ w), using DPM, ANSYS Fluent can provide one-way and two-way coupling between the continuous and the dispersed phase.

In simple one-way coupling, the continuous flow field can be obtained regardless of the particulate phase. The solution of continuous phase can then be used to predict the trajectories of the particles by solving equations of motion for the particles. On the other hand, in the two-way coupling, particles can affect the primary phase through the exchange of momentum, mass and heat. The typical calculation starts with the solution of the continuous phase prior to the injection of the particles. Then, the trajectories of the injected particles will be calculated and the continuous phase flow field will be updated to account for the exchange of momentum, heat and mass. Finally applying the modified continuous phase solution, the discrete phase trajectories will be recalculated (ANSYS, 2011a). Lathouwers (Lathouwers, 1999) (Lathouwers, 1999), however, stated that the coupling with the Lagrangian-Eulerian method might be erroneous. He argued that for the coupling, the particle motion is postulated to be instantaneous and the solution of the continuous phase involves only averaged quantities which lead to uncertainty in the coupling approach. Moreover, in practice it was recommended (ANSYS, 2011b) to limit the application of DPM for the multiphase flow where the volume fraction of the dispersed phases is less than 10%. For the case of the flotation tests used in this study for validations, the gas phase volume fraction in some cases exceeds this limit. In addition to the high volume fraction of the secondary phase, the multiple reference frames was used in this study to model the impeller inside the domain. Combination of the moving reference frames with the DPM model will lead to numerical uncertainty in the predictions of particle trajectories (ANSYS, 2011a). Using MRF in conjunction with the DPM model for particle tracking will strongly change the display of the particle tracks dependent on the location of walls inside the moving frame.

To summarize why the application of Eulerian-Lagrangian approach is avoided in this research, even though it would provide two-way coupling between the dispersed phase and the continuous phase, the reasons are bulleted here:

- The volume fraction of the particulate phase should be below 10%.
- The coupling of the instantaneous data for the particulate phase with the averaged data of the continuous phase results in uncertainties in the modelling.
- The combination of MRF and DPM will not yield meaningful particle tracks.

The remaining method for the multiphase modelling within the framework of ANSYS Fluent is the Eulerian-Eulerian approach. This approach treats the dispersed phase as a continuum and all the available phases share a pressure domain and thus they can interpenetrate. In this approach the particulate phase is defined by a local average volume fraction and other averaged properties. The coupling of the phases is more direct in the Eulerian-Eulerian method, since the properties of the continuous phase and the dispersed phase are averaged. Furthermore, since this method adds a set of continuity and momentum balance equations corresponding to each particulate phase presented in the domain, the volume fraction of the secondary phase is only limited by the available computational resources. The coupling between phases is controlled by the pressure and interphase exchange coefficient where user can manipulate the exchange coefficient using UDFs.

ANSYS Fluent can execute the Eulerian-Eulerian framework through three different methods namely, VOF, mixture and Eulerian-Eulerian. The VOF is a simple surface-tracking method that can be used for stratified flows. However, both mixture and Eulerian-Eulerian models can handle the dispersed multiphase flows. The mixture model solves the momentum equation for the mixture phase and applies a relative velocity formulation for the dispersed phase, while Eulerian-Eulerian, as the most complete multiphase approach, solves the conservation equations for each phase separately with a shared pressure field. In order to identify the most adequate modelling strategy, one should take into consideration the influence of particulate loading factor, β , and Stokes number, St . The particulate loading is defined by Eq. 5.41 and it affects the interaction between phases:

Eq. 5.41

where α_d is the volume fraction of the dispersed phase, ρ_d is its density, and α_c and ρ_c represent the volume fraction and the density of the carrier phase, respectively. The particulate loading can identify the level of interaction between phases as well as the most practical multiphase approach. ANSYS Fluent classifies the multiphase flows based on the particle loading into low, intermediate and high loading suspensions. The low loading flows should be handled using either mixture or Eulerian with one-way coupling, while the multiphase flows with the intermediate particle loading requires two-way coupling and both Eulerian and mixture models can be applied. For high loading, the granular option of Eulerian model can be used in which two-way coupling is combined with particle pressure and viscous stresses due to particle (i.e., four-way coupling).

In this study the validation of the CFD model is performed using the experimental data of Pyke and Newell for the flotation rate constants of quartz and galena. They both carried out their experiments with the volume fraction of the solid phase less than 0.02. Figure 5-7 displays the particulate loading factor as a function of volumetric solid percentage for quartz (solid line) and galena (dashed line). For the volumetric solid percentage of 0.02 the particulate loading factors are 0.00005 and 0.00015 for quartz and galena, respectively. The low particulate loading factors for both quartz and galena show that the influence of the dispersed phase on the liquid phase is insignificant for low solid percentage.

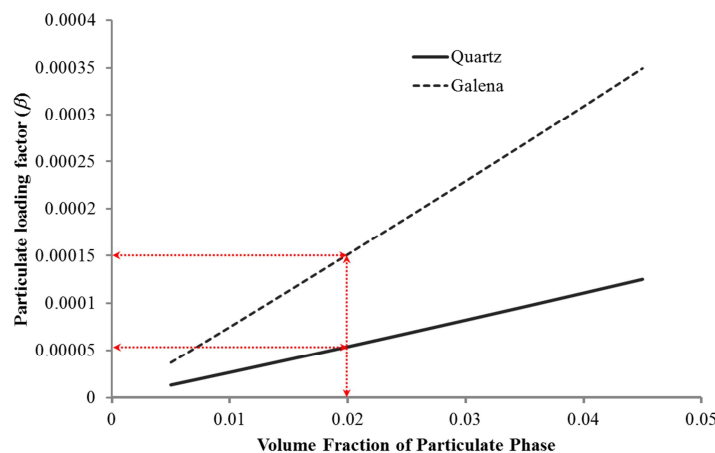


Figure 5-7 Particulate loading factor as a function of volume fraction for quartz and galena

In addition to the particulate loading factor, Stokes number can be another representative of how substantial the interphase interactions between the continuous

and dispersed phase is. This parameter was also calculated for both quartz and galena based on the reported d_{90} for the particle size by Pyke and Newell. Figure 5-8 shows the Stokes number as a function of angular velocity of the impeller for quartz (solid line) and galena (dashed line). As can be seen, even for the highest rotational speed the $St < 1$ assures that the solid particles follow the liquid phase. In other words, the solid particles effects on the liquid phase can be neglected, as their behaviour has been dictated by the continuous phase.

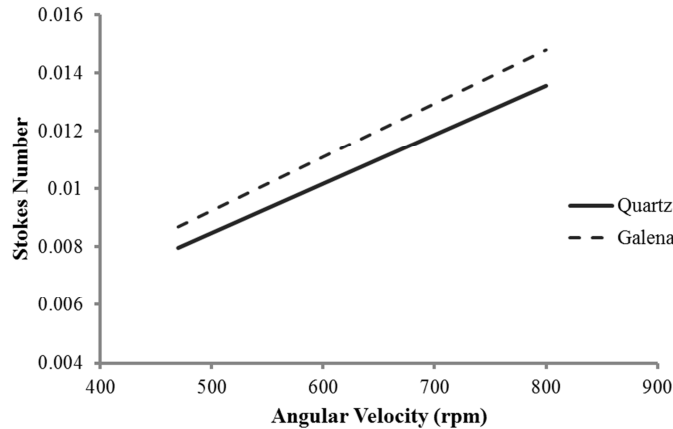


Figure 5-8 Stokes number as a function of angular velocity of impeller for quartz and galena

Therefore, in this study an Eulerian-Eulerian approach was selected for two-phase modelling, the primary phase is being slurry with certain solid percentage and the secondary being air bubbles. Introduction of the solid particles as a perfect mixture of constant diameter spheres with water has been used by Koh and Schwarz for the numerical modelling of the flotation process e.g. (Koh and Schwarz, 2003b, Koh and Schwarz, 2006b). Even though high volumetric solid percentage (i.e., 0.08%) was applied (Koh and Smith, 2010), they confirmed that the one-way coupling between the slurry and air bubbles results in acceptable agreement between the CFD predictions of the flotation rate constant and the corresponding experimental data. They showed that the movements of the solid particles within the slurry are controlled by the liquid phase and their influences on both the liquid phase and the air bubbles are negligible. It should be also pointed out here that the momentum exchange term in Koh and Schwarz studies was modelled using drag force. The Schiller-Naumann drag coefficient correlation, which was derived for a single bubble in an infinite pool, was applied to account for the influence of the drag on the air bubbles. Although this drag coefficient is mostly applicable for the laminar flow, they applied it for the fully

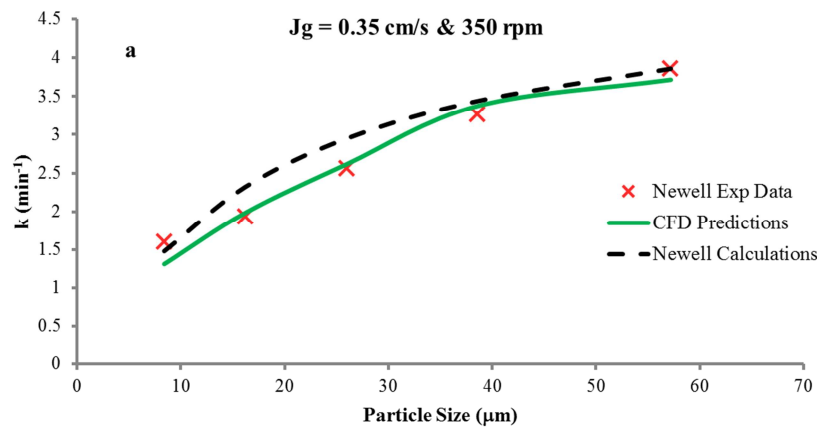
turbulent flow encountered in flotation vessels. However, in the present study the turbulence effects on the air bubble behaviour have been simulated using the drag correlation coefficient proposed by Lane. The numerical predictions of gas holdup for different operational and geometrical conditions, reported in Chapter 4, showed that the capability of this formulation on the successful coupling between the continuous and the dispersed phase is better than the Schiller-Naumann equation.

Clearly in a real flotation vessel with high solid percentage, the role of inter-particle interactions cannot be omitted. The impact of the particle-particle, bubble-particle and the bubble-bubble interactions on the flotation sub-processes requires higher order coupling between the available phases. As discussed above, this can be achieved by solving the continuous phase governing equations with a CFD solver, while the motion of the dispersed phase is being modelled by DEM method. Integration of these two methods will result in four-way coupling in which the full interphase coupling is taken into consideration. Furthermore, the application of a constant bubble size per simulation can be replaced by adding an extra partial differential equation for the bubble number density. This accounts for the changes in the bubble size due to the coalescence and breakup phenomenon. However, in this study within the defined structure of Eulerian-Eulerian framework in ANSYS Fluent the momentum exchange between the phases is quantified by the description of the fluid-fluid exchange coefficient (see Eq. 4.10 and Eq. 4.11). Due to the limitations of the CFD solver for the inclusion of high order coupling techniques and the demanding computational time, it was therefore decided to apply the “pulp” concept for the introduction of the solid particles into the vessel. This approach was also followed in the various studies of Koh and Schwarz. Additionally, the solid particles were assumed to follow the movement of the liquid phase and their effects on the continuous and dispersed phase (i.e. air bubble) are assumed to be insignificant. In this way, the governing equations for the turbulent two-fluid multiphase flow were solved in which the air bubbles interact with the liquid phase through the drag force and turbulent characteristics of the mixture.

5.3.3. Validation of the model for quartz flotation rate constants

To verify the hypothesis that the incorporation of CFD data into the fundamental property based model will be able to produce practical flotation rate constants, CFD simulations of the flotation process for hydrophobic quartz particles

over a range of different angular velocities of the impeller at a constant gas flow rate have been carried out. In order to calculate the flotation rate the bubble diameters have been kept constant for the entire tank and the values are based on the experimental measurements of Pyke (i.e., $d_b = 0.415$ mm for 350 rpm, $d_b = 0.372$ mm for 450 rpm, $d_b = 0.352$ mm for 550 rpm and $d_b = 0.330$ mm for 800 rpm). The operational conditions of all the simulations including angular velocities of impeller, superficial gas velocity, bubble size, and contact angle are elaborated in Appendix D. The numerical predictions of the flotation rate constants, k , have been validated with the experimental values of Newell (Newell, 2006) to investigate the applicability of the method. To provide additional corroboration, the CFD results have also been compared to the computations of Newell, where the fundamental flotation model due to Pyke was used to estimate the flotation rate constants and bubble velocity was used as a fitting parameter. Figure 5-9 (a) illustrates the numerical predictions of the flotation rate constants as a function of particle size for the superficial gas velocity $J_g = 0.35$ cm/s and the impeller speed of 350 rpm. In this figure, the symbols represent the experimental measurements of Newell, the solid line corresponds to the CFD-based prediction of k and the dashed line displays the computations of Newell using the equation derived by Pyke for the flotation rate constant.



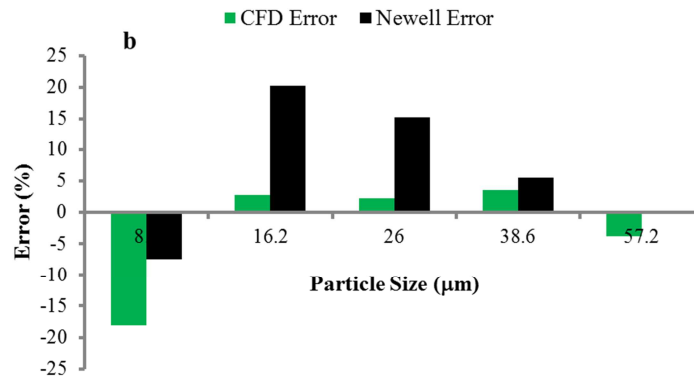


Figure 5-9 (a) flotation rate constant as a function of particle size (b) comparison of the CFD and Newell computation errors for the prediction of the flotation rate constant [Operational conditions: $J_g = 0.35$ cm/s and impeller speed = 350 rpm]

The results show that the general trend of the experimental data has been correctly captured by both the CFD and the theoretical computations. For the finest particle size range investigated the CFD results and Newell's computations underpredict the rate constants with an average difference of 18.1% and 7.5%, respectively. This can be attributed to fact that the low mass and inertia force of the fine particles reduces the collision probability. On the other hand, the small surface area of fine particles decreases the stability probability. In other words, the small interface area between a fine solid particle and an air bubble reduces the chance of the solid particle to remain attached and travel to the froth phase. The CFD predictions of the flotation rate constant for the other ranges in the particle size distribution ($d_b > 8.4$ μm) match the experimental data very closely to within average differences of 2.75%, 2.22%, 3.52%, and 3.71% for the particle sizes equal to 16.2 μm , 26 μm , 38.6 μm and 57.2 μm . Also, the computed root mean square deviation (RMSD) reveals that the performance of the CFD model is slightly better for this case (i.e., with a RMSD value of 0.16 for the CFD predictions compared to 0.26 for the analytical computations). The bar chart shown in Figure 5-9 (b) compares the errors for the prediction of the flotation rate constants with CFD and analytical calculation. As seen, both analytical computations and the numerical modelling provide acceptable predictions of k for different particle sizes. Using the local values of the flow variables from the CFD data improves the agreement level for the particle size range of $16.2 \mu\text{m} < d_p < 57.2 \mu\text{m}$ compared with Newell's computations using the property based model with inferred

bubble velocity. However, for the finest and coarsest particle sizes the analytical calculations shows slightly better agreement with the experiments.

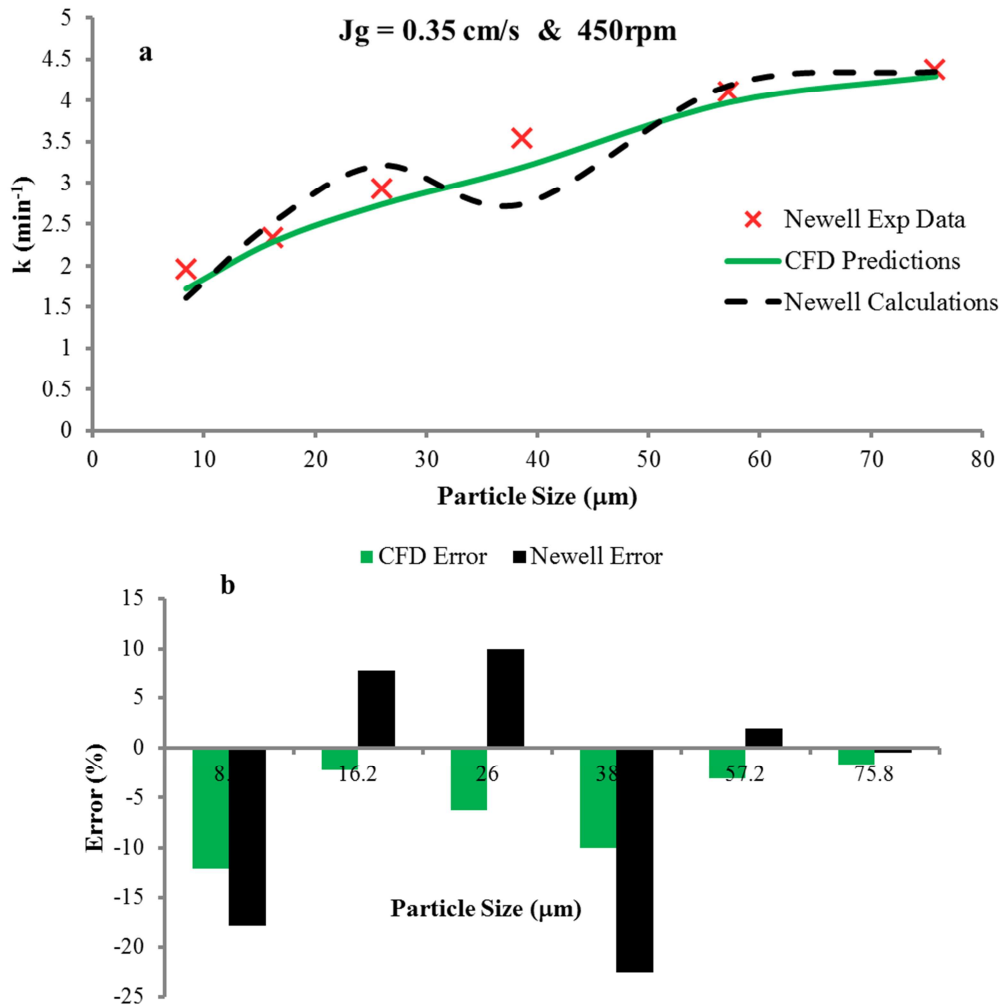


Figure 5-10 (a) flotation rate constant as a function of particle size (b) comparison of the CFD and Newell computation errors for the prediction of the flotation rate constant [Operational conditions: $J_g = 0.35 \text{ cm/s}$ and impeller speed = 450 rpm]

Figure 5-10 (a) shows the numerical predictions of the flotation rate constant for a range of particle sizes at a superficial gas velocity $J_g = 0.35 \text{ cm/s}$ and an impeller speed of 450 rpm. Similar to the previous figure, the symbols display Newell's measurements, the solid line represents the CFD computations, and the dashed line is for Newell's calculations using the fundamental model with spatially averaged flow properties. The CFD predictions resemble the increasing trend of the rate constant with the particle size. A drop in the flotation rate constant computations for $d_p = 38.6 \mu\text{m}$ was reported by Newell that is not consistent with the trend of his experimental data that might be explained by the application of bubble velocity as a fitting

parameter. The computations of Newell for the last two sizes (i.e., $d_b = 57.2 \mu\text{m}$ and $d_b = 75.8 \mu\text{m}$) in the particle size range shows slightly better match with the experiments when they are compared with the CFD results. The deviations of the flotation rate constant from experimental data, expressed as a percentage error, are 1.9%, and 0.5% in the calculations compared with 3.1% and 1.7% in the CFD results. However, for $d_b < 57.2 \mu\text{m}$ the CFD data result in better agreement when they are compared with Newell's computations. For example, for particle diameter finer than $57.2 \mu\text{m}$, the percentage error for the CFD results (i.e., 7.6%) is approximately half of the error percentage of the Newell's computations (i.e., 14.5%). In addition, the RMSD value for the CFD calculations of the flotation rate constants, 0.2, is less than that of the Newell computations (i.e., 0.38). The deviation for each size fraction between the predictions and the experiments is elaborated in the bar chart in Figure 5-10 (b). As can be seen, the lower error percentage of the CFD data compared with the error of the analytical computations using spatially averaged properties strongly indicates that applying local values for the fluid flow in the fundamental flotation model due to Pyke can improve the capability of this model for the prediction of the flotation rate constants.

Figure 5-11 (a) validates the numerical predictions of the flotation rate constants at $J_g = 0.35 \text{ cm/s}$ and the impeller speed of 550 rpm. The symbols represent the measurements of Newell, the solid line is the computed values of k by CFD and the dashed line corresponds to the analytical calculations as reported by Newell. Looking at the trend of experiments shows that both analytical and numerical computations capture the experimental trend (i.e., increasing the flotation rate with the particle size). Moreover, for both the CFD predictions and the analytical computations the overall average error is less than 10% (i.e., 4.61% for the CFD results and 6.18% for the analytical computations) which confirms that both strategies are feasible for the flotation modelling. However, the size-by-size comparison reveals that, for the finest particle size fraction, the CFD data yields closer prediction to the experiments with an average difference of 1.5%, while the error percentage of the Newell computations for this size fraction shows higher magnitude (i.e., 17.8%). For $d_b = 16.2 \mu\text{m}$ the computations of Newell perfectly matched the experiments (with an average difference of 0%), whereas the flotation rate constant determined by CFD for this size range shows 15.2% of difference with the measurements. It is also found that

when the particle size is larger than 16.2 μm the computations and CFD outcomes result in approximately similar level of confidence in the predictions. Figure 5-11 (b) is a bar chart that ensures for $d_b > 16.2 \mu\text{m}$ both methods for the prediction of rate constant are successful. A slight improvement is observed using CFD data, since the root mean square error for the CFD data, 0.19, is lower than the Newell computations RMSD, 0.22.

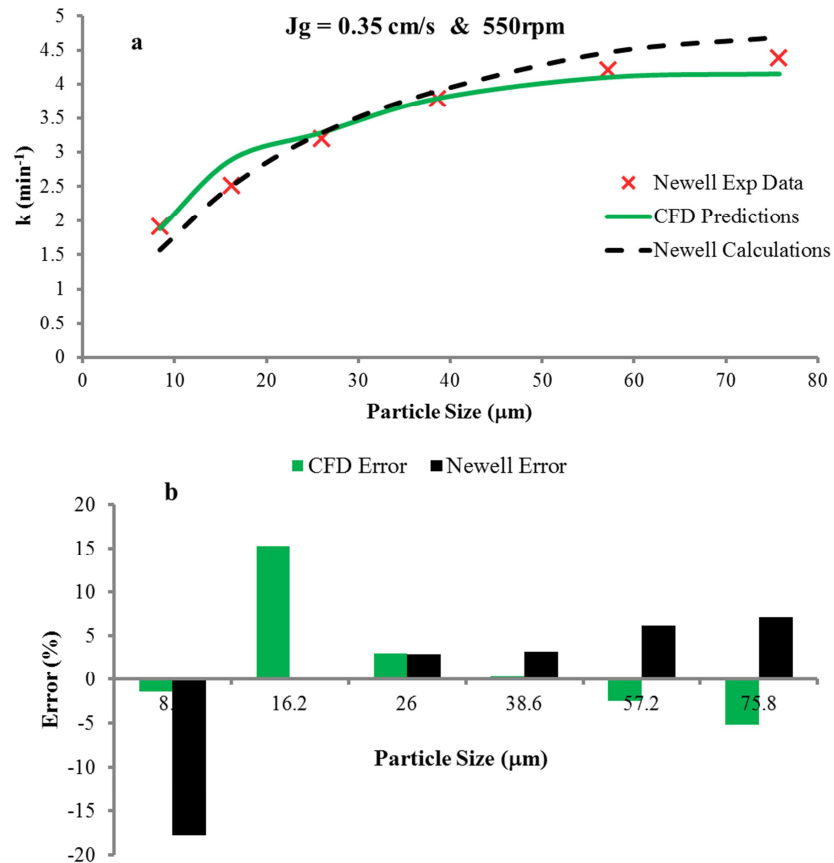


Figure 5-11 (a) flotation rate constant as a function of particle size (b) comparison of the CFD and Newell computation errors for the prediction of the flotation rate constant [Operational conditions: $J_g = 0.35 \text{ cm/s}$ and impeller speed = 550 rpm]

The highest impeller speed that has been tested in this section for investigating the ability of the applied CFD approach for the flotation modelling is 800 rpm. The results of this angular velocity at the superficial gas velocity of $J_g = 0.35 \text{ cm/s}$ are shown in Figure 5-12 (a), where the symbols represent the Newell measurements for the flotation rate constant, the dashed line corresponds to his calculations and the solid line displays the CFD predictions of k at 800 rpm. The predicted trend of the spatially averaged model computations and CFD data both correctly follow the measured flotation rate constants for various particle diameters. Interestingly, at this angular

velocity of the impeller, Newell reported no error in his computations and the predicted values of k_s ideally fit the experiments. This can be attributed to the fact that the bubble velocity term in Eq. 5.12 is treated as a fitting factor in his computations and he showed that lowering the bubble velocity is required to produce the best fit with the experiments. Nonetheless, the application of local values of the flow obtained by CFD yield an acceptable agreement with the measurements. On the size-by-size basis comparison, the error percentages in the CFD results are less than 10.5% (Figure 5-12 (b)), which shows that for the highly turbulent and constantly fluctuating flow field inside the flotation tank, the CFD methodology yields acceptable results. It is noteworthy that for the CFD predictions of rate constants, local values of the gas phase velocity have been utilized, unlike the analytical computations of Newell, in which a spatial average bubble velocity was used as a fitting parameter. The discrepancies between the CFD based results and the experimental data and analytically computed results can be explained by this fact.

The results for the predictions of flotation rate constants at a single superficial gas velocity and various impeller rotational speeds reveal that the CFD approach, combining the temporal and spatial variations of the flow variables with the fundamental flotation model due to Pyke, is able to simulate the flotation separation process with an acceptable degree of confidence in the results. The validations against the experimental data of Newell for quartz particles have built reliance on the developed CFD-kinetic methodology. Moreover, a comparison with the Newell's computations under the same circumstances was performed to inspect the comparability of the CFD strategy with the analytical calculations. The results show that generally the CFD is comparable with the theoretical computations of the k and even for some cases it has provided closer predictions to the experiments. Discrepancies are, however, observed specially at the higher impeller speed. Newell resolved these inconsistencies by reducing the bubble velocity to achieve a closer agreement with the measurements of the rate constants. It can be seen that the model calibration is a common task to manipulate the model's formulation for providing better outcome under different circumstances. Thus, for the remainder of the CFD simulations of the flotation rate constant a multiplicative scaling factor (f_c) is added to the sub-processes term (i.e., $E_c \cdot E_a \cdot E_s$) in Eq. 5.12 to account for the underpredictions observed. The constant value of this parameter was found to be 1.25 to provide closest

agreement with the experiments. Further, it was found that in the computation of the induction time (i.e., t_{ind} in Eq. 5.20) for the attachment efficiency (see: Eq. 5.18 & Eq. 5.19) the β factor was needed to be adapted. Pyke and Newell in their predictions used the recommendation of Dai (Dai et al., 1999) for this value (i.e., $\beta = 0.6$). However, it was found that a range of values $0.6 < \beta < 0.9$ led to better quantitative predictions of flotation rate constants.

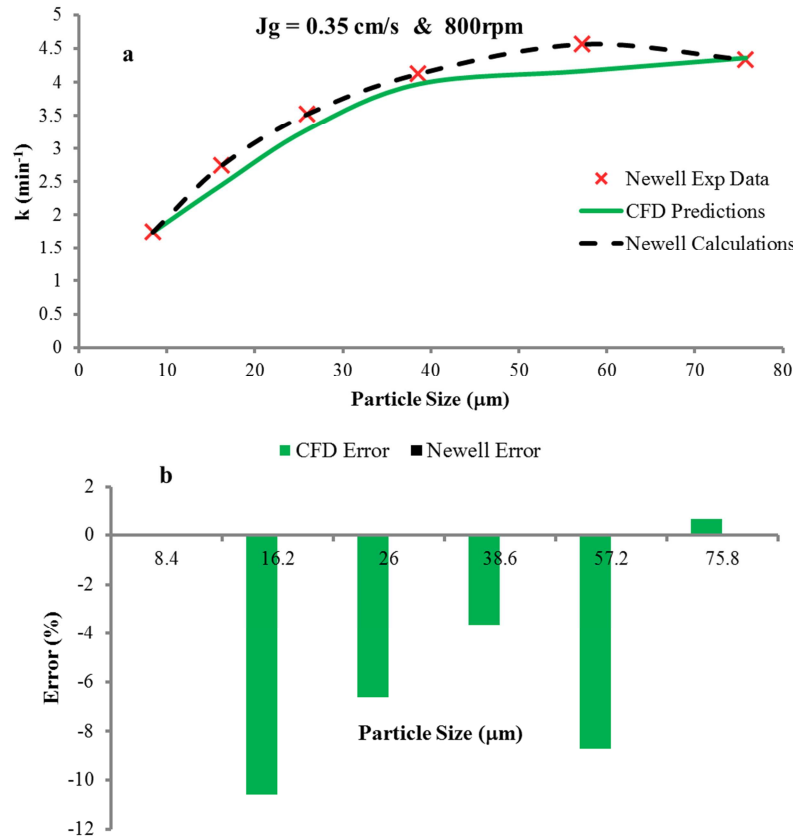


Figure 5-12 (a) flotation rate constant as a function of particle size (b) comparison of the CFD and Newell computation errors for the prediction of the flotation rate constant [Operational conditions: $J_g = 0.35 \text{ cm/s}$ and impeller speed = 800 rpm]

The results presented above support the first hypothesis on the suitability of the CFD method for the flotation modelling. With this established, it can be utilized to address the effects of different parameters on the flotation rate constant. The following sub-sections present the CFD predictions of the flotation rate constants for different particle hydrophobicity, impeller rotational speed and different superficial gas velocities for the sparger.

5.3.3.1. CFD simulation of flotation rate constant for different particle hydrophobicity

The CFD simulations of the flotation rate constant at an impeller speed of 470 rpm, $Jg = 0.45$ cm/s, and $d_b = 0.12$ cm for two different contact angles are carried out (see appendix D for the details of the operational conditions). The influence of the solid particle surface hydrophobicity, leading to different contact angles, is depicted in Figure 5-13. In this figure the cross and triangle symbols represent the experimental data of Pyke and Newell for $\theta_a = 73^\circ$ and $\theta_a = 80^\circ$, respectively and the solid and dotted lines are for the CFD predictions of the two contact angles. The experimental trend of the flotation rate constant has been appropriately captured with the CFD data. For the largest particle size with $\theta_a = 80^\circ$, the numerical predictions show a decrease in the rate constant, whereas the increasing trend of the rate constant continues for the full size range in the experimental measurements. This can be explained because the larger particles increase the Bond number, which accordingly reduces the probability of the stability, E_s , defined as:

$$E_s = 1 - \exp\left(1 - \frac{F_{att}}{F_{det}}\right) \quad \text{Eq. 5.42}$$

At larger particle sizes in the range considered, the detachment forces begin to dominate attachment forces. For the coarsest particle size, the computed value of E_s is 0.96, while for the bulk of the size range investigated, $E_s = 1$. This effect, which is unrelated to the CFD aspect of the simulation, led to a drop in the prediction of rate constant. The quantitative comparison with the experimental data of Newell for $\theta_a = 80^\circ$, shows a very good agreement for $d_p < 75.8$ μm with an overall average difference of 7%. The experimental measurements for $\theta_a = 73^\circ$ reveal that the rate constant has a peak at $d_p = 23.2$ μm , which has been underpredicted with the CFD results (with an average difference of 25%). However, for the other particle sizes in the tested range (i.e., 4.8 $\mu\text{m} < d_p < 15.6$ μm and 23.2 $\mu\text{m} < d_p < 75.8$ μm) the quantitative comparisons yield a reasonable match with the experimental information (within an overall average difference of 19.8% for 4.8 $\mu\text{m} < d_p < 15.6$ μm and 12.3% for 23.2 $\mu\text{m} < d_p < 75.8$ μm). The results presented here show that for a given particle diameter the more hydrophobic the surface of a particle the higher the flotation rate constant. In addition, for the higher contact angle the flotation rate constant increases almost linearly with the particle size, while for $\theta_a = 73^\circ$ after a certain size ($d_b = 23.2$

μm) increasing the particle diameter decreases the flotation rate constant. It is also interesting to point out that the effect of hydrophobicity for the coarser particles is more pronounced. In other words, although the particles with larger diameters might detach from the air bubbles (as seen for the lower contact angle) because of their weights, increasing their hydrophobicity will enhance the attachment forces relative to the detachment forces.

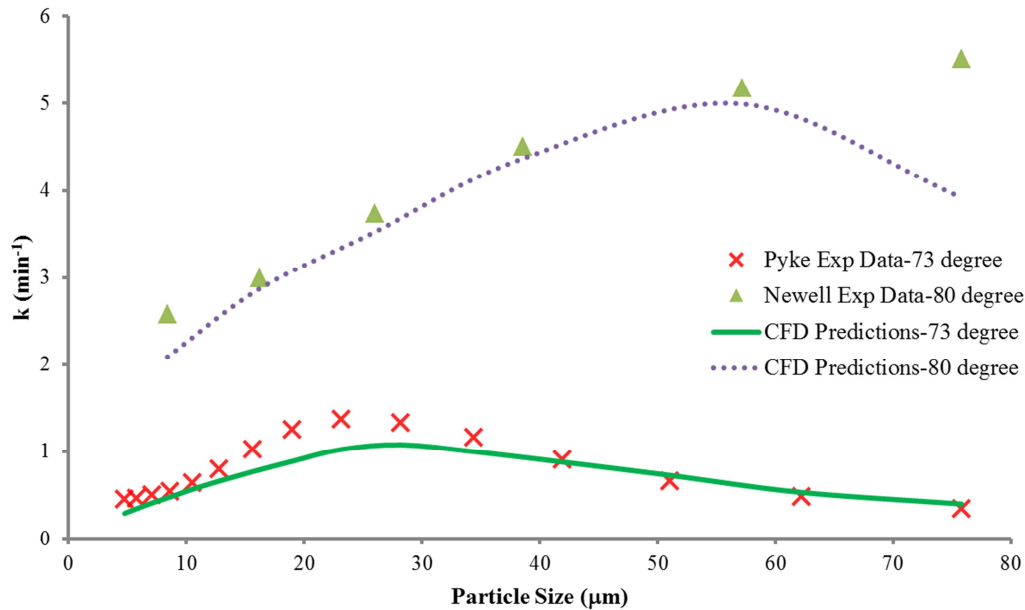


Figure 5-13 Flotation rate constant of quartz as a function of particle size for two contact angles, $\theta_a = 73^\circ$ and $\theta_a = 80^\circ$ [Operational conditions: $Jg = 0.45$ cm/s and impeller speed = 470 rpm]

5.3.3.2. CFD simulation of flotation rate constant for different impeller speeds

The CFD simulations of the flotation rate at a constant $Jg = 0.45$ cm/s and $\theta_a = 73^\circ$ for two different angular velocities of the impeller, 470 rpm and 650 rpm corresponding to two different bubble diameters $d_b = 0.117$ cm and $d_b = 0.139$ cm, are conducted. Figure 5-14 is a plot that shows the effect of impeller speed on the flotation rate constant. The two different symbols and line styles illustrate the experimental measurements and the numerical predictions for the different speeds, respectively. The experiments exhibit a bell shape distribution of flotation rate constant with a bias to the particles with the smaller diameters. The numerical predictions not only capture the maximum flotation rate constants, but for the entire size ranges of the particles the trend of experiments and the simulated data are alike. Further, the size-by-size comparison shows that the CFD results of the maximum

flotation rate constants match the experiments very closely with an average difference of 2% for 470 rpm and 4.3% for 650 rpm. Moreover, the overall error percentage for the investigated impeller speeds is reduced from 7.5% to 5.3% by increasing the impeller angular velocity.

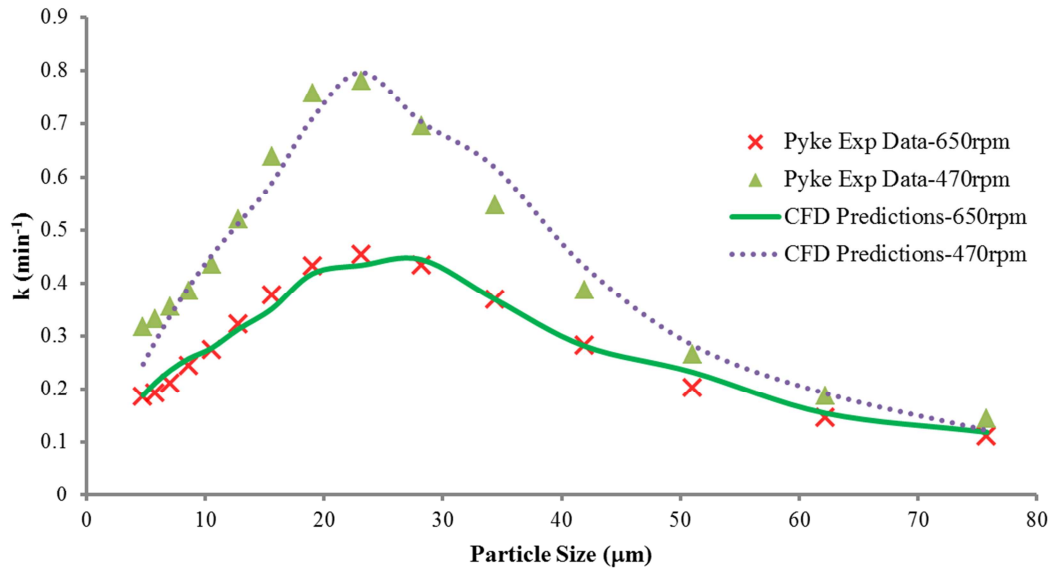


Figure 5-14 Flotation rate constant of quartz as a function of particle size for two impeller rotational speeds, 470 rpm and 650 rpm [Operational conditions: $J_g = 0.35$ cm/s and $\theta_a = 73^\circ$]

Increasing the agitation rate at a constant gas flow rate and hydrophobicity of particle decreases the flotation rate constant. This is explainable by the fact that higher impeller speed generates more turbulence within the tank resulting in more detachment of the solid particles from the air bubbles. At the both levels of the impeller speeds the rate constant increase with increasing the particle size up to 23.2 μm . For the coarser particle diameters ($d_p > 23.2$ μm), however, the decrease in the bubble-particle stability yields a reduction in the rate constant.

5.3.3.3. CFD simulation of flotation rate constant for different superficial gas velocities

The CFD simulations of the flotation rate constant at 470 rpm for quartz particles with $\theta_a = 73^\circ$ were performed to investigate the influence of the gas flow rate on the flotation separation behaviour. Two different superficial gas velocities, namely 0.35 cm/s and 0.45 cm/s, have been tested. Figure 5-15 compares the numerical predictions of k with the measurements of Pyke. In this graph two symbols, triangles and crosses, represent the experimental data for the gas velocities of 0.35 cm/s and

0.45 cm/s, respectively, while the dotted and dashed lines correspond to the CFD predictions of k for the applied gas velocities. The flotation rate constant shows a maximum for $d_p = 23.2 \mu\text{m}$ for both gas flow rates investigated. The trend of the flotation rate computed by the CFD approach has also illustrated a maximum for the same particle diameter. Further, the decreasing in the rate constant for $d_p > 23.2 \mu\text{m}$ for both gas velocities has been correctly captured with the CFD predictions. However, increasing the gas flow rate from 3.5 l/min to 4.5 l/min increases the percentage error for the prediction of the maximum flotation rate constant from 2% to 25.1%. This can be attributed to the fact that increasing the gas flow rate yields an increase in the turbulent properties of the gas phase. However, using the dispersed k- ϵ turbulence model only accounted for the turbulence in the liquid phase and the gas phase is assumed to be laminar. One possible solution to reduce the magnitude of error between the predicted flotation rate constants for the high gas flow rate and the experiments is inclusion of an additional source term for the governing equations to take into account the turbulence caused by the high superficial gas velocity.

For the finer particles the numerical calculations show a reasonable agreement with the experiments, e.g. at the gas flow rate of 3.5 l/min the overall average difference for $d_p < 23.2 \mu\text{m}$ is 7.5%, where the corresponding value for the gas flow rate of 4.5 l/min increases to 21.5%. The numerical predictions of flotation rate constant for the intermediate and coarse particles $d_p > 23.2 \mu\text{m}$ also shows good agreement with the experimental data (with an overall average difference of 8.3% for the gas flow rate of 3.5 l/min and an overall average difference of 12.3% for the gas flow rate of 4.5 l/min). In addition, an increase is evident by sparging more gas into the tank for all particle sizes. However, this increase is more noticeable for the intermediate particle size range of $15.6 \mu\text{m} < d_p < 34.4 \mu\text{m}$.

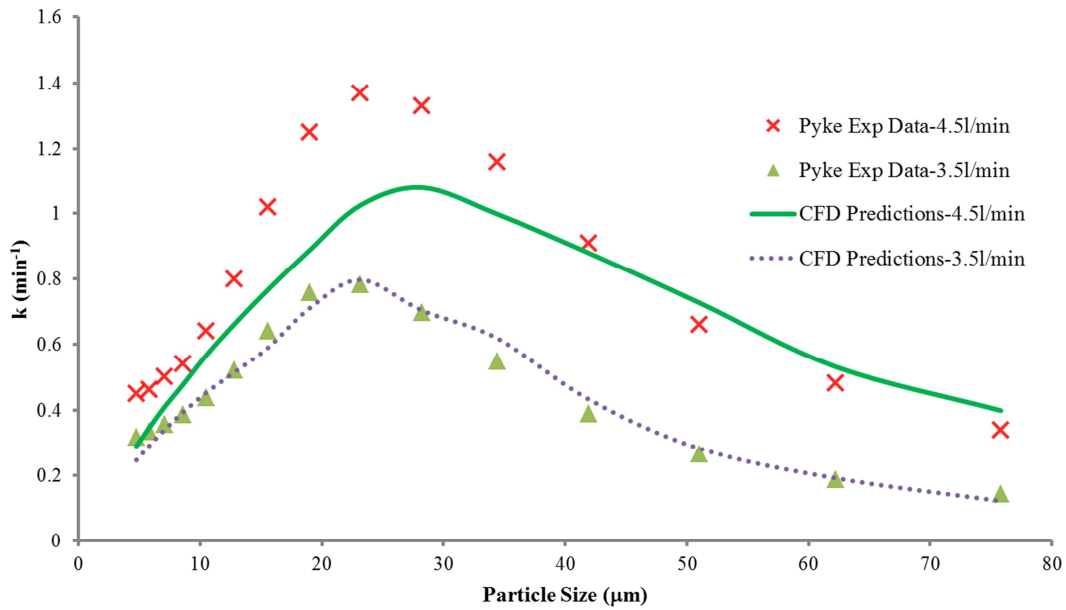


Figure 5-15 Flotation rate constant of quartz as a function of particle size for two gas flow rates, 3.5 l/min and 4.5 l/min [Operational conditions: impeller speed = 470 rpm cm/s and $\theta_a = 73^\circ$]

5.3.4. Validation of the model for galena flotation rate constants

The previous sub-section on the flotation modelling of quartz particle confirms that the developed CFD-based methodology is able to predict the flotation rate constant over a range of particle diameters. This section evaluates the potential of the CFD-kinetic model to simulate the flotation of galena under different conditions. The influence of the particle hydrophobicity and the angular velocity of the impeller on the flotation rate constant were investigated. Figure 5-16 is a chart that summarizes the CFD simulations performed for this parametric study. The accuracy of the numerical predictions is validated against the experimental measurements of Pyke for the same operational conditions (Pyke, 2004). The results of this investigation are presented in the following sub-sections.

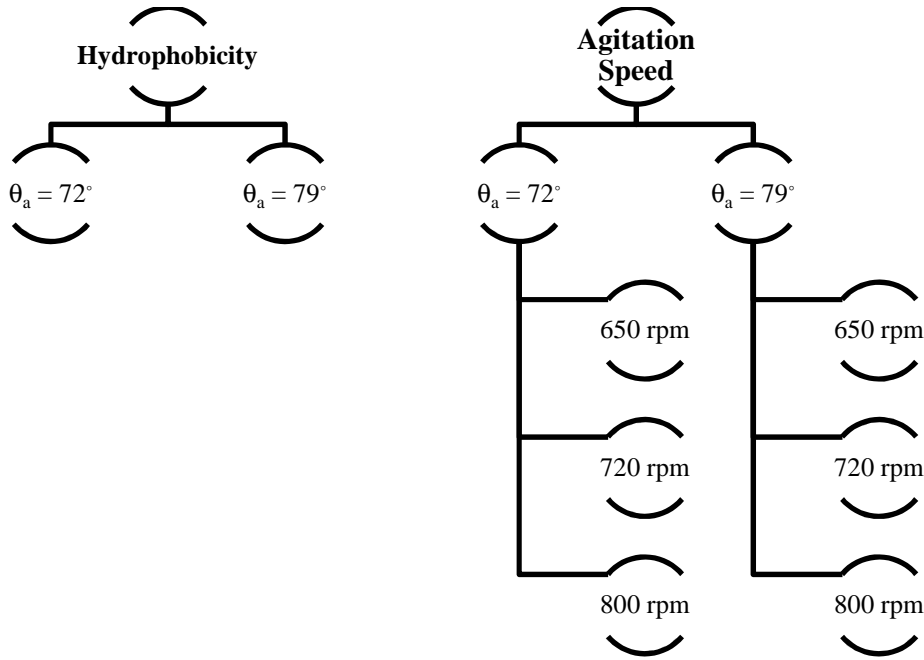


Figure 5-16 Summary of the CFD simulations for the investigation of the effect of hydrophobicity and agitation speed on the flotation rate constant of galena

5.3.4.1. CFD simulation of flotation rate constant for different particle hydrophobicity

The CFD simulations of galena flotation rate constant at the superficial gas velocity of 0.55 cm/s, impeller speed of 650 rpm and a constant bubble diameter of 0.065 cm were performed. The details of operational conditions for the galena flotation simulations performed are summarized in Appendix D. The main objectives in these simulations are to explore that whether the CFD-kinetic model provides reasonable predictions for the galena flotation rate constant and then to consider the effect of increasing hydrophobicity on the floatability of the galena particles. Figure 5-17 shows and validates the results of flotation rate constants for a range of galena particle size distribution. In this figure the circle and triangle symbols display the galena particles with contact angles of $\theta_a = 79^\circ$ and $\theta_a = 72^\circ$, respectively, whereas the solid and dashed lines correspond to the numerical predictions of the rate constants for the applied contact angles. For the less hydrophobic case with contact angle of 72° increasing the particle size did not significantly change the rate constant and an approximately flat line for $d_p > 12.8 \mu\text{m}$ is shown in Figure 5-17. This trend has been properly captured with the numerical predictions, too. For $\theta_a = 79^\circ$ an initial increase in the rate constant for the particles with $d_p < 23.2 \mu\text{m}$ transforms to a declining line

for the intermediate and coarse particles. The captured trend of the galena flotation rate constant by CFD predictions also follows the same path.

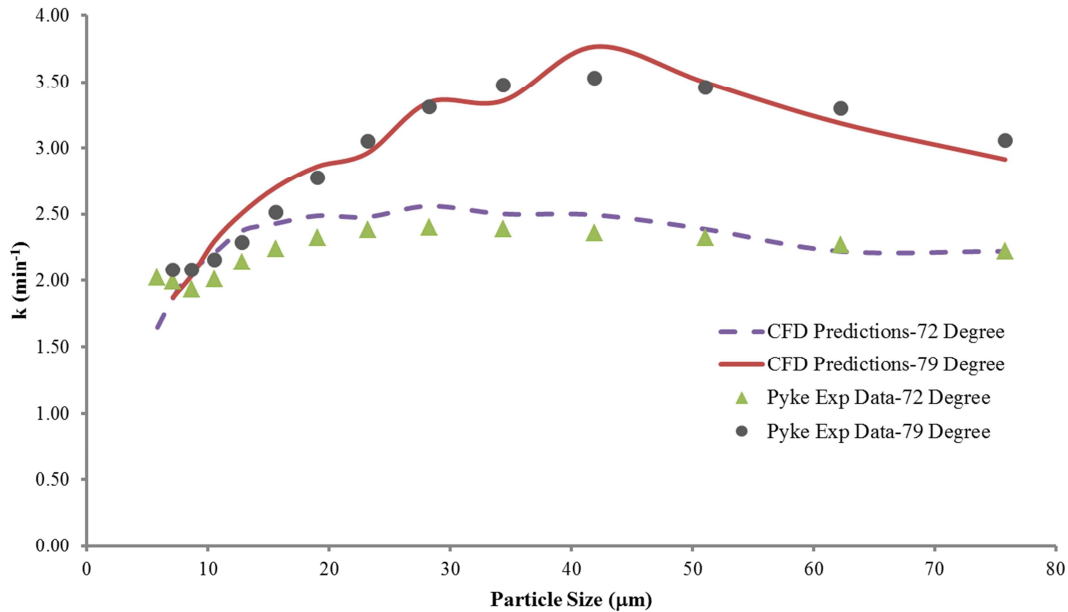


Figure 5-17 Flotation rate constant of galena as a function of particle size for two contact angles, $\theta_a = 72^\circ$ and $\theta_a = 79^\circ$ [Operational conditions: $J_g = 0.55$ cm/s and impeller speed = 650 rpm]

Quantitative comparison reveals that for fine particles with $d_p < 12.8$ μm the CFD results match the experiments reasonably well with an average difference of 10.6% for $\theta_a = 72^\circ$ and 7% for $\theta_a = 79^\circ$. Moreover, the low overall error percentages for the particle diameters larger than 12.8 μm (i.e., 4.6% for $\theta_a = 72^\circ$ and 3.8% for $\theta_a = 79^\circ$) indicate that the applied CFD methodology can simulate the behaviour of the galena particles with different hydrophobicity. Increasing the hydrophobicity of the particle surface for fine particle $d_p < 12.8$ μm merely increases the flotation rate constants for these particles. However, using more collectors to enhance the contact angles of the medium and large size galena particles considerably increases the flotation rate constants, as can be seen in Figure 5-17.

5.3.4.2. CFD simulation of flotation rate constant for different impeller speeds

The CFD simulations of the galena flotation rate constant at the superficial gas velocity of 0.55 cm/s for three different angular impeller velocities, namely 650, 720, and 800 rpm with corresponding bubble diameters of 0.065 cm, 0.07 cm and 0.07 cm, were carried out. The simultaneous effects of agitation rate and the particle hydrophobicity on the rate constant are the main aim of this analysis. Figure 5-18

displays the numerical predictions and the experimental measurements of the galena rate constants for $\theta_a = 72^\circ$ and $\theta_a = 79^\circ$ as a function of particle size. In this figure three different symbols are used to illustrate the experimental measurements of Pyke for the various rotational speeds, while the three line styles represent the CFD computations for different impeller speeds. Figure 5-18 (a) shows that at different agitation speeds for $d_p < 19 \mu\text{m}$ the rate constant increases with the particle size and this behaviour has been captured by the numerical predictions of k . The experimental measurements also show that for 650 rpm and 800 rpm the rate constant is less sensitive to the particle size, as the rate constant for these two speeds shows an almost flat line for $d_p > 28.2 \mu\text{m}$. The numerical predictions for the lowest and highest rpms also reveal independency from the particle size. For the impeller speed of 720 rpm both CFD and experimental data show a maximum flotation rate constant at $d_p = 28.2 \mu\text{m}$ that is followed by a slight reduction in the rate constant for $d_p > 28.2 \mu\text{m}$. In addition to the good qualitative agreement, the quantitative comparison of the numerical predictions with the experimental measurements at various rpms shows that the CFD method successfully predict the experiments with an overall average difference of 6.8% for 650 rpm, 11.26% for 720 rpm and 6.5% for 800 rpm.

Figure 5-18 (b) confirms that for the particle diameters less than $34.4 \mu\text{m}$ a linear increase by the particle size in the rate constant is evident. However, this increase for $d_p > 34.4 \mu\text{m}$ is reduced and becomes somewhat independent of the particle size. The predicted trends with the CFD method are also similar to the trends of experiments for $\theta_a = 79^\circ$ at different agitation rates. The size-by-size comparison of the k for the galena particles with $\theta_a = 79^\circ$ reveals that the numerical predictions of the flotation rate constants match the experiments sensibly well (with an overall error percentages of 4.2% for 650 rpm, 7.7% for 720 rpm and 9.2% for 800 rpm).

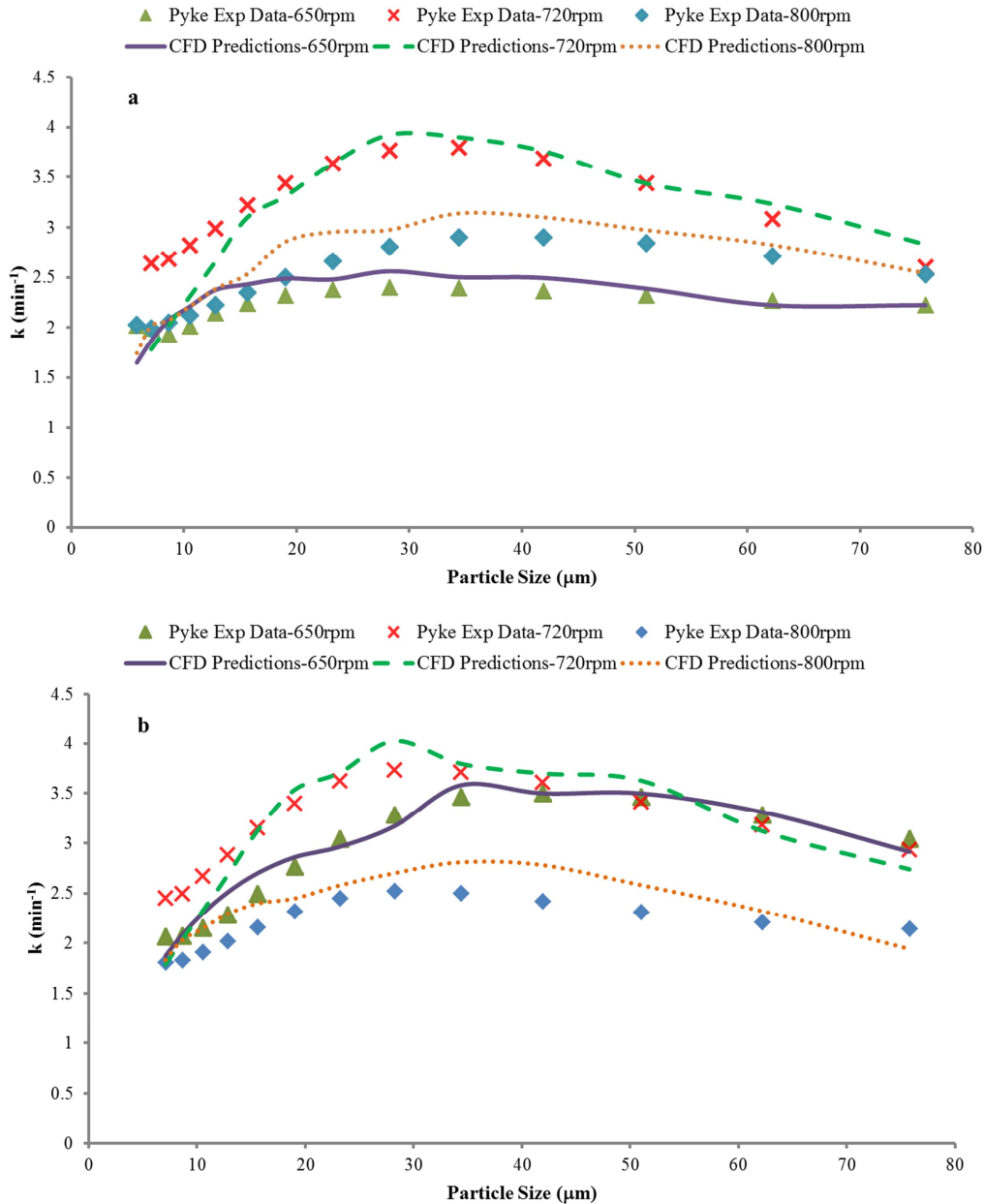


Figure 5-18 Flotation rate constant of galena as a function of particle size at different agitation speeds of impeller (a) for $\theta_a = 72^\circ$ and (b) for $\theta_a = 79^\circ$ [Operational conditions: $J_g = 0.55$ cm/s]

For the less-hydrophobic galena particles in Figure 5-18 (a) increasing the angular velocity from 650 rpm to 720 rpm substantially increases the flotation rate constant for all the particle diameters. However, further increase in the impeller speed from 720 rpm to 800 rpm reduces the flotation rate, significantly. This effect is more severe for the fine particles, as can be seen for $d_p < 19$ μm both the numerical predictions and the experimental measurements at 650 and 800 rpm are overlapped. It implies that for the galena particles with $\theta_a = 72^\circ$ an optimum rotational velocity of impeller exists for which the highest flotation rate can be achieved.

Regarding the more hydrophobic galena particles with $\theta_a = 79^\circ$ increasing the impeller speed from 650 rpm to 720 rpm only has an intensifying impact on the intermediate and fine particles (i.e., $d_p < 34.4 \mu\text{m}$) and for coarse particles negligible effect is observed. Additionally, at 800 rpm the flotation rate constants across all particle sizes is considerably decreased, which is similar to the flotation behaviour of the particle with $\theta_a = 72^\circ$. The significant reduction in the flotation rate constants by increasing the rpm from 720 rpm to 800 rpm observed for both contact angles can be explained by the fact that at the higher turbulent intensity the stability efficiency will be decreased. In that, the interaction of the turbulent eddies with the bubble-particle aggregates at high turbulent region in the tank results in more destruction of the aggregates which in turn reduces the overall flotation rate constant. It is also found that for both contact angles investigated the optimized angular velocity of the impeller, 720 rpm, yields the maximum flotation rate constant for the galena particles.

5.3.5. Comparison of the developed CFD methodology with the available alternatives

The results presented in this chapter show that the developed CFD methodology was able to predict the flotation rate constants for different minerals with reasonable level of agreement when compared with the experimental data. As discussed in sub-section 2.6.2, there is another CFD methodology capable of predicating the flotation rate constant developed by Koh and his colleagues (Koh et al., 2000, Koh and Schwarz, 2003b, Koh and Schwarz, 2006b). In their approach a population balance equation was solved for the number of free particles within the tank. In order to account for the flotation sub-processes two source terms were included in the population balance model calculating the influence of the attachment and the detachment sub-processes. They have also incorporated a bubble loading factor which assumed 20 to 30% of a bubble can be occupied by the solid particles. The bubble-particle collision rate was calculated using Abrahamson equation (Eq. 2.3) (Abrahamson, 1975) with a probability function (Yoon and Luttrell, 1989) evaluating the efficiency of the collisions between the air bubbles and solid particles. Similar to this study the detachment probability was assessed based on the force balance between the attaching and detaching forces using Bond number. Furthermore, the probability of the attachment in Koh studies was quantified using the proposed equation of Yoon and Luttrell (Yoon and Luttrell, 1989), while in the current study

Eq. 5.18 formulated by Dobby and Finch (Dobby and Finch, 1987) was applied for the attachment efficiency. Regarding to the attachment probability Koh et al., used an empirical equation with the fitted constants for the calculation of the induction time. However, in this study, Eq. 5.20 attained the induction time with two constants one recommended by Dai (Dai et al., 1999) and the second one was calculated based on Eq. 5.21. It is also noteworthy that in the current study there exist a term in Eq. 5.12 that comprises the mechanical features of the flotation cell by having the gas flow rate and the volume of the apparatus. However, the mechanical aspects of the flotation tank have not been integrated in Koh's approach.

As mentioned, one of the main differences of this study with that of Koh et al. is that they included a population balance model and the resultant graph of the recovery as a function of time was used to obtain the overall rate constant. In the current study the flotation rate constant was computed directly and weight-averaged for the entire tank, without the necessity for solving an extra partial differential equation. This can eventually help to reduce the computational demands when CFD is aimed for the industrial flotation tanks. It is also worth pointing out that the exact CFD-kinetic model developed in this study can be incorporated into a population balance model which eliminates the need for two sources, as used by Koh et al. The general format of a population balance equation by application of the developed strategy in this study is as follows:

$$\frac{dN_p}{dt} = -k \times N_p \quad \text{Eq. 5.43}$$

where N_p is the number of free particles and k can be calculated by Eq. 5.12.

Overall, both methodologies are able to predict the flotation rate constants using CFD. From the practical point of view, they can be applied for laboratory scale flotation tanks; however for application of these methods for the industrial flotation tanks special attention should be given to the inclusion of the extra set of equation and the level of mesh refinement.

5.4. Conclusion

In order to apply the CFD method for flotation modelling, three hypotheses were investigated throughout this chapter. The first one concentrated on the applicability of the CFD data for modelling of the flotation separation. The kinetic-

based fundamental flotation model due to Pyke for the flotation rate constant allowed us to test this hypothesis. The model was analysed and its potential to be combined with the numerical modelling was confirmed. The proposed model of Pyke utilizes three aspects of the flotation process to explain the flotation rate constant of solid particles. The first parameter, which indicates the mechanical properties of the flotation tank, cannot be enhanced by addition of CFD modelling. However, it was found that the second term in the expression due to Pyke, accounting for the turbulent nature of the flow field inside the tank, can be integrated with the numerical analysis. The turbulent dissipation rate and the turbulent velocity of the fluid in the Pyke's equation were replaced with the CFD data. This was done to verify the theory that using local hydrodynamic properties of the flow will lead to a presentation of the turbulent flow inside the flotation tank which is closer to the reality.

The last term, determining the flotation sub-processes, in the flotation model due to Pyke can also be enhanced with the detailed information of the flow field obtained by CFD. The local values of the bubble velocity and the turbulent dissipation rate are implemented into the last term of the model to calculate the efficiencies of the micro processes. The CFD solver was then enhanced with different UDFs to investigate whether CFD is suitable for flotation modelling. In order to assess the viability of this assumption, CFD simulations of the flotation of quartz particles for different impeller speeds were carried out. The validations against the experimental data revealed that the numerical modelling resulted in accurate computations of the flotation rate constants for the different angular velocities of the impeller. The developed CFD methodology only followed the trend of the experimental data for a range of particle size distribution but also yielded precise results, reflecting the suitability of the numerical analysis.

The second hypothesis, concerning possible improvements in flotation modelling by using CFD, was evaluated through comparing the numerical analysis with the analytical computations. The CFD results for the quartz flotation rate constants were compared with the Newell's calculations. Similar to the Pyke's approach, Newell also applied the average hydrodynamic values of the slurry and used the bubble velocity as fitting factor for the fundamental flotation model due to Pyke to compute the flotation rate constant of quartz. The comparison of the CFD modelling and the theoretical computations for different impeller speeds showed that

the numerical strategy is comparable with the analytical computations. Besides, it was established that for the lower impeller speeds the CFD predictions were superior to the analytical computations due to the fact that the transient and fluctuating magnitudes of the flow quantities resemble the flotation phenomenon closer to the real situation. Also, there was no requirement for using the bubble velocity as fitting parameters, which made the model more predictive. Therefore, the confirmation of the second hypothesis tested in this chapter paved the path to apply the CFD-kinetic model for the further investigations.

As the final step in this chapter, the effects of particles hydrophobicity, agitation speed, and gas flow rate on the flotation rate constants of quartz and galena minerals were determined using the CFD method. The numerical predictions were validated with the experimental data of Pyke for a laboratory scale standard Rushton turbine flotation tank. The main conclusions that can be drawn from this parametric study are articulated here:

- For quartz particles:
 - Increasing the hydrophobicity increases the flotation rate constant. This effect is more noticeable for the coarse particles.
 - Decreasing the angular velocity of the impeller increases the floatability of the intermediate size particles.
 - Sparging more air bubbles into the flotation tank increases the rate constant for the intermediate size particles which is reduced by the particle size.
- For galena particles
 - Increasing the contact angle demonstrates an increase in the flotation rate constants of the intermediate and coarse particles.
 - Increasing the rpm has insignificant effect of the flotation rate constant of the fine particles.
 - Increasing the impeller speed shows that there exists an optimized angular velocity, regardless of the hydrophobicity level of the particles, for which the maximum flotation rate constant can be obtained.

The correlations between the flotation rate constants and the influential parameters of the flotation separation process have been both qualitatively and

quantitatively simulated by the developed CFD-kinetic model. The findings in this chapter have shown that CFD can be used as a reliable and cost-effective tool for the flotation modelling. Furthermore, the application of this methodology can be easily extended for the other types of minerals and flotation tanks, since the quantitative comparisons, presented in this chapter, have ensured us about the predictive capability of the CFD-kinetic model under different conditions. One might conclude from this chapter that the typical weakness of the empirical equations for the flotation modelling (i.e., assuming that the flow parameters are spatially constant) has been shown and amended through the application of the varying flow properties. CFD determined the velocity components and turbulent properties at every grid points inside a Rushton turbine flotation tank. The values were then applied by a property based model to predict the flotation rate constant. This current strategy improved the predictive capability of the kinetic based model, compared to when it was used to obtain the flotation rate constant using the spatially averaged values for the hydrodynamic characteristics of the flow field. However, there are potential points in the developed methodology that can be further studied and improved. The next chapter of this dissertation describes how one can advance this modelling method.

Chapter 6 Conclusions and Recommendations

6.1. Research summary

The main aim of this research was to establish a CFD-based model to improve the physical understanding and the prediction of the separation process inside the flotation tank. This was approached through a series of distinct stages in which three different CFD methodologies were developed. In each step of this work, special attention was placed on the two features of the modelling methods. The model should provide accurate predictions of the fundamental flow variables inside the flotation tanks, while the required computational resources of processing time and memory storage remain affordable.

The first step was to conduct a thorough review of the previous literature on CFD applications for mechanically agitated vessels. One of the key points in the single-phase modelling of stirred tanks is the difficulty in predicting the turbulent properties. The disagreement between the numerical predictions with the real turbulent flow features (i.e., the turbulent kinetic energy and the turbulent dissipation rate) is often attributed to the mesh refinement level. Due to the lack of computational power for conducting simulations over an extremely fine mesh, this problem has remained. In addition, the inherent uncertainties in the single-phase modelling of stirred tanks were often not quantified owing to the absence of a standard approach for reporting the numerical uncertainties. It was also found from previous research on gas-liquid modelling inside the stirred tank that the issue of the drag force has received considerable attention. Hence, various formulations for the drag coefficient correlations were proposed to accurately incorporate the interactions between the dispersed air bubbles and the continuous liquid phase.

Establishing the current state of art for the CFD modelling of the fluid flow for mechanically agitated tanks enabled us to initiate the first stage of this work. In the preliminary step, the governing equations for modelling water inside stirred tanks were undertaken. In order to develop a robust model, the equations were solved for

different stirred tanks including an unbaffled mixer and a standard Rushton turbine tank. The model uncertainties for the predictions of the velocity components and the turbulent characteristics were minimized using different dimensions for the rotational zone as well as exploring different turbulence models. The results for two computational domains tested showed that the optimized extensions of the rotational zone around the impeller would lead to the best predictions of the flow properties if the standard k - ϵ model is applied. Moreover, the inherent numerical uncertainties for the simulated data were evaluated with the GCI method which is a verified strategy to quantify the required level of grid density for attaining asymptotic values of the flow variables. The findings from the GCI test showed that the observed discrepancies between the turbulent flow responses and the experimental measurements are not caused by the grid resolution and they might be improved using LES or DNS modelling approaches. Finally, the developed methodology for the single-phase was utilized to explore the effects of angular velocity on the flow patterns, turbulent properties and the generation of trailing vortices.

The second step of this research focused on improving the modelling techniques for gas-liquid simulation inside stirred tanks. The gas-liquid modelling strategies were constructed on the single-phase basic findings. An Eulerian-Eulerian multiphase model along with the dispersed k - ϵ turbulence model was applied to model the dispersed air bubbles with constant diameter in the continuous liquid phase. Different configurations for the sparger were implemented to minimize the model uncertainties of the numerical predictions. It was evident that a sparger placed at the mid-clearance with a diameter of 40% relative to the impeller diameter provided the closest predictions of the gas holdup compared to the measurements. In addition, the Eulerian-Eulerian framework was extended by the available drag coefficient correlations (i.e., Schiller-Naumann, Baker, Brucato, Khopkar, and Lane) to compare the predictive potential of them for the multiphase modelling. The best correlation for the drag coefficient was then used to perform a comparative study for three stirred tanks with 2.5 l, 10 l, and 50 l volumes. The influences of the gas flow rate and impeller rotational speed on the gas volume fraction inside the tank were investigated. The observed results confirmed that the developed CFD methodology was able to correctly represent the flow field characteristics for the further studies.

The final step was to extend the multiphase methodology for flotation modelling. This involved incorporating the CFD outcomes into a kinetic based model. The fundamental flotation model due to Pyke (Pyke, 2004) for the flotation rate constant was analysed and the pertinent points where the formulation could benefit from the CFD data were identified. The flotation model due to Pyke in conjunction with the equations for the flotation sub-processes were coded into the CFD solver. The validity of the CFD-kinetic model was evaluated for the simulation of the hydrophobic quartz particles in a laboratory scale Rushton turbine flotation tank. The numerical predictions of the flotation rate constants were validated against the experimental data of Newell (Newell, 2006). The observed agreement ensured that CFD can be practically used for the flotation modelling. The analytical computations of Newell were also compared with the numerical predictions from CFD and it was found that the implemented local values of the fluid flow for the flotation rate constant modelling provided either comparable results to the experiments or more accurate estimations of the quartz flotation rate constants for the lower impeller speeds. The CFD-kinetic model was also applied to study the effects of the agitation rate, gas flow rate and the surface hydrophobicity for the flotation of quartz and galena particles. The results yielded acceptable agreement with the experimental measurements in all cases. Thus the viability of the developed CFD-kinetic model was established, suggesting that the new model can help for the flotation analysis and optimization.

6.2. Summary of the fundamental findings

This research has developed a CFD-kinetic model for the flotation modelling. To achieve this, the project has been divided into three major phases entailing developments of models for the single-phase, gas-liquid and the flotation separation. The following are the significant contributions of this dissertation:

- A comprehensive review of the previous literature on the CFD modelling of single-phase, gas-liquid, and flotation process in stirred tanks will serve as a convenient point to start the future research in this field.
- It was found that for the single-phase modelling of the stirred tank the model uncertainties caused by the impeller modelling approach (i.e.,

MRF) can be minimized by using a rather small rotational zone around the impeller.

- The choice of turbulence model for the single-phase modelling was found to contribute significantly to the model uncertainties due to the different formulations and the assumptions that each model uses. It was also found that choice between the standard k- ϵ turbulence model and LES, is predicated by making a balance between the higher computational demands of LES with its sophisticated method to deal with the small scale eddies and the isotropic assumption of the standard k- ϵ with its affordable CPU time.
- The GCI method was introduced to quantify the inherent numerical uncertainties in the CFD predictions of the single-phase modelling inside the tank. The computed values of the GCI revealed that the common underpredictions of the turbulent properties cannot be improved with the mesh refinement and the modification should be performed on the modelling approaches.
- It was found that the single-phase method is able to predict the flow patterns, turbulence properties and the formation of trailing vortices behind the blades. Moreover, increasing the rotational speed of the impeller was found to have an increasing influence on the swirling motion of the vortices.
- An Eulerian-Eulerian multiphase framework was established for the gas-liquid modelling inside the stirred tank. This approach provides a computationally economic model that predicts the two-phase flow details inside the stirred tank with an acceptable level of accuracy.
- The commonly omitted CFD issue in the gas-liquid modelling, application of different sparger designs, was accounted for in the current study. It was found that the method of sparging air into the computational domain can significantly contribute to the model uncertainties of the CFD data.
- Comparison of the various sparger configurations showed that not only the sparger diameter and shape could alter the gas holdup inside the

tank but its placement with respect to the impeller would change the air bubble behaviour within the domain.

- It was found that among the different arrangements for the sparger, the disk sparger with a diameter of 40% of the impeller diameter would lead to minimum error in the gas holdup predictions when it is located at the mid-clearance.
- A thorough comparison of the different drag coefficient correlations for the laminar and turbulent modelling of the gas-liquid inside the mechanically agitated tank was carried out. It was found that the Schiller-Naumann model (Schiller and Naumann, 1935) for the laminar flow could determine the gas holdup closer to the measurements, whereas the turbulent flow of the gas-liquid inside the stirred tank was correctly captured using Lane drag model (Lane, 2006). This model provides accurate predictions of the gas holdup as well as the location and formation of the gas cavity inside the vessel.
- The predictive ability of the Lane model for the drag coefficient was tested for operational and geometrical changes. The predicted gas holdup values for 3 different scales stirred tanks operating with diverse impeller speeds and gas flow rates corroborated the credibility of the Lane model for the stirred tanks modelling.
- The Eulerian-Eulerian multiphase approach was extended to model the flotation separation process. In order to do that a CFD-kinetic based model was constructed by combining the CFD outcomes with the fundamental flotation model due to Pyke (Pyke, 2004).
- The CFD-kinetic model was tested for the predictions of quartz flotation rate constants under different angular velocities. It was found that the new model can quantify the flotation rate over a range of particle size distributions. The validations against the experimental measurements ensured the practicality of the new method.
- In developing the CFD-kinetic model for the flotation rate constant, the bubble velocity was extracted from the local values of the gas phase velocity magnitudes, unlike the theoretical computations in which this term was treated as a fitting factor.

- The model was also compared with the analytical computations of Newell for the flotation rate constant of quartz (Newell, 2006). It was found that the new model produced comparable results with the theoretical calculations and for the impeller speed < 800 rpm the agreement with the experiments was improved compared with the analytical computations using spatially averaged flow parameters.
- The CFD-kinetic model was also utilized to simulate the flotation behaviour of quartz and galena particles to investigate the influence of hydrophobicity, impeller speed and gas flow rate on the flotation rate constants. The developed numerical approach correctly predicted the flotation rate constants of quartz and galena for different operational conditions.
- It was found that for quartz flotation, one can increase the rate constant by increasing the hydrophobicity of the particles and the gas flow rate, while the agitation rate is decreased. In addition, for the galena particles increasing the contact angle and the impeller speed resulted in an increase for the flotation rate constant.

6.3. Recommendations

In order to further extend this research, it must be remembered that a three-step method was applied to develop a CFD model for the flotation process. Thus, future study can be conducted on single-phase, gas-liquid, and flotation modelling to improve the simplifying assumptions applied in the current work. Even though significant accumulated knowledge is available for the single phase modelling of water inside the stirred tanks, nowadays the enhanced computational power (combination of CPU and graphics processing unit (GPU)) can enable researcher to start applying DNS modelling of water around the agitation system. This will directly reduce or even eliminate the model and numerical uncertainties in the CFD predictions. This will also allow a deeper understanding of the flow features around the impeller to emerge. Further, it is recommended that the GCI method will be applied for future studies as a standard convention of reporting the numerical uncertainties. This can be combined with the typical grid independence study to find the optimized mesh resolution for which two criteria will be satisfied: first a solution

independent of the number of elements and second, minimized numerical uncertainty for the optimized grid density.

For gas-liquid modelling, other types of sparger such as porous media can be incorporated into the CFD model to provide a configuration closer to the industrial flotation tanks. The results can also be compared with the predictions of the disk sparger in the current study to assess the predictive performance of the modified methodology. Although the proposed drag model of Lane resulted in reasonable agreement with the measurements, the observed discrepancies between the numerical predictions and the experimental data, especially for the larger scale stirred tanks, can be subject of future studies. As Doroodchi et al., (Doroodchi et al., 2008) suggested, the Lane drag coefficient correlation can be modified by including the Richardson number to improve the level of accuracy in the numerical predictions. In this study the effects of bubble size diameters were assumed to be constant. Future study can, however, apply the Lane drag coefficient (or a modified version of this formulation) for the prediction of the air bubble size distribution for different scale stirred tanks working under various impeller speeds and superficial gas velocities. In addition, since this work has concentrated on the Rushton turbine agitation system; the application of Lane drag coefficient for other types of the impeller such as downward/upward pitched blades can be used for future works.

The CFD-kinetic flotation model developed in this study has only applied for two minerals (i.e., quartz and galena), as a recommendation, the model can be run for the predictions of the flotation rate constant of the other minerals. This will help to gain more insights into the effectiveness of the model for the particles with different densities and hydrophobicity. It is also recommended that the potential of the new model will be examined by simulating ore systems instead of only single mineral. This will be a challenge for the model and additional calibrations might be required, since the presence of valuable minerals and gangue in an ore system would not only reduce the hydrophobicity of the solid particles but also the hydrodynamics properties of the slurry would be significantly affected. Another extension of this work can be performed by using other formulations for the sub-processes. The proposed model of Pyke uses GSE, Dobby and Finch and Schulze models for collision, attachment and stability efficiencies, respectively. As described there are certain approximations and simplifications for the flotation sub-process models. However, other equations are

also available to determine the probabilities of the sub-processes. Thus, further investigation is required to explore other alternatives for the simulation of the flotation micro processes. One approach that can investigate the capabilities of models for the sub-processes is “zoning”. In other words, the computational domain can be sliced into various regions and the efficiencies of the flotation micro phenomena can be computed in each zone using local values of flow field. In this way, the flotation tank and accordingly the probabilities of the sub-processes can be compartmentalized based upon the flow hydrodynamics. This will lead to the definitions of different zones within the tank where one can assess which micro process is more dominant. A preliminary example of this concept was shown in sub-section 5.2.1 for the calculation of the Bond number.

Moreover, recent studies showed that coupling CFD and DEM will incorporate the inter-particulate interactions for the flotation modelling, although it was carried out on a micro scale. Thus, it is recommended that future study concentrates on the integration of the four-way coupling for the developed CFD-kinetic methodology. This will assess the influence of the particle-particle and bubble-bubble interactions during the flotation process which were assumed insignificant in this study. Furthermore, the combination of this methodology with a multiphase model capable of predicting the bubble size distribution inside flotation tanks will result in a two-step modelling approach accounted for the bubble size distribution inside the tank. In other words, the numerical predictions of the air bubble sizes in different zones inside the tank can be used as the input data for the CFD-kinetic model. Finally, the CFD-kinetic model that was constructed in the current study showed promising results for a laboratory scale flotation tank. Considering the growth in the computational power, future work could involve testing and improving the model for the industrial practices. Special attention should be given on the practical level of mesh resolution for the industrial scale tanks. Moreover, the drag coefficient correlation should include the influence of the turbulence induced by the gas phase by comprising additional equations for the turbulent properties of the gas phase.

Publications from this Work

1. M. Karimi, G. Akdogan, S. M. Bradshaw, “A computational Fluid Dynamics Model for the Flotation Rate Constant, Part I: Model Development”, submitted to **Minerals Engineering**, August 2013.
2. M. Karimi, G. Akdogan, S. M. Bradshaw, “Effects of Different Mesh Schemes and Turbulence Models in CFD Modelling of Stirred Tanks,” **Physicochemical Problems of Mineral Processing**, Vol. 48(2), pp. 513 – 531, 2012.
3. M. Karimi, G. Akdogan, K. Dellimore, S. M. Bradshaw, “Comparison of Different Drag Coefficients in CFD Modelling of a Laboratory Scale Rushton-Turbine Flotation Tank,” **Proceedings of the Ninth International Conference on CFD in the Minerals and Process Industries**, CSIRO, Melbourne, Australia, December 2012.
4. M. Karimi, G. Akdogan, K. Dellimore, S. M. Bradshaw, “Quantification of Numerical and Model Uncertainties in the CFD Simulation of the Gas Holdup and Flow Dynamics in a Laboratory Scale Rushton-turbine Flotation Tank,” **Proceedings of the Ninth International Conference on CFD in the Minerals and Process Industries**, CSIRO, Melbourne, Australia, December 2012.

Bibliography

- ABRAHAMSON, J. 1975. Collision rates of small particles in a vigorously turbulent fluid. *Chemical Engineering Science*, 30, 1371-1379.
- AHMED, A. & ELGHOBASHI, S. 2001. Direct numerical simulation of particle dispersion in homogeneous turbulent shear flows. *Physics of Fluids*, 13, 3346.
- AKITI, O., YEBOAH, A., BAI, G. & ARMENANTE, P. M. 2005. Hydrodynamic effects on mixing and competitive reactions in laboratory reactors. *Chemical Engineering Science*, 60, 2341-2354.
- ALVES, S., MAIA, C. & VASCONCELOS, J. 2002. Experimental and modelling study of gas dispersion in a double turbine stirred tank. *Chemical Engineering Science*, 57, 487-496.
- ANFRUNS, J. & KITCHENER, J. 1977. Rate of capture of small particles in flotation. *Trans. Inst. Min. Metal*, 86, C9-c15.
- ANSYS 2011a. ANSYS FLUENT Theory Guide. Canonsburg: ANSYS, Inc.
- ANSYS 2011b. ANSYS FLUENT User's Guide. Canonsburg: ANSYS, Inc.
- ARBITER, N. & HARRIS, C. 1969. Impeller speed and air rate in the optimization and scale-up of flotation machinery. *Trans. AIME*, 244, 115-117.
- ARMENANTE, P. M., LUO, C., CHOU, C.-C., FORT, I. & MEDEK, J. 1997. Velocity profiles in a closed, unbaffled vessel: comparison between experimental LDV data and numerical CFD predictions. *Chemical Engineering Science*, 52, 3483-3492.
- AUBIN, J., FLETCHER, D. F. & XUERE, C. 2004. Modeling turbulent flow in stirred tanks with CFD: the influence of the modeling approach, turbulence model and numerical scheme. *Experimental thermal and fluid science*, 28, 431-445.
- BAKKER, A. & AKKER, H. A. 1994. A computational model for the gas-liquid flow in stirred reactors. *Chemical Engineering Research and Design*, 72, 594-606.
- BAKKER, A. & OSHINOWO, L. 2004. Modelling of turbulence in stirred vessels using large eddy simulation. *Chemical Engineering Research and Design*, 82, 1169-1178.
- BAKKER, A., OSHINOWO, L. M., MARSHALL, E. M. & AKKER HEAVD, D. J. The use of large eddy simulation to study stirred vessel hydrodynamics. 10th European conference on mixing, 2000. Delft, 2-5.
- BAKKER, A. & VAN DEN AKKER, H. 1994. Single-phase flow in stirred reactors. *Chemical engineering research & design*, 72, 583-593.
- BARIGOU, M. & GREAVES, M. 1992. Bubble-size distributions in a mechanically agitated gas—liquid contactor. *Chemical Engineering Science*, 47, 2009-2025.
- BARTELS, C., BREUER, M., WECHSLER, K. & DURST, F. 2002. Computational fluid dynamics applications on parallel-vector computers: computations of stirred vessel flows. *Computers & Fluids*, 31, 69-97.
- BATCHELOR, G. K. 1982. *The theory of homogeneous turbulence*, Cambridge university press.
- BATCHELOR, G. K. 2000. *An introduction to fluid dynamics*, Cambridge university press.
- BLAZEK, J. 2001. *Computational Fluid Dynamics: Principles and Applications: Principles and Applications*, Elsevier Science.
- BLOOM, F. 2006. A mathematical model of continuous flotation deinking. *Mathematical and Computer Modelling of Dynamical Systems*, 12, 277-311.

- BLOOM, F. & HEINDEL, T. J. 1999. An Approximate Analytical Expression for the Probability of Attachment by Sliding. *Journal of Colloid and Interface Science*, 218, 564-577.
- BLOOM, F. & HEINDEL, T. J. 2002. On the structure of collision and detachment frequencies in flotation models. *Chemical Engineering Science*, 57, 2467-2473.
- BLOOM, F. & HEINDEL, T. J. 2003. Modeling flotation separation in a semi-batch process. *Chemical Engineering Science*, 58, 353-365.
- BOGDANOV, O. S. & FILANOVSKI, M. S. 1940. On the question of attachment of mineral particles to air bubbles. *J Phys Chem*, 14, 243-247.
- BOMBAČ, A., ŽUN, I., FILIPIČ, B. & ŽUMER, M. 1997. Gas-filled cavity structures and local void fraction distribution in aerated stirred vessel. *AIChE Journal*, 43, 2921-2931.
- BOOTHROYD, R. G. 1971. *Flowing gas-solids suspensions*, Chapman and Hall London.
- BRUCATO, A., CIOFALO, M., GRISAFI, F. & MICALE, G. 1998a. Numerical prediction of flow fields in baffled stirred vessels: A comparison of alternative modelling approaches. *Chemical Engineering Science*, 53, 3653-3684.
- BRUCATO, A., GRISAFI, F. & MONTANTE, G. 1998b. Particle drag coefficients in turbulent fluids. *Chemical Engineering Science*, 53, 3295-3314.
- BUFFO, A., VANNI, M. & MARCHISIO, D. 2012. Multidimensional population balance model for the simulation of turbulent gas-liquid systems in stirred tank reactors. *Chemical Engineering Science*, 70, 31-44.
- CAMP, T. R. & STEIN, P. C. 1943. Velocity gradients and internal work in fluid motion. *Journal of the Boston Society of Civil Engineers*, 85, 219-37.
- CELIK, I. B., GHIA, U. & ROACHE, P. J. 2008. Procedure for estimation and reporting of uncertainty due to discretization in {CFD} applications. *Journal of fluids {Engineering-Transactions} of the {ASME}*, 130.
- CLIFT, R., GRACE, J. & WEBER, M. 1978. Bubbles, Drops and Particles Academic. *New York*, 346.
- CORONEO, M., MONTANTE, G., PAGLIANTI, A. & MAGELLI, F. 2011. CFD prediction of fluid flow and mixing in stirred tanks: Numerical issues about the RANS simulations. *Computers & Chemical Engineering*, 35, 1959-1968.
- CRAWFORD, R. & RALSTON, J. 1988. The influence of particle size and contact angle in mineral flotation. *International Journal of Mineral Processing*, 23, 1-24.
- CROWE, C., SOMMERFELD, M. & TSUJI, Y. 1998. *Multiphase Flows with Droplets and Particles* CRC. *Boca Raton, FL*.
- CROWE, C., TROUTT, T. & CHUNG, J. 1995. Particle interactions with vortices. *Fluid Vortices*. Springer.
- CUNDALL, P. A. & STRACK, O. D. 1979. A discrete numerical model for granular assemblies. *Geotechnique*, 29, 47-65.
- DAI, Z. 1998. Particle-bubble heterocoagulation. *PhD, University of South Australia, Adelaide*.
- DAI, Z., DUKHIN, S., FORNASIERO, D. & RALSTON, J. 1998. The inertial hydrodynamic interaction of particles and rising bubbles with mobile surfaces. *Journal of Colloid and Interface Science*, 197, 275-292.
- DAI, Z., FORNASIERO, D. & RALSTON, J. 1999. Particle-Bubble Attachment in Mineral Flotation. *Journal of Colloid and Interface Science*, 217, 70-76.

- DAI, Z., FORNASIERO, D. & RALSTON, J. 2000. Particle–bubble collision models—a review. *Advances in Colloid and Interface Science*, 85, 231-256.
- DASKOPOULOS, P. & HARRIS, C. Three dimensional CFD simulations of turbulent flow in baffled stirred tanks: an assessment of the current position. Institution of Chemical Engineers Symposium Series, 1996. HEMISPHERE PUBLISHING CORPORATION, 1-14.
- DEGLON, D. & MEYER, C. 2006. CFD modelling of stirred tanks: Numerical considerations. *Minerals Engineering*, 19, 1059-1068.
- DERJAGUIN, B. & DUKHIN, S. 1993. Theory of flotation of small and medium-size particles. *Progress in Surface Science*, 43, 241-266.
- DERJAGUIN, B., DUKHIN, S. & RULYOV, N. 1984. Kinetic theory of flotation of small particles. *Surface and colloid science*. Springer.
- DOBBY, G. & FINCH, J. 1987. Particle size dependence in flotation derived from a fundamental model of the capture process. *International Journal of Mineral Processing*, 21, 241-260.
- DONG, L., JOHANSEN, S. T. & ENGH, T. A. 1994a. Flow induced by an impeller in an unbaffled tank—I. Experimental. *Chemical Engineering Science*, 49, 549-560.
- DONG, L., JOHANSEN, S. T. & ENGH, T. A. 1994b. Flow induced by an impeller in an unbaffled tank—II. Numerical modelling. *Chemical Engineering Science*, 49, 3511-3518.
- DOROODCHI, E., EVANS, G., SCHWARZ, M., LANE, G., SHAH, N. & NGUYEN, A. 2008. Influence of turbulence intensity on particle drag coefficients. *Chemical Engineering Journal*, 135, 129-134.
- DUAN, J., FORNASIERO, D. & RALSTON, J. 2003. Calculation of the flotation rate constant of chalcopyrite particles in an ore. *International Journal of Mineral Processing*, 72, 227-237.
- DUKHIN, S. 1982. Role of inertial forces in flotation of small particles. *Coll. J*, 44, 388-397.
- DUKHIN, S., DERJAGUIN, B. & MATIJEVIC, E. 1974. Surface and colloid science. Vol. 7Wiley, New York, 143-145.
- DUKHIN, S. S., KRETZSCHMAR, G. & MILLER, R. 1995. *Dynamics of adsorption at liquid interfaces: theory, experiment, application*, Elsevier Science.
- EGGELS, J. G. M. 1996. Direct and large-eddy simulation of turbulent fluid flow using the lattice-Boltzmann scheme. *International Journal of Heat and Fluid Flow*, 17, 307-323.
- ELGHOBASHI, S. 1991. Particle-laden turbulent flows: direct simulation and closure models. *Applied Scientific Research*, 48, 301-314.
- ELGHOBASHI, S. 1994. On predicting particle-laden turbulent flows. *Applied Scientific Research*, 52, 309-329.
- ELGHOBASHI, S. & ABOU-ARAB, T. 1983. A two-equation turbulence model for two-phase flows. *Physics of Fluids*, 26, 931.
- ELGHOBASHI, S. & TRUESDELL, G. 1992. Direct simulation of particle dispersion in a decaying isotropic turbulence. *Journal of Fluid Mechanics*, 242, 655-700.
- EVANS, G., DOROODCHI, E., LANE, G., KOH, P. & SCHWARZ, M. 2008. Mixing and gas dispersion in mineral flotation cells. *Chemical Engineering Research and Design*, 86, 1350-1362.

- FALLENIOUS, K. 1987. Turbulence in flotation cells. *International Journal of Mineral Processing*, 21, 1-23.
- FAN, J., WANG, Y. & FEI, W. 2007. Large eddy simulations of flow instabilities in a stirred tank generated by a Rushton turbine. *Chinese Journal of Chemical Engineering*, 15, 200-208.
- FDHILA, R. B. & SIMONIN, O. Eulerian prediction of a turbulent bubbly flow downstream of a sudden pipe expansion. 6th Workshop on Two-Phase Flow Prediction, 1992. 85-115.
- FENG, X., CHENG, J., LI, X., YANG, C. & MAO, Z.-S. 2012. Numerical simulation of turbulent flow in a baffled stirred tank with an explicit algebraic stress model. *Chemical Engineering Science*, 69, 30-44.
- FERRANTE, A. & ELGHOBASHI, S. 2003. On the physical mechanisms of two-way coupling in particle-laden isotropic turbulence. *Physics of Fluids*, 15, 315.
- FERZIGER, J. H. & PERIĆ, M. 1996. *Computational methods for fluid dynamics*, Springer Berlin.
- FLETCHER, C. A. 1991. *Computational techniques for fluid dynamics*, Springer Verlag.
- FREITAS, C. J. 2002. The issue of numerical uncertainty. *Applied Mathematical Modelling*, 26, 237-248.
- GAUDIN, A. M. 1932. *Flotation*, McGraw-Hill.
- GEURTS, B. J. & VREMAN, B. 2006. Dynamic self-organization in particle-laden channel flow. *International Journal of Heat and Fluid Flow*, 27, 945-954.
- GEZORK, K. M., BUJALSKI, W., COOKE, M. & NIENOW, A. W. 2001. Mass Transfer and Hold-up Characteristics in a Gassed, Stirred Vessel at Intensified Operating Conditions. *Chemical Engineering Research and Design*, 79, 965-972.
- GIDASPOW, D., BEZBURUAH, R. & DING, J. 1991. Hydrodynamics of circulating fluidized beds: kinetic theory approach. Illinois Inst. of Tech., Chicago, IL (United States). Dept. of Chemical Engineering.
- GONIVA, C., KLOSS, C., HAGER, A. & PIRKER, S. An open source CFD-DEM perspective. Proceedings of OpenFOAM workshop Gothenburg, Sweden, 2010.
- GONIVA, C., WIERINK, G., HEISKANEN, K., PIRKER, S. & KLOSS, C. Modelling three-phase flow in metallurgical processes. Ninth International Conference on CFD in the Minerals and Process Industries, 2012 CSIRO, Melbourne, Australia.
- GORAIN, B., FRANZIDIS, J.-P. & MANLAPIG, E. 1995a. Studies on impeller type, impeller speed and air flow rate in an industrial scale flotation cell—Part 1: Effect on bubble size distribution. *Minerals Engineering*, 8, 615-635.
- GORAIN, B., FRANZIDIS, J.-P. & MANLAPIG, E. 1995b. Studies on impeller type, impeller speed and air flow rate in an industrial scale flotation cell part 2: Effect on gas holdup. *Minerals Engineering*, 8, 1557-1570.
- GORAIN, B., FRANZIDIS, J.-P. & MANLAPIG, E. 1996. Studies on impeller type, impeller speed and air flow rate in an industrial scale flotation cell. Part 3: Effect on superficial gas velocity. *Minerals Engineering*, 9, 639-654.
- GORAIN, B., FRANZIDIS, J. & MANLAPIG, E. 1997. Studies on impeller type, impeller speed and air flow rate in an industrial scale flotation cell. Part 4: Effect of bubble surface area flux on flotation performance. *Minerals Engineering*, 10, 367-379.

- GOSMAN, A. D., LEKAKOU, C., POLITIS, S., ISSA, R. I. & LOONEY, M. K. 1992. Multidimensional modeling of turbulent two-phase flows in stirred vessels. *AIChE Journal*, 38, 1946-1956.
- HARTMANN, H., DERKSEN, J., MONTAVON, C., PEARSON, J., HAMILL, I. & VAN DEN AKKER, H. 2004. Assessment of large eddy and RANS stirred tank simulations by means of LDA. *Chemical Engineering Science*, 59, 2419-2432.
- HEINDEL, T. J. & BLOOM, F. 1999. Exact and approximate expressions for bubble-particle collision. *Journal of Colloid and Interface Science*, 213, 101-111.
- HUI, S. 2000. *Three-phase Mixing and Flotation in Mechanical Cells*. University of Newcastle.
- JAMESON, G., NAM, S. & YOUNG, M. M. 1977. Physical factors affecting recovery rates in flotation. *Miner. Sci. Eng.*, 9, 103-118.
- JAVED, K., MAHMUD, T. & ZHU, J. 2006. Numerical simulation of turbulent batch mixing in a vessel agitated by a Rushton turbine. *Chemical Engineering and Processing: Process Intensification*, 45, 99-112.
- JORDAN, C. & SPEARS, D. 1990. Evaluation of a turbulent flow model for fine-bubble and fine-particle flotation. *Miner. Metall. Process*, 65-73.
- JOSHI, J., NERE, N., RANE, C. V., MURTHY, B., MATHPATI, C. S., PATWARDHAN, A. & RANADE, V. 2011a. CFD Simulation of Stirred Tanks: Comparison of Turbulence Models.(Part II: Axial Flow Impellers, Multiple Impellers and Multiphase Dispersions). *Can. J. Chem. Eng.*, 89, 754-816.
- JOSHI, J. B., NERE, N. K., RANE, C. V., MURTHY, B. N., MATHPATI, C. S., PATWARDHAN, A. W. & RANADE, V. V. 2011b. CFD simulation of stirred tanks: Comparison of turbulence models. Part I: Radial flow impellers. *The Canadian Journal of Chemical Engineering*, 89, 23-82.
- JOWETT, A. 1980. Formation and disruption of particle-bubble aggregates in flotation. *Fine Particles Processing*, 1, 720-754.
- JULIEN SAINT AMAND, F. 1999. Hydrodynamics of deinking flotation. *International Journal of Mineral Processing*, 56, 277-316.
- KARIMI, M., AKDOGAN, G. & BRADSHAW, S. M. 2012. Effects of different mesh schemes and turbulence models in CFD modelling of stirred tanks. *Physicochemical Problems of Mineral Processing*, 48, 513-531.
- KARNIADAKIS, G. E. 1995. Toward a numerical error bar in CFD. *Journal of Fluids Engineering*, 117, 7.
- KERDOUSS, F., BANNARI, A. & PROULX, P. 2006. CFD modeling of gas dispersion and bubble size in a double turbine stirred tank. *Chemical Engineering Science*, 61, 3313-3322.
- KESLIN, J. 1978. Viscosity of Liquid Water in the Range—8 C to 150 C. *J. Phys. Chem. Ref. Data*, 7.
- KHOPKAR, A., KASAT, G., PANDIT, A. & RANADE, V. 2006. CFD simulation of mixing in tall gas-liquid stirred vessel: Role of local flow patterns. *Chemical Engineering Science*, 61, 2921-2929.
- KHOPKAR, A., RAMMOHAN, A., RANADE, V. & DUDUKOVIC, M. 2005. Gas-liquid flow generated by a Rushton turbine in stirred vessel: CARPT/CT measurements and CFD simulations. *Chemical Engineering Science*, 60, 2215-2229.
- KHOPKAR, A. R. & RANADE, V. V. 2006. CFD simulation of gas-liquid stirred vessel: VC, S33, and L33 flow regimes. *AIChE Journal*, 52, 1654-1672.

- KIM, W.-W. & MENON, S. 1997. Application of the localized dynamic subgrid-scale model to turbulent wall-bounded flows. *AIAA paper*, 97-0210.
- KING, R. P. 2001. *Modeling and simulation of mineral processing systems*, Butterworth-Heinemann.
- KOH, P., MANICKAM, M. & SCHWARZ, M. 2000. CDF simulation of bubble-particle collisions in mineral flotation cells. *Minerals Engineering*, 13, 1455-1463.
- KOH, P. & SCHWARZ, M. 2003a. CFD modelling of bubble-particle collision rates and efficiencies in a flotation cell. *Minerals Engineering*, 16, 1055-1059.
- KOH, P. & SCHWARZ, M. 2006a. CFD modelling of bubble-particle attachments in flotation cells. *Minerals Engineering*, 19, 619-626.
- KOH, P. & SCHWARZ, M. 2008. Modelling attachment rates of multi-sized bubbles with particles in a flotation cell. *Minerals Engineering*, 21, 989-993.
- KOH, P. & SCHWARZ, M. CFD models of Microcel and Jameson flotation cells. Seventh International Conference on CFD in the Minerals and Process Industries, CSIRO, Melbourne, Australia, 2009.
- KOH, P., SCHWARZ, M., ZHU, Y., BOURKE, P., PEAKER, R. & FRANZIDIS, J. Development of CFD models of mineral flotation cells. Third International Conference on Computational Fluid Dynamics in the Minerals and Process Industries, Melbourne, Australia, 2003. 171-175.
- KOH, P. & SMITH, L. 2010. Experimental validation of a flotation cell model XXV *International Mineral Processing Congress (IMPC)*. Brisbane, Australia.
- KOH, P. & SMITH, L. 2011. The effect of stirring speed and induction time on flotation. *Minerals Engineering*, 24, 442-448.
- KOH, P. T. & SCHWARZ, M. 2007. CFD model of a self-aerating flotation cell. *International Journal of Mineral Processing*, 85, 16-24.
- KOH, P. T. L. & SCHWARZ, M. P. 2003b. CFD modelling of bubble-particle collision rates and efficiencies in a flotation cell. *Minerals Engineering*, 16, 1055-1059.
- KOH, P. T. L. & SCHWARZ, M. P. 2006b. CFD modelling of bubble-particle attachments in flotation cells. *Minerals Engineering*, 19, 619-626.
- KRESTA, S. M. & WOOD, P. E. 1991. Prediction of the three-dimensional turbulent flow in stirred tanks. *AIChE Journal*, 37, 448-460.
- KUMARESAN, T., NERE, N. K. & JOSHI, J. B. 2005. Effect of Internals on the Flow Pattern and Mixing in Stirred Tanks. *Industrial & Engineering Chemistry Research*, 44, 9951-9961.
- LAAKKONEN, M., HONKANEN, M., SAARENINNE, P. & AITTAMAA, J. 2005. Local bubble size distributions, gas-liquid interfacial areas and gas holdups in a stirred vessel with particle image velocimetry. *Chemical Engineering Journal*, 109, 37-47.
- LANE, G. & KOH, P. CFD simulation of a Rushton turbine in a baffled tank. Proceedings of International Conference on Computational Fluid Dynamics in Mineral and Metal Processing and Power Generation, CSIRO, Melbourne, 1997. 377-385.
- LANE, G., SCHWARZ, M. & EVANS, G. Comparison of CFD methods for modelling of stirred tanks. 10th European Conference on Mixing. Delft, Netherlands, 2000a. 273-280.
- LANE, G., SCHWARZ, M. & EVANS, G. Modelling of the interaction between gas and liquid in stirred vessels. 10th European Conference on Mixing, 2000b. 197-204.

- LANE, G., SCHWARZ, M. & EVANS, G. 2002. Predicting gas–liquid flow in a mechanically stirred tank. *Applied Mathematical Modelling*, 26, 223-235.
- LANE, G., SCHWARZ, M. & EVANS, G. Development of improved methods for computational modelling of gas dispersion in stirred tanks. 3rd International Conference on CFD in the Minerals and Process Industries, Melbourne, Australia, 2003.
- LANE, G., SCHWARZ, M. & EVANS, G. 2005. Numerical modelling of gas–liquid flow in stirred tanks. *Chemical Engineering Science*, 60, 2203-2214.
- LANE, G. L. 2006. *Computational Modelling of Gas-Liquid Flow in Stirred Tanks*. PhD, University of Newcastle
- LANGMUIR, I. & BLODGETT, K. 1946. Mathematical investigation of water droplet trajectories.
- LATHOUWERS, D. 1999. *Modelling and Simulation of Turbulent Bubble Flow*. PhD, Technical University of Delf.
- LAUNDER, B. E. & SPALDING, D. B. 1972. Lectures in mathematical models of turbulence.
- LEJA, J. 1982. Surface chemistry of froth flotation.
- LIU, T., KOH, P. & SCHWARZ, M. 2005. CFD-based multiscale modelling of bubble-particle collision rates and efficiencies in a flotation cell. *CHEMECA, Brisbane, Australia*.
- LIU, T. & SCHWARZ, M. 2009a. CFD-based multiscale modelling of bubble–particle collision efficiency in a turbulent flotation cell. *Chemical Engineering Science*, 64, 5287-5301.
- LIU, T. Y. & SCHWARZ, M. 2009b. CFD-based modelling of bubble-particle collision efficiency with mobile bubble surface in a turbulent environment. *International Journal of Mineral Processing*, 90, 45-55.
- LU, W.-M., WU, H.-Z. & JU, M.-Y. 1997. Effects of baffle design on the liquid mixing in an aerated stirred tank with standard Rushton turbine impellers. *Chemical Engineering Science*, 52, 3843-3851.
- LUO, J., ISSA, R. & GOSMAN, A. Prediction of impeller induced flows in mixing vessels using multiple frames of reference. Institution of Chemical Engineers Symposium Series, 1994. HEMISPHERE PUBLISHING CORPORATION, 549-549.
- MARTIN, J. L. & MACCUTCHEON, S. C. 1999. *Hydrodynamics and transport for water quality modeling*, CRC Press.
- MAVROS, P. 2001. Flow visualization in stirred vessels: A review of experimental techniques. *Chemical Engineering Research and Design*, 79, 113-127.
- MAXEY, M. R. & RILEY, J. J. 1983. Equation of motion for a small rigid sphere in a nonuniform flow. *Physics of Fluids*, 26, 883.
- MENTER, F. R. 1994. Two-equation eddy-viscosity turbulence models for engineering applications. *AIAA journal*, 32, 1598-1605.
- MIKA, T. & FUERSTENAU, D. A microscopic model of the flotation process. Proceedings of the eighth international mineral processing congress, Leningrad, 1968. 246.
- MORUD, K. & HJERTAGER, B. 1996. LDA measurements and CFD modelling of gas-liquid flow in a stirred vessel. *Chemical Engineering Science*, 51, 233-249.

- MURTHY, B., GHADGE, R. & JOSHI, J. 2007. CFD simulations of gas–liquid–solid stirred reactor: Prediction of critical impeller speed for solid suspension. *Chemical Engineering Science*, 62, 7184-7195.
- NAPIER-MUNN, T. & LYNCH, A. 1992. The modelling and computer simulation of mineral treatment processes—current status and future trends. *Minerals Engineering*, 5, 143-167.
- NEWELL, R. 2006. *Hydrodynamics and scale-up in Rushton turbine flotation cells*. PhD, University of South Australia.
- NG, K., FENTIMAN, N. J., LEE, K. C. & YIANNESKIS, M. 1998. Assessment of Sliding Mesh CFD Predictions and LDA Measurements of the Flow in a Tank Stirred by a Rushton Impeller. *Chemical Engineering Research and Design*, 76, 737-747.
- NGUYEN-VAN, A. 1994. The collision between fine particles and single air bubbles in flotation. *Journal of Colloid and Interface Science*, 162, 123-128.
- NGUYEN-VAN, A. & KMEŤ, S. 1994. Probability of collision between particles and bubbles in flotation: the theoretical inertialess model involving a swarm of bubbles in pulp phase. *International Journal of Mineral Processing*, 40, 155-169.
- NGUYEN, A. V. 1999. Hydrodynamics of liquid flows around air bubbles in flotation: a review. *International Journal of Mineral Processing*, 56, 165-205.
- NGUYEN, A. V. 2003a. New method and equations for determining attachment tenacity and particle size limit in flotation. *International Journal of Mineral Processing*, 68, 167-182.
- NGUYEN, A. V. 2003b. New method and equations for determining attachment tenacity and particle size limit in flotation. *International Journal of Mineral Processing*, 68, 167-182.
- NGUYEN, A. V., RALSTON, J. & SCHULZE, H. J. 1998. On modelling of bubble–particle attachment probability in flotation. *International Journal of Mineral Processing*, 53, 225-249.
- NICOUD, F. & DUCROS, F. 1999. Subgrid-scale stress modelling based on the square of the velocity gradient tensor. *Flow, Turbulence and Combustion*, 62, 183-200.
- OBERKAMPF, W. L., SINDIR, M. & CONLISK, A. 1998. Guide for the verification and validation of computational fluid dynamics simulations. *Am. Institute of Aeronautics and Astronautics*.
- OCHIENG, A., ONYANGO, M. S., KUMAR, A., KIRIAMITI, K. & MUSONGE, P. 2008. Mixing in a tank stirred by a Rushton turbine at a low clearance. *Chemical Engineering and Processing: Process Intensification*, 47, 842-851.
- OLDSHUE, J. Y. 1983. *Fluid Mixing Technology*, New York, McGraw-Hill.
- ORSZAG, S. A., YAKHOT, V., FLANNERY, W. S., BOYSAN, F., CHOUDHURY, D., MARUZEWSKI, J. & PATEL, B. 1993. Renormalization group modeling and turbulence simulations. *Near-wall turbulent flows*, 1031-1046.
- OSHINOWO, L., JAWORSKI, Z., DYSTER, K. N., MARSHALL, E. & NIENOW, A. W. Predicting the tangential velocity field in stirred tanks using the multiple reference frames (MRF) Model with validation by LDA measurements. 10th European Conference on Mixing, 2000 Delf, Netherland. 281-288.
- PAN, Y. & BANERJEE, S. 1996. Numerical simulation of particle interactions with wall turbulence. *Physics of Fluids*, 8, 2733.
- PAN, Y. & BANERJEE, S. 1997. Numerical investigation of the effects of large particles on wall-turbulence. *Physics of Fluids*, 9, 3786.

- PATEL, V. C., RODI, W. & SCHEUERER, G. 1985. Turbulence models for near-wall and low Reynolds number flows—a review. *AIAA journal*, 23, 1308-1319.
- PETRILA, T. & TRIF, D. 2005. *Basics of fluid mechanics and introduction to computational fluid dynamics*, Springer Verlag.
- PYKE, B. 2004. *Bubble-particle capture in turbulent flotation systems*. PhD, University of South Australia.
- PYKE, B., FORNASIERO, D. & RALSTON, J. 2003. Bubble particle heterocoagulation under turbulent conditions. *Journal of Colloid and Interface Science*, 265, 141-151.
- RANADE, V. 1997. An efficient computational model for simulating flow in stirred vessels: a case of Rushton turbine. *Chemical Engineering Science*, 52, 4473-4484.
- RANADE, V., PERRARD, M., LE SAUZE, N., XUERE, C. & BERTRAND, J. 2001. Trailing vortices of Rushton turbine: PIV measurements and CFD simulations with snapshot approach. *Chemical Engineering Research and Design*, 79, 3-12.
- RANADE, V. V. 2002. *Computational flow modelling for chemical reactor engineering ranade*, London, Academic Press.
- RANADE, V. V. & DESHPANDE, V. R. 1999. Gas-liquid flow in stirred reactors: Trailing vortices and gas accumulation behind impeller blades. *Chemical Engineering Science*, 54, 2305-2315.
- RANADE, V. V., TAYALIA, Y. & KRISHNAN, H. 2002. CFD predictions of flow near impeller blades in baffled stirred vessels: Assessment of computational snapshot approach. *Chemical Engineering Communications*, 189, 895-922.
- RANADE, V. V. & VAN DEN AKKER, H. E. A. 1994. A computational snapshot of gas—liquid flow in baffled stirred reactors. *Chemical Engineering Science*, 49, 5175-5192.
- READ, A. & KITCHENER, J. 1969. Wetting films on silica. *Journal of Colloid and Interface Science*, 30, 391-398.
- REWATKAR, V. & JOSHI, J. 1993. Role of sparger design on gas dispersion in mechanically agitated gas-liquid contactors. *The Canadian Journal of Chemical Engineering*, 71, 278-291.
- REWATKAR, V. B. & JOSHI, J. B. 1991a. Role of sparger design in mechanically agitated gas-liquid reactors. Part I: Power consumption. *Chemical engineering & technology*, 14, 333-347.
- REWATKAR, V. B. & JOSHI, J. B. 1991b. Role of sparger design in mechanically agitated gas-liquid reactors. Part II: Liquid phase mixing. *Chemical engineering & technology*, 14, 386-393.
- RICHARDSON, L. F. 1911. The approximate arithmetical solution by finite differences of physical problems involving differential equations, with an application to the stresses in a masonry dam. *Philosophical Transactions of the Royal Society of London. Series A, Containing Papers of a Mathematical or Physical Character*, 210, 307-357.
- RICHARDSON, L. F. & GAUNT, J. A. 1927. The deferred approach to the limit. Part I. Single lattice. Part II. Interpenetrating lattices. *Philosophical Transactions of the Royal Society of London. Series A, Containing Papers of a Mathematical or Physical Character*, 226, 299-361.
- RIGBY, G., EVANS, G. & JAMESON, G. 1997. Bubble breakup from ventilated cavities in multiphase reactors. *Chemical Engineering Science*, 52, 3677-3684.
- RIGBY, G., LANE, G. & EVANS, G. 2000. CFD Modelling of Hydrodynamic Conditions within the Wake of Mixing Impeller Blades. *Mixing and Crystallization*. Springer.

- RIGBY, G. D. & EVANS, G. M. 1998. CFD simulation of gas dispersion dynamics in liquid cross-flows. *Applied Mathematical Modelling*, 22, 799-810.
- ROACHE, P. 1994. Perspective: a method for uniform reporting of grid refinement studies. *TRANSACTIONS-AMERICAN SOCIETY OF MECHANICAL ENGINEERS JOURNAL OF FLUIDS ENGINEERING*, 116, 405-405.
- ROACHE, P. J. 1997. Quantification of uncertainty in computational fluid dynamics. *Annual Review of Fluid Mechanics*, 29, 123-160.
- RUSHTON, J. H. 1952. Mixing of liquids in chemical processing. *Industrial & Engineering Chemistry*, 44, 2931-2936.
- SAFFMAN, P. & TURNER, J. 1956. On the collision of drops in turbulent clouds. *J. Fluid Mech*, 1, 16-30.
- SCARGIALI, F., D'ORAZIO, A., GRISAFI, F. & BRUCATO, A. 2007. Modelling and simulation of gas-liquid hydrodynamics in mechanically stirred tanks. *Chemical Engineering Research and Design*, 85, 637-646.
- SCHILLER, L. & NAUMANN, A. 1935. A drag coefficient correlation. *Vdi Zeitung*, 77, 318-320.
- SCHUBERT, H. 2008. On the optimization of hydrodynamics in fine particle flotation. *Minerals Engineering*, 21, 930-936.
- SCHUBERT, H. & BISCHOFBERGER, C. 1978. On the hydrodynamics of flotation machines. *International Journal of Mineral Processing*, 5, 131-142.
- SCHUBERT, H. & BISCHOFBERGER, C. 1998. On the microprocesses air dispersion and particle-bubble attachment in flotation machines as well as consequences for the scale-up of macroprocesses. *International Journal of Mineral Processing*, 52, 245-259.
- SCHULZE, H. 1977. New theoretical and experimental investigations on stability of bubble/particle aggregates in flotation: a theory on the upper particle size of floatability. *International Journal of Mineral Processing*, 4, 241-259.
- SCHULZE, H. 1989. Hydrodynamics of bubble-mineral particle collisions. *Mineral Processing and Extractive Metallurgy Review*, 5, 43-76.
- SCHULZE, H. & BIRZER, J. 1987. Stability of thin liquid films on Langmuir-Blodgett layers on silica surfaces. *Colloids and surfaces*, 24, 209-224.
- SCHULZE, H. J. & DOBIAS, B. 1993. Coagulation and flocculation. Dekker, New York.
- SCHULZE, H. J. & HECKER, M. 1984. *Physico-chemical elementary processes in flotation: an analysis from the point of view of colloid science including process engineering considerations*, Elsevier Amsterdam.
- SCHWARZ, M. P. 1991. Flow simulation in minerals engineering. *Minerals Engineering*, 4, 717-732.
- SHIH, T.-H., LIOU, W., SHABBIR, A., YANG, Z. & ZHU, J. 1994. A new k-epsilon eddy viscosity model for high Reynolds number turbulent flows: Model development and validation. *NASA STI/Recon Technical Report N*, 95, 11442.
- SMAGORINSKY, J. 1963. GENERAL CIRCULATION EXPERIMENTS WITH THE PRIMITIVE EQUATIONS: I. THE BASIC EXPERIMENT*. *Monthly weather review*, 91, 99-164.
- SMOLUCHOWSKI, M. V. 1917. Versuch einer mathematischen Theorie der Koagulationskinetik kolloider Lösungen. *Z. phys. Chem*, 92, 9.

- SOO, S.-L. 1967. *Fluid dynamics of multiphase systems*, Blaisdell Publishing Company Waltham, Massachusetts.
- SPALART, P. R. & ALLMARAS, S. R. A one-equation turbulence model for aerodynamic flows. AIAA, Aerospace Sciences Meeting and Exhibit, 30 th, Reno, NV, 1992. 1992.
- SPELT, P. & BIESHEUVEL, A. 1997. On the motion of gas bubbles in homogeneous isotropic turbulence. *Journal of Fluid Mechanics*, 336, 221-244.
- STANISIC, M. M. 1985. *Mathematical theory of turbulence*.
- SUTHERLAND, K. 1948. Physical chemistry of flotation. XI. Kinetics of the flotation process. *The Journal of Physical Chemistry*, 52, 394-425.
- SVEN-NILSSON, I. 1934. Effect of contact time between mineral and air bubbles on flotation. *Kol loid*, 230.
- TABIB, M. V. & SCHWARZ, P. 2011. Quantifying sub-grid scale (SGS) turbulent dispersion force and its effect using one-equation SGS large eddy simulation (LES) model in a gas-liquid and a liquid-liquid system. *Chemical Engineering Science*, 66, 3071-3086.
- TAKEDA, H., NARASAKI, K., KITAJIMA, H., SUDOH, S., ONOFUSA, M. & IGUCHI, S. 1993. Numerical simulation of mixing flows in agitated vessels with impellers and baffles. *Computers & Fluids*, 22, 223-228.
- TENNEKES, H. & LUMLEY, J. L. 1972. *First course in turbulence*, MIT press.
- THOMAS, P. 1992. On the influence of the Basset history force on the motion of a particle through a fluid. *Physics of Fluids A: Fluid Dynamics*, 4, 2090.
- TORRÉ, J.-P., FLETCHER, D. F., LASUYE, T. & XUEREB, C. 2007. Single and multiphase CFD approaches for modelling partially baffled stirred vessels: Comparison of experimental data with numerical predictions. *Chemical Engineering Science*, 62, 6246-6262.
- TRAHAR, W. 1981. A rational interpretation of the role of particle size in flotation. *International Journal of Mineral Processing*, 8, 289-327.
- TRAHAR, W. & WARREN, L. 1976. The flotability of very fine particles—a review. *International Journal of Mineral Processing*, 3, 103-131.
- VAKILI, M. & ESFAHANY, M. N. 2009. CFD analysis of turbulence in a baffled stirred tank, a three-compartment model. *Chemical Engineering Science*, 64, 351-362.
- VAN'T RIET, K. & SMITH, J. M. 1975. The trailing vortex system produced by Rushton turbine agitators. *Chemical Engineering Science*, 30, 1093-1105.
- VENNEKER, B. C., DERKSEN, J. J. & VAN DEN AKKER, H. E. 2002. Population balance modeling of aerated stirred vessels based on CFD. *AIChE Journal*, 48, 673-685.
- VREMAN, B., GEURTS, B. J., DEEN, N., KUIPERS, J. & KUERTEN, J. 2009. Two-and four-way coupled Euler-Lagrangian large-eddy simulation of turbulent particle-laden channel flow. *Flow, Turbulence and Combustion*, 82, 47-71.
- WALTERS, D. K. & COKLJAT, D. 2008. A three-equation eddy-viscosity model for Reynolds-averaged Navier-Stokes simulations of transitional flow. *Journal of Fluids Engineering*, 130, 121401.
- WENDT, J. F. & ANDERSON, J. D. 2009. *Computational fluid dynamics*, Springer.
- WIERINK, G. & HEISKANEN, K. Momentum coupling in flotation modelling. Computational Modelling 08, 2008 Cape Town, South Africa.

- WIERINK, G. & HEISKANEN, K. 2010. Modelling bubble–particle interaction with dynamic surface tension. *Minerals Engineering*, 23, 973-978.
- WIERINK, G., TIITINEN, J. & HEISKANEN, K. Mapping of collision regimes in flotation modeling. Seventh International Conference on CFD in the Minerals and Process Industries (CSIRO, Melbourne, Australia, 2009), 2009.
- WIERINK, G. A. 2012. *A computational framework coupled modelling of three-phase systems with soluble surfactant*. PhD, Aalto University.
- WILCOX, D. C. 1994. Simulation of transition with a two-equation turbulence model. *AIAA journal*, 32, 247-255.
- WU, J., ZHU, Y. & PULLUM, L. 2001. Impeller geometry effect on velocity and solids suspension. *Chemical Engineering Research and Design*, 79, 989-997.
- XIA, J., RINNE, A. & GRÖNSTRAND, S. 2009. Effect of turbulence models on prediction of fluid flow in an Outotec flotation cell. *Minerals Engineering*, 22, 880-885.
- YE, Y. & MILLER, J. 1988. Bubble/particle contact time in the analysis of coal flotation. *Coal Perparation*, 5, 147-166.
- YIANATOS, J. 2007. Fluid flow and kinetic modelling in flotation related processes: Columns and mechanically agitated cells—A review. *Chemical Engineering Research and Design*, 85, 1591-1603.
- YOON, H., SHARP, K., HILL, D., ADRIAN, R., BALACHANDAR, S., HA, M. & KAR, K. 2001a. Integrated experimental and computational approach to simulation of flow in a stirred tank. *Chemical Engineering Science*, 56, 6635-6649.
- YOON, H. S., SHARP, K. V., HILL, D. F., ADRIAN, R. J., BALACHANDAR, S., HA, M. Y. & KAR, K. 2001b. Integrated experimental and computational approach to simulation of flow in a stirred tank. *Chemical Engineering Science*, 56, 6635-6649.
- YOON, R.-H. & YORDAN, J. 1991. The critical rupture thickness of thin water films on hydrophobic surfaces. *Journal of Colloid and Interface Science*, 146, 565-572.
- YOON, R. & LUTTRELL, G. 1989. The effect of bubble size on fine particle flotation. *Mineral Processing and Extractive Metallurgy Review*, 5, 101-122.
- ZHOU, G., SHI, L. & YU, P. CFD study of mixing process in Rushton turbine stirred tanks. Third International Conference on CFD in the Minerals and Process Industries, CSIRO, Melbourne, Australia, 2003. 10-12.
- ZHOU, Z., EGIEBOR, N. & PLITT, L. 1993. Frother effects on bubble motion in a swarm. *Canadian metallurgical quarterly*, 32, 89-96.

Appendix A: CFD results of the tangential velocity predicted by different turbulent models

This appendix is intended to provide more details on the numerical predictions of tangential velocity for the stirred tanks. As shown two types of stirred tanks, an unbaffled mixer and a standard Rushton turbine flotation tank were tested in this study. Two groups of turbulence models including the RANS based with the isotropic turbulence assumption and the LES turbulence models were compared.

A.1. Numerical predictions of tangential velocity for the unbaffled mixer

The following graphs show the computed tangential velocity on five different planes (see: Figure 3-1) inside the unbaffled mixer. In each figure the experimental data are demonstrated with the discrete symbols, while the various line styles represent the numerical predictions with the different turbulence models applied.

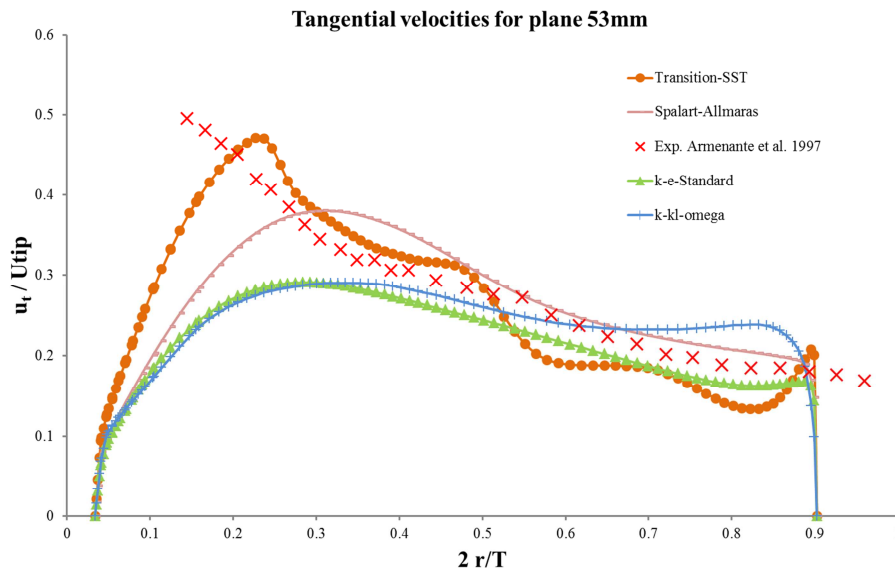


Figure A. 1 Numerical predictions of the tangential velocity with the RANS-based turbulence models for plane 53mm from the bottom of the unbaffled mixer

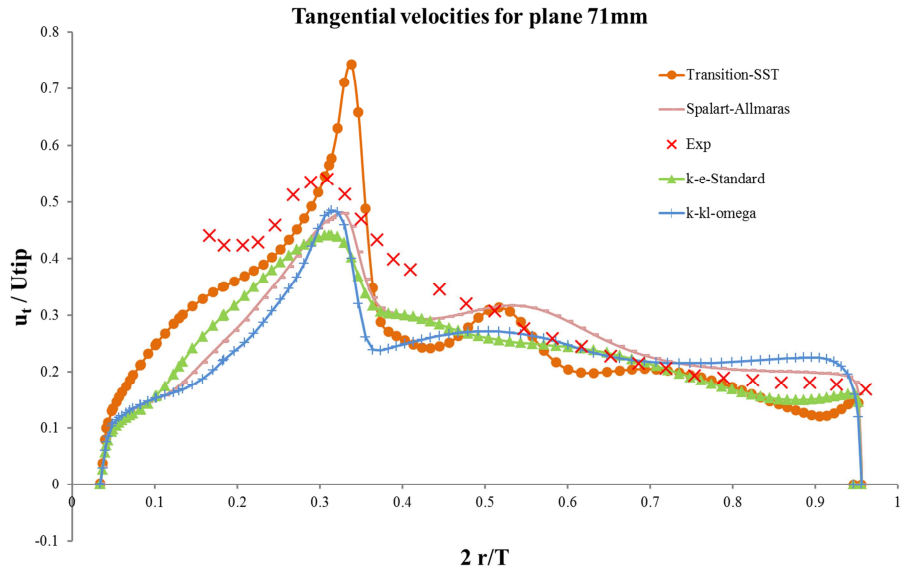


Figure A. 2 Numerical predictions of the tangential velocity with the RANS-based turbulence models for plane 71mm from the bottom of the unbaffled mixer

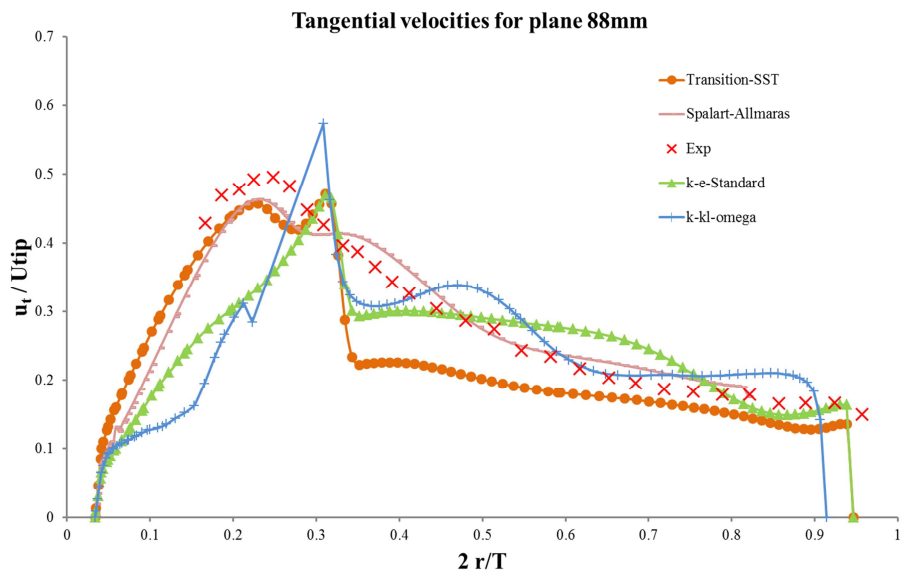


Figure A. 3 Numerical predictions of the tangential velocity with the RANS-based turbulence models for plane 88mm from the bottom of the unbaffled mixer

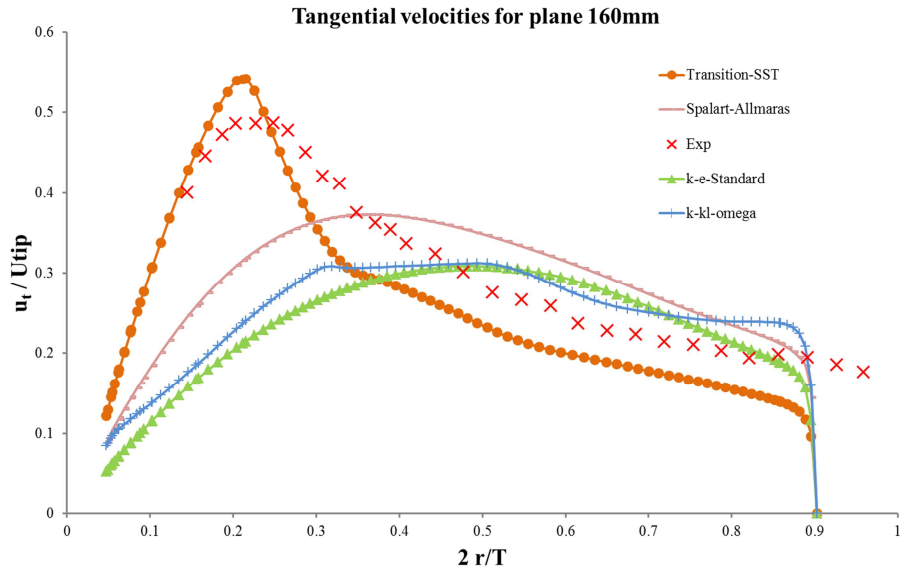


Figure A. 4 Numerical predictions of the tangential velocity with the RANS-based turbulence models for plane 160mm from the bottom of the unbaffled mixer

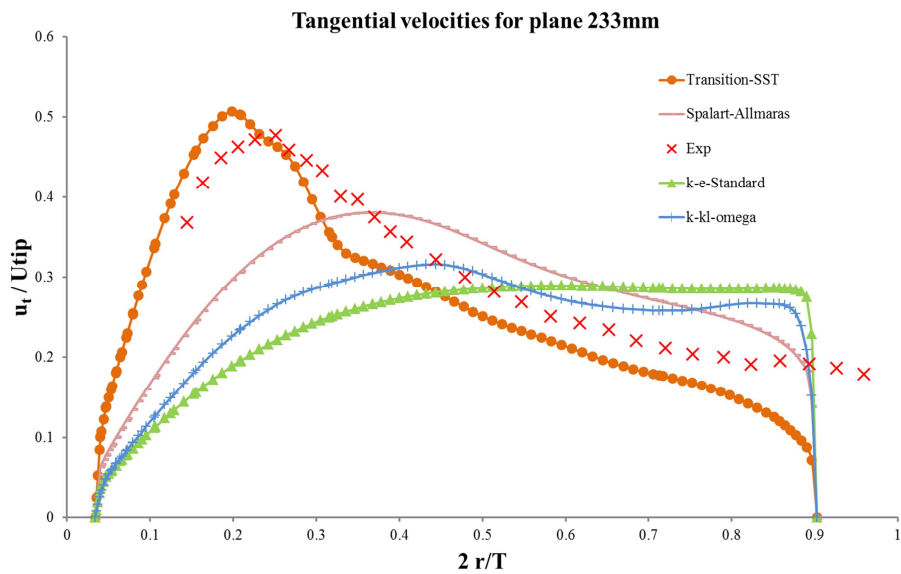


Figure A. 5 Numerical predictions of the tangential velocity with the RANS-based turbulence models for plane 233mm from the bottom of the unbaffled mixer

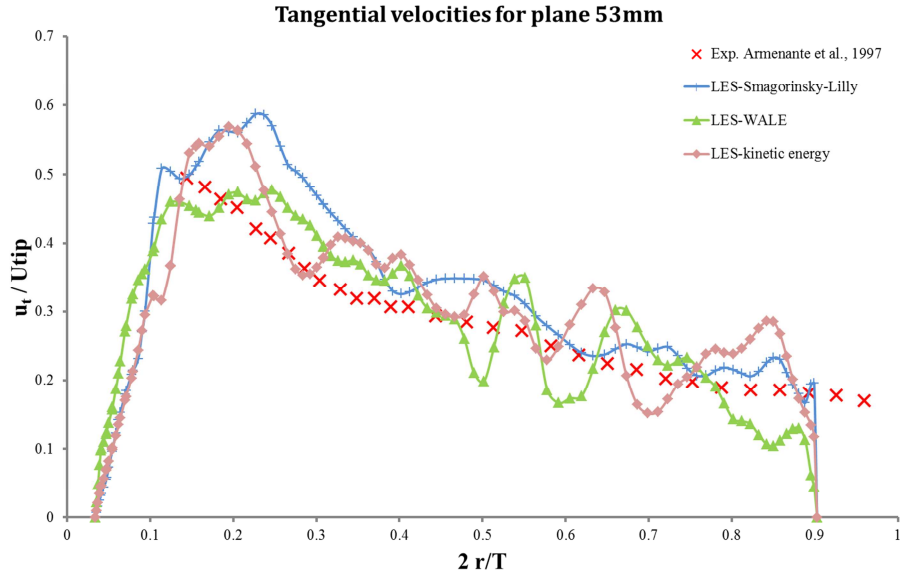


Figure A. 6 LES predictions of the tangential velocity for plane 53mm from the bottom of the unbaffled mixer

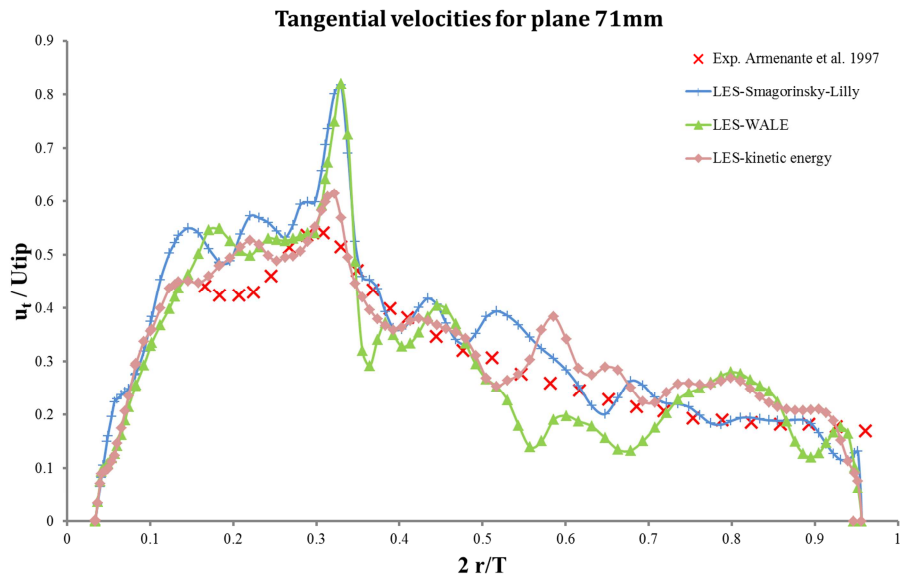


Figure A. 7 LES predictions of the tangential velocity for plane 71mm from the bottom of the unbaffled mixer

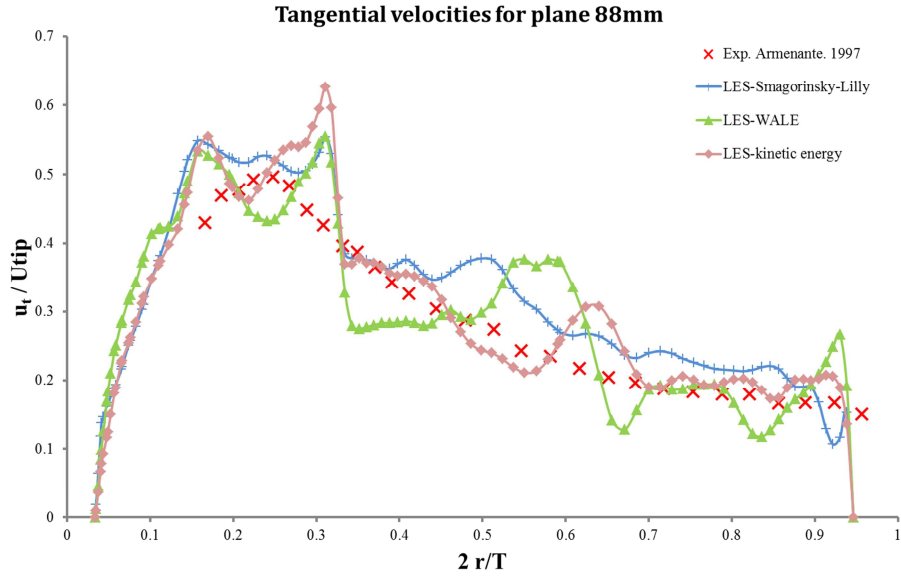


Figure A. 8 LES predictions of the tangential velocity for plane 88mm from the bottom of the unbaffled mixer

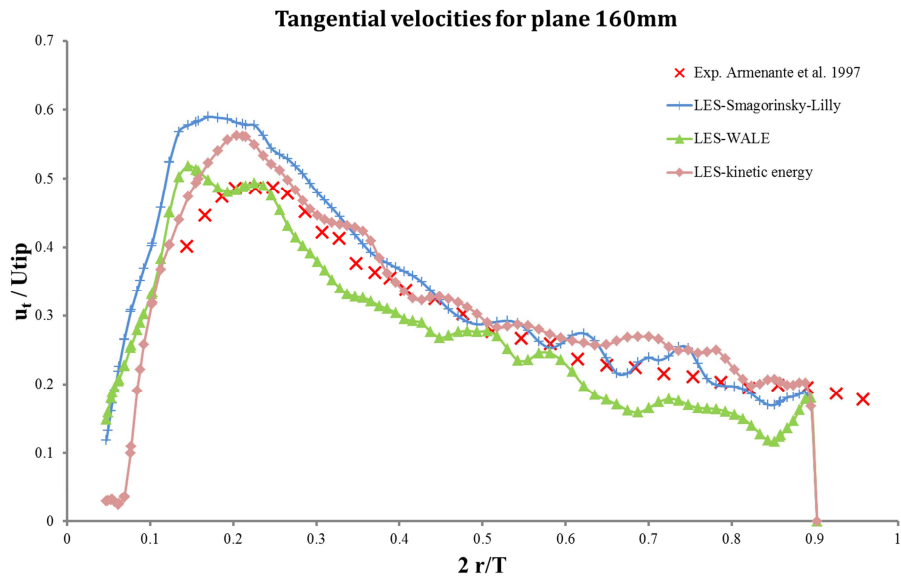


Figure A. 9 LES predictions of the tangential velocity for plane 160mm from the bottom of the unbaffled mixer

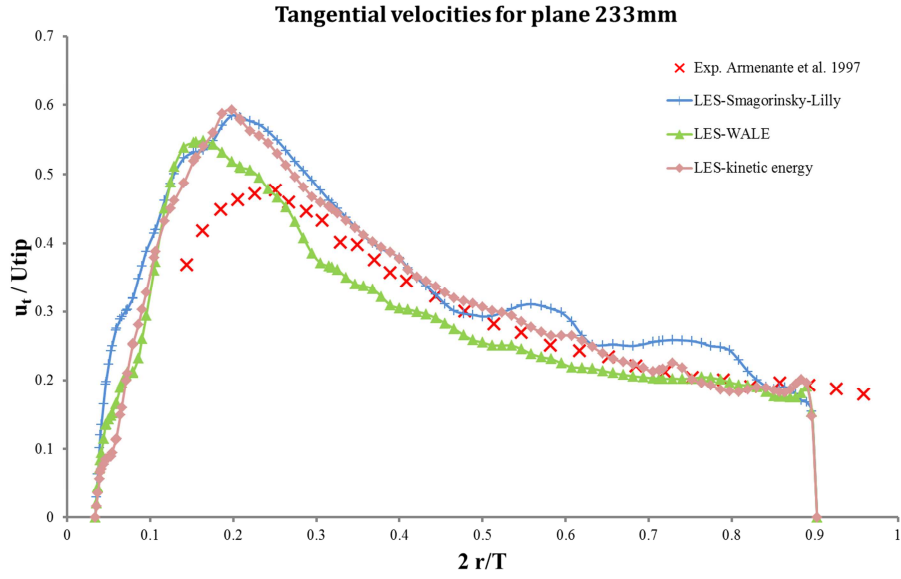


Figure A. 10 LES predictions of the tangential velocity for plane 233mm from the bottom of the unbaffled mixer

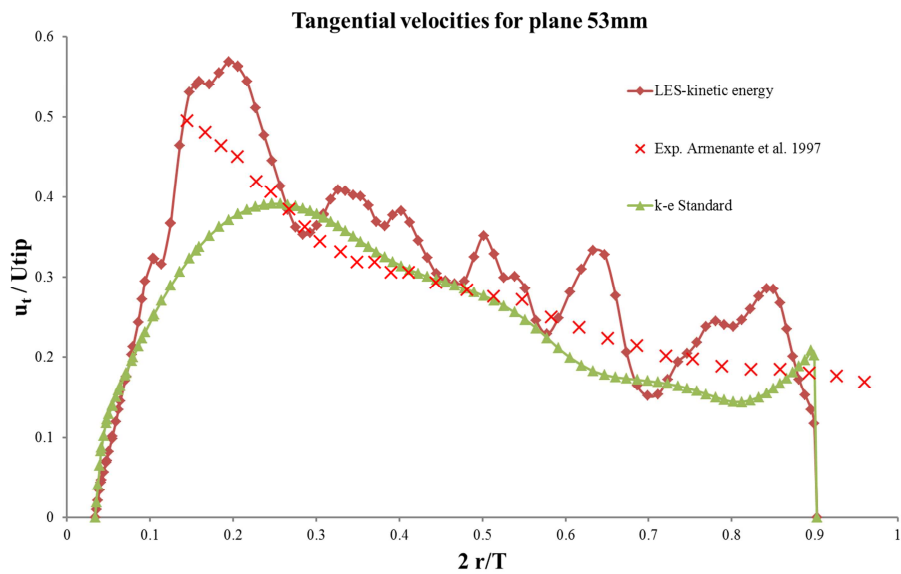


Figure A. 11 Numerical predictions of the tangential velocity on plane 53mm from the bottom of the unbaffled mixer with k-ε standard and LES-kinetic energy

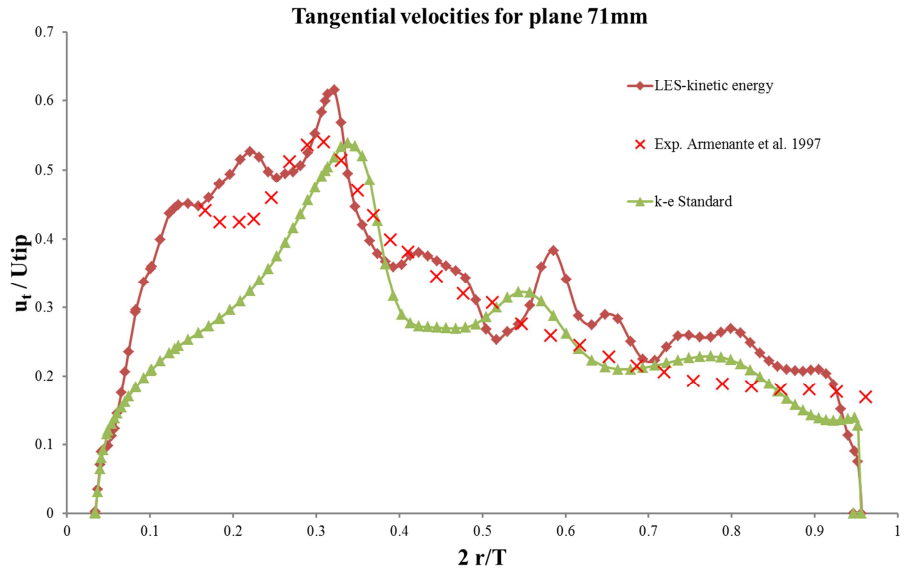


Figure A. 12 Numerical predictions of the tangential velocity on plane 71mm from the bottom of the unbaffled mixer with k-ε standard and LES-kinetic energy

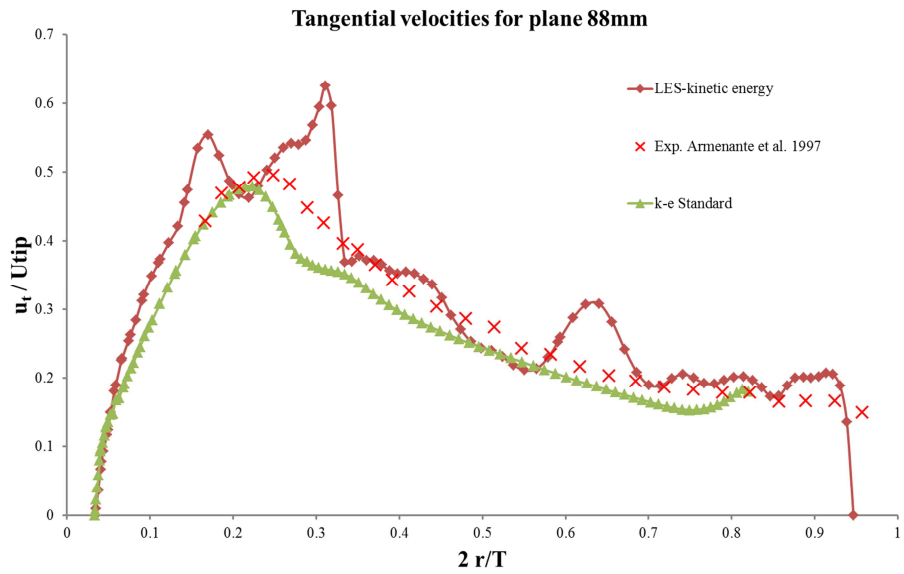


Figure A. 13 Numerical predictions of the tangential velocity on plane 88mm from the bottom of the unbaffled mixer with k-ε standard and LES-kinetic energy

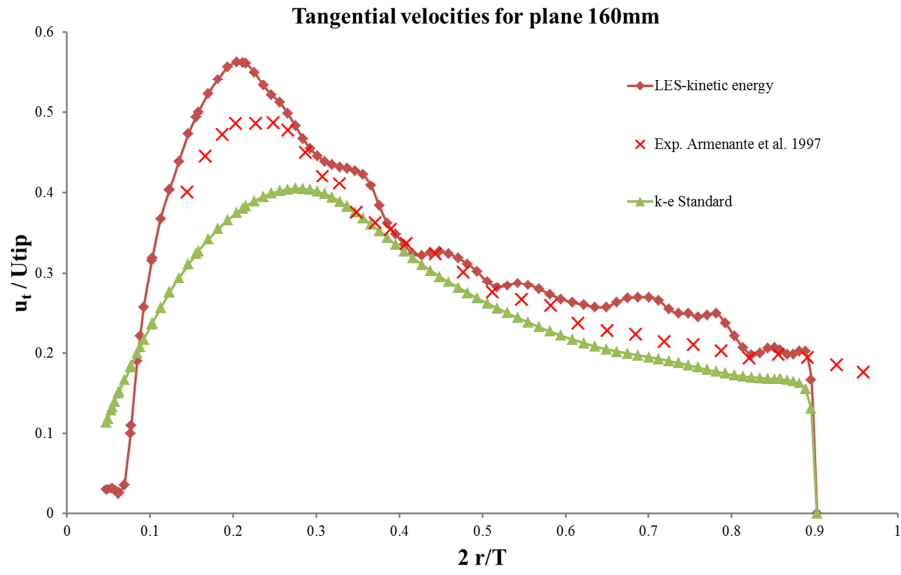


Figure A. 14 Numerical predictions of the tangential velocity on plane 160mm from the bottom of the unbaffled mixer with k-ε standard and LES-kinetic energy

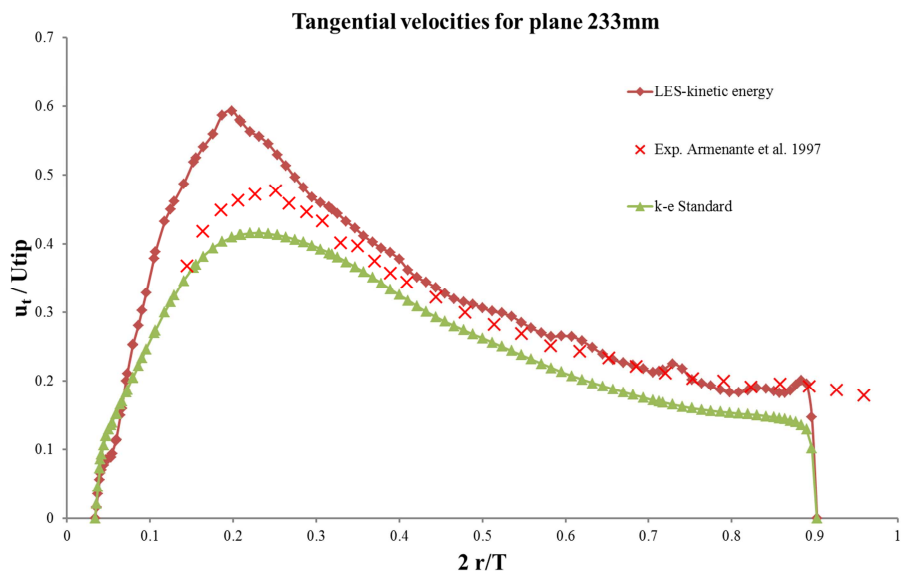


Figure A. 15 Numerical predictions of the tangential velocity on plane 233mm from the bottom of the unbaffled mixer with k-ε standard and LES-kinetic energy

A.2. Numerical predictions of tangential velocity for the standard Rushton turbine flotation tank.

The following graphs show the numerical predictions of tangential velocity for the standard Rushton turbine tank at three regions, high, medium and low turbulent zones (see: Figure 3-18). In all graphs the symbols display the experimental measurements of Newell and the line styles correspond to the different turbulence models.

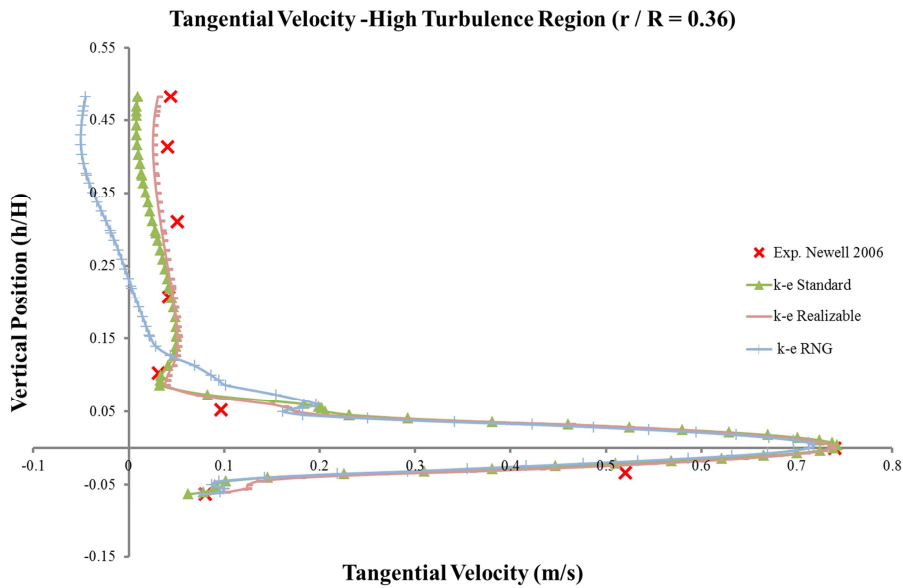


Figure A. 16 Numerical predictions of tangential velocity as a function of non-dimensional distance from the top of the tank with different RANS-based turbulence model for standard Rushton turbine tank at high turbulence region

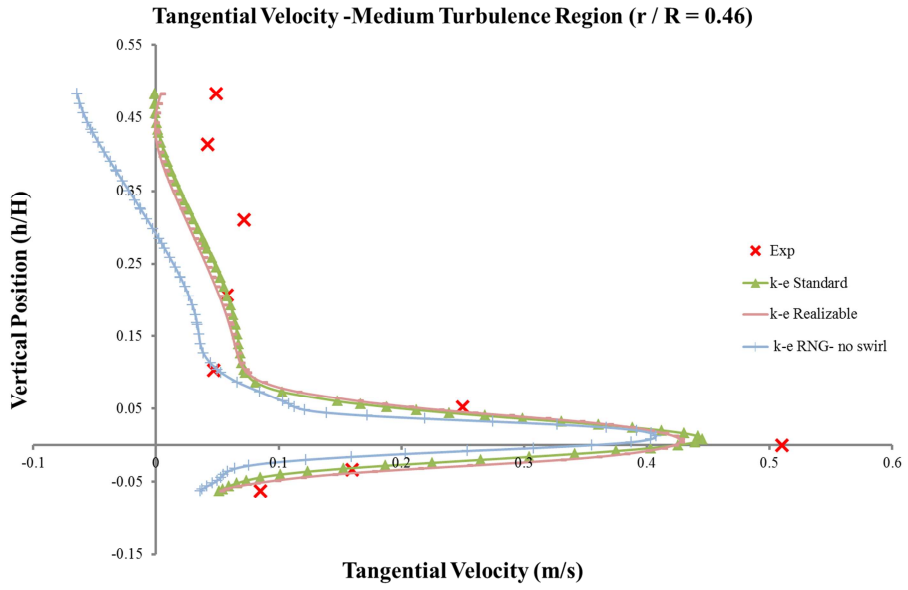


Figure A. 17 Numerical predictions of tangential velocity as a function of non-dimensional distance from the top of the tank with different RANS-based turbulence model for standard Rushton turbine tank at medium turbulence region

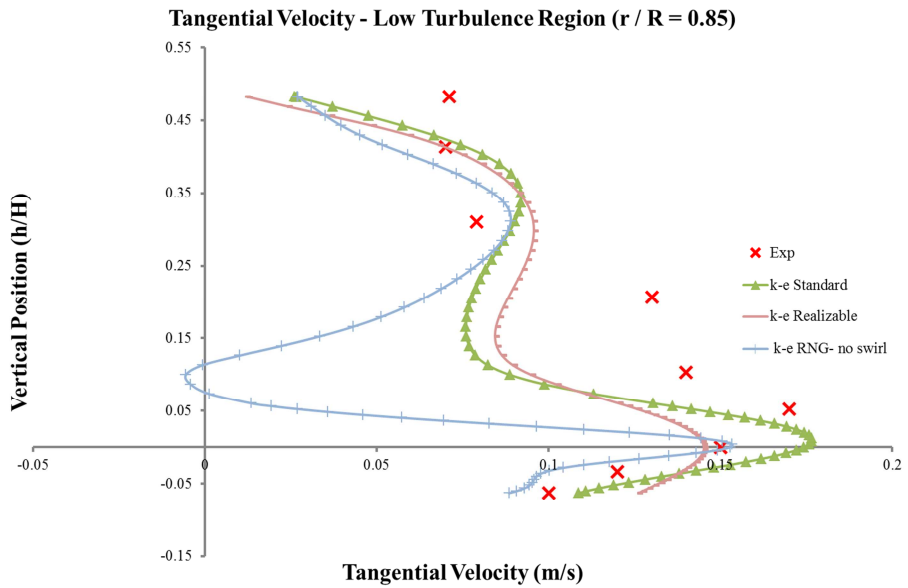


Figure A. 18 Numerical predictions of tangential velocity as a function of non-dimensional distance from the top of the tank with different RANS-based turbulence model for standard Rushton turbine tank at low turbulence region

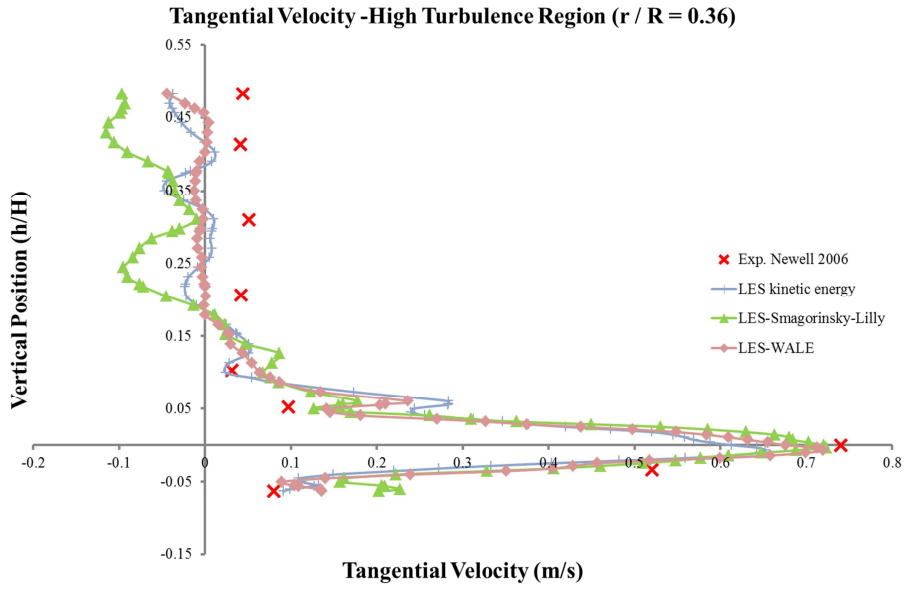


Figure A. 19 LES predictions of tangential velocity as a function of non-dimensional distance from the top of the tank with sub-grid scale models for standard Rushton turbine tank at high turbulence region

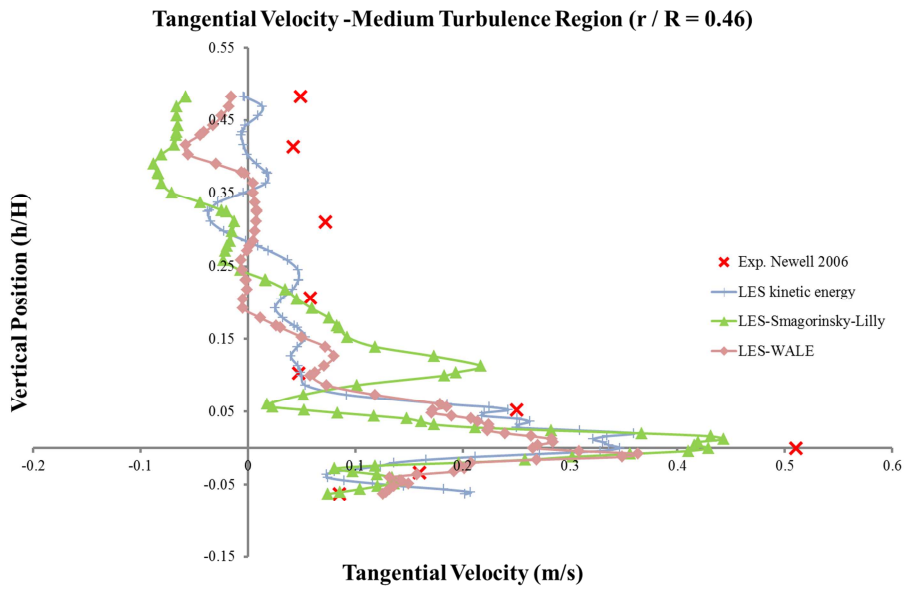


Figure A. 20 LES predictions of tangential velocity as a function of non-dimensional distance from the top of the tank with sub-grid scale models for standard Rushton turbine tank at medium turbulence region

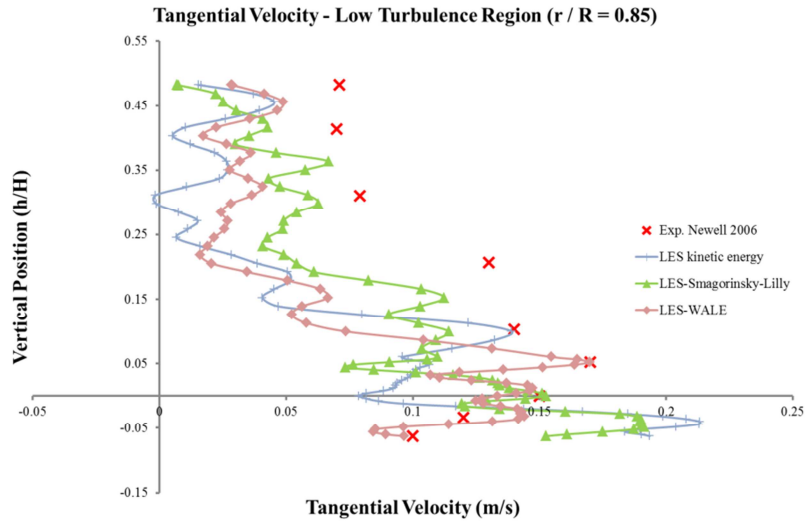


Figure A. 21 LES predictions of tangential velocity as a function of non-dimensional distance from the top of the tank with sub-grid scale models for standard Rushton turbine tank at low turbulence region

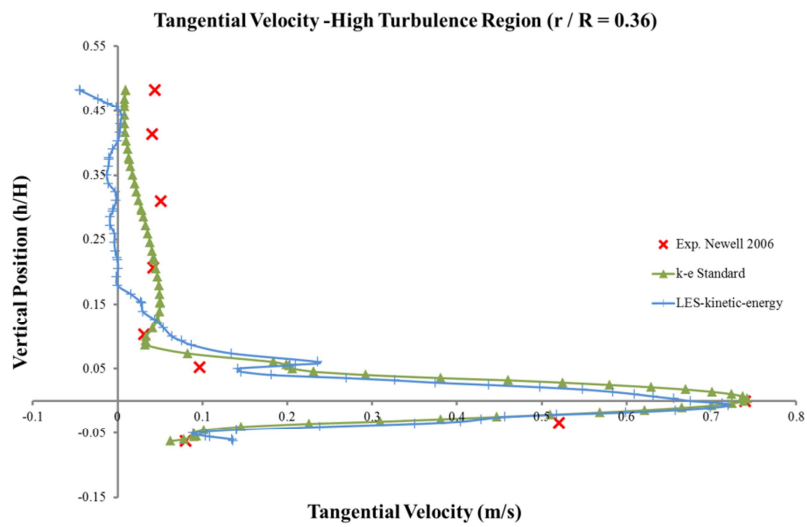


Figure A. 22 Numerical predictions of the tangential velocity; comparison of the k-ε standard turbulence model and LES with kinetic-energy subgrid scale model for the standard Rushton turbine tank at the high turbulence region

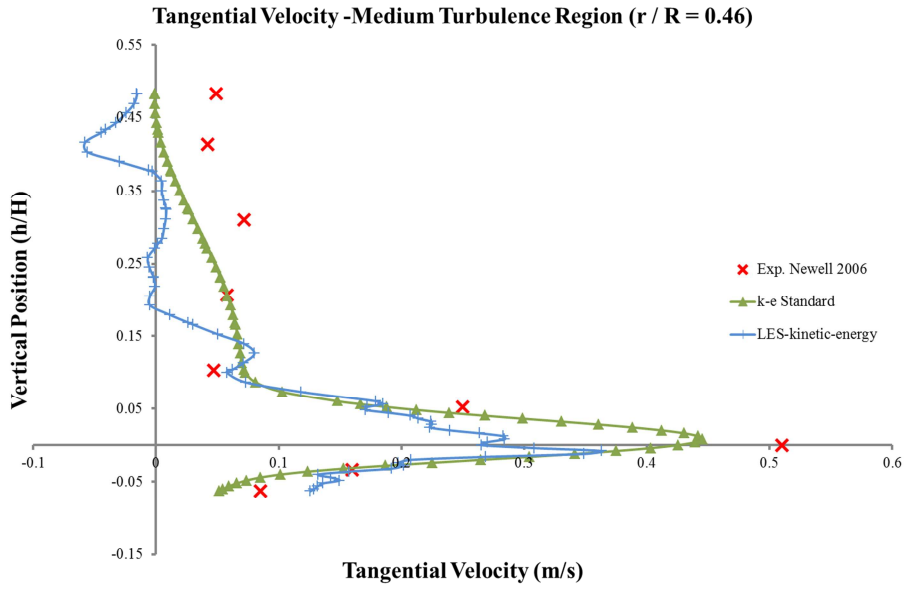


Figure A. 23 Numerical predictions of the tangential velocity; comparison of the k-ε standard turbulence model and LES with kinetic-energy subgrid scale model for the standard Rushton turbine tank at the medium turbulence region

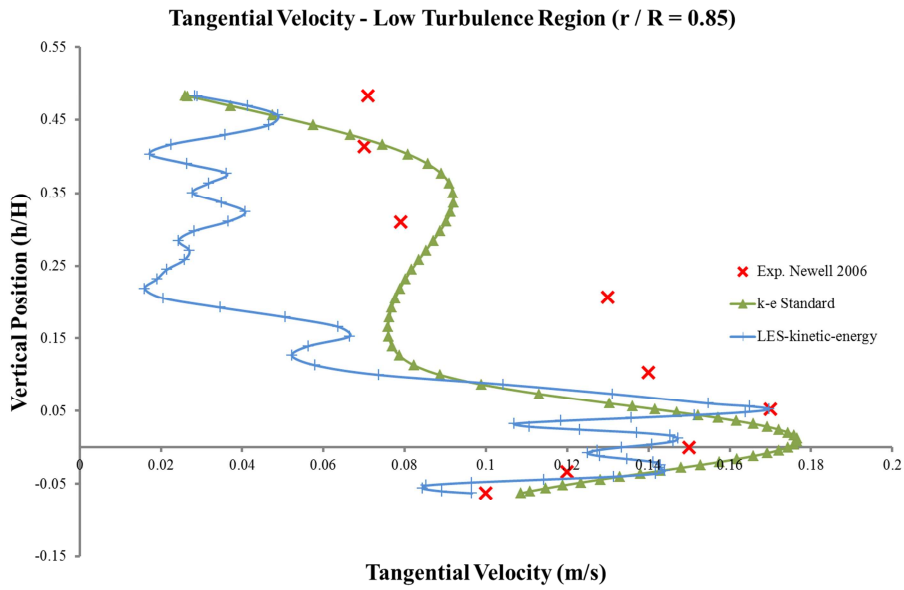


Figure A. 24 Numerical predictions of the tangential velocity; comparison of the k-ε standard turbulence model and LES with kinetic-energy subgrid scale model for the standard Rushton turbine tank at the low turbulence region

Appendix B: Results of the gas-liquid simulations for different operational and geometrical conditions

The purpose of this appendix is to report the numerical predictions of the gas holdup using the developed CFD methodology from Chapter 4. The proposed correlation of Lane was used for the drag coefficient and the last column in the table reports the percentage of difference between the CFD data and the experimental measurements of Newell.

Table B. 1. Numerical predictions of the gas holdup for different geometrical and operational conditions using Lane's drag coefficient correlations.

Case no.	Tank volume (l)	Impeller speed (rpm)	Superficial gas velocity (cm/s)	Exp. Gas holdup (%)	Sim. Gas holdup (%)	Error (%)
S1	2.25	350	0.35	5.2	6.51	25.17
S2		350	0.45	6.7	6.59	-1.58
S3		350	0.55	7.4	8.03	8.46
S4		450	0.35	6.7	6.98	4.16
S5		450	0.45	7.8	8.23	5.56
S6		450	0.55	8.9	9.06	1.78
S7		550	0.35	7.8	7.90	1.32
S8		550	0.45	8.9	8.96	0.71
S9		550	0.55	10.7	9.26	-13.50
S10		800	0.35	10.7	10.75	0.46
S11		800	0.45	12.6	13.61	8.00
S12		800	0.55	14.1	14.17	0.51
M1	10	300	0.35	6.4	8.04	25.62
M2		300	0.45	8.5	9.36	10.12
M3		300	0.55	10.6	10.49	-1.04
M4		380	0.35	7.2	8.20	13.86
M5		380	0.45	8.5	9.05	6.47
M6		380	0.55	9.8	9.05	-7.62
M7		470	0.35	8.5	9.53	12.12
M8		470	0.45	9.8	7.66	-21.84
M9		470	0.55	11.1	13.18	18.74
L1	50	255	0.1	2	3.24	38.25
L2		255	0.17	4.5	6.08	26.05
L3		255	0.35	6.5	8.44	22.99
L4		330	0.1	3	4.07	26.38
L5		330	0.17	4.5	5.46	17.57
L6		330	0.35	7.5	6.92	-8.44

Appendix C: An user defined function example for the flotation sub-processes modelling

This appendix shows an UDF example for the flotation sub-processes modelling. The following UDF has been implemented in the CFD solver to compute the collision rate between the solid particles and air bubbles based on Eq. 5.6 and Eq. 5.7.

```
#include "udf.h"

DEFINE_ON_DEMAND(collision_probability)

{

    Domain *mixd;
    /*INPUTS*/
    real d_b = 0.0015675;
    real d_p = 0.000040;
    real kin_vis = 4.15e-7;
    real re_b;
    real x_vel_g, y_vel_g, z_vel_g, x_vel_f, y_vel_f,
z_vel_f, slip_x, slip_y, slip_z, slip_vel;
    real p_c;
    Thread *t;
    cell_t c;
    Thread *mixt;
    Thread *thread_g;
    Thread *thread_f;
    thread_loop_c(mixt,mixd)
    {

        thread_g = THREAD_SUB_THREAD(mixt,1);
        thread_f = THREAD_SUB_THREAD(mixt,0);
        begin_c_loop(c,mixt)
        {

            /*Slip velocity*/
            x_vel_f = C_U(c,thread_f);
            y_vel_f = C_V(c,thread_f);
            z_vel_f = C_W(c,thread_f);
            x_vel_g = C_U(c,thread_g);
            y_vel_g = C_V(c,thread_g);
            z_vel_g = C_W(c,thread_g);
            slip_x = -x_vel_f + x_vel_g;
            slip_y = -y_vel_f + y_vel_g;
            slip_z = -z_vel_f + z_vel_g;
```

```

slip_y*slip_y + slip_z*slip_z);
slip_vel = sqrt(slip_x*slip_x +
re_b = (d_b*slip_vel)/kin_vis;
p_c = (1.50 +
0.266667*pow(re_b,0.72))*((d_p*d_p)/(d_b*d_b));
C_UDMI(c,mixt,1) = p_c;
}
end_c_loop(c,mixt)
}

}
DEFINE_ON_DEMAND(collision_rate)
{
Domain *d;
/*INPUTS*/
real rho_g = 1.2250;
real rho_f = 1032.13;
real rho_p = 2650;
real mu_f = 0.000431145;
real d_b = 0.00156750;
real d_p = 0.000040;
real kin_vis = 4.15e-7;
real c_v = 0.0194742;
real epsilon, u_b, u_p, n_b, n_p, void_g, void_f;
real x_vel_f, y_vel_f, z_vel_f, vel_f, d2_crit;
real z_pb;
Thread *t;
cell_t c;
Thread *mixt;
Thread *mixd;
d = Get_Domain(2);
thread_loop_c(t,d)
{
mixt = THREAD_SUPER_THREAD(t);
begin_c_loop(c,t)
{
epsilon = C_D(c,t);
x_vel_f = C_U(c,t);
y_vel_f = C_V(c,t);
z_vel_f = C_W(c,t);
vel_f = sqrt(x_vel_f*x_vel_f +
y_vel_f*y_vel_f + z_vel_f*z_vel_f);
C_UDMI(c,mixt,2) = vel_f;

```

```

                                d2_crit                =
(15.0*mu_f*vel_f*vel_f)/(0.5*rho_f*epsilon);
                                void_f = C_VOF(c,t);
                                void_g = 1.0 - void_f;
                                n_b = (void_g)/(0.523598776*d_b*d_b*d_b);
                                n_p                =
(void_f*c_v)/(0.523598776*d_p*d_p*d_p);
                                C_UDMI(c,mixt,3) = n_b;
                                C_UDMI(c,mixt,4) = n_p;
                                if(d_b*d_b>d2_crit)
                                    {
                                u_b                =
(0.4*pow(d_b,0.77778)/pow(kin_vis,0.3333)) * (pow((rho_f-
rho_g)/rho_f,0.66667)) * pow(epsilon,0.44444);
                                u_p                =
(0.4*pow(d_p,0.77778)/pow(kin_vis,0.3333)) * (pow((rho_p-
rho_f)/rho_f,0.66667)) * pow(epsilon,0.44444);
                                z_pb                =
5.0*n_p*n_b*((d_p+d_b)/2.0)*((d_p+d_b)/2.0)*sqrt(u_p*u_p+u_b*u_b);
                                C_UDMI(c,mixt,5) = u_b;
                                C_UDMI(c,mixt,6) = u_p;
                                C_UDMI(c,mixt,7) = z_pb;
                                    }
                                else
                                    {
                                z_pb                =
1.29441728*n_p*n_b*pow(((d_b+d_p)/2.0),3.0)*sqrt(epsilon/kin_vis);
                                C_UDMI(c,mixt,7) = z_pb;
                                    }
                                }
                                end_c_loop(c,t)
                                }
}

```

Appendix D: Summary of the operational conditions for the flotation simulations.

This appendix summarizes the operational conditions namely, angular velocities of impeller, superficial gas velocity, bubble size, and contact angle for the flotation simulations reported in Chapter 5.

Table D. 1. Operational conditions for the flotation simulations.

Mineral	Impeller speed (rpm)	Superficial gas velocity (cm/s)	Bubble diameter (cm)	Contact angle (degree)
Quartz	350	0.35	0.415	80
	450	0.35	0.372	80
	550	0.35	0.352	80
	800	0.35	0.330	80
	470	0.45	0.120	73
	470	0.45	0.120	80
	470	0.35	0.117	73
	650	0.35	0.139	73
	470	0.35	0.117	73
	470	0.45	0.120	73
Galena	650	0.55	0.065	72
	650	0.55	0.065	79
	650	0.55	0.065	72
	720	0.55	0.070	72
	800	0.55	0.070	72
	650	0.55	0.065	79
	720	0.55	0.070	79
	800	0.55	0.070	79